Université de Valenciennes et du Hainaut-Cambrésis

THESE DE DOCTORAT / UNIVERSITE DE VALENCIENNES ET DU HAINAUT-CAMBRESIS

Pour le grade de

DOCTEUR DE L'UNIVERSITE DE VALENCIENNES

Mention : Micro Nano Technologies, Acoustique et Télécommunications
Ecole Doctorale : Ecole Doctorale Régionale des Sciences Pour l'Ingénieur (SPI 072)
Laboratoire : Institut d'Electronique, de Micro-Electronique et de Nanotechnologie/Département d'Opto-Acousto-Electronique (IEMN/DOAE)

Présentée par

BANDAR ALSHEHRI

DESIGN, FABRICATION AND CHARACTERIZATION OF III-NITRIDES-BASED PHOTODIODES: APPLICATION TO HIGH-SPEED DEVICES

CONCEPTION, FABRICATION ET CARACTERISATION DE PHOTODIODES A BASE DE NITRURES SEMICONDUCTEURS : APPLICATION AUX COMPOSANTS ULTRA-RAPIDES

Soutenance le 7 Octobre 2016 devant le jury composé de

Prof. Hongwu LI   Rapporteur Université de Nantes

Prof Xixiang ZHANG   Rapporteur University KAUST Thuwal

Pr Abderrahim RAMDANE   Examinateur LPN Marcoussis

Prof Didier DECOSTER   Examinateur Université Lille 1

Prof Tuami LASRI   Examinateur Université de Lille 1 (**Président du jury**)

Prof Elhadj DOGHECHE   Directeur de thèse, Université de Valenciennes

Table of Contents

General introduction

III-Nitride materials have exhibited a major attention in the research community. These materials with bandgap varying from 0.7 eV to 6 eV allow several prospects ranging from deep ultraviolet up to near infrared. Lately, numerous optical applications have been developed using these materials such as light emitting diodes (LED), laser diodes (LD) and UV detectors [1][2][3]. Besides, solar cells based on nitride materials have actually attracted researchers for terrestrial and space-based applications [4]. High power electronics have been developed using nitride-based devices such as transistors [5]. As well as, researchers have considered III-Nitride materials as the key element in the ground-based communications and biological agent detection [6][7].

The properties of III-Nitride materials have led to consider the development of this project. In the Institute of Electronics, Microelectronics and Nanotechnology (IEMN), this research topic has been one of the optoelectronics-group's preoccupations. The main motivation has been the continuation to develop InGaN/GaN based photodetectors. It has been started with PhD student GAUTHIER-BRUN Aurélien through the joint collaboration between IEMN and the Institute of Materials Research and Engineering (IMRE) in Singapore. It has occurred within the framework of MERLION project supported by the Embassy of France in Singapore. Both sides have created a long-term collaborations with the aim of enhancing the knowledge of III-nitride materials. The optimization of InGaN materials has been the main purpose of GAUTHIER's PhD project. The IMRE has a strong capabilities in the epitaxial growth and material characterization. Where the IEMN has the strong side in the fabrication and device characterization. However, the achievement of photodetector based on InN material has met difficulty due to the low quality of material. Photodetector design and fabrication process are subjected to be optimized in order to substitute the InN by the InGaN material which is well-known. It means the expected photodetector in our project will work in the visible range of electromagnetic spectrum instead of infrared range.

As IMRE has encountered technical issues in the InGaN/GaN growth, we have aimed our collaboration to King Abdullah University of Science and Technology (KAUST), and particularly Photonics Lab.

The growth of material is achieved using Molecular Beam Epitaxy (MBE). Moreover, a commercial grower of InGaN/GaN materials (NOVAGAN) has been communicated in order to provide samples with different indium content using Metal-Organic Chemical Vapor Deposition (MOCVD).

The plan of our research is firstly to study the material quality issued from commercial and institutional provider. This will permit to investigate the different configurations of material growth using MBE and MOCVD. The indium content will also be investigated as function of absorbent wavelength in the PIN structure. The study of material quality will provide information about the expected device performance permitting to achieve high quality photodetector. The second objective is to design PIN structure suitable for different size of photodiode and adapted to the requirements of device characterization. Once photodiodes are fabricated, static and dynamic characterizations are planned in order to achieve the photodiode response.

The challenge in the fabrication of InGaN/GaN materials is to obtain high quality of device. The III-Nitride compounds are known in the research community to be critical in the fabrication process. Several optimizations and tests in clean room are imperatives before proceeding the photodiode fabrication. It is noted that a commercial wafer is rather costly in the order of 2500 euro. For this reason, the good preparation of such fabrication process should be taken into account. Besides, the device characterization should be sufficiently prepared due to the lack of experience in our group against this type of materials. Physical justifications in each stage are crucial in order to understand the device response which is fundamental in the performance improvement.

The manuscript is organized in three chapters. The first describes an introduction to III-Nitride based high speed devices. In this chapter, an overview of III-N Nitride materials and their applications is detailed. The GaN as a potential candidate for high speed devices is described as well as its figure of merit. Principal of the photodiode as a key element is presented. The fundamental properties of piezoelectric polarization, mechanical properties, crystal growth techniques and substrates are illustrated. Electronic band structure and electrical properties are also presented. Optical properties of III-nitride materials are shown in order to clarify the different properties of InGaN alloy. The state of the art in GaN photodetectors is described before conclusion of chapter 1.

The second chapter describes the material characterization of InGaN/GaN layers. It shows the different growth of InGaN/GaN structure with different indium composition. The characterization techniques used during this phase will be briefly explained as structural and optical characterization techniques. Samples in PIN structure, Single Layer (SL) and Multiple Quantum Well (MQW) of InGaN are fully characterized with different indium content varying from 10% to 50 %. A detailed explanation of results issued from structural and optical characterizations are illustrated. Samples grown by MOCVD and MBE are also subjected to comparison. Besides, characterization of nanostructured GaN are described before conclusion of chapter 2.

Chapter III describes the fabrication and device characterization of PIN photodiodes. Different designs have been performed for planar large-scale and micro-scale photodiode. Electrical characterizations techniques will be detailed in order to extract external quantum efficiency as well as photocurrent measurement using laser source. The setup of noise measurement is described to obtain the cut-off frequency of fabricated photodiodes. Study of GaN deep etching and annealing effect are also presented. Moreover, the influence of the MQW configuration and growth technique on the device performance are also studied. The fabrication of vertical micro-photodiode is presented before the conclusion of chapter 3.

General conclusions issued from different stages are shown in the last section of manuscript. Overview of achieved results during material characterizations and device fabrication are described. Perspective works related to the present achievements are illustrated in order to optimize the photodiode design leading to high device performance.

Chapter I.   Introduction to III-Nitride based high speed devices

1.1. Overview of III-N Nitride materials and their applications

Flexible and direct bandgap of III-Nitride compounds (AlGaInN) offers significant advantage for several applications over the whole spectral. It ranges from deep ultraviolet of 200 nm (AlN) to near infrared 1770 nm (InN) which delivers a tuning spectrum as shown in Figure 1.1 [8]. An additional eventual benefits by the use of these materials are their radiation hardness and the expected lower intrinsic noise and dark current in comparison with narrow-band-gap materials [9].
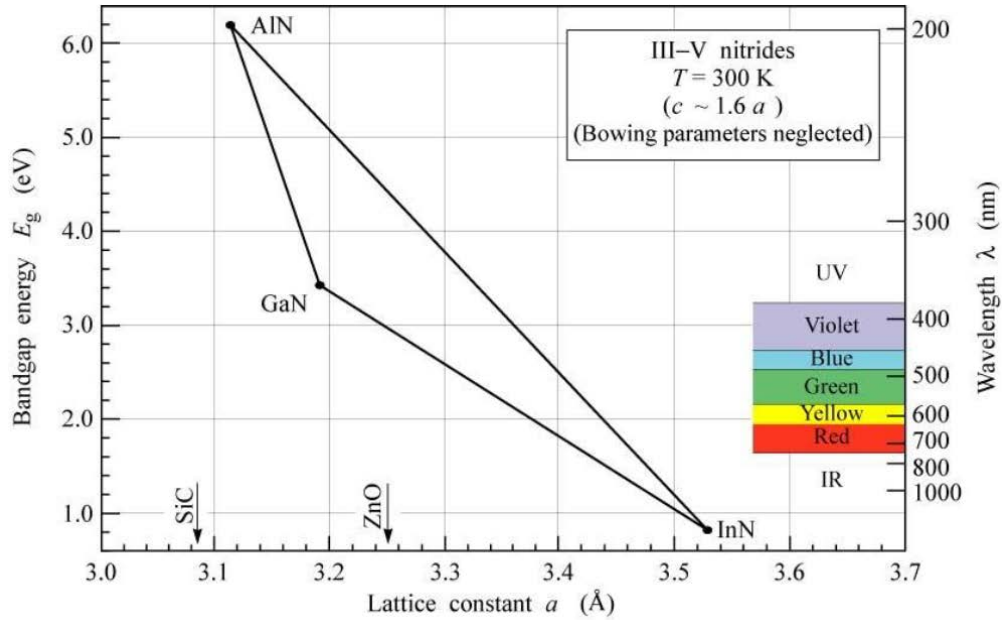
Figure 1.1: Bandgap energy vs. lattice constant a for III-nitrides at 300 K

In 1990's, the realization of LED has been the revolution of the decade [1][10]. This finding has motivated the investigation of III-Nitrides group and several devices based on these materials have been developed. LED technology was an important key for solid-state lighting (SSL), it holds promise as potential device with more efficiency, more compact and longer lasting comparing to incandescent and fluorescent light sources [11]. InGaN materials have achieved more attention as potential materials for fabricating efficient blue-emitting devices as well as laser diodes [12]. In 2014 the Nobel Prize has been awarded to I. Akasaki, H. Amano and S. Nakamura for "the invention of efficient blue light-emitting diodes" which has enabled bright

and energy- saving white light sources. The tuning of the band gap could be directly acquired by varying the In composition in InGaN alloys. High-brightness blue, green and yellow LEDs with quantum well structures have been achieved by changing the In content [13]. Researchers have been interested to the ultraviolet (UV) and Visible spectral regimes due to their important applications which promise more reliability and higher efficiency for optoelectronic devices. III-Nitride applications expand from quotidian needs to military and space usages thanks to their remarkable properties such as robust and compact materials.

The direct and tunable band gap of $In_xGa_{1-x}N$ alloys spanning from 0.7 to 3.4 eV is very attractive for designing multijunction solar cells for both terrestrial and space-based applications due to high absorption coefficients [4][14]. The realization of highly efficient solar cells using InGaN compounds is a promising technology to increase the conversion efficiency of current photovoltaic cells [15]. InGaN compounds have the benefits of radiation resistance, high carrier mobility, high temperature and high drift velocity which will altogether contribute to the realization of efficient device for potential use under concentrated sunlight [4][15][16].

Further important applications of III-nitride materials are the high-frequency and the high-power electronics using high-electron-mobility transistors (HEMT) and photodetectors [5][17]. The $Al_xGa_{1-x}N$ material system covering the 200–365 nm regime is an excellent material choice for biological agent detection which are luminescent in the UV region [6]. It enables also the non-line-of-sight secure ground-based communications and combustion monitoring [7][18], as well as in astronomy for cosmic events analysis and in space exploration [9][19]. A novel gas-sensing devices based on Schottky diodes besides high-electron-mobility transistors (HEMT) are reported for missile plume detection [18]. AlGaN is also a potential candidate for photodetection in the solar-blind region with a strong absorption of UV in the ozone layer below 280 nm [20].

The optimization of epitaxial techniques for gallium nitride (GaN) has been delayed for several decades because of the lattice mismatch with the substrate. The information related to structural quality, dislocation density and optical properties is still highly required. In 1969, Maruska et al. have demonstrated the first deposition of GaN grown by hydride vapor phase epitaxy [21]. It was determined that GaN has a direct energy bandgap of 3.39 eV with high inherent electron concentration about n = 10^{19} cm^{-3}. Generally, GaN films are grown by Metal

Organic Chemical Vapor Phase Deposition (MOCVD). Lately, plasma-induced or gas-source Molecular Beam Epitaxy (MBE) was introduced [22]. Nowadays, sapphire substrates are generally used for the epitaxial growth of thin III-nitrides layers and their related applications to electronic and optoelectronic devices, regardless of a large lattice mismatch of about 16% with GaN [23]. The first deposition of InGaN has been reported by Osamura et al [24]. The samples were polycrystallites and grown by electron-beam plasma deposition on sapphire and quartz substrates. InGaN deposition has been optimized since the 2000's and device manufacturing based on this alloy will become an important research topic [25]. The growth of p-GaN and n-GaN layers has been achieved and permitted to demonstrate the first LED based on p-n junction [26]. In order to improve the surface morphology with High-quality GaN films, Nakamura et al. have proposed the growth of a low-temperature GaN buffer layer to decrease the dislocations formed at the GaN/sapphire interface [27]. Using this method, they have achieved a very high electron mobility of 900 cm^2/Vs and a relatively low background electron concentration n ≈ 2×10^{16} cm^{-3}. P-GaN/n-InGaN/n-GaN double-heterostructure (DH) LEDs were fabricated successfully for the first time in 1993 .

Regarding the indium nitride (InN), Davydov and Wu have recently analysed the InN material and concluded a bandgap of 0.7 eV [28]. These analysis leads to the conclusuion that the InN bandgap is much smaller than the value of 1.8 eV previously reported [29].

Quantum cascade lasers (QCLs) for terahertz (THz) applications are typically based on III-Nitride materials and could be a potential candidate for room temperature (RT) operation [30]. Recent experimental demonstrations offer opportunities toward an efficient THz QCL realization [31].

1.2. GaN as a potential candidate for high speed devices

A major efforts have been revealed in the high speed devices and terahertz (THz) applications in terms of research topics. It has early been produced numerous devices as high speed electronics, ultraviolet emitters and detectors [32][33]. III-V and III-Nitride materials based devices have attracted the research community for power switching and millimeter-wave

applications due to their outstanding properties. Recent improvements in the device development have illustrated the cutting-edge results in high-speed data rate connectivity and integrated circuits [34]. Actually, imaging sensors based on high speed electronics show an interest matter due to their sensitive applications in military domain and homeland security [35].

Gallium nitride (GaN) as a member of III-Nitride family has become the revolutionary material thanks to its electronic and optical properties. Direct, flexible and wide bandgap of GaN makes this materiel a crucial candidate offering high-frequency, high bandwidth, high power and high efficiency devices. Early, light emitting diode (LED) has been the first theme of GaN research followed later by UV photodetectors and laser sources [32], [36][37]. GaN based detectors are actually suitable in the use of full color display, high density information storage, and under water communication [17]. Si and GaAs as conventional semiconductors cannot be used in these areas. The capacity of GaN-based devices is highly competitive to any other materials for high speed applications. Missile interception and space based optical communications require high speed photodetector [38]. Actually, the main challenge in nitride materials is the red and green visible emitters and deep UV laser sources. GaN is a significant candidate for RF power amplifiers in microwave and high frequencies, and high-voltage switching devices. Due to its reduced system current and high operation voltage in RF technology, GaN is able to offer high power and gain as well as high efficiency. The bandgap of 3.4 eV makes GaN a robust material due to its bonded atoms with a very ionic gallium-nitrogen bond comparing to GaAs and Si with 1.4 and 1.1 eV respectively [39]. This property offers high breakdown field which permit to operate at much higher voltage. GaN has a high electron saturation velocity which can deliver a high current density. High voltage and high current density can produce high RF power with small device leading to lower cost, lower combining loss, lower capacitance and lighter weight.

Comparing to GaAs, GaN devices provides about ten times power density as well as five times higher voltage operation. It could also deliver twice higher current leading to higher bandwidth capability and less fallout rate. It means GaN can deliver higher critical field comparing to GaAs (3.3 MV/cm vs. 0.4 MV/cm respectively) which supplies higher power density and higher electron saturation velocity ($2.5{\times}10^7$ cm/sec vs. $1{\times}10^7$ cm/sec respectively) [40][41]. These will lead to ultrafast transition time and consequently higher frequency because

the saturation velocity is directly proportional to frequency. In the same way as the diamond, GaN has outstanding thermal conductivity comparing to GaAs and could be subject to high temperature operation as well as heat dissipation (2.3 W/cm.K for GaN vs. 0.46W/cm.K for GaAs) [42]. In space application, GaN material is an ideal candidate thanks to its radiation-resistance comparing to others materials as GaAs, also in term of high thermal stability [4][43]. Regarding the electron mobility, GaN has six times lower mobility than GaAs (1000 vs 6000 $cm^2.V^{-1}s^{-1}$ respectively) which almost similar to silicon electron mobility (1000 vs 1200 $cm^2.V^{-1}s^{-1}$ respectively) [44][45]. However, the use of heterojunction structures could resolve this issue and provides a higher mobility than many other semiconductors [46].

Among the most important optical property which possesses GaN material and related alloys is the absorption coefficient which directly influence the device operation. It has value in excess of $10^5 cm^{-1}$ comparing to GaAs (10^4 cm^{-1}) and Si (10^3 cm^{-1}) measured near the band edge [47]. It means the incident light will be efficiently absorbed in very short thickness of material. 10^4 cm^{-1} of absorption coefficient needs 1 µm of absorption thickness, while $10^5 cm^{-1}$ needs only 100 nm of thickness to be efficiently absorbed. This parameter allows designing a PIN structure with very thin intrinsic layer which will reduce the transit time and subsequently increasing the cut-off frequency (RC negligible in a small area of mesa). This makes GaN a primary candidate for high speed photodetectors.

III-Nitride seems to be very promising materials due to its electrical and optical properties. As it can deliver higher critical field, this will supply higher power density as well as higher electron saturation velocity. Accordingly, ultrafast transition time will be achieved and consequently we will reach higher frequency. Optical and electrical properties for GaN have been reported at high frequencies using THz time-domain spectroscopy [48]. THz frequencies have been demonstrated using existing input sources in the radio frequencies (RF) domain with non-linear devices based on GaAs Schottky diodes. Though, the system efficiency seems to be very low in terms of output power due to the limitation of GaAs material which impacts on the system performance. As GaN and related alloys have demonstrated an efficient candidate in optoelectronics, it preserves a potentiality to be an efficient, compact and tunable source/detector for THz domain. The comparison of the Figure of Merits hereafter promotes GaN as a perspective candidate in THz regime.

As a potential application, THz radiation is absorbed very close to the surface of skin in the human body and could be a promising candidate to detect diseases as skin cancer. As well as, it could be used in airport for body scanners. The current resolution for used scanner is about one centimeter while using GaN could achieve a hundred of microns in resolution scan. One more advantage in the use of GaN, it is reliable and can operate under extreme conditions. THz provides safer analysis comparing to conventional X-ray based techniques because of deep penetration through body and tissue selectivity.

In electronic approach, recent investigations have reported ultra-fast transistors delivering frequencies above 100 GHz. High electron mobility transistors (HEMTs) and heterojunction bipolar transistors (HBT) are the electronic devices employed to generate high frequency [49]. However, the limitation of frequency in these electronic devices remains an obstacle due to its capacitive effects and carrier transit time. That is why transistors and diodes in electronic approach meet difficulty in the range of THz.

In optic approach, the generation of THz waves are based on increasing the wavelength of laser source. Within the first THz source, gas laser has been a candidate to produce terahertz radiations as well as germanium-based lasers. In these systems, the difficulty has been the control of heating effect which require liquid helium cooling [50].

Optoelectronic approach, a third approach within electronic and optic could be a potential technique in order to achieve THz radiation by means of photoconduction and Photomixing phenomena. Capacitive effects and carrier transit time will be in consideration. Photodetector with the non-linearity property in which the current or potential is related to the received optical power, will generate signal and then will be radiated through antenna. High responsivity and high speed photodetector are fundamental factors associated to the quality of material growth.

1.3. GaN: Figure of merit

The concept of figure of merit has been introduced in order to better represent and compare the performance or efficiency of a given device, material, or procedure. It connects the electrical parameters to the physical properties of the concerned material. It is for this reason that

various figures of merit have been developed. Johnson, Baliga and Keyes are predominant Figures of Merit. Johnson's Figure of Merit (JFM) evaluates the potential of the materiel in term for application at high frequency taking into account the breakdown field and saturation velocity of carriers [51]. Baliga's Figure of Merit (BFM) evaluates the electrical permittivity of material, the breakdown field and mobility [52]. Keyes's Figure of Merit (KFM) involves the thermal conductivity of material, the electrical permittivity and the saturation velocity of carriers [53]. Table 1.1, illustrates Figures of Merit for conventional semiconductors normalized to silicon. These results demonstrate the significant potential candidate GaN comparing to both Si and GaAs in terms of power, breakdown voltage and thermal conductivity despite relatively low values of electron mobility in its conduction band. This makes GaN an optimal material for the fabrication of electronic devices, the control and the conversion of electrical energy. Diamond appears as a promising semiconductor for all applications in microelectronics. However, its potential applications are currently unreachable, mainly because of dopants.

Figure of Merit	Si	GaN	GaAs	4H-SiC	Diamond
JFM	1	1100	1.44	655	3657
KFM	1	2.6	0.3	5.1	32
BFM	1	1400	9.2	1303	8400

Table 1.1: Figures of Merit for conventional semiconductors normalized to silicon.

1.4. Photodiode as a key element

A photodetector is a device allowing the detection of the light according to the application requirements. It is based on three stages, the generation of free carriers due to the absorption of incident photons, the transport of photogenerated carriers and the interaction of the electrical signal with the circuit. External quantum efficiency and responsivity are means of quantification for photodetectors. There are several types of photodetectors: photodiodes (PN, PIN, UTC,

Schottky and avalanche), photoresistor, phototransistor and photoconductor. In the following, we focus on PIN photodiodes.

1.4.1. PIN photodiode

Photodiode are one of the common devices for light detection and measurement. It delivers a current when photons are absorbed by means of light exposition. The electron-hole pairs are generated when a semiconductor is under illumination with photon having energy greater than the energy bandgap of the material. PIN photodiode is achieved by creating a large depletion region where the light conversion takes place by adding an intrinsic area into the PN junction to create a PIN junction. Accordingly, it consists of three layers: an intrinsic layer sandwiched between n and p layers, both heavily doped. Under reverse bias, the depletion region extends all over the intrinsic layer and becomes the absorption layer. When the carriers are crossing the depletion region, this will permit to define the transit time and the capacity of the junction. Consequently, they depend on the relative permittivity of the semiconductor, the surface of the top layer and the thickness of the absorption layer. The speed of the photodiode is determined by two factors: the first depends of the physical mechanism in the photodiode (transit time), the second is the product of the equivalent load circuit and the capacity of the photodiode (RC time constant). There is a compromise in the realization of high bandwidth photodiode between transit time and the capacity. Increasing the thickness of the intrinsic layer improves the quantum efficiency and decreases the capacity which leads to increase the bandwidth, but the transit time will increases, which conversely tends to decrease the bandwidth. These factors are subject to an optimal study in order to improve the bandwidth and to enhance the photodiode efficiency. The external quantum efficiency (*EQE*) describes the number of electrons/holes pairs generated by absorbed photon where are participating in the photocurrent. The EQE is calculated using the formula:

$$EQE = R \times \frac{hc}{q\lambda} \qquad \qquad \textit{Equation 1.1}$$

Where (*R*) is the responsivity at the wavelength (*λ*), (*h*) is the Planck's constant, (*c*) is the speed of light and (*q*) is the electron charge. The responsivity (A/W) illustrates the ratio between the photocurrent of the photodiode and the incident power of the light source as:

$$R = \frac{photocurrent\ (A)}{total\ power(W)}$$

<div align="right">*Equation 1.2*</div>

The cut-off frequency at 3dB related to the transit time is expressed as following:

$$F_t = \frac{3.5\ v}{2\ \pi\ L}$$

<div align="right">*Equation 1.3*</div>

Where (L) is the thickness of the intrinsic layer and (v) introduces the saturation velocity of electrons (v_e) and holes (v_h) as:

$$\frac{1}{v^4} = 0.5 \left[\frac{1}{v_e{}^4} + \frac{1}{v_h{}^4} \right]$$

<div align="right">*Equation 1.4*</div>

The cut-off frequency at 3dB related to RC time constant is expressed as following:

$$F_{RC} = \frac{1}{2\pi RC}$$

<div align="right">*Equation 1.5*</div>

Where (R) is the total resistance of photodiode and the load resistance and (C) is the capacity of the photodiode which is defined by:

$$C = \frac{S\ \varepsilon}{L}$$

<div align="right">*Equation 1.6*</div>

Where (S) is the photodiode surface, (ε) is the absolute permittivity which is defined as $\varepsilon = \varepsilon_r\ \varepsilon_0$, (ε_r) is the relative permittivity of the material and (ε_0) is the vacuum permittivity $(8.854\times10^{-12}$ F/m). The cut-off frequency of the photodiode at 3dB can be illustrated as:

$$\frac{1}{Fc^2} = \frac{1}{Ft^2} + \frac{1}{F_{RC}^2}$$

<div align="right">*Equation 1.7*</div>

1.5. Fundamental properties

1.5.1. Crystal Structure

III-nitrides structure crystalize in different forms, hexagonal wurtzite, cubic zinc-blende and rock salt structures. The more commonly studied configuration is the wurtzite one, as it is the more thermodynamically stable form under ambient conditions for bulk AlN, GaN, and InN at

low pressure [54]. Cubic zinc-blende structure compared to the hexagonal structure, it theoretically has better electrical properties as higher mobility, isotopic properties (due to its cubic symmetry) and high optical gain. However, these benefits have not been observed experimentally because of the difficulties in producing a uniphasic material with low defect density [55]. The rock salt structure is very problematic to grow for GaN due to high pressure condition to produce with an estimated pressure value of 52.2 GPa [56]. This structure is therefore impossible to obtain by any epitaxial growth and thus will not be further developed here. Figure 1.2 illustrates the wurtzite GaN crystallographic structures along [0 0 0 1], [1 1 $\bar{2}$ 0] and [1 0 $\bar{1}$ 0] directions, where the large circles indicate gallium atoms and the small circles nitrogen [57].

(a)   (b)   (c)
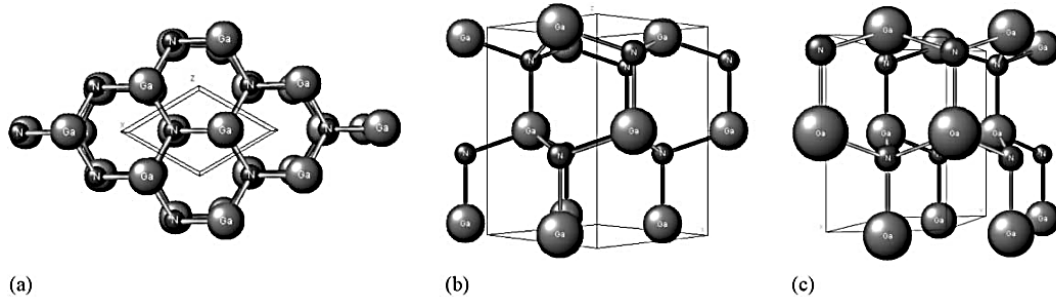
Figure 1.2: Wurtzite structure of GaN for different directions, (a) [0 0 0 1], (b) [1 1 $\bar{2}$ 0] and (c) [1 0 $\bar{1}$ 0].

Under special conditions of pressure and temperature on a cubic substrate, it is possible to grow the III-nitride cubic structure in the form of zinc-blende. Perspective views of the zinc-blende structure are presented in Figure 1.3 [57].
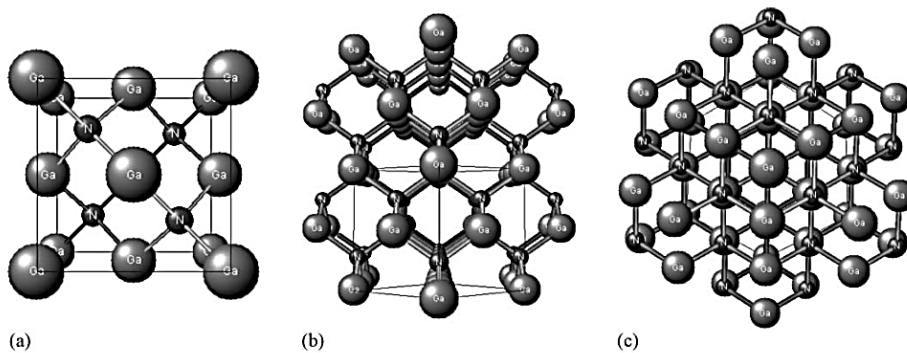

(a)   (b)   (c)

Figure 1.3: Perspective views of zinc-blende GaN along various direction: (a) [1 0 0]; (b) [1 1 0] and (c) [1 1 1].

Lattice parameters of GaN, AlN and InN are usually measured at room temperature by X-ray diffraction (XRD), which is the most accurate technique, using the Bragg law [58], [59]. This technique is used also to determine the composition of ternary compounds, taking into account that free charge, impurities, stress (strain) and temperature could affect the lattice parameters [60].

The wurtzite structure may be represented by the anions (N^{3-}) and the cations (Ga^{3+}), shifted along the c axis. While anions and cations do not overlap and forming an interatomic distance, thus is creating an internal polarization and a piezoelectric property.

The wurtzite structure is symbolized by lattice parameters *a*, *c* and *u*. The *a* parameter is defined by the basal plane of lattice which represents the edge length of the basal plane hexagon. The *c* signifies the axial lattice parameter which describes the perpendicular to the basal plane (the unit cell height). The internal parameter u depicts the interatomic distance in the basic unit. Figure 1.4 illustrates the lattice parameters *a*, *c* and *u* for wurtzite crystallographic structures, larger and smaller spheres represent cations and anions, respectively.
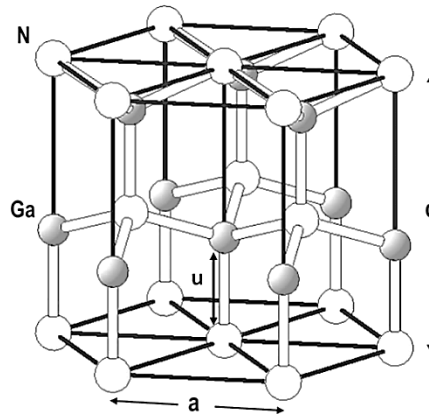

Figure 1.4: Wurtzite lattice parameter a, c and u for GaN.

In the Table 1.2, ideal crystal and experimental wurtzite lattice parameters for GaN, AlN, and InN are presented. The experimental *c/a* ratio and *u* values for GaN is close to the ideal value, 1.633 and 0.375 respectively, whereas those of AlN and InN diverge slightly [61].

Parameter	GaN		AlN		InN	
	Ideal	Exp.	Ideal	Exp.	Ideal	Exp.
u	0.375	0.377	0.375	0.382	0.375	0.379
a (Å)	3.199	3.199	3.110	3.110	3.585	3.585
c/a	1.633	1.634	1.633	1.606	1.633	1.618

Table 1.2: Calculated and experimental lattice parameter for wurtzite GaN, AlN and InN.

1.5.2. Spontaneous and Piezoelectric Polarization

Due to inversion asymmetry and highly ionic bonds resulting from the large electronegativity difference between group III elements (Ga, Al, In) and N, wurtzite III-nitride materials consist of spontaneous polarization property. The spontaneous polarization is separating the electrons and holes, thus creating a charge accumulation perpendicular to the c axis on the surface of the epitaxial layer or at the interface of substrate / epitaxial layer. This accumulation of charges may change the electrical properties and the reactivity of the material. It is therefore important to know the direction of this polarization in order to control it, which is possible with the growth process. As shown in Figure 1.5, if the first deposited atomic layer is composed of nitrogen, then the latter will consist of gallium atoms. This will provide an excess of holes in the surface. This configuration is called Ga polarization and the direction of growth will be [0001]. Vice versa, if the first layer is composed of gallium, the latter will consist of nitrogen and therefore presents an excess of electrons. We will then have N polarization and the direction of growth will be [000$\bar{1}$].
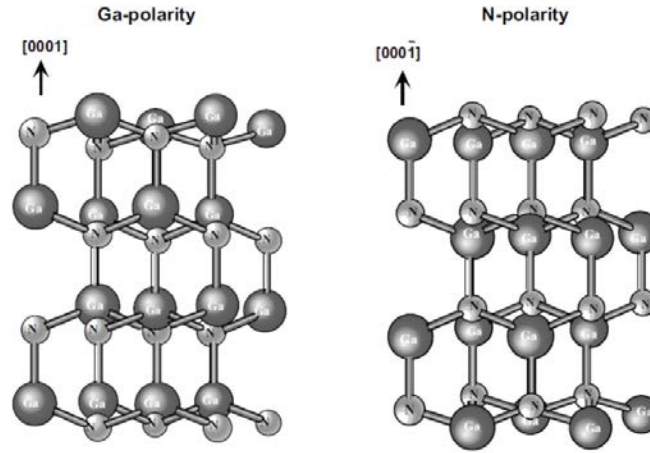
Figure 1.5: Ga and N polarity for GaN.

The growth process and surface treatment before the growth are important factors to perform the spontaneous polarization in the desired direction. The polarization can also interfere with the device behavior. If the field associated with the spontaneous polarization of the material separates electrons and holes, thus reducing the probability of recombination [62]. The electrical current will be reduced if the electric field created by the spontaneous polarization is opposite to the carrier direction, it means the electrons are then "blocked" in the P material and holes in the N material.

III-nitride materials have a piezoelectric property. It is the formation of an electric field due to mechanical stress and strain, and inversely the creation of mechanical stress when applying an electric field to the material. Polarization effects and crystal polarity are significant factors in the nitride materials and have influence in the field-effect. Combined effects of spontaneous and piezoelectric polarization are found to account well for carrier concentrations and depend on alloy concentration [63]. Piezoelectrical polarization could be due to lattice mismatch between the material and the substrate. For example, as there is a mismatch in thermal expansion coefficients of GaN and sapphire, this release of strain due to a change in temperature can lead to the formation of threading dislocations, if the strain is not released, a piezoelectric field will be induced.

In the absence of external polarization, the polarization of the wurtzite structure materials (P), has two components, the spontaneous polarization (Psp) and the piezoelectric polarization (Ppiezo) issued by the deformations in the material [64].

$$P = P_{sp} + P_{piezo} \qquad \textit{Equation 1.8}$$

The piezoelectric polarization is simply expressed via the piezoelectric coefficients e_{33} and e_{31} as

$$P_{piezo} = e_{33}\epsilon_3 + e_{31}(\epsilon_1 + \epsilon_2) \qquad \textit{Equation 1.9}$$

$$\epsilon_3 = (c - c_0)/c_0 \qquad \textit{Equation 1.10}$$

$$\epsilon_1 = \epsilon_2 = (a - a_0)/a_0 \qquad \textit{Equation 1.11}$$

Where, e_{33} and e_{31} are the piezoelectric coefficients of the material [C.m-2], ϵ_3 is the strain along the c axis, ϵ_1 and ϵ_2 are the in-plane strain and assumed to be isotropic, c_0 and a_0 are the equilibrium values of the lattice parameters [64].

Vurgaftman et al. calculated the spontaneous polarization P_{sp} in GaN and InN as –0.034 C/m and –0.042 C/m², respectively [40]. Previously, Bernardini et al have mentionned different values of –0.029 C/m² and –0.032 C/m² for GaN and InN respectively [64].

In the Table 1.3, we illustrate the values of piezoelectric coefficients and calculated spontaneous polarization in the literature.

Parameter	GaN	InN
P_{sp} (C/m²)	– 0.034 [40]	– 0.042 [40]
	– 0.029 [64]	– 0.032 [64]
e_{33}(C/m²)	0.73 [64] [65]	0.97 [64]
e_{31}(C/m²)	– 0.49 [64]	– 0.75 [64]
	– 0.32 [65]	

Table 1.3: Piezoelectric coefficients and calculated spontaneous polarization for GaN, AlN and InN

1.5.3. Mechanical Properties

The mechanical properties of nitride as elastic constants, bulk modulus, phonons and modulus of elasticity have been reported [66]. The stress tensor follows according to Hooke's law, if the material is under tension (being stretched), the deformation will be positive, and conversely, if the material is in compression, the deformation will be negative. Its tensile stress σ is linearly proportional to its fractional extension or strain ϵ by the modulus of elasticity E:

$$\sigma = E . \epsilon \hspace{3cm} \textit{Equation 1.12}$$

Where ϵ describes the strain and σ for the stress. Using the Voigt notation in the anisotropic form of Hooke's law, the expression of stress will be:

$$\sigma_{xx} = (C_{11} + C_{12})\epsilon_{xx} + C_{13}\epsilon_{zz} \hspace{2cm} \textit{Equation 1.13}$$

$$\sigma_{zz} = 2\, C_{13}\epsilon_{xx} + C_{33}\epsilon_{zz} \hspace{2cm} \textit{Equation 1.14}$$

Where ϵ describes the strain and σ for the stress, for the in-plane ($\epsilon_{xx} = \epsilon_{yy}$) and the normal ϵ_{zz} for the strain sensor with $\epsilon_{xx} = (a - a_0)/a_0$ and $\epsilon_{zz} = (c - c_0)/c_0$, a and c are the tow hexagonal lattice constants. C_{11} is the elastic constant for x axis, C_{12} is the elastic constant for (x, y) plan, C_{13} is the elastic constant for (x, z) plan, C_{33} is the elastic constant for z axis.

The bulk modulus B of wurtzite GaN has been calculated according to Fukumoto and Miwa [67]:

$$B = \frac{(C_{11} + C_{12})C_{33} - 2\, C_{13}^{2}}{C_{11} + C_{12} + 2C_{33} - 4C_{13}} \hspace{2cm} \textit{Equation 1.15}$$

For wurtzite GaN, The bulk modulus has been calculated for 195 GPa, 203 GPa and 190 GPa [67].

Elastic constants, modulus of elasticity and bulk modulus values are listed in the Table 1.4 according to [68] for GaN and [69] for InN.

Parameter	GaN	InN
B [GPa]	192	139
C_{11} [GPa]	373	190
C_{12} [GPa]	141	104
C_{13} [GPa]	80.4	121
C_{33} [GPa]	387	182
E [GPa]	362	---

Table 1.4: Reported values of Elastic constants, modulus of elasticity and bulk modulus for wurtzite GaN and InN.

1.5.4.   Crystal growth techniques

As all III-V compounds, gallium nitride does not exist in the natural form. Like all other semiconductors, it must be prepared by artificial synthesis. Johnson et al have been the first to produce GaN in 1932 by reacting metallic gallium with ammonia gas [70].

Many techniques are used for epitaxial growth of III- nitride materials; Reactive Molecular Beam Epitaxy (RMBE), Plasma-Assisted Molecular Beam Epitaxy (PAMBE), Hydride Vapor Phase Epitaxy (HVPE), Organometalic Vapor Phase Epitaxy (OMVPE), and bulk crystal growth from Ga solution. According to the source used, several terms are employed for VPE as organic, inorganic, hydride, organometallic [71]. The terms of Organometallic chemical vapor deposition (OMCVD) and metal organic chemical vapor deposition (MOCVD) are also used [72].

The first technique used to grow epitaxial III-N materials has been the Inorganic VPE. Lately, it has provided a high crystal quality layers including thick buffer layers and templates in order to grow thin films using OMVPE and MBE technique.

The most used technique is OMVPE because it has large growth rates, this technique does not need a high vacuum, and the produced layers have a good quality [73]. OMVPE method also offers sharp heterojunctions for devices. Moreover, it is considered as the principal technique of growth for LEDs and lasers and other optoelectronic devices due to enhanced reactor designs and source improvements.

Recently, the growth of GaN using HVPE technique implemented between 1000 and 1300°C, provides significant growth rates, in the order of µ/min with high crystal quality [74]. Thick GaN layers are frequently grown using HVPE technique. If these layers are thick enough, they could be peeled from sapphire substrate.

For III-V nitride thin films, MOCVD and MBE have provided the highest quality GaN based materials for semiconductor heterostructures. The disadvantage of MBE technique is the conditions of deposition process; it takes long time with a very low growth rate and requires an ultra-vacuum environment. The growth rate in MBE technique is roughly 1 µm/h equivalent to one monolayer per second (ML/s) [75]. In this technique usually, the thin films are grown on a heated substrate under ultra-vacuum. MBE thin films grown on HVPE buffers have demonstrated an improved quality than films grown by OMVPE technique. The complexity and the high cost of MBE reactor maintenance make this technique challenging to use. However the growth of GaN based materials using MOCVD technique doesn't require high vacuum. This technique is considered as the main growth technique in the optoelectronics manufacturing using high growth rate and multi-wafer capability. The deposition of layers in this growth method occurs at higher temperatures compared to MBE and creates thermodynamically metastable GaN.

1.5.5. Substrates for III-Nitride materials

One of the key issues in the study of III-nitride materials is the unavailability of native substrates with high quality single crystalline in large quantities. The large lattice constant and

thermal expansion coefficient mismatches with GaN have been the major concern of studies by many researchers.

Recently, the majority of III-nitride growth has been carried out on c-plane sapphire substrates regardless of a lattice parameter and a thermal expansion coefficient which are very different from those of GaN. These differences will result in defects in the GaN material such as density of dislocations which reducing the quality of the layers. The lattice mismatch parameter relating to GaN epilayer is about 15 % for sapphire. In 1969, Maruska and Tietjen have been the first to grow single crystalline GaN on sapphire substrate [21].

In order to optimize a high crystalline quality GaN, researchers have proposed the deposition of very thick layers GaN (several microns) to move away from the interface. Actually, GaN epitaxy on sapphire substrate by MOCVD has a Ga polarity type with density of dislocation in the order of 10^8 cm^{-2}. The sapphire is still relatively expensive material for large-scale use.

Akasaki et al. have improved the quality of GaN films through the deposition of a thin AlN buffer layer, called also nucleation layer. This has led to high crystalline quality with remarkably improved performances. The role of the AlN nucleation layer is to be the supply of nucleation centers which having the same orientation as the substrate [76].

It is to note that an ideal substrate does not exist either in terms of physical parameters or in terms of cost. In terms of overall performance, aluminum nitride (AlN) appears to be a concurrent candidate due to its wurtzite structure. However, the diameter of 2 inches is currently too small for a mass production of components. The lattice mismatch parameter relating to GaN epi-layer is about 2.7 % for AlN substrate. One of the earlier studies of bulk AlN has been reported by Slack and McNelly [77]. The attention to AlN substrates has increased recently due to the low mismatch with nitrides materials for the purpose of high AlN content aimed to AlGaN detectors. The AlN also has the advantage of being easily chemically etched with KOH, to be a good insulator and have good thermal conductivity. To date, AlN is mostly used as buffer layer.

Similarly, silicon carbides (SiC) seem to be also a pertinent candidate and an alternative choice of sapphire substrate. There are several polytypes of SiC which could be distinguished by their stacking sequence. The lattice mismatch parameter of SiC substrate relating to GaN epi-

layer is about 3.1 %. Lately, the achievability of 6 inches diameter substrates of 4H-SiC has been announced by CREE Company. The drawback of SiC substrate is its high roughness, in the order of 1 nm RMS (0.1 nm RMS for sapphire), which can cause defects in the GaN layer. This explains why the SiC has not generalized as a substrate in the growth of GaN. The cost of the SiC substrate is furthermore high, which makes it uncompetitive compared to the sapphire substrates for GaN thin films with regard to the application at large-scale development.

Lately, GaN substrate has become an optimal choice as a substrate for GaN epitaxy due to homoepitaxy instead of heteroepitaxy in the case of another substrate is used. It offers high crystal quality of material in terms of polarity, thickness, dopant concentration and defect-free layers without stress-relaxation. One more advantage of GaN substrate, it doesn't require a nucleation layer to improve the growth quality. In order to produce bulk GaN, the development of production technique has attracted a lot of attention to optimize the large area crystal. In Poland, High Pressure Research Center in Warsaw has demonstrated high quality bulk GaN using high nitrogen pressure solution (HNPS) growth technique with low dislocation density of 10^5 cm^{-2} [84]. Electrical and optical properties issued from bulk GaN have been degraded comparing to epitaxial GaN on sapphire due to high residual impurities. Up to date, the GaN substrate remains difficult to produce large crystals at high rates.

The silicon (Si) substrate is an attractive substrate for GaN-based growth thanks to its physical properties, high crystalline quality and low cost. Moreover, it provides the possibility of integration between GaN based optoelectronic and Si based optoelectronic devices. The lattice parameter of Si relating to GaN is 17 % with a coefficient of thermal expansion of 2.6×10^{-6} K^{-1} versus 6×10^{-6} K^{-1} for GaN. This difference in thermal expansion leads to cracks after growth cooling. Other disadvantage of Si substrate is the high density of dislocation in the epitaxial GaN, defects are illustrated in polycrystalline form due to the creation of SiNx layer. Usually AlN buffer layer is deposited before growing GaN in in order to avoid this issue and reduce the difference in thermal expansion coefficient between Si and GaN [78].

As well as sapphire, AlN, SiC and Si substrates, ZnO and MgO are further substrate materials. ZnO substrates are wurtzite structures and fit well with wurtzite nitride with 1.8 % of lattice mismatch [79]. On the other hand, MgO is a cubic zinc-blende structure and could be good

candidate for zinc-blende nitride material growth. In the Table 1.5 , the main properties of GaN and the most used substrates are listed [57], [80], [81].

Substrate	Structure	Energy bandgap (eV)	Thermal conductivity (W/cm.K) at 300 K	Thermal expansion coefficient ($\times 10^{-6}$ K^{-1})	Mismatch %
GaN	Wurtzite	3.44	2.1	5,6	0
Al$_2$O$_3$	Rhombohedral	8,1	0.23	6.66	15
AlN	Wurtzite	6.2	2.85	2.9	2.7
SiC	4H (W)	3.26	--	3.9	3.1
Si	Diamond	1.12	1.56	2.61	17
ZnO	Wurtzite	3.3	0.3	4.3	1.8

Table 1.5: Comparison of different substrates used for GaN growth.

1.5.6. Defects in nitride materials

Thanks to direct and flexible band gap of nitride materials, a major interest in the topological analysis of defects in GaN and related alloys has been observed in order to obtain a satisfactory performance of devices in several domains of applications and particularly in the optoelectronic field. The semiconductor lattice is continuous with perfect energy band structure in the ideal state. Though the experimentations in the semiconductor growth demonstrate that the lattice will constantly contain defects in different forms. These defects will disturb the continuous lattice and introduce unwanted energy states inside the forbidden band gap.

Knowing that epitaxial GaN is grown on diversity of substrates as sapphire, SiC, Si, etc…, defects will arise in GaN epilayers whatever the deposition technique is used (MBE, MOCVD or VPE). Understanding the topological properties including various forms of defects is

necessary in the objective to interpret and expect the experimental observations. The crystalline structure of the grown material is subject to the underlying template. The mismatch between epilayer and substrate due to differences of symmetry, structure, and orientation will produce tensions in the materiel and will be relaxed by deformation. This will generate dislocation and may propagate along the material up to the top layer and possibly initiating unintentional emission wavelengths, non-radiative recombination and poor optical performance [82]. The device performance is generally related to the dislocation density of the grown material, reducing the defect content will improve the device quality. However, few defects could behave unintentionally as donors or acceptors leading to free carriers called "native defects" [83].

The microstructural defects in GaN materials and its alloys are presents in several forms such as threading dislocation (edge, screw or mixed dislocation), misfit, nanopipes, stacking-faults (SFs), inversion domain boundaries, twins, and grain boundaries [84]. The misalignment of symmetry axes and missing atom from its designated position in the lattice (called vacancy or point defect) are also forms of defects and lead to local discontinuity. Figure 1.6 illustrates the different forms of defects which could be led by deformed lattice as dislocation (b, f, and g), by impurities (e and h), by missing atom (d), by interstitial impurity atom (a) or by self-interstitial atom (c) [85].
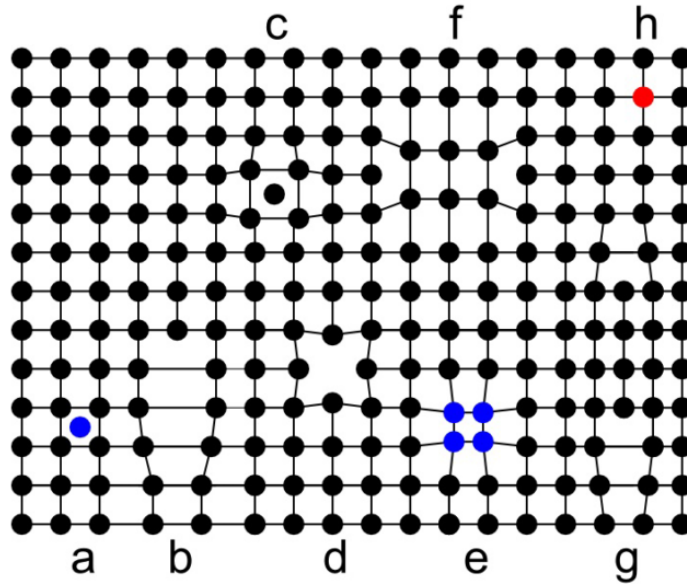

Figure 1.6: Different types of lattice defect formed during epitaxial growth.

Researchers have developed different techniques with the purpose of improving the layer quality and reducing the interface tensions in the epitaxial GaN layers [86]. These techniques have reduced the effect of high lattice mismatch between the substrate and the grown films. Buffer layers, growth conditions and surface patterning are actually the main techniques used to grow a high quality GaN with reduced values of defect density. Nowadays, the state of the arte in the dislocation density for epitaxial GaN grown on sapphire substrate is 2.2×10^5 cm^{-2} [87].

1.5.7. Doping

The control of doping in different concentrations for GaN and related materials stands to be a major concern in the development of device performance. Until early 1990s, the difficulty to dope wide bandgap semiconductors has been the principal challenge for researchers. Doping is the technique used to increase the amount of material electrons or holes by substituting a very small amount of the atoms by other atoms of different nature. If we add one or more atoms containing more electrons, the type of doping here is called n-type and the electrical conduction will be directed primarily by electrons. Conversely If we add atoms having less electrons, it means more holes, the doping here will be p-type and the current conduction is promoted by the holes.

Connecting the n-type material with a p-type material will cause a shift of load to meet the electrical balance and creating an internal field. This type of device is called a PN junction and it is the basis of almost electronic components (transistors, LEDs, solar cell, etc.). It is therefore important to have good doping n-type and p-type in order to obtain efficient components. The most commonly used doping technique is the introduction of dopant directly into the growth chamber in the form of gas when nitride materials are produced by a chemical vapor deposition method (CVD). Moreover, Ion implantation is also a doping technique allowing accurate control of doping profile. However, it must be followed by annealing in order to activate the dopants and reduce the disorder induced by implantation.

Undoped GaN (called also intrinsic GaN, or not-intentionally-doped GaN) has been experimented and it has been observed that undoped GaN is slightly n-type doped. It may be due

to nitrogen vacancy VN (native defects), impurities or defect complexes which can act as free carriers [83]. Lately, undoped GaN has electron concentration approximately 10^{16} cm^{-3}.

As nitrides are intrinsically n-type with an excess of electrons, increasing the n-type doping is easily achieved. The most commonly used is silicon (Si) which occupies the site of a cation (Ga) as a single donor [88]. Its concentration in the nitride layer is typically in the order of 10^{18} cm^{-3}. The silicon dopant is introduced by silane (SiH4) during the growth process when MOVPE technique is used with a resistivity of n-GaN as low as 1-10^{-2} Ω.cm [88]. Other dopants have also been studied as oxygen, hydrogen or germanium but less effective than Si because of its defects introduced in the layers [89].

The primary challenge for researchers has been the optimization of high p-type doping level. The highly resistive films resulting from the p-type doping is a major obstacle in the nitride community because of slightly n-type nature of GaN. They should initially compensate the electron excess in the material before creating an excess of holes. Defects are subject to p-type doping due to the introduction of p-dopant in the lattice which create n-type defect. The only successful dopant has been the magnesium (Mg) which forms complexes with hydrogen leading to dopant passivation. In order to reduce the high resistivity value of the layer, a post growth activation is implemented by annealing the sample inside the reactor once the growth is performed. Amano et al. have been the first to realize p-type conduction in Mg doped GaN using low-energy electron-beam irradiation (LEEBI) treatment [26]. They have obtained hole concentration about 2×10^{16} cm^{-3}, hole mobility as 8 cm^2/V·s and resistivity of 35 Ω·cm. Later, Nakamura et al. have obtained low-resistivity p-type GaN films using N$_2$-ambient thermal annealing as low as 2 Ω·cm with hole carrier concentration as 3×10^{17}cm^{-3} [90].

1.5.8. Electronic band structure and electrical properties

The energy bandgap Eg and the carrier density are the main features defining electrical properties of a material. Like most "III nitrides", (In, GaN, AlN), the band structure of GaN compound has a direct gap [91].

Before detailing these values for GaN and InN, we will quickly recall some basic concepts of physics. The bandgap is defined as the difference in energy between the top of the

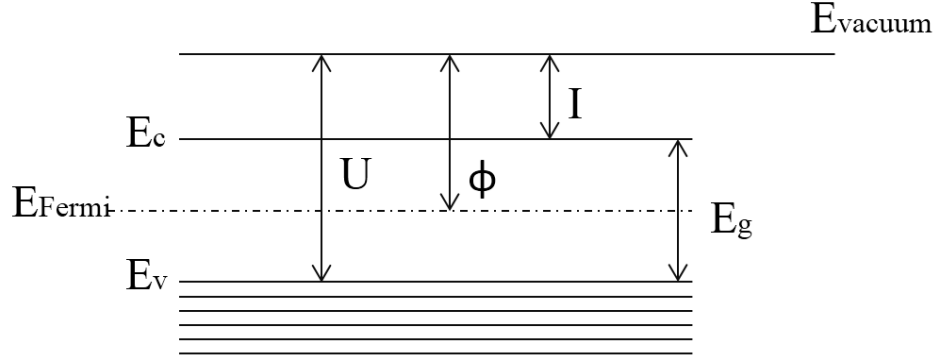valence band and the bottom of the conduction band. The energy diagram for material is shown in Figure 1.7.

Figure 1.7: Energy diagram for material.

As illustrated in Figure, the vacuum level (Evacuum) is defined by the potential energy of an electron in vacuum taken as zero. The inner potential (I) is the total potential seen by the electrons. It is specified by the electrostatic potential caused by the distribution of charge density (Poisson equation), plus the exchange-correlation potential produced by electron-electron correlations. The work function is the energy needed to remove an electron from the highest filled level in the Fermi distribution of a solid to a point in the vacuum immediately outside the solid surface. In a semiconductor and insulator, the work function φ is defined: φ = Evacuum - EFermi. The electron affinity is the energy gained by an electron when it enters a solid, it is the difference in energy between the vacuum level and the bottom of the conduction band. The minimum energy needed to remove a particular electron from the atom is the binding energy (U).

The band diagram could be illustrated as a function of the wave vector k. the conduction band is considered as "unfilled band" and inversely, the valence band is considered as "filled band" as shown in Figure 1.8.
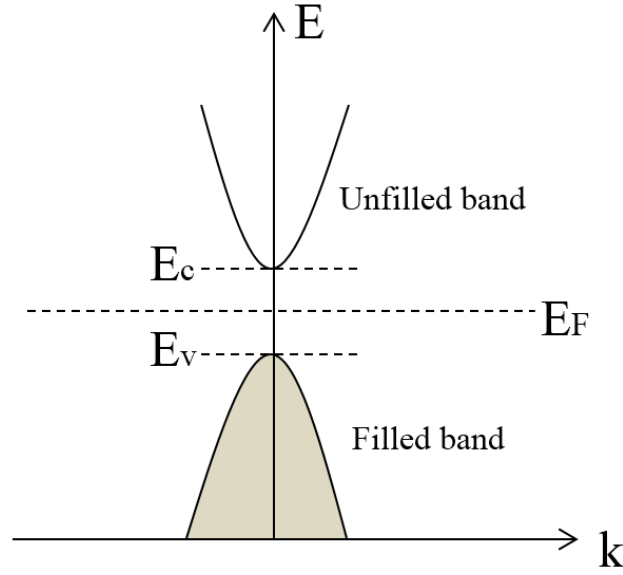
Figure 1.8: Band diagram as a function of wave vector k.

The charge state of a particular defect can be determined by the Fermi level. Defects can be either donor-type, acceptor-type, or amphoteric. GaN doped with donor or acceptors can have its Fermi level located near midgap, below the conduction-band edge or above the valence-band edge [92].

The Fermi level, E_F, is the highest energy level filled by an electron at 0 K. The probability of occupancy of an energy level E by an electron obeys the Fermi-Dirac distribution function. The probability of occupancy of an energy E by a hole is *1-f (E)* [47].

$$f(E) = \frac{1}{1 + exp^{\frac{(E-E_F)}{kT}}}$$ *Equation 1.16*

Where E_F is the Fermi level [eV], k is the Boltzmann constant [8.617 x 10^{-5} eV.K^{-1}] and T is the temperature [°K].

The electron concentration can be expressed as following equation:

$$n = N_C \, e^{-(E_C - E_F)/kT}$$ *Equation 1.17*

Where N_C is the total density of states in the conduction band and given by:

$$N_C = 2\left(\frac{2\pi m_n kT}{h^2}\right)^{3/2} \qquad \textit{Equation 1.18}$$

It will reduce to:

$$N_C = 2.5 . 10^{19} \left(\frac{m_n}{m_0}\right)^{3/2} \left(\frac{T\ [K]}{300}\right)^{3/2} cm^{-3} \qquad \textit{Equation 1.19}$$

Where, m_n is the conduction-band density-of-states effective mass, ($m_n=0.2\ m_0$ for the GaN and $0.11\ m_0$ for the InN) [MeV.c^{-2}], m_0 is the electron mass [0.5101 MeV.c^{-2}] and h is the Planck constant [4.136 x 10^{-15} eV.s].

When the Fermi level is above the valence band by several kT values, the Fermi-Dirac distribution can be replaced by the Boltzmann distribution leading to the hole concentration equation:

$$p = N_V\ e^{(E_V-E_F)/kT} \qquad \textit{Equation 1.20}$$

Where N_V is the total density of states in the valence band and given by:

$$N_V = 2\left(\frac{2\pi m_p kT}{h^2}\right)^{3/2} \qquad \textit{Equation 1.21}$$

It will reduce to:

$$N_V = 2.5 . 10^{19} \left(\frac{m_p}{m_0}\right)^{3/2} \left(\frac{T\ [K]}{300}\right)^{3/2} cm^{-3} \qquad \textit{Equation 1.22}$$

Where, m_p is the valence-band density-of-states effective mass, ($m_p=0.8\ m_0$ for the GaN and $0.65\ m_0$ for the InN) [MeV.c^{-2}].

For the GaN, $N_C \approx 4.3 \times 10^{14}\ T^{3/2}$, $N_V \approx 8.9 \times 10^{15}\ T^{3/2}$. For the InN, $N_C \approx 1.76 \times 10^{14}\ T^{3/2}$, $N_V \approx 10^{16}\ T^{3/2}$.

The main characteristic for which nitrides are studied is their energy bandgap including their alloys [25]. Rezaei et al have studied the electronic band structure for the III-nitride compound semiconductors GaN, InN and AlN using the empirical pseudopotential approach [93]. This method provides the calculated full band structure for GaN and InN shown in Figure 1.9.

The energy bandgap for the GaN is 3.39 eV (366 nm) and 0.7 eV (1771 nm) for the InN at room temperature (300 K) [94].
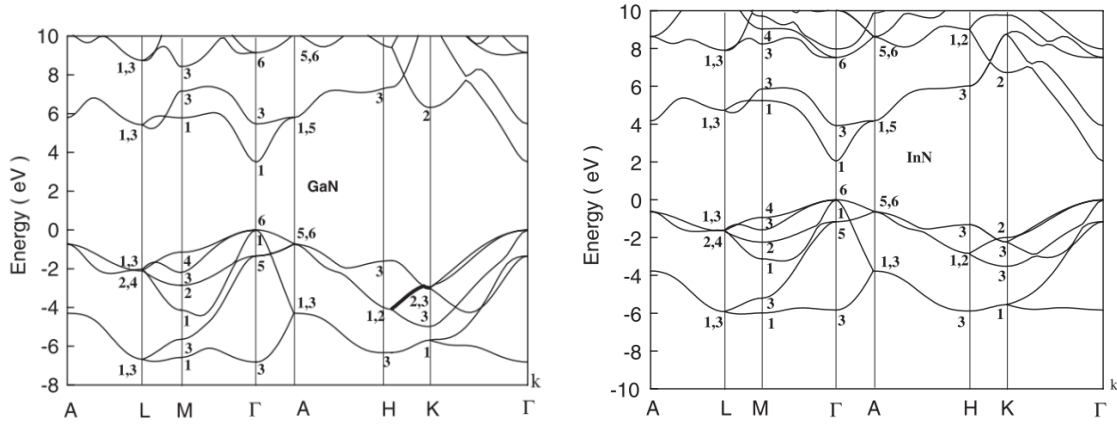

Figure 1.9: Band structure of a) wurtzite GaN, b) InN

Band structure of nitrides is composed of one conduction band and three valence bands. In wurtzite materials, both the spin-orbit and the crystal- field splittings affect the structure of the valence band and degenerate three valence sub-bands. These sub-bands are called heavy holes (HH), light holes (LH) and spin-orbit holes [40]. The light hole sub-band shows an asymmetry along kx and kz directions of the wave-vector. The valence bands around Γ point calculated by Rezaei et al. for GaN and InN are depicted in Figure 1.10 [93].

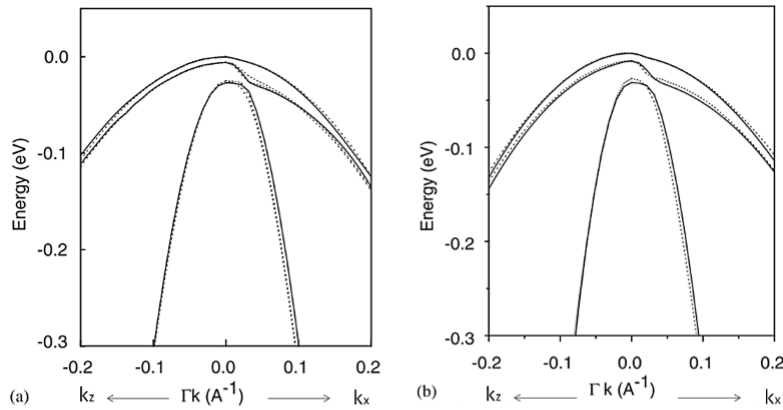*Figure 1.10: Calculated valence band structures using the k.p (solid line) and empirical pseudopotential method (dotted line) for (a) GaN, (b) InN.*

The hole effective mass is lower along kx direction than kz direction [95]. In the vast majority of current GaN materials, experimental effective mass of the holes is much less than the

mass of heavy holes. It can be simply explained by the effect of the stress in the crystal, which tends to raise the summit of the light hole band relative to the heavy hole band. In the literature, the reported effective mass values for the holes differs, most probably because the stress of the epitaxial material varies according to the epitaxial process used. The implemented adaptation layers in the growth process may be another reason to vary the effective masse values. The electron (m_e) and heavy (m_{hh}), light (m_{lh}) and crystal-field split (m_{ch}) hole effective masses for GaN and InN are listed in Table 1.6 [93]. ‖ and ⊥ correspond to the values parallel and perpendicular to c-axis, m_0 is the electron mass [0.5101 MeV.c^{-2}] or [9.11×10^{-31} kg].

Effective mass	GaN	InN
$m_e^{\parallel}$	0.16 m_0	0.12 m_0
$m_e^{\perp}$	0.13 m_0	0.11 m_0
$m_{hh}^{\parallel}$	1.45 m_0	1.39 m_0
$m_{hh}^{\perp}$	1.52 m_0	1.41 m_0
$m_{lh}^{\parallel}$	1.45 m_0	1.39 m_0
$m_{lh}^{\perp}$	0.168 m_0	0.12 m_0
$m_{ch}^{\parallel}$	0.14 m_0	0.1 m_0
$m_{ch}^{\perp}$	1.96 m_0	1.69 m_0

Table 1.6: Electron (me) and heavy (mhh), light (mlh) and crystal-field split (mch) hole effective masses for GaN and InN with values in parallel and perpendicular to c-axis.

The evolution of the energy bandgap as a function of temperature for III-nitrides materials have been studied [96]. A relation for the variation of the energy gap (Eg) with temperature (T) has been proposed by Varshni [96]. The empirical relationship is expressed as:

$$E_g(T) = E_g(T = 0) - \frac{\alpha T^2}{\beta + T} \qquad \textit{Equation 1.23}$$

Where, Eg(0) is the excitonic transition energy at 0 K [eV], α [eV.K-1] and β [K] are the Varshni coefficients. In Figure 1.11 (left), the temperature as a function of the experimental values of the transition energies corresponding respectively to the A, B, and C excitons, is plotted [97], the solid lines are least-square fits to the Varshni empirical relationship. The Figure 1.11 (right) is illustrating the measured band gap of InN by transmission and photoluminescence spectroscopy as a function of temperature [98].
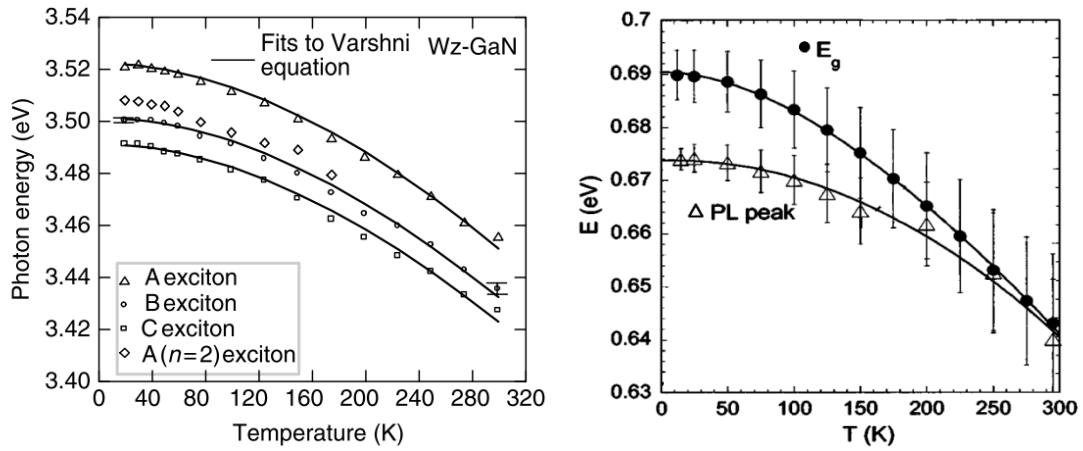

Figure 1.11: Energy bandgap dependence of temperature for Wurtzite GaN (left) and for InN (right).

The reported values of, E_g *(T=300)* [eV], α [meV.K^{-1}] and β [K] for Wurtzite GaN and InN are listed in the Table 1.7.

Parameter	GaN	InN
E_g **(eV) at 300K**	3.44 [40]	0.75 [40]
	3.39 [99]	0.64 [98]
α **(meV/K)**	0.909 [40]	0.245 [40]
	0.77 [99]	0.41[98]
β **(K)**	830 [40]	624 [40]
	600 [99]	454 [98]

Table 1.7: Varshni parameters and energy bandgap at 300K for GaN and InN.

1.5.9. InGaN alloy

InGaN as a ternary alloy of wurtzite GaN and InN having a direct bandgap varying from 0.7 eV to 3.4 eV, is subject to considerable effort for the fabrication of optical devices as LED, laser etc. It has provided an optical spectrum ranging from near-UV, violet, and blue to green emissions by means of high efficiency InGaN. The x in $In_xGa_{1-x}N$ is defining the GaN and InN molar fraction. In 1989, Nagatomo et al. have carried out the first epitaxial film of $In_{0.42}Ga_{0.58}N$ by MOVPE growth method [100]. The calculation of InGaN bandgap is expressed using the following empirical equation:

$$E^g_{In_xGa_{1-x}N} = x\, E^g_{InN} + (1-x)E^g_{GaN} - b_{InGaN}\, x(1-x) \qquad \textit{Equation 1.24}$$

Where E^g_{GaN}= 3.44 eV, E^g_{InN}= 0.75 eV and the bowing parameter b_{InGaN} is the deviation from a linear interpolation between the InN and GaN as reported b_{InGaN} =1.43 eV [101]. However, external effects such as deformation, doping, or the fluctuation of the composition can vary the the bowing parameter b. Figure 1.12 illustrates the variation of InGaN bandgap as a function of In composition determined by optial absorption [101].
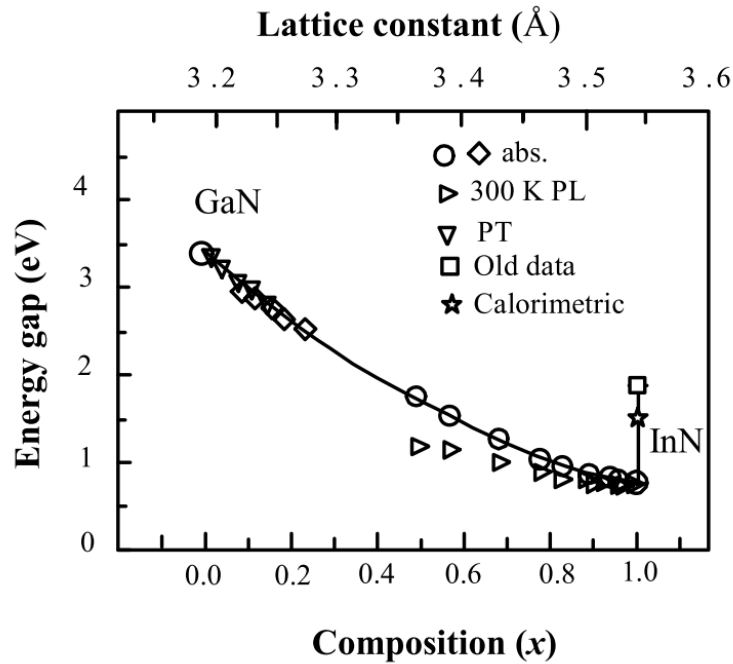

Figure 1.12: InGaN bandgap variation dependence of In composition and measured by optical absorption.

1.5.10. Carrier transport: low-field mobility for electron and hole

The electrical of a charge carrier represents the response of the average velocity of the carriers toward the average electric field applied in the crystal. When an electrical field is applied, the electron and holes mobility describe how quickly an electron or hole can move through a material, the general term is the carrier mobility. In the literature, several mobility values for holes and electrons in the GaN are reported for various temperatures and carrier concentrations [102].
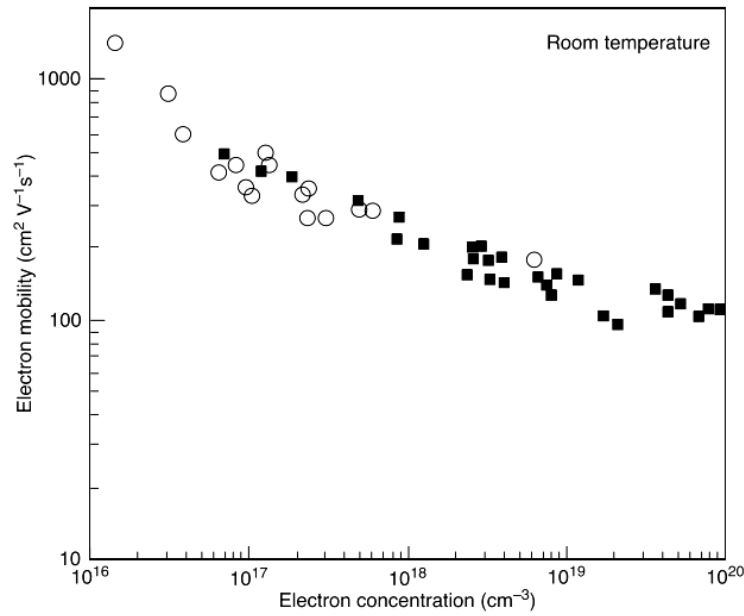

Figure 1.13: 300K Hall mobility versus electron concentration for GaN.

The measured mobility in n-type GaN was reported by many authors in the literature. Generally, mobility can be measured as a function of temperature. Hall mobility and Hall electron concentration can be calculated with respect to temperature, in p-type, it would be the hole concentration. It is possible to determine the donor and acceptor concentrations accurately by fitting the temperature as a function of the electron concentration with the temperature as a function of the mobility [102]. A high electron mobilities were reported on freestanding sample of GaN produced by Samsung at room temperature of $\mu = 1425$ cm^{2}V^{-1} s^{-1} at T = 273 K and $\mu = 7385$ cm^{2}V^{-1} s^{-1} at T = 48.2 K [103]. In Figure 1.13, experimental electron mobility at room-

temperature reported by several studies is illustrated, open circles are for unintentionally doped samples and the squares are for samples doped with either Si or Ge [104].

In order to calculate accurately the mobility, the method as the numerical iterative solution of the Boltzmann transport equation (BTE) was used for the sample of GaN produced by Samsung [105]. The donor concentration (Nd) and the acceptor concentration (Na) are the key parameters in the BTE method calculation.

Figure 1.14 illustrates the calculated electron mobility by BTE-based theory (lines) for three values of the acceptor concentrations as a function of temperature. It was then fitted to experiment results expressed in the temperature dependence of electron concentration (squares). An acceptor concentration of $Na = 2.4 \times 10^{15}$ cm^{-3} demonstrates the best fitting to the experiment result comparing the upper and lower lines for $Na = 1.4 \times 10^{15}$ cm^{-3} and $Na = 3.4 \times 10^{15}$ cm^{-3} respectively. This method indicates the effect of the acceptor concentration on the calculation of the mobility [102].

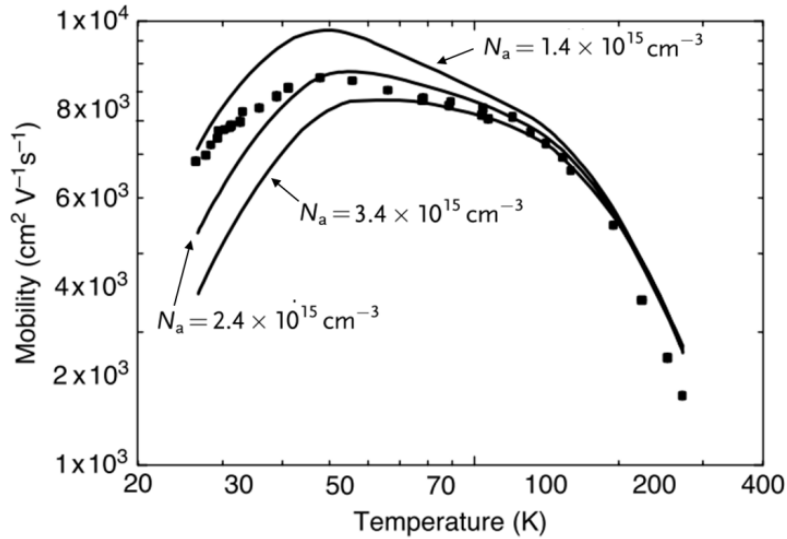*Figure 1.14: Experimental and calculated electron mobilities using iterative BTE method as a function of temperature for different acceptor concentrations.*

Several analytical models have been reported in order to obtain the temperature and the carrier concentration as a function of low-field mobility in GaN at various temperatures [106]. Schwierz et al. have evaluated experimental mobility values and simulated Monte Carlo data in

order to describe the behavior of the mobility on the carrier concentration, temperature and electric field [45].

Roschke et al. have reported an approach for an electron mobility model, the electron transport caused by an electric field E is described according to [107]:

$$v = \mu \times E \qquad \qquad Equation\ 1.25$$

Where, v is the electron drift velocity and μ is the electron mobility. The electron velocity increases with field and the mobility remains constant (μ_0) at low electric fields. The mobility depends on the electron concentration n, on the temperature T, and on the material quality. Schwierz has provided a wurtzite GaN model based on the Caughey and Thomas empirical expression for modeling low-field mobility as a function of the electron concentration [45][44]:

$$\mu_0 = \mu_{min} + \frac{\mu_{max} - \mu_{min}}{1 + \left(\dfrac{n}{n_{ref}}\right)^{\alpha}} \qquad \qquad Equation\ 1.26$$

Where, μ_{min}, μ_{max}, n_{ref} and α are fitting parameters. μ_{max} is the mobility of undoped sample, μ_{min} is the mobility of highly doped material, α is a measure of how quickly the mobility changes from μ_{min} to μ_{max} and n_{ref} is the carrier concentration.

One of the major issues in the GaN and its alloys is the poor hole mobility. It is perhaps due to the various valence bands which consist of heavy mass and non-parabolic structure. The main interest of research in the GaN materials and its compounds is to optimize the transport in the p-type materials by providing high p-type conductivity. The hole mobility in the p-type materials is generally ranging from 10 to 20 cm^{2}V^{-1} s^{-1}. The hole mobility is inversely related to the carrier concentration, it is meaning that the hole mobility decrease in case of increasing the carrier concentration [108].

Figure 1.15 demonstrates the p-GaN Hall mobilities as a function of the hole concentration. The experiment was performed at room-temperature for Mg-doped samples prepared by OMVPE and MBE then activated by N2 heat treatment [109].
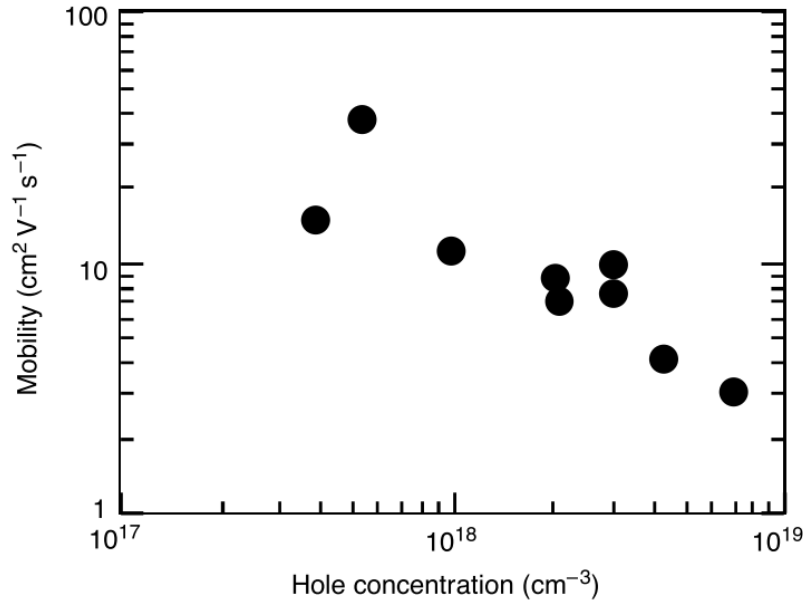
Figure 1.15: Hall mobilities of p-GaN dependence of hole concentration for Mg-doped samples.

In the InN, the lack of a suitable substrate materials leads to a high defect in the epitaxial layer with the presence of high electron concentration in unintentionally doped InN. Different electron mobility values have been reported in the literature due to InN low quality layer [19]. Lu et al. have reported a Hall of about 800 $cm^2 V^{-1} s^{-1}$ at room temperature in a concentration of 2-3 $\times 10^{18} cm^{-3}$ [110]. A mobility of 500 $cm^2 V^{-1} s^{-1}$ [111], 800 $cm^2 V^{-1} s^{-1}$ [112], 820 $cm^2 V\text{-}1 s^{-1}$ [113] and 1700 $cm^2 V^{-1} s^{-1}$ [114] have been reported in a concentration varying from 3-9 $\times 10^{18} cm^{-3}$ at room temperature.

Concerning the mobility in the GaN alloys, the estimation becomes more complex than binary GaN. Authors have studied the GaN alloys Hall mobility with different conditions as temperature, carrier concentration and InN or AlN molar fraction [115]. Chin et al. have used a variational method in order to calculate the electron mobility for InGaN, InAlN, and AlGaN [115], [116]. Figure 1.16 shows the electron mobility of InGaN as a function of InN molar fraction with a concentration of $10 \times 10^{16} cm^{-3}$ and alloy potentials in the range from 0 to 1.4V at 300 K [102].
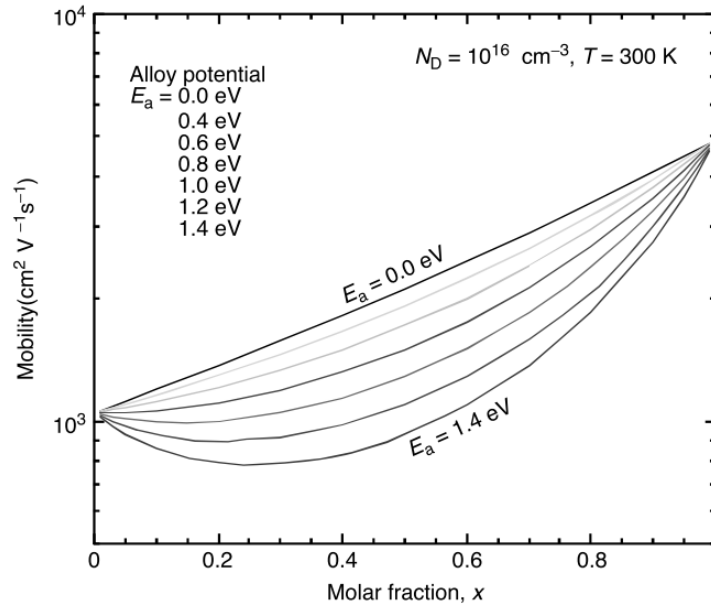
Figure 1.16: Electron mobility for InGaN dependence of InN molar fraction different alloy potential.

1.5.11. High-Field carrier Velocity

As explained previously, at low electric fields the electron velocity increases almost linearly with electric field and the mobility remains constant (low-field mobility) for Wurtzite GaN. Under the influence of a high electric field, the carrier velocity is no longer proportional to the electrical field. The non-linear relationship between carrier velocity and electric field could be described as the evolution of effective electrical mobility as $\mu = dv/dE$ and μ *(E)* will be defined by:

$$v\ (E) = \ \mu(E)\ E \qquad\qquad Equation\ 1.27$$

Where v *(E)* is the carrier velocity as a function of the electrical field. In the case of GaN with T= 300 K, v *(E)* can be expressed by the following expression:

$$v(E) = \frac{\mu_0\ E + v_{sat}\left(E/E_c\right)^{n_1}}{1 + \left(E/E_c\right)^{n_1} + n_2\left(E/E_c\right)^{n_3}} \qquad\qquad Equation\ 1.28$$

Where v_{sat} is the electron saturation velocity, E_c is the critical electrical field, n_1, n_2 and n_3 are fitting parameters [45]. The ability to increase the frequency of component is determined by

its transition frequency F_T. In the case of transistor with gate length (L), it corresponds to the frequency in which the transistor gain is equal to 1 (0 dB). In the case of HEMT, it is directly proportional to the saturation velocity of the carriers (v_{sat}), as the following expression:

$$F_T = \frac{v_{sat}}{2\,\pi\,L} \qquad\qquad Equation\ 1.29$$

Wraback et al. have determined the electron transit time and steady-state velocity at room-temperature as a function of electrical field using a femtosecond optically detected time-of-flight technique [117]. They demonstrated the peak electron velocity at 1.9×10^7 cm/s, corresponding to a transit time of 2.5 ps, attained at 225 kV/cm. This study was based on theoretical calculations reported by authors in which the electron velocity-field characteristic predict a peak steady-state velocity of 2–3×10^7 cm/s [118].

Figure 1.17 illustrates the experimental steady-state electron velocity values determined by Wraback et al. [117], and the Monte Carlo calculations reported by Kolnik et al.[118].
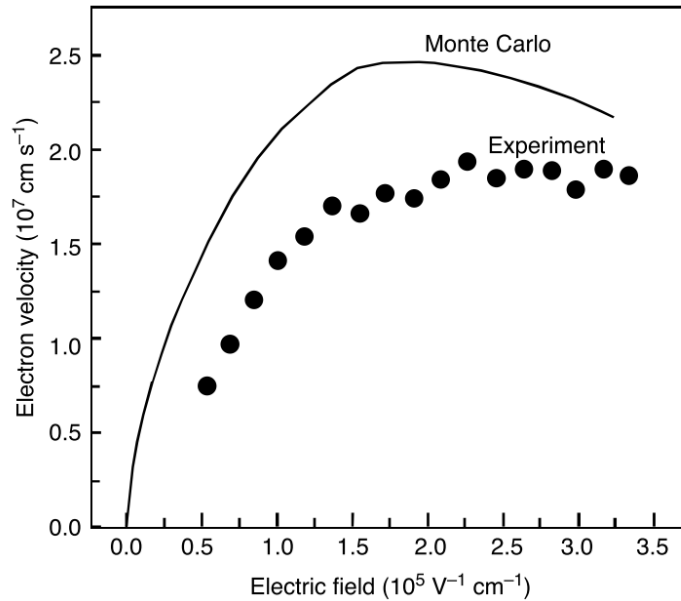

Figure 1.17: Simulated and experimental steady state electron velocity in Wurtzite bulk GaN as a function of applied electric field [102].

The holes drift are significantly lower than the electrons drift. The theoritical calculations of the hole velocity reveals that the hole velocity (v_h) is roughly less than $0.15v_e$ over the entire

range of electric fields [117]. The calculation of the hole transport properities of wurtzite GaN using Monte Carlo simulator has indicated 5×10^6 cm/s at 1000 kV/cm [119].

1.5.12. Optical properties

Within the most important characterization of materials in semiconductors are the optical processes which provide useful information regarding the material properties. Direct bandgap, absorption coefficient, refractive index and dielectric constant are results of optical characterization using several methods. These parameters have significant influence on the device operation. Electroluminescence (EL), photoluminescence (PL), thermoluminescence and absorption/emission spectroscopies are means of optical characterizations based on light emission in response to excitation by electrical injection, optical beam or raising the temperature. Optimizing optical properties is essential for optoelectronic applications as LED, photodetectors and lasers.

Photons are characterized by their energy E (h is Planck's constant), the speed of light in vacuum (c) and the wavelength of medium as the following expression:

$$E = \frac{h\,c}{\lambda} \qquad\qquad \textit{Equation 1.30}$$

This leads to a useful relation allowing a quick calculation of the energy E (in eV) or the wavelength λ (in nm):

$$E = \frac{1.24}{\lambda} \qquad\qquad \textit{Equation 1.31}$$

The refractive index of a material is defined by the ratio of the speed of light in vacuum (c) on the phase velocity of light in the medium (v) as following:

$$n = \frac{c}{v} \qquad\qquad \textit{Equation 1.32}$$

But the speed of light in a material is not constant and depends on the wavelength. The refractive index is also involved in the determination of the coefficients of reflection and transmission through the relationship of Snell-Descartes as:

$$n_1 \sin \theta_1 = n_2 \sin \theta_2 \qquad \text{Equation 1.33}$$

Where n1 and n2 are refractive indices of two medium, θ1 and θ2 are light angles relative to the normal. R and T are the coefficients of reflection and transmission respectively.

$$R = \frac{n_1 - n_2}{n_1 + n_2} , T = \frac{2\,n_1}{n_1 + n_2} \qquad \text{Equation 1.34}$$

It is noted that the light tends to propagate in the materials with the highest refractive index in a multilayer structure.

In order to describe the response of a material when electrical field is applied, relative permittivity of a material, also called dielectric constant is defined as:

$$\varepsilon_r = \chi\,\varepsilon_0 \qquad \text{Equation 1.35}$$

Where εr is the relative permittivity, χ is the susceptibility of the material and ε0 is the vacuum permittivity.

The absorption coefficient is defined how far into a material light of a specific wavelength can get through before it is absorbed. It means the rate of decrease in the intensity of light as it penetrates through a given substance. Material with high absorption coefficient, the light will be absorbed efficiently with taking into account the quality of material and the wavelength of absorbed light. The absorption coefficient (α) is related to the extinction coefficient (k) and the wavelength (λ) as the following equation:

$$\alpha = \frac{4\,\pi k}{\lambda} \qquad \text{Equation 1.36}$$

For photodetectors, the absorption coefficient is an important parameter since it will determine the amount of photons absorbed by the material, and thus the quantity of carriers that can be produced. That is why the choice of materials with high absorption coefficients is key for the manufacture. GaN and related alloys have high absorption coefficients of 10^5cm^{-1}, which make them very well for LEDs, lasers, and detectors.

Reported optical properties of GaN, AlN and InN semiconductors are presented in Table 1.8 [94][120]–[122].

Parameter	GaN	AlN	InN
Index of refraction at 300K	2.3 (633nm)	2.1 (infrared)	2.9
Dielectric constants static at 300K (E∥c)	9.5	9.14	14.4
Absorption coefficient (cm^{-1})	1×10^{-5}	2×10^{-5}	5×10^{-4}

Table 1.8: Optical properties of binary III-nitride compounds.

1.6. State of the art of high speed photodiode

Many efforts have been achieved in order to obtain higher output powers, efficiencies and cut-off frequencies [123]–[125]. The main limitations to accomplish these objectives are basically the saturation under high injection regime, the thermal failure related to the power absorbed actively and passively, the intrinsic bandwidth, the coupling between the input power and the active region and finally the coupling between the RF power and the antenna.

RF output power for LT-GaAs photomixer with wideband design was reported [123]. Output powers on the order of 1 µW were measured for various designs spanning 0.6–2.7 THz. The improvement in output power ranged from 3 to 10 dB over more conventionally designed photomixers using broad-band log-spiral antennas.

Although the first Uni-Traveling-Carrier (UTC) photodiode realization has been existent from 1997, NTT3 laboratories conducted their experiments of THz photomixing since 2002 including the UTC-photodiode fabrication. A power of 120 µW at 300 GHz, for a photocurrent of 20 mA has been radiated by a photomixer composed of a UTC photodiode and a planar log-periodic antenna [124].

Huggard et al. have obtained powers of 10 µW at 150 GHz and 100 nW at 625 GHz with a commercial PIN photodiode. The photodiode is inserted into a WR-10 waveguide; the power generated is then radiated by a cornet and then detected by a Golay cell [125]. More recently,

with the same kind of photomixer illuminated by a Bi-color Fabry-Perot laser diode, Osborne et al were able to detect a power of 20 nW to 485 GHz [126].

Ito et al. investigated on photonic generation of millimeter sub-millimeter waves up to terahertz range using an antenna integrated uni-travelling-carrier photodiode [127]. They have developed a compact narrowband Uni-Traveling-Carrier photodiode (UTC-PD) module with a WR-8 rectangular waveguide output port for operation in the F-band (90–140 GHz) [127]. A resonating matching circuit integrated with a UTC-photodiode and a microstrip-line-to-rectangular-waveguide transformer were designed to have high output powers with a wide bandwidth covering the F-band. The fabricated module exhibited a millimeter-wave output power of 17mW at 120 GHz for a bias voltage of -3V. A test device measured on wafer exhibited a record maximum output-power of 2.6 µW at 1.04 THz with good linearity [128]. A fabricated quasi-optical module operates at frequencies of up to 1.5 THz [129].

An enhancement of output power has been achieved by Nakajima et al. at frequencies from 0.7 to 1.6 THz by means of narrowband Uni-Travelling-Carrier photodiodes. Through a resonant antenna which generate a high-power continuous terahertz waves, the maximum output power obtained at 1.04 THz was 10.9 µW [130].

Schoenherr et al. have presented a photomixer composed of a "spot-size converter", an optical waveguide, a PIN photodiode and a planar antenna. The photodiode had a response of 0.36 A/W for a polarization of -1.6 volts. Using a Golay cell, it was measured a power of 3 µW at 200 GHz and 30 nW at 700 GHz for a photocurrent of 4.1 mA [131].

More recently, An output power as high as 0.57 mW at 350 GHz has been achieved by Wakatsuki et al. using a high-power and broadband photomixer module [132]. Moreover, Rouvalis et al. have reported 148 µW at 457 GHz, 24 µW at 914 GHz when integrated with resonant antennas and 105 µW at 255 GHz, 30 µW at 408 GHz, 16 µW at 510 GHz and 10 µW at 612 GHz [133].

The Figure 1.18 issued by G. Bett [134], illustrates a comparison of reported output powers for UTC-photodiodes, PIN-photodiodes and LT-GaAs photomixers with wideband designs, the results for narrowband UTC-photodiodes are also shown for comparison [123]–

[125], [135], [126]–[128], [136], [129]–[133]. It is noted that the output power of device decreases inversely proportional to the frequency, the PIN-photodiodes are almost two orders of magnitude lower than the UTC-photodiodes due to the high saturation current levels of the UTC-photodiodes detailed hereafter. The output power of reported LT-GaAs photomixers is moreover lower than reported output power for UTC-photodiodes. Concerning the UTC-photodiode design, the results demonstrate that the output power of narrow-band is higher than those illustrated for wide-band design.
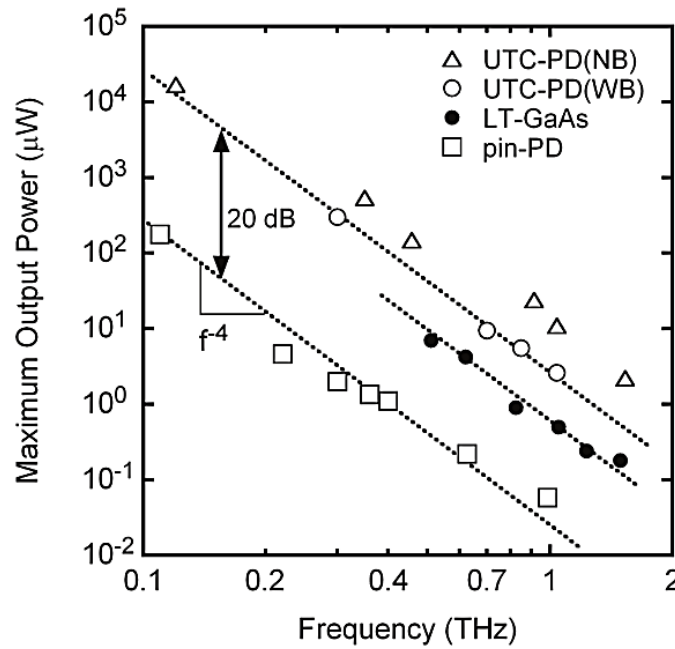

Figure 1.18: Reported output powers for PIN-PDs, LT-GaAs photomixers, wideband UTC-PD designs and narrowband UTC-PDs.

An intermediate photodiode between PIN and UTC photodiodes, named Partially Depleted Absorber (PDA) photodiodes have been reported [137]. Their particularity is to have an absorber layer partially p-type doped and the other part being undoped. This new photodiode design permits to reduce space charge effects and minimize thermal heat loading. These photodiodes have generated greater than 110 mA of photocurrent at a bandwidth of 1 GHz and over 57 mA at 10 GHz. The saturation current achieved from PDA photodiodes are lower than UTC but higher than PIN photodiodes.

In IEMN, Beck has demonstrated in his thesis a UTC photodiode with an absorbent layer thickness 100 nm, a collector thickness 250 nm and a diameter of junction 2 microns [138]. He has concluded a responsivity of 46 mA/W. With an optical signal of 50 mW at the wavelength of 1.55 µm; he has demonstrated a power transmission of 1.1 µW at 940 GHz using photomixing technique through a wide bandwidth antenna [139]. A wireless transmission system using this photodiode has demonstrated a digital signal transmission of 1 Gbit/s using a 200 GHz carrier frequency [140].

In the Figure 1.19, saturation current levels are illustrated as a function of frequency for UTC-photodiodes [25]. PIN-photodiodes and partially depleted absorber (PDA) photodiodes. PIN photodiodes using illumination by the surface, reach saturation current of 17.5 mA at 20 GHz [141]. The use of mixed depletion layers provides a saturation current of ~28 mA at 10 GHz followed by an enhancement study of 44 mA [142]. At higher frequencies, saturation currents of 11 mA [143] et 14 mA [144] have been obtained for Evanescently coupled photodiodes operating at 40 GHz. The structure of the UTC photodiode achieves saturation currents much higher than those of the PIN photodiodes with illumination through the rear face, saturation currents of 90 mA and 50 mA have been reported respectively at 20 GHz and 50 GHz [145]. Evanescently coupled photodiodes showed saturation currents of 32 mA and 22 mA at 40 GHz [146] and 50 GHz [147] respectively. Evanescently coupled PDA photodiodes, have demonstrated saturation current of 17 mA at 40 GHz [148], 120 mA at 14 GHz and 52 mA at 30 GHz [149].
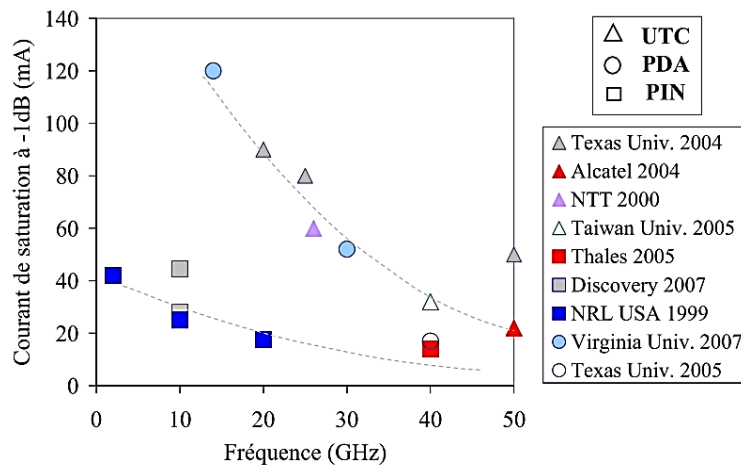

Figure 1.19: Saturation current plotted against the frequency for UTC-PDs, PDA-PDs and PIN-PDs

1.7. GaN-based material for photodetectors: state of the art

The optimization of the epitaxial techniques of this material has been delayed for several decades because of the lack of a lattice matched substrate. Nowadays, sapphire substrates are generally used for the epitaxial growth of thin III-Nitride layers and their related applications to electronic and optoelectronic devices, regardless of a large lattice mismatch of about 16% with GaN together with a large difference of thermal expansion coefficients. The Metalorganic Vapor Phase Epitaxy growth method, in addition to plasma-induced or gas-source Molecular Beam Epitaxy which were more lately introduced, allow the growth of device quality GaN and related compounds for a number of applications such as short wavelength LEDs emitting from the green to the blue light, and even reach the UV spectrum, blue lasers, field effect transistors and UV photodetectors. The first study for the photocurrent characterization of polycrystalline Gallium Nitride (GaN) was more than 30 years old [150].

Several kinds of III-nitride based UV photodetectors were studied as photoconductors [151], Schottky photodiodes [152], Metal-Semiconductor-Metal (MSM) photodiodes [153], PIN and avalanche photodiodes [154], [155]. Some relevant less classical features in the field of nitride-based detectors were also covered such as nitride-based UV phototransistors [156], multiple quantum well photodiodes [157] and polarization sensitive detectors [158]. As regards the studies on temporal and the frequency response of PIN ultraviolet photodetectors fabricated on single crystal GaN, Carrano et al also have measured a rise-time of ~43 psec at 15 V reverse bias for a 60 µm diameter mesa with 1 µm thick intrinsic region. Analysis indicated that small area PIN photodetectors are transit-time limited, while the larger area PIN's are RC-limited [159].

Carrano et al have been reported a very fast PIN photodiodes GaN-based material with time responses lower than 1 ns at a -5V bias [160]. This result demonstrated that extremely low capacitance values in the device require a higher thickness of the intrinsic layer up to 1 µm. Therefore, the transit time of the carriers is the only factor limiting the time response, while the RC factor is not any more the limiting factor. The disadvantage of this design is its low responsivity value (30 mA/W at a –5V bias) since the intrinsic region is thicker than the carrier

diffusion length. Such devices can operate at high bias voltages, and for this reason they are ideal for the ultrafast signal detection.

A limited number of studies have been dedicated to the generation, detection, and applications of InGaN/GaN-based terahertz waves. Laboratory tools as Terahertz time domain spectroscopy (THz-TDS) and terahertz emission spectroscopy have become useful tools, particularly for studying electronic processes in semiconductors connected with carrier dynamics and lattice vibrations [161].

A dynamical screening of built-in piezoelectric fields by photo-excited charge carriers has been proposed as a main reason for the occurrence of terahertz radiation during the excitation of InGaN/GaN MQWs by femtosecond laser pulses [162]. A strong built-in fields and high concentrations of charge carriers in InGaN/ GaN MQWs may lead to more efficient terahertz generation compared to generation from semiconductor surfaces [163]. Series of experiments on terahertz generation from InGaN/GaN light-emitting diode heterostructures at one- and two-photon excitation by femtosecond laser pulses has been conducted [164]. It was found that the terahertz pulse amplitude increases and its spectrum shifts towards higher frequencies with an increasing number of quantum wells in the heterostructures.

As green emitter, ultrafast carrier dynamics and recombination of InGaN MQW were reported [165]. Millimeter and sub-millimeter detections by AlGaN/GaN heterostructure Schottky diodes were reported for a performance up to 2.24 THz [166].

Numerous Studies demonstrate the functionalities of GaN self-switching diode SSDs as direct and heterodyne detectors and provide the guidelines for improving their performances at sub-THz frequencies [167]. Studied of capabilities of SSDs based on an AlGaN/GaN heterostructure operating as detectors and mixers have been experimentally demonstrated. More recently, experimental measurements were performed in order to optimize GaN-based nano-diodes for broadband Terahertz direct detection (in terms of responsivity) and mixing (in terms of output power). The capabilities of the so-called self-switching diode (SSD) were analyzed for different dimensions [168]. An efficient terahertz generation within InGaN/GaN multiple quantum wells has been reported. [163]. The mechanism for the THz generation has been attributed to either spontaneous dipoles radiation [162] or optical induced dynamic screening

[169]. The output power generated just by an 8-period InGaN/GaN QWs can reach the μW power level [163]. From InGaN / GaN Dot-in-a-Wire Light Emitting Diodes, an Enhanced Terahertz Generation was obtained by utilizing the internal field inside InGaN/GaN quantum wells (QWs) [170]. This result illustrates that these QWs correspond to one of the most efficient materials for THz generation.

The first InGaN/GaN based solar cells were proposed by Wu et al which promoting the advantage of resistance to high-energy radiation damage and flexible energy bandgap [4]. Thereafter, InGaN/GaN-based photovoltaic cells have been reported for several designs in homojunction as PIN [171], PN [172] and AlN [173]. As double heterojunction P-GaN/I-InGaN/N-GaN, many papers have been reported with improvement of external quantum efficiency [174]. The best performances of InGaN-GaN-based solar cells have been reported by Jani et al with open circuit voltage (Voc) of 2.4 V , 3.7 mA/cm² of short circuit current (Jsc) and fill factor (FF) of 0.78 comparing to Neufeld et al. with Voc of 1.81 V, Jsc of 4.2 mA/cm² and FF of 0.75 [15] [174]. As active layer, Multiple Quantum Wells (MQW) InGaN/GaN-based have improved the efficiency of the solar cells due to the high quality crystalline of InGaN [175]. Today, Dahal et al. have been reported un experimental conversion efficiency of 2.95 % [176].

In this chapter, we have described an introduction to III-Nitride based high speed devices. An overview of III-N Nitride materials and their applications has been detailed. The GaN material as a potential candidate for high speed devices has been considered as well as its figure of merit. Principal of the photodiode as a key element in the fabrication phase has been presented. The different fundamental properties as piezoelectric polarization, mechanical properties, crystal growth techniques and substrates have been illustrated. Electronic band structure and electrical properties have been also presented. The optical properties of III-nitride materials have been shown in order to clarify the different properties of InGaN alloy. The state of the art in GaN photodetectors has been reported. In the next chapter, the characterization of the grown material in different configurations will be studied. Structural and optical characterizations will be detailed for whole samples with different indium content.

References

[1] S. Nakamura, T. Mukai, and M. Senoh, "Candela-class high-brightness InGaN/AlGaN double-heterostructure blue-light-emitting diodes," *Appl. Phys. Lett.*, vol. 64, no. 13, p. 1687, 1994.

[2] A. Castiglia, M. Rossetti, M. Duelk, C. Vélez, and N. Grandjean, "InGaN laser diodes emitting at 500nm with p-layers grown by molecular beam epitaxy," *Appl. Phys. Express*, vol. 8, p. 022105, 2015.

[3] C. Rivera, J. Pereiro, Á. Navarro, E. Muñoz, O. Brandt, and H. T. Grahn, "Advances in Group-III-Nitride Photodetectors," pp. 1–9, 2010.

[4] J. Wu, W. Walukiewicz, K. M. Yu, W. Shan, J. W. Ager, E. E. Haller, H. Lu, W. J. Schaff, W. K. Metzger, and S. Kurtz, "Superior radiation resistance of In 1-xGa xN alloys: Full-solar-spectrum photovoltaic material system," *J. Appl. Phys.*, vol. 94, no. 10, pp. 6477–6482, 2003.

[5] U. K. Mishra, L. Shen, T. E. Kazior, and Y. F. Wu, "GaN-based RF power devices and amplifiers," *Proc. IEEE*, vol. 96, no. 2, pp. 287–305, 2008.

[6] G. A. Wilson and J. Brady, "Design considerations and signal processing algorithms for laser-induced fluorescence airborne pathogen sensors," in *Optically based biological and chemical sensing for defence*, vol. 5617, 2004, pp. 1–13.

[7] G. A. Shaw, M. Nischan, M. Iyengar, S. Kaushik, and M. K. Griffin, "NLOS UV communication for distributed sensor systems," *Proc. SPIE*, vol. 4126, pp. 83–96, 2000.

[8] E. F. Schubert, *Light-Emitting Diodes - 2nd Edition*. 2006.

[9] M. Razeghi and A. Rogalski, "Semiconductor ultraviolet detectors," *J. Appl. Phys.*, vol. 79, no. 10, pp. 7433–7473, 1996.

[10] N. Iwasa, S. Nagahama, and S. Nakamura, *Nitride semiconductor device*. 1999.

[11] S. Nakamura and G. Fasol, *The Blue Laser Diode*. Berlin: Springer, 1997.

[12] K. Suzue, S. N. Mohammad, Z. F. Fan, W. Kim, O. Aktas, A. E. Botchkarev, and H. Morkoç, "Electrical conduction in platinum–gallium nitride Schottky diodes," *J. Appl. Phys.*, vol. 80, no. 8, pp. 4467–4478, 1996.

[13] S. Nakamura, N. Senoh, N. Iwasa, and S. I. Nagahama, "High-Brightness InGaN Blue, Green and Yellow Light-Emitting-Diodes with Quantum-Well Structures," *Japanese J. Appl. Phys. Part 2-Letters*, vol. 34, no. 7A, pp. L797–L799, 1995.

[14] J. Wu, W. Walukiewicz, K. M. Yu, J. W. Ager, E. E. Haller, H. Lu, and W. J. Schaff, "Small band gap bowing in In 1−x Ga x N alloys," *Appl. Phys. Lett.*, vol. 80, no. 25, p. 4741, 2002.

[15] O. Jani, I. Ferguson, C. Honsberg, and S. Kurtz, "Design and characterization of GaNInGaN solar cells," *Appl. Phys. Lett.*, vol. 91, no. 13, pp. 13–15, 2007.

[16] Y. Nanishi, Y. Saito, and T. Yamaguchi, "RF-Molecular Beam Epitaxy Growth and Properties of InN and Related Alloys," *Jpn. J. Appl. Phys.*, vol. 42, no. Part 1, No. 5A, pp. 2549–2559, 2003.

[17] E. Muñoz, E. Monroy, J. L. Pau, F. Calle, F. Omnès, and P. Gibart, "III nitrides and UV detection," *J. Phys. Condens. Matter*, vol. 13, pp. 7115–7137, 2001.

[18] J. Schalwig, G. Müller, M. Eickhoff, O. Ambacher, and M. Stutzmann, "Group III-nitride-based gas sensors for combustion monitoring," *Mater. Sci. Eng. B Solid-State Mater. Adv. Technol.*, vol. 93, no. 1–3, pp. 207–214, 2002.

[19] S. N. Mohammad, A. A. Salvador, and H. Morkoc, "Emerging gallium nitride based devices," *Proc. IEEE*, vol. 83, no. 10, pp. 1306–1355, 1995.

[20] D. Kabra, K. Sardar, and K. S. Narayan, "Gallium nitride nanoparticles for solar-blind detectors," *J. Chem. Sci.*, vol. 115, no. 5–6, pp. 459–463, 2003.

[21] H. P. Maruska and J. J. Tietjen, "The preparation and properties of vapor-deposited single-crystal-line GaN," *Appl. Phys. Lett.*, vol. 15, no. 10, pp. 327–329, 1969.

[22] S. Nakamura, "GaN Growth Using GaN Buffer Layer," *Jpn. J. Appl. Phys.*, vol. 30, no. Part 2, No. 10A, pp. L1705–L1707, 1991.

[23] H. Amano, N. Sawaki, I. Akasaki, and Y. Toyoda, "Metalorganic vapor phase epitaxial growth of a high quality GaN film using an AlN buffer layer," *Appl. Phys. Lett.*, vol. 48, no. 5, p. 353, 1986.

[24] K. Osamura, K. Nakajima, Y. Murakami, P. H. Shingu, and A. Ohtsuki, "Fundamental absorption edge in GaN, InN and their alloys," *Solid State Commun.*, vol. 11, no. 5, pp. 617–621, 1972.

[25] J. Wu, "When group-III nitrides go infrared: New properties and perspectives," *J. Appl. Phys.*, vol. 106, no. 1, pp. 1–28, 2009.

[26] H. Amano, M. Kito, K. Hiramatsu, and I. Akasaki, "P-Type Conduction in Mg-Doped GaN Treated with Low-Energy Electron Beam Irradiation (LEEBI)," *Jpn. J. Appl. Phys.*, vol. 28, no. Part 2, No. 12, pp. L2112–L2114, 1989.

[27] S. Nakamura, T. Mukai, and M. Senoh, "In situ monitoring and Hall measurements of GaN grown with GaN buffer layers," *J. Appl. Phys.*, vol. 71, no. 11, pp. 5543–5549, 1992.

[28] V. Y. Davydov, a. a. Klochikhin, V. V. Emtsev, D. a. Kurdyukov, S. V. Ivanov, V. a. Vekshin, F. Bechstedt, J. Furthmüller, J. Aderhold, J. Graul, a. V. Mudryi, H. Harma, a. Hashimoto, a. Yamamoto, and E. E. Haller, "Band gap of hexagonal InN and InGaN alloys," *Phys. Status Solidi Basic Res.*, vol. 234, no. 3, pp. 787–795, 2002.

[29] T. L. Tansley and C. P. Foley, "Optical band gap of indium nitride," *J. Appl. Phys.*, vol. 59, no. 9, pp. 3241–3244, 1986.

[30] D. Hofstetter, E. Baumann, F. R. Giorgetta, R. Theron, H. Wu, W. J. Schaff, J. Dawlaty, P. A. George, L. F. Eastman, F. Rana, P. K. Kandaswamy, F. Guillot, and E. Monroy, "Intersubband Transition-Based Processes and Devices in AlN / GaN-Based Heterostructures," *Proc. IEEE*, vol. 98, no. 7, p. 1234, 2010.

[31] H. MacHhadani, Y. Kotsar, S. Sakr, M. Tchernycheva, R. Colombelli, J. Mangeney, E. Bellet-Amalric, E. Sarigiannidou, E. Monroy, and F. H. Julien, "Terahertz intersubband absorption in GaN/AlGaN step quantum wells," *Appl. Phys. Lett.*, vol. 97, p. 191101, 2010.

[32] D. Walker, X. Zhang, A. Saxler, P. Kung, J. Xu, and M. Razeghi, "AlxGa1−xN (0≤x≤1) ultraviolet photodetectors grown on sapphire by metal-organic chemical-vapor deposition," *Appl. Phys. Lett.*, vol. 70, no. 8, p. 949, 1997.

[33] J. C. Carrano, T. Li, D. L. Brown, P. A. Grudowski, C. J. Eiting, R. D. Dupuis, and J. C. Campbell, "High-speed pin ultraviolet photodetectors fabricated on GaN," *Electron. Lett.*, vol. 34, no. 18, pp. 1779 – 1781, 1998.

[34] G. Leds, S. Zhang, S. Watson, J. J. D. Mckendry, D. Massoubre, A. Cogman, E. Gu, R. K. Henderson, A. E. Kelly, and M. D. Dawson, "1.5 Gbit/s Multi-Channel Visible Light Communications Using CMOS-Controlled GaN-Based LEDs," vol. 31, no. 8, pp. 1211–1216, 2013.

[35] C. Skierbiszewski, "Growth and characterization of AlInN/GaInN quantum wells for high-

speed intersubband devices at telecommunication wavelengths," *Proc. SPIE*, vol. 6121, no. 2006, pp. 612109–612109–12, 2006.

[36] S. Nakamura, "InGaN/AlGaN blue-light-emitting diodes," *J. Vac. Sci. Technol. A Vacuum, Surfaces, Film.*, vol. 13, no. 3, p. 705, 1995.

[37] G. L. D. Processing, M. Fikry, C. Assissted, and I. Beam, "Investigations of Processing Methods for GaN-Based Laser Diodes," pp. 27–34.

[38] G. Parish, S. Keller, P. Kozodoy, J. P. Ibbetson, H. Marchand, P. T. Fini, S. B. Fleischer, S. P. DenBaars, U. K. Mishra, and E. J. Tarsa, "High-performance (Al,Ga)N-based solar-blind ultraviolet p–i–n detectors on laterally epitaxially overgrown GaN," *Appl. Phys. Lett.*, vol. 75, no. 2, p. 247, 1999.

[39] H. Morkoç, *Handbook of Nitride Semiconductors and Devices Vol. 1: Materials Properties, Physics and Growth*, vol. 1. 2009.

[40] I. Vurgaftman and J. R. Meyer, "Band parameters for nitrogen-containing semiconductors," *J. Appl. Phys.*, vol. 94, no. 6, pp. 3675–3696, 2003.

[41] M. Henini, "Properties, Processing and Applications of Gallium Nitride and Related Semiconductors," *Microelectronics Journal*, vol. 31, no. 3. p. 217, 2000.

[42] L. Lindsay, D. A. Broido, and T. L. Reinecke, "Thermal conductivity and large isotope effect in GaN from first principles," *Phys. Rev. Lett.*, vol. 109, no. 9, 2012.

[43] K.-C. Shen, T.-Y. Wang, D.-S. Wuu, and R.-H. Horng, "High thermal stability of high indium content InGaN films grown by pulsed laser deposition.," *Opt. Express*, vol. 20, no. 19, pp. 21173–80, 2012.

[44] D. M. Caughey and R. E. Thomas, "Carrier Mobilities in Silicon Empirically Related to Doping and Field," *Proc. IEEE*, vol. 55, no. 12, pp. 2192–2193, 1967.

[45] F. Schwierz, "An electron mobility model for wurtzite GaN," *Solid. State. Electron.*, vol. 49, no. 6, pp. 889–895, 2005.

[46] S. M. Sze and K. K. Ng, *Physics of Semiconductor Devices*. 2007.

[47] H. Morkoç, *Nitride Semieonduetors and Devices*. Springer-Verlag Berlin Heidelberg, 1999.

[48] T. Tsai, S. Chen, C. Chang, S. Hsu, and T. Lin, "Terahertz response of GaN thin films," *Opt. Soc. Am.*, vol. 14, no. 11, pp. 4898–4907, 2006.

[49] R. Krithivasan, Y. Lu, J. D. Cressler, J. S. Rieh, M. H. Khater, D. Ahlgren, and G. Freeman, "Half-Terahertz operation of SiGe HBTs," *IEEE Electron Device Lett.*, vol. 27, no. 7, pp. 567–569, 2006.

[50] H.-W. Hübers, S. G. Pavlov, and V. N. Shastin, "Terahertz lasers based on germanium and silicon," *Semicond. Sci. Technol.*, vol. 20, no. 7, pp. S211–S221, 2005.

[51] E. Johnson, "Physical limitations on frequency and power parameters of transistors," *IRE Int. Conv. Rec.*, vol. 13, pp. 27–34, 1966.

[52] B. J. Baliga, "Power Semiconductor Device Figure of Merit for High-Frequency Applications," *IEEE Electron Device Lett.*, vol. 10, no. 10, pp. 455–457, 1989.

[53] R. W. Keyes, "Figure of merit for semiconductors for high-speed switches," *Proc. IEEE*, vol. 60, no. 2, p. 225, 1972.

[54] J. H. Edgar, *Properties of group III nitrides*. 1994.

[55] H. Morkoç, *Handbook of Nitride Semiconductors and Devices*. 2008.

[56] P. Perlin, C. Jauberthie-Carillon, J. P. Itie, A. San Miguel, I. Grzegory, and A. Polian, "Raman scattering and x-ray-absorption spectroscopy in gallium nitride under high pressure," *Phys. Rev. B*, vol. 45, no. 1, pp. 83–89, 1992.

[57] L. Liu and J. H. Edgar, "Substrates for gallium nitride epitaxy," *Mater. Sci. Eng. R Reports*, vol. 37, no. 3, pp. 61–127, 2002.

[58] H. Angerer, D. Brunner, F. Freudenberg, O. Ambacher, M. Stutzmann, R. Hopler, T. Metzger, E. Born, G. Dollinger, A. Bergmaier, S. Karsch, and H. J. Korner, "Determination of the Al mole fraction and the band gap bowing of epitaxial AlxGa1-xN films," *Appl. Phys. Lett.*, vol. 71, no. 11, pp. 1504–1506, 1997.

[59] S. J. Pearton and F. Ren, "GaN Electronics," *Adv. Mater.*, vol. 12, no. 21, pp. 1571–1580, 2000.

[60] M. Leszczynski, H. Teisseyre, T. Suski, I. Grzegory, M. Bockowski, J. Jun, S. Porowski, K. Pakula, J. M. Baranowski, C. T. Foxon, and T. S. Cheng, "Lattice parameters of gallium nitride," *Appl. Phys. Lett.*, vol. 69, no. 1, p. 73, 1996.

[61] O. Ambacher and J. Majewski, "Pyroelectric properties of Al (In) GaN/GaN hetero-and quantum well structures," *J. Physics-Condensed Matter*, vol. 14, pp. 3399–3434, 2002.

[62] S. Mokkapati and C. Jagadish, "III-V compound SC for optoelectronic devices," *Mater. Today*, vol. 12, no. 4, pp. 22–32, 2009.

[63] E. T. Yu, X. Z. Dang, P. M. Asbeck, S. S. Lau, and G. J. Sullivan, "Spontaneous and piezoelectric polarization effects in III–V nitride heterostructures," *J. Vac. Sci. Technol. B Microelectron. Nanom. Struct.*, vol. 17, no. 4, p. 1742, 1999.

[64] F. Bernardini, V. Fiorentini, and D. Vanderbilt, "Spontaneous polarization and piezoelectric constants of III-V nitrides," *Phys. Rev. B*, vol. 56, no. 16, p. 4, 1997.

[65] K. Shimada, T. Sota, and K. Suzuki, "First-principles study on electronic and elastic properties of BN, AlN, and GaN," *J. Appl. Phys.*, vol. 84, no. 9, p. 4951, 1998.

[66] F. Demangeot, J. Frandon, M. A. Renucci, O. Briot, B. Gil, and R. L. Aulombard, "Raman determination of phonon deformation potentials in alpha-GaN," *Solid State Commun.*, vol. 100, no. 4, pp. 207–210, 1996.

[67] A. Fukumoto and K. Miwa, "First-principles calculation of the structural, electronic, and vibrational properties of gallium nitride and aluminum nitride," *Phys. Rev. B*, vol. 48, no. 11, pp. 7897–7902, 1993.

[68] T. Deguchi, D. Ichiryu, K. Toshikawa, K. Sekiguchi, T. Sota, R. Matsuo, T. Azuhata, M. Yamaguchi, T. Yagi, S. Chichibu, and S. Nakamura, "Structural and vibrational properties of GaN," *J. Appl. Phys.*, vol. 86, no. 1999, p. 1860, 1999.

[69] A. Polian, M. Grimsditch, and I. Grzegory, "Elastic constants of gallium nitride," *J. Appl. Phys.*, vol. 79, no. 6, pp. 3343–3344, 1996.

[70] W. C. Johnson, J. B. Parson, and M. C. Crew, "Nitrogen Compounds of Gallium. III," *J. Phys. Chem.*, vol. 36, no. 10, pp. 2651–2654, 1931.

[71] D. Sugihara, A. Kikuchi, K. Kusakabe, S. Nakamura, Y. Toyoura, T. Yamada, and K. Kishino, "High-quality GaN on AlN multiple intermediate layer with migration enhanced epitaxy by RF-molecular beam epitaxy," *Japanese J. Appl. Physics, Part 2 Lett.*, vol. 39, no. 3 A/B, 2000.

[72] S. Nakamura, Y. Harada, and M. Seno, "Novel metalorganic chemical vapor deposition system for GaN growth," *Appl. Phys. Lett.*, vol. 58, no. 18, pp. 2021–2023, 1991.

[73] O. H. Nam, T. S. Zheleva, M. D. Bremser, D. B. Thomson, and R. F. Davis, "Organometallic Vapor Phase Lateral Epitaxy of Low Defect Density GaN Layers," *MRS Proc.*, vol. 482, no. 18, pp. 2638–2641, 1997.

[74] C. L. Chao, C. H. Chiu, Y. J. Lee, H. C. Kuo, P. C. Liu, J. D. Tsay, and S. J. Cheng, "Freestanding high quality GaN substrate by associated GaN nanorods self-separated

hydride vapor-phase epitaxy," *Appl. Phys. Lett.*, vol. 95, no. 5, 2009.

[75] S. Nakamura, A. Kikuchi, K. Kusakabe, D. Sugihara, Y. Toyoura, T. Yamada, and K. Kishino, "InGaN/GaN MQW and Mg-doped GaN growth using a shutter control method by rf-molecular beam epitaxy," *Phys. Status Solidi Appl. Res.*, vol. 176, no. 1, pp. 273–277, 1999.

[76] I. Akasaki, H. Amano, Y. Koide, K. Hiramatsu, and N. Sawaki, "Effects of AlN buffer layer on crystallographic structure and on electrical and optical properties of GaN and GaAlN," *J. Cryst. Growth*, vol. 98, pp. 209 – 219, 1989.

[77] G. A. Slack and T. F. McNelly, "Growth of high purity AlN crystals," *J. Cryst. Growth*, vol. 34, no. 2, pp. 263–279, 1976.

[78] Y. E. Romanyuk, D. Kreier, Y. Cui, K. M. Yu, J. W. Ager, and S. R. Leone, "Molecular beam epitaxy of InGaN thin films on Si(111): Effect of substrate nitridation," *Thin Solid Films*, vol. 517, no. 24, pp. 6512–6515, 2009.

[79] C. Jagadish and S. . Pearton, *Zinc oxide bulk, thin films and nanostructures: processing, properties and applications.*, Oxford. Elsevier, 2006.

[80] D. I. Florescu, V. M. Asnin, F. H. Pollak, a. M. Jones, J. C. Ramer, M. J. Schurman, and I. Ferguson, "Thermal conductivity of fully and partially coalesced lateral epitaxial overgrown GaN/sapphire (0001) by scanning thermal microscopy," *Appl. Phys. Lett.*, vol. 77, no. 10, p. 1464, 2000.

[81] J. T. Torvik, M. W. Leksono, J. I. Pankove, C. Heinlein, J. K. Grepstad, and C. Magee, "Interfacial effects during GaN growth on 6H-SiC," *J. Electron. Mater.*, vol. 28, no. 3, pp. 234–239, 1999.

[82] J. Elsner, R. Jones, P. K. Sitch, V. D. Porezag, M. Elstner, T. Frauenheim, M. I. Heggie, S. Oberg, and P. R. Briddon, "Theory of Threading Edge and Screw Dislocations in GaN," *Phys. Rev. Lett.*, vol. 79, no. 19, pp. 3672–3675, 1997.

[83] P. Boguslawski, E. L. Briggs, and J. Bernholc, "Native defects in gallium nitride," *Phys. Rev. B*, vol. 51, no. 23, pp. 17255–17258, 1995.

[84] X. H. Wu, L. M. Brown, D. Kapolnek, S. Keller, B. Keller, S. P. DenBaars, and J. S. Speck, "Defect structure of metal-organic chemical vapor deposition-grown epitaxial (0001) GaN/Al2O3," *J. Appl. Phys.*, vol. 80, no. 6, p. 3228, 1996.

[85] H. T. Nykänen, *Low energy electron beam irradiation of gallium nitride.* .

[86] H. Y. Shin, S. K. Kwon, Y. I. Chang, M. J. Cho, and K. H. Park, "Reducing dislocation density in GaN films using a cone-shaped patterned sapphire substrate," *J. Cryst. Growth*, vol. 311, no. 17, pp. 4167–4170, 2009.

[87] H.-Y. Shih, M. Shiojiri, C.-H. Chen, S.-F. Yu, C.-T. Ko, J.-R. Yang, R.-M. Lin, and M.-J. Chen, "Ultralow threading dislocation density in GaN epilayer on near-strain-free GaN compliant buffer layer and its applications in hetero-epitaxial LEDs," *Sci. Rep.*, vol. 5, no. August, p. 13671, 2015.

[88] N. Koide, H. Kato, M. Sassa, S. Yamasaki, K. Manabe, M. Hashimoto, H. Amano, K. Hiramatsu, and I. Akasaki, "Doping of GaN with Si and properties of blue m/i/n/n+ GaN LED with Si-doped n++-layer by MOVPE," *J. Cryst. Growth*, vol. 115, no. 1–4, pp. 639–642, 1991.

[89] A. Janotti and C. G. Van De Walle, "Sources of unintentional conductivity in InN," *Appl. Phys. Lett.*, vol. 92, no. 3, 2008.

[90] S. Nakamura, T. Mukai, M. Senoh, and N. Iwasa, "Thermal Annealing Effects on P-Type Mg-Doped GaN Films," *Jpn. J. Appl. Phys.*, vol. 31, no. Part 2, No. 2B, pp. L139–L142,

1992.

[91]   H. Morkoç, *Handbook of Nitride Semiconductors and Devices Vol. 3: GaN-based Optical and Electronic Devices*. 2009.

[92]   J. Piprek, *Nitride Semiconductor Devices Principles and Simulation*. 2007.

[93]   B. Rezaei, A. Asgari, and M. Kalafi, "Electronic band structure pseudopotential calculation of wurtzite III-nitride materials," *Phys. B Condens. Matter*, vol. 371, no. 1, pp. 107–111, 2006.

[94]   F. K. Yam and Z. Hassan, "InGaN: An overview of the growth kinetics, physical properties and emission mechanisms," *Superlattices and Microstructures*, vol. 43, no. 1. pp. 1–23, 2008.

[95]   M. Suzuki, T. Uenoyama, and A. Yanase, "First-principles calculations of effective-mass parameters of AlN and GaN," *Phys. Rev. B*, vol. 52, no. 11, pp. 8132–8139, 1995.

[96]   Y. P. Varshni, "Temperature dependence of the energy gap in semiconductors," *Physica*, vol. 34, no. 1, pp. 149–154, 1967.

[97]   Y. S. Huang, F. H. Pollak, S. S. Park, K. Y. Lee, and H. Morkoç, "Contactless electroreflectance, in the range of 20 K<T<300 K, of freestanding wurtzite GaN prepared by hydride-vapor-phase epitaxy," *J. Appl. Phys.*, vol. 94, no. 2, pp. 899–903, 2003.

[98]   J. Wu, W. Walukiewicz, W. Shan, K. M. Yu, J. W. Ager, S. X. Li, E. E. Haller, H. Lu, and W. J. Schaff, "Temperature dependence of the fundamental band gap of InN," *J. Appl. Phys.*, vol. 94, no. 7, pp. 4457–4460, 2003.

[99]   V. Bougrov, M. E. Levinshtein, S. L. Rumyantsev, and A. Zubrilov, "Gallium Nitride (GaN)," in *Properties of Advanced SemiconductorMaterials GaN, AlN, InN, BN, SiC, SiGe*, 2001, pp. 1–20.

[100] T. Nagatomo, T. Kuboyama, H. Minamino, and O. Omoto, "Properties of Ga1- x In x N Films Prepared by MOVPE," *Jpn. J. Appl. Phys.*, vol. 28, no. 8, pp. 1334–1336, 1989.

[101] J. Wu, W. Walukiewicz, K. M. Yu, J. W. Ager, E. E. Haller, H. Lu, and W. J. Schaff, "Small band gap bowing in In1-xGaxN alloys," *Appl. Phys. Lett.*, vol. 80, no. 25, pp. 4741–4743, 2002.

[102] H. Morkoç, *Handbook of nitride semiconductors and devices Vol2: Electronic and Optical Processes in Nitrides*. 2008.

[103] D. Huang, F. Yun, M. A. Reshchikov, D. Wang, H. Morko??, D. L. Rode, L. A. Farina, ?? Kurdak, K. T. Tsen, S. S. Park, and K. Y. Lee, "Hall mobility and carrier concentration in free-standing high quality GaN templates grown by hydride vapor phase epitaxy," *Solid. State. Electron.*, vol. 45, no. 5, pp. 711–715, 2001.

[104] M. Ilegems and H. C. Montgomery, "Electrical properties of n-type vapor-grown gallium nitride," *J. Phys. Chem. Solids*, vol. 34, no. 5, pp. 885–895, 1973.

[105] D. L. Rode, "Low-Field Electron Transport," *Semicond. Semimetals*, vol. 10, no. C, pp. 1–89, 1975.

[106] T. T. Mnatsakanov, M. E. Levinshtein, L. I. Pomortseva, S. N. Yurkov, G. S. Simin, and M. a Khan, "Carrier mobility model for GaN," *Solid. State. Electron.*, vol. 47, no. 1, pp. 111–115, 2003.

[107] M. Roschke and F. Schwierz, "Electron mobility models for 4H, 6H, and 3C SiC," *IEEE Trans. Electron Devices*, vol. 48, no. 7, pp. 1442–1447, 2001.

[108] T. Tanaka, A. Watanabe, H. Amano, Y. Kobayashi, I. Akasaki, S. Yamazaki, and M. Koike, "P-type conduction in Mg-doped GaN and Al0.08Ga0.92N grown by metalorganic vapor phase epitaxy," *Appl. Phys. Lett.*, vol. 65, no. 5, pp. 593–594, 1994.

[109] D. K. Gaskill, L. B. Rowland, and K. Doverspike, "electrical properties of AlN, GaN, AlGaN," in *Properties of Group III Nitrides*, Volume 11., J. H. Edgar, Ed. London, 1994, pp. 101–116.

[110] H. Lu, W. J. Schaff, J. Hwang, H. Wu, G. Koley, and L. F. Eastman, "Effect of an AlN buffer layer on the epitaxial growth of InN by molecular-beam epitaxy," *Appl. Phys. Lett.*, vol. 79, no. 10, pp. 1489–1491, 2001.

[111] J. Aderhold, V. Y. Davydov, F. Fedler, H. Klausing, D. Mistele, T. Rotter, O. Semchinova, J. Stemmer, and J. Graul, "InN thin films grown by metalorganic molecular beam epitaxy on sapphire substrates," *J. Cryst. Growth*, vol. 222, pp. 701–705, 2001.

[112] H. Lu, W. J. Schaff, J. Hwang, H. Wu, W. Yeo, a Pharkya, and L. F. Eastman, "Improvement on epitaxial grown of InN by migration enhanced epitaxy," *Appl. Phys. Lett.*, vol. 77, no. 16, pp. 2548–2550, 2000.

[113] Y. Saito, T. Yamaguchi, H. Kanazawa, K. Kano, T. Araki, Y. Nanishi, N. Teraguchi, and A. Suzuki, "Growth of high-quality InN using low-temperature intermediate layers by RF-MBE," *J. Cryst. Growth*, vol. 237–239, no. 1–4 II, pp. 1017–1021, 2002.

[114] T. Inushima, V. Mamutin, V. Vekshin, S. Ivanov, T. Sakon, M. Motokawa, and S. Ohoya, "Physical properties of InN with the band gap energy of 1.1 eV," in *Proceeding of the Eleventh International Conference on Molecular Beam Epitaxy*, 2001, vol. 227, p. 481.

[115] V. W. L. Chin, T. L. Tansley, and T. Osotchan, "Electron mobilities in gallium, indium, and aluminum nitrides," *J. Appl. Phys.*, vol. 75, no. 11, pp. 7365–7372, 1994.

[116] J. C. Phillips, "Ionicity of the chemical bond in crystals," *Rev. Mod. Phys.*, vol. 42, no. 3, pp. 317–356, 1970.

[117] M. Wraback, H. Shen, J. C. Carrano, C. J. Collins, J. C. Campbell, R. D. Dupuis, M. J. Schurman, and I. T. Ferguson, "Time-resolved electroabsorption measurement of the transient electron velocity overshoot in GaN," *Appl. Phys. Lett.*, vol. 79, no. 9, pp. 1303–1305, 2001.

[118] J. Kolnik, I. H. Oguzman, K. F. Brennan, R. Wang, P. P. Ruden, and Y. Wang, "Electronic transport studies of bulk zincblende and wurtzite phases of GaN based on an ensemble Monte Carlo calculation including a full zone band structure," *J. Appl. Phys.*, vol. 78, no. 2, pp. 1033–1038, 1995.

[119] I. H. Oguzman, J. Kolnik, K. F. Brennan, R. Wang, T.-N. Fang, and P. P. Ruden, "Hole transport properties of bulk zinc-blende and wurtzite phases of GaN based on an ensemble Monte Carlo calculation including a full zone band structure," *J. Appl. Phys.*, vol. 80, no. 8, pp. 4429–4436, 1996.

[120] M. E. Levinshtein, S. L. Rumyantsev, and M. Shur, *Properties of advanced semiconductor materials : GaN, AlN, InN, BN, SiC, SiGe*. 2001.

[121] D. Fritsch, H. Schmidt, and M. Grundmann, "Band-structure pseudopotential calculation of zinc-blende and wurtzite AlN, GaN, and InN," *Phys. Rev. B*, vol. 67, no. 23, pp. 1–13, 2003.

[122] T. P. Chow and M. Ghezzo, "SiC power devices, in III-Nitride, SiC, and Diamond Materials for Electronic Devices," in *SiC Power Devices. MRS Proceedings*, 1996, p. 423.

[123] S. M. Duffy, S. Verghese, K. A. McIntosh, A. Jackson, A. C. Gossard, and S. Matsuura, "Accurate modeling of dual dipole and slot elements used with photomixers for coherent terahertz output power," *IEEE Trans. Microw. Theory Tech.*, vol. 49, no. 6 I, pp. 1032–1038, 2001.

[124] H. Ito, T. Furuta, Y. Hirota, T. Ishibashi, A. Hirata, T. Nagatsuma, H. Matsuo, T. Noguchi, and M. Ishiguro, "Photonic millimetre-wave emission at 300 GHz using an antenna-integrated uni-travelling-carrier photodiode," *Electronics Letters*, vol. 38, no. 17. p. 989, 2002.

[125] P. G. Huggard, B. N. Ellison, P. Shen, N. J. Gomes, and J. M. Payne, "Generation of millimetre and sub-millimetre waves by photomixing in 1.55 µm wavelength photodiode," *Electron. Lett.*, vol. 38, no. 7, pp. 327–328, 2002.

[126] S. Osborne, S. O'Brien, E. P. O'Reilly, P. G. Huggard, and B. N. Ellison, "Generation of CW 0.5 THz radiation by photomixing the output of a two-colour 1.49 µm Fabry-Perot diode laser," *Electronics Letters*, vol. 44, no. 4. p. 296, 2008.

[127] H. Ito, T. Ito, Y. Muramoto, T. Furuta, and T. Ishibashi, "Rectangular waveguide output unitraveling-carrier photodiode module for high-power photonic millimeter-wave generation in the F-band," *J. Light. Technol.*, vol. 21, no. 12, pp. 3456–3462, 2003.

[128] H. Ito, S. Kodama, Y. Muramoto, T. Furuta, T. Nagatsuma, and T. Ishibashi, "High-speed and high-output InP-InGaAs unitraveling-carrier photodiodes," *IEEE J. Sel. Top. Quantum Electron.*, vol. 10, no. 4, pp. 709–727, 2004.

[129] H. Ito, T. Furuta, F. Nakajima, K. Yoshino, and T. Ishibashi, "Photonic generation of continuous THz wave using uni-traveling-carrier photodiode," *J. Light. Technol.*, vol. 23, no. 12, pp. 4016–4021, 2005.

[130] F. Nakajima, T. Furuta, and H. Ito, "High-power continuous-terahertz-wave generation using resonant-antenna-integrated uni-travelling-carrier photodiode," *Electronics Letters*, vol. 40, no. 20. p. 1297, 2004.

[131] D. Schoenherr, C. Sydlo, T. Goebel, M. Feiginov, H. L. Hartnagel, P. Meissner, H.-G. Bach, R. Kunkel, G. G. Mekonnen, and R. Zhang, "Characterization of THz emitter based on a high-speed p-i-n photodiode," *2007 Jt. 32nd Int. Conf. Infrared Millim. Waves 15th Int. Conf. Terahertz Electron.*, 2007.

[132] A. Wakatsuki, T. Furuta, Y. Muramoto, T. Yoshimatsu, and H. Ito, "High-power and broadband sub-terahertz wave generation using a J-band photomixer module with rectangular-waveguide output port," in *33rd International Conference on Infrared and Millimeter Waves and the 16th International Conference on Terahertz Electronics, 2008, IRMMW-THz 2008*, 2008.

[133] E. Rouvalis, C. C. Renaud, D. G. Moodie, M. J. Robertson, and A. J. Seeds, "Traveling-wave Uni-Traveling Carrier photodiodes for continuous wave THz generation.," *Opt. Express*, vol. 18, no. 11, pp. 11105–11110, 2010.

[134] G. D. Bett, *Advances in Photodiodes*. Rijeka, Croatia: InTech, 2011.

[135] P. G. Huggard, B. N. Ellison, P. Shen, N. J. Gomes, P. A. Davies, W. P. Shillue, A. Vaccari, and J. M. Payne, "Efficient generation of guided millimeter-wave power by photomixing," *IEEE Photonics Technol. Lett.*, vol. 14, no. 2, pp. 197–199, 2002.

[136] H. Ito, F. Nakajima, T. Furuta, K. Yoshino, Y. Hirota, and T. Ishibashi, "Photonic terahertz-wave generation using antenna-integrated uni-travelling-carrier photodiode," *Electron Lett*, vol. 39, no. 25, pp. 1437–1439, 2003.

[137] X. Li, N. Li, X. Zheng, S. Demiguel, J. C. Campbell, D. a. Tulchinsky, and K. J. Williams, "High-saturation-current InP-InGaAs photodiode with partially depleted absorber," *IEEE Photonics Technol. Lett.*, vol. 15, no. 9, pp. 1276–1278, 2003.

[138] A. Beck, "Réalisation et caractérisation de photodiodes à transport unipolaire pour la génération d'ondes térahertz," 2008.

[139] A. Beck, G. Ducournau, M. Zaknoune, E. Peytavit, T. Akalin, J. F. Lampin, F. Mollot, F. Hindle, C. Yang, and G. Mouret, "High-efficiency uni-travelling-carrier photomixer at 1.55 [micro sign]m and spectroscopy application up to 1.4 THz," *Electronics Letters*, vol. 44, no. 22. p. 1320, 2008.

[140] G. Ducournau, P. Szriftgiser, D. Bacquet, a. Beck, T. Akalin, E. Peytavit, M. Zaknoune, and J. F. Lampin, "Optically power supplied Gbit/s wireless hotspot using 1.55 [micro sign]m THz photomixer and heterodyne detection at 200 GHz," *Electron. Lett.*, vol. 46, no. 19, p. 1349, 2010.

[141] K. J. Williams and R. D. Esman, "Large-signal compression-current measurements in high-power microwave pin photodiodes," *Electron. Lett.*, vol. 35, no. 1, p. 82, 1999.

[142] A. Joshi and D. Becker, "GRIN Lens-Coupled Top-Illuminated Photodetectors for High-Power Applications," pp. 18–20, 2007.

[143] S. Demiguel, L. Giraudet, L. Joulaud, J. Decobert, F. Blache, V. Coupé, F. Jorge, P. Pagnod-Rossiaux, E. Boucherez, M. Achouche, and F. Devaux, "Evanescently coupled photodiodes integrating a double-stage taper for 40-Gb/s applications - Compared performance with side-illuminated photodiodes," *J. Light. Technol.*, vol. 20, no. 12, pp. 2004–2014, 2002.

[144] N. Michel, V. Magnin, J. Harari, A. Marceaux, O. Parillaud, D. Decoster, N. Vodjdani, and Abstract:, "High-power evanescently-coupled waveguide photodiodes," *IEE Proc. - Optoelectron.*, vol. 153, no. 4, pp. 199–204, 2006.

[145] N. Li, X. Li, S. Demiguel, X. Zheng, J. C. Campbell, D. a. Tulchins, K. J. Williams, T. D. Isshiki, G. S. Kinsey, and R. Sudharsansan, "High-Saturation-Current Charge-Compensated InGaAs-InP Uni-Traveling-Carrier Photodiode," *IEEE Photonics Technol. Lett.*, vol. 16, no. 3, pp. 864–866, 2004.

[146] J. Shi, Y. Wu, C. Wu, P. Chiu, and C. Hong, "Performance of Near-Ballistic Uni-Traveling-Carrier Photodiode at 1 . 55 µm Wavelength," *IEEE Photonics Technol. Lett.*, vol. 17, no. 9, pp. 1929–1931, 2005.

[147] M. Achouche, V. Magnin, J. Harari, F. Lelarge, E. Derouin, C. Jany, D. Carpentier, F. Blache, and D. Decoster, "High Performance Evanescent Edge Coupled Waveguide Unitraveling-Carrier Photodiodes for >40-Gb/s Optical Receivers," *IEEE Photonics Technol. Lett.*, vol. 16, no. 2, pp. 584–586, 2004.

[148] S. Demiguel, X. Li, N. Li, H. Chen, J. C. Campbell, J. Wei, and A. Anselm, "Analysis of partially depleted absorber waveguide photodiodes," *J. Light. Technol.*, vol. 23, no. 8, pp. 2505–2512, 2005.

[149] X. W. X. Wang, N. D. N. Duan, H. C. H. Chen, and J. C. Campbell, "InGaAs–InP PhotodiodesWith High Responsivity and High Saturation Power," *IEEE Photonics Technol. Lett.*, vol. 19, no. 16, pp. 1272–1274, 2007.

[150] J. I. Pankove, "Properties of Zn-doped GaN. II. Photoconductivity," *J. Appl. Phys.*, vol. 45, no. 9, p. 3892, 1974.

[151] E. Muñoz, E. Monroy, J. a. Garrido, I. Izpura, F. J. Sánchez, M. a. Sánchez-García, E. Calleja, B. Beaumont, and P. Gibart, "Photoconductor gain mechanisms in GaN ultraviolet detectors," *Appl. Phys. Lett.*, vol. 71, no. 7, p. 870, 1997.

[152] E. Monroy, F. Calle, E. Muñoz, F. Omnès, P. Gibart, and J. a. Muñoz, "Al[sub x]Ga[sub 1−x]N:Si Schottky barrier photodiodes with fast response and high detectivity," *Appl. Phys. Lett.*, vol. 73, no. 15, p. 2146, 1998.

[153] E. Monroy, F. Calle, E. Muñoz, and F. Omnès, "AlGaN metal–semiconductor–metal

photodiodes," *Appl. Phys. Lett.*, vol. 74, no. 22, p. 3401, 1999.

[154] X. Zhang, P. Kung, D. Walker, J. Piotrowski, a. Rogalski, a. Saxler, and M. Razeghi, "Photovoltaic effects in GaN structures with p-n junctions," *Appl. Phys. Lett.*, vol. 67, no. 14, p. 2028, 1995.

[155] a. Osinsky, S. Gangopadhyay, R. Gaska, B. Williams, M. a. Khan, D. Kuksenkov, and H. Temkin, "Low noise p-π-n GaN ultraviolet photodetectors," *Appl. Phys. Lett.*, vol. 71, no. 16, p. 2334, 1997.

[156] W. Yang, T. Nohava, S. Krishnankutty, R. Torreano, S. McPherson, and H. Marsh, "High gain GaN/AlGaN heterojunction phototransistor," *Appl. Phys. Lett.*, vol. 73, no. 7, p. 978, 1998.

[157] C. Rivera, J. L. Pau, J. Pereiro, and E. Muñoz, "Properties of Schottky barrier photodiodes based on InGaN/GaN MQW structures," *Superlattices Microstruct.*, vol. 36, no. 4–6, pp. 849–857, 2004.

[158] C. Rivera, J. L. Pau, E. Muñoz, P. Misra, O. Brandt, H. T. Grahn, and K. H. Ploog, "Polarization-sensitive ultraviolet photodetectors based on M-plane GaN grown on LiAlO[sub 2] substrates," *Appl. Phys. Lett.*, vol. 88, no. 21, p. 213507, 2006.

[159] J. C. Carrano, T. Li, D. L. Brown, P. a. Grudowski, C. J. Eiting, R. D. Dupuis, and J. C. Campbell, "Very high-speed metal-semiconductor-metal ultraviolet photodetectors fabricated on GaN," *Appl. Phys. Lett.*, vol. 73, no. 17, pp. 2405–2407, 1998.

[160] J. Carrano, T. Li, C. Eiting, R. Dupuis, and J. Campbell, "Very high-speed ultraviolet photodetectors fabricated on GaN," *J. Electron. Mater.*, vol. 28, no. 3, pp. 325–333, 1999.

[161] S. L. Dexheimer, *Terahertz Spectroscopy: Principles and Applications*. 2007.

[162] D. Turchinovich, P. Uhd Jepsen, B. S. Monozon, M. Koch, S. Lahmann, U. Rossow, and a. Hangleiter, "Ultrafast polarization dynamics in biased quantum wells under strong femtosecond optical excitation," *Phys. Rev. B*, vol. 68, no. 24, p. 241307, 2003.

[163] G. Sun, G. Xu, Y. J. Ding, H. Zhao, G. Liu, J. Zhang, and N. Tansu, "Efficient Terahertz Generation Within InGaN/GaN Multiple Quantum Wells," *IEEE J. Sel. Top. Quantum Electron.*, vol. 17, no. 1, pp. 48–53, Jan. 2011.

[164] I. Prudaev, S. Sarkisov, O. Tolbanov, and A. Kosobutsky, "Photoluminescence and terahertz generation in InGaN/GaN multiple quantum well light-emitting diode heterostructures under laser excitation," *Phys. Status Solidi*, vol. 252, no. 5, pp. 946–951, 2014.

[165] M. Jamil, V. Jindal, C. Wetzel, P. Li, and T. Dtechprohm, "Ultrafast Carrier Dynamics and Recombination in Green Emitting InGaN MQW LED," in *MRS Proceedings / Volume 916*, 2006.

[166] D. Veksler, F. Aniel, S. Rumyantsev, and M. S. Shur, "GaN Heterodimensional Schottky Diode for THz Detection," in *5th IEEE Conf. Sensors*, 2006, no. 0333314, pp. 323–326.

[167] P. Sangaré, G. Ducournau, B. Grimbert, V. Brandli, M. Faucher, C. Gaquière, A. Í. De-La-Torre, I. Í. De-La-Torre, J. F. Millithaler, J. Mateos, and T. González, "Experimental demonstration of direct terahertz detection at room-temperature in AlGaN/GaN asymmetric nanochannels," *J. Appl. Phys.*, vol. 113, no. 3, pp. 0–6, 2013.

[168] I. Íñiguez-de-la-torre, C. Daher, J. Millithaler, J. Torres, P. Nouvel, L. Varani, P. Sangaré, G. Ducournau, C. Gaquière, T. González, S. Member, and J. Mateos, "Operation of GaN Planar Nanodiodes as THz Detectors and Mixers," *IEEE Trans. Terahertz Sci. Technol.*, vol. 4, no. 6, pp. 670–677, 2014.

[169] P. C. M. Planken, M. C. Nuss, W. H. Knox, D. a. B. Miller, and K. W. Goossen, "THz

pulses from the creation of polarized electron-hole pairs in biased quantum wells," *Appl. Phys. Lett.*, vol. 61, no. 17, p. 2009, 1992.

[170] G. Sun, R. Chen, Y. J. Ding, H. P. . Nguyen, and Z. M, "Enhanced Terahertz Generation from InGaN / GaN Dot-in-a-Wire Light Emitting Diodes," *Opt. Soc. Am.*, vol. 1, pp. 10–11, 2013.

[171] S. W. Zeng, B. P. Zhang, J. W. Sun, J. F. Cai, C. Chen, and J. Z. Yu, "Substantial photo-response of InGaN p–i–n homojunction solar cells," *Semicond. Sci. Technol.*, vol. 24, no. 5, p. 055009, 2009.

[172] C. Yang, X. Wang, H. Xiao, J. Ran, C. Wang, G. Hu, X. Wang, X. Zhang, J. Li, and J. Li, "Photovoltaic effects in InGaN structures with p-n junctions," *Phys. Status Solidi Appl. Mater.*, vol. 204, no. 12, pp. 4288–4291, 2007.

[173] X. Chen, K. D. Matthews, D. Hao, W. J. Schaff, and L. F. Eastman, "Growth, fabrication, and characterization of InGaN solar cells," *Phys. Status Solidi Appl. Mater. Sci.*, vol. 205, no. 5, pp. 1103–1105, 2008.

[174] C. J. Neufeld, N. G. Toledo, S. C. Cruz, M. Iza, S. P. DenBaars, and U. K. Mishra, "High quantum efficiency InGaN/GaN solar cells with 2.95 eV band gap," *Appl. Phys. Lett.*, vol. 93, no. 14, pp. 14–17, 2008.

[175] R. Dahal, B. Pantha, J. Li, J. Y. Lin, and H. X. Jiang, "InGaN/GaN multiple quantum well solar cells with long operating wavelengths," *Appl. Phys. Lett.*, vol. 94, no. 6, p. 063505, 2009.

[176] R. Dahal, J. Li, K. Aryal, J. Y. Lin, and H. X. Jiang, "InGaN/GaN multiple quantum well concentrator solar cells," *Appl. Phys. Lett.*, vol. 97, no. 7, p. 073115, 2010.

Chapter II.   Material characterization of InGaN/GaN layers

II.1.   Introduction

In this chapter, we provide a detailed study of material quality for several types of structures InGaN/GaN. Our study concerns different compositions of indium for InGaN intrinsic layer in the PIN structure. We will analyze the InGaN material as function of indium percentage. The growth of studied samples was provided from numerous collaborators. Commercials and academic entities have established highly regarded collaboration with our group in order to have a significant feedback of their materials in terms of quality and device performance subsequently. As we work on a photodetector based on InGaN/GaN material, it is important to adjust the indium content in the InGaN layer (absorbent layer) in order to identify the optimal wavelength of excitation in the absorption phase. It is noted that the availability in the market of laser source which is expected to be the light source of excitation is a key factor. It should be defined according to requested samples in order to improve the photodetection of fabricated devices. In the Figure 2.1, we made a synthesis of reported cutoff frequency measured by optical absorption for different indium composition of InGaN layer [1]–[11].
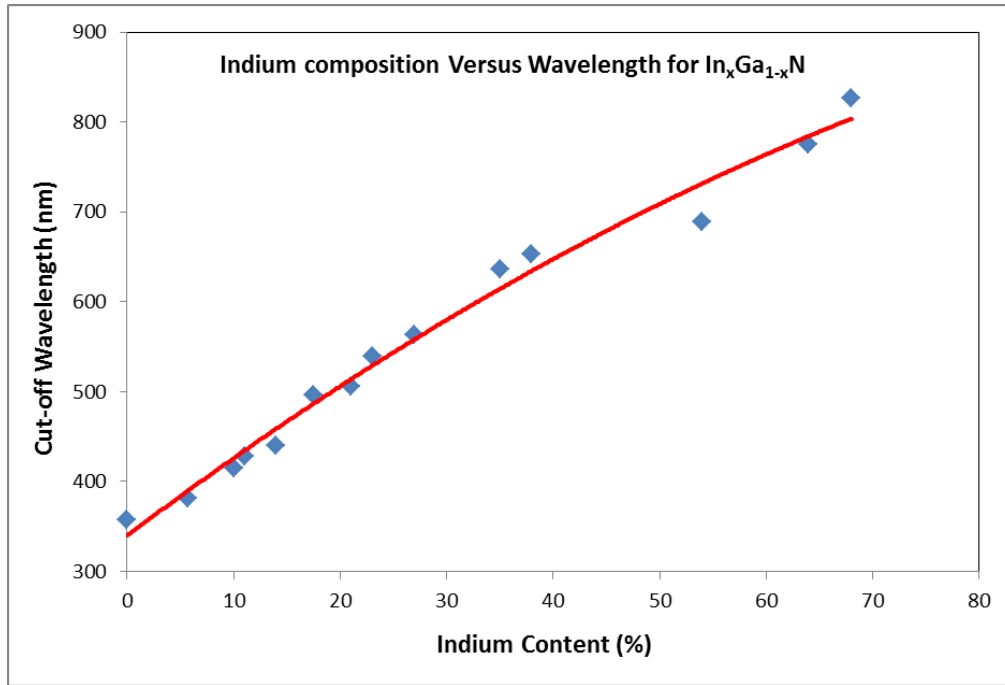
Figure 2.20: Reported cutoff wavelengths for different values of indium composition for InGaN layer measured by optical absorption.

The objective of this synthesis is to identify the laser source used later for the characterization phase. The fact is that the quality of material decreases with the incorporation of indium due to increased lattice mismatch with the substrate and the disorder introduced by the indium atoms, causing the formation of many defects. For that, it has been decided to proceed with low concentrations of indium ($x = 10\%$) of $In_xGa_{1-x}N$ layer since the quality of material had better improvement and good crystalline quality. It is worth noting that the evaluation of the photodiode in high percentage of indium content permits to work around the red wavelength 600 nm. This will enable more availability in terms of laser sources. For this purpose, increasing the indium composition of InGaN toward 20%, 30% and 50% will be the succeeding objectives once we have optimized the fabrication process. According to the Figure 2.1, the laser source of excitation should be in the range of 400-700 nm (visible spectrum) in order to evaluate the photodiode response in different percentage of indium composition in InGaN layer. The first phase of fabrication and characterization will be performed for 10% of indium content of InGaN samples. For this reason, a laser source of 400 nm is expected to be the excited source of photodiode and could also excite the other composition of InGaN (20%, 30% and 50%). However this 400 nm laser source is not the optimal wavelength for the higher indium composition samples, but it allows estimating the photodiode response.

During this project it has been conducted to study the optical waveguiding properties into porous GaN structures. Samples have been grown and structured by Korea Advanced Institute of Science and Technology (KAIST) in South Korea. Films have been prepared on sapphire by MOCVD and the microstructure has been characterized in IEMN. The dispersion of refractive index for porous GaN has been studied and compared to the GaN bulk material. The control of the refractive index into GaN is therefore fundamental for the design of active and passive optical devices. The objective of this study is to control the light emission by an increased coupling of the active material with optical modes, as well as the enhancement of the light collection efficiency.

In this chapter, the configuration of InGaN/GaN for the PIN structure is discussed. As the growth of materiel is carried out by external collaborators, a number of growth options will be also mentioned. In order to evaluate the crystalline quality, density of dislocations, surface morphology, layer thickness and indium composition, structural and microstructural

characterization are detailed. X-Ray Diffraction measurement (XRD) will be presented. Besides, Scanning Electron Microscopy (SEM), Transmission Electron Microscopy TEM, Energy-dispersive X-ray spectroscopy (EDX), and Atomic Force Microscopy (AFM) are also illustrated. We will also determine the optical properties such as refractive index, photoluminescence spectra and cut-off wavelength of absorption/transmission. For this, Prism coupling, Ellipsometry, Micro-Photoluminescence (µPL) and Spectrophotometer will be employed. Samples with differnet indium composition of InGaN 10%, 20%, 30% and 50% will be compared in terms of surface morphology and dislocation density. As we acquire two different growth techniques MBE and MOCVD, the grown samples will be also evaluated. Finally, the porous GaN structure is optically characterized.

II.2.   Growth of InGaN/GaN structure with different indium composition

Two important factors have been discussed in terms of material growth, the first is the substrate and the second is the growth technique. As explained in the first chapter, it is known that the large lattice constant and thermal expansion coefficient mismatches of substrates with GaN have been the major concern of studies. Recently, the majority of III-nitride growth has been performed on c-plane sapphire substrates regardless of a lattice parameter and a thermal expansion coefficient which are different from those of GaN and cause defects in the GaN material. The lattice mismatch parameter relating to GaN epilayer is about 15% for sapphire [12]. According to our requirements, grower expertizes and cost issue, the sapphire substrate will be the best candidate.

Concerning the growth technique for InGaN/GaN structures, MOCVD and MBE have provided the highest quality GaN based materials for semiconductor heterostructures. MOCVD grower in Europe has been identified and well known as one of the best III-Nitrides supplier for electronic and photonic applications, named NOVAGAN Company. It has provided 10%, 20% and 30% of indium composition of InGaN/GaN/Sapphire wafers throughout the whole project. 50% of InGaN indium content sample has been grown by MOCVD also and provided by the

Institute of Materials Research and Engineering (IMRE) in Singapore. For the MBE growth provider, we have established a long-term collaboration with King Abdullah University of Science and Technology (KAUST) in Saudi Arabia. Photonics Lab in this university has grown 10% of InGaN/GaN/sapphire wafers by MBE in order to compare it with MOCVD samples in terms of material quality and device performance. The structure of PIN photodiode has been discussed with the growers according to their expertise in order to obtain the best configuration of growth. Tow type of structures will be studied in each phase of InGaN growth, multi quantum well of InGaN layer (MQW-InGaN) and Single Layer of InGaN (SL-InGaN). The objective is to analyze two different configurations in each indium percentage of InGaN and to investigate the effect of heterostructure on the photodiode response.

The proposed PIN structure consists of a thick not-intentionally-doped (n.i.d) GaN buffer layer (called also undoped GaN) on c-plane (0001) sapphire. In order to optimize a high crystalline quality GaN and to move away from the interface GaN/Sapphire, the thickness of this layer is chosen to be 2.5 µm. It is followed by 3.5 µm thick Si-doped n-type GaN layer with a carrier concentration of 3×10^{18} cm^{-3}.

The thickness of "i" layer or the absorption layer, is a critical parameter and should be optimized. It is known that the collection efficiency decreases sharply with the increase in the thickness of the absorption layer [13]. As the absorption coefficient influence directly on the device operation, it is important to adjust this factor to obtain an optimal thickness of absorption layer (InGaN layer). With the value of 10^{5}cm^{-1} of absorption coefficient for InGaN reported in chapter 1, we need 100 nm of thickness in order to absorb efficiently the emitted light. However, a critical thickness depending on the InGaN indium content is a major criteria and could be estimated to reported models [14]. Accordingly, 100 nm of intrinsic layer of SL-InGaN will be grown for the SL configuration. For the MQW-InGaN configuration, several possibilities exist in the literature. A synthesis of reported adjustment of MQW-InGaN/GaN layer has been carried out in the Table 1.

active layer thickness (nm)	Number of periods of InGaN/GaN	Period thickness InGaN/GaN (nm)	Indium composition (%)	Wavelength (nm)	bandgap (eV)	Reference
100	10	2.5/7.5	20	NC	NC	[15]
140	5	3/25	6	410	3.024	[16]
280	10	3/25	10	460	2.695	[16]
50	5	3/7	23	470	2.638	[17]
48	6	2/6	15	476.9	2.600	[18]
50	5	2/8	20	470	2.638	[19]
75	5	3/12	20	NC	NC	[20]
90	9	2.5/7.5	15	380	3.293	[21]

Table 9: Synthesis of MQW configuration reported in the literature for InGaN/GaN.

Consequently, 10 pairs of InGaN/GaN MQWs with 2.5 nm of InGaN and 12 nm of GaN barrier has been proposed to growers and fit well with their optimized configurations. Finally, 100 nm Mg-doped p-type GaN layer is grown with a carrier concentration of 5×10^{17} cm^{-3}. It has been agreed that the PIN structure will be carried out according to the Figure 2.2.
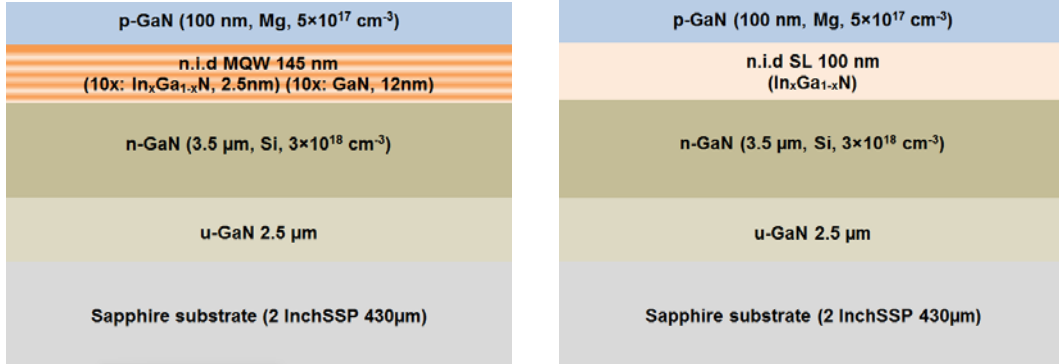
Figure 2.21: PIN structure for MQW-InGaN configuration (left) and SL-InGaN configuration (right).

In the Table 2, we illustrate all studied samples with related indium composition, growth type and used abbreviation in the manuscript in order to simplify designations.

Chapter II. Material characterization of InGaN/GaN layers

Sample ID	Absorption layer	Configuration	Growth technique	Provider	Structure	Sample abbreviation
18161	NC	P–type	MOCVD	NOVAGAN	P-GaN/Sapphire	P1
17351	$In_{0.1}Ga_{0.9}N$	Single layer	MOCVD	NOVAGAN	PIN/sapphire	SL10-1
17361	$In_{0.1}Ga_{0.9}N/GaN$	MQW	MOCVD	NOVAGAN	PIN/sapphire	MQ10-1
18041	$In_{0.1}Ga_{0.9}N$	Single layer	MOCVD	NOVAGAN	PIN/sapphire	S10-2
18021	$In_{0.1}Ga_{0.9}N/GaN$	MQW	MOCVD	NOVAGAN	PIN/sapphire	MQ10-2
S334	$In_{0.1}Ga_{0.9}N$	Single layer	MBE	KAUST	PIN/sapphire	SL10-3
S336	$In_{0.1}Ga_{0.9}N/GaN$	MQW	MBE	KAUST	PIN/sapphire	MQ10-3
21822	$In_{0.2}Ga_{0.8}N$	Single layer	MOCVD	NOVAGAN	PIN/sapphire	SL20
21981	$In_{0.2}Ga_{0.8}N/GaN$	MQW	MOCVD	NOVAGAN	PIN/sapphire	MQ20
19471	$In_{0.3}Ga_{0.7}N$	Single layer	MOCVD	NOVAGAN	PIN/sapphire	SL30
19511	$In_{0.3}Ga_{0.7}N/GaN$	MQW	MOCVD	NOVAGAN	PIN/sapphire	MQ30
IGN4050	$In_{0.5}Ga_{0.5}N$	Single layer	MOCVD	IMRE	IN/sapphire	SL50
1305	NC	Bulk GaN layer	MOCVD	KAIST	GaN/sapphire	BK
1317	NC	20% Porous GaN layer	MOCVD	KAIST	GaN/sapphire	POR20
1318	NC	40% Porous GaN layer	MOCVD	KAIST	GaN/sapphire	POR40

Table 10: List of studied samples with different configurations and related abbreviations.

II.3. Characterization techniques

II.3.1. Structural characterization techniques

II.3.1.1. X-Ray Diffraction (XRD)

The X-ray diffraction is a widely used structural analysis just as powerful and non-destructive experimental technique. XRD analysis can provide information about structural quality such as lattice parameters of crystals, strain state, crystalline orientation, layer thickness and chemical composition of alloys. X-rays has a very small wavelength in the order of atomic range and the typical wavelength used for crystallography is 1 Å (0.1 nm). It is typically produced using cupper (Cu) or molybdenum (Mo) sources. XRD technique consists of probing a crystal through x-ray radiation owning wavelength (λ) close to the interatomic spacing, and then will be scattered by atoms. The X-ray beam is generated by bombarding a metal with electrons in incidence angle called (ω) then scattered by ions which produce diffractions on different planes of the structure with angle of 2θ then collected by a removable sensor. Figure 2.3 shows the principal of XRD with planes of atoms where indicated by dotted lines [22].
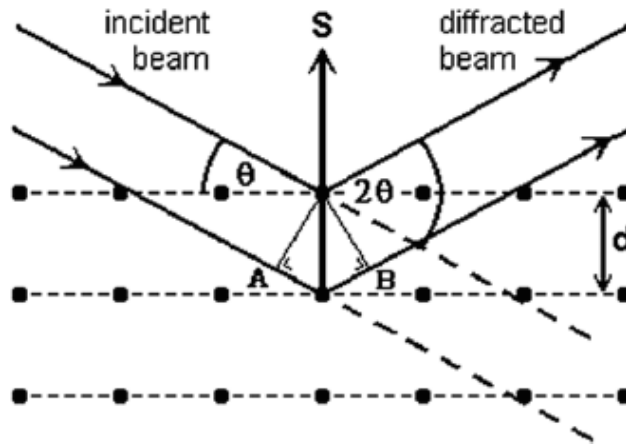
Figure 2.22: Schematic of XRD.

The Bragg's law is used in order to achieve the maximal intensity of scattered radiations which relates the spacing between the planes of atoms from which diffraction is occurring (d) to the angle (θ) at which the incident monochromatic beam must probe the plane to give constructive interference (Equation 2.1). The Bragg's law equation illustrates that constructive

interference occurs among the scattered x-rays when the path difference AB (n λ) is equivalent to 2d sin θ, where (n) is the order of the reflection [23].

$$n\,\lambda = 2d\,sin\,\theta$$ *Equation 2.37*

There are two configurations on diffraction scan analysis using XRD technique: out-of-plane (symmetrical, asymmetrical and skew symmetrical) and in-plan scattering, shown in the Figure 2.4 [22]. In the symmetrical configuration, sample and detector are keeping 2θ = 2ω condition. Two types of scan are usually performed in this symmetrical configuration, the first is ω-scan which permits to obtain the different orientation of crystal. The second is the ω-2θ scan which provides the layers structure, periods, thickness and the interatomic distance (c-parameter in (0001)-oriented GaN).
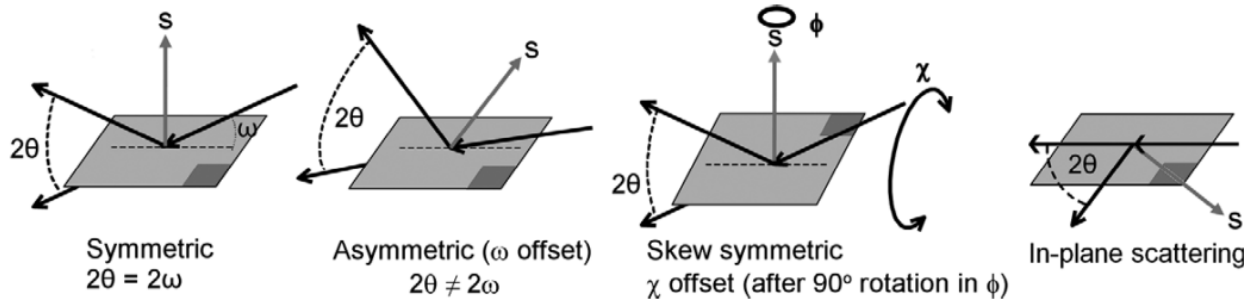
Figure 2.23: Possibility of diffraction scan geometry

The asymmetrical scan is performed with respect to the conditions 2θ ≠2ω. This could deliver the measurements of the interplanar distance (d) between planes and could provide information about strain states and in-planar lattice parameter (a-parameter in (0001)-oriented GaN). The skew symmetrical scan is used generally to extract edge dislocation density, the Full Width Half Maximum (FWHM) data should be extracted using scan in the (121) plane. The in-plan scattering configuration is performed to estimate very thin films by measuring the intensities from lattice planes [22].

Rocking curve (RC) is another type of scan which is similar to out-of-plane scan and determining the mean spread in orientation of the different crystalline domains of a non-perfect crystal. RC could be achieved in symmetric, asymmetric or skew-symmetric scan.

The calculation of θ angle from rocking curve measurement leads to the calculation of c-parameter using Bragg's law. So the indium composition x is can be calculated using Vegard's law with respect of a linear interpolation of lattice parameter. For InGaN, the indium composition is calculated using the following formula:

$$c_{In_xGa_{1-x}N} = x_{indium} \times c_{InN} + (1 - x_{indium}) \times c_{GaN} \qquad \textit{Equation 2.38}$$

$$x_{indium} = \frac{c_{In_xGa_{1-x}N} - c_{GaN}}{c_{InN} - c_{GaN}} \qquad \textit{Equation 2.39}$$

Knowing the c-parameter for InGaN calculated by XRD technique (as c=2.d for (0002) planes) and the values of reported c-parameter of InN and GaN in chapter 1 [24], consequently we can calculate the indium composition.

We can also consider the calculation of θ angle of studied structure as an important parameter which offers of the estimation of the dislocation density (D_{dis}) of GaN films. The calculation of dislocation density is possible using the following equation:

$$D_{dis} = D_{screw} + D_{edge} \qquad \textit{Equation 2.40}$$

Where, D_{screw} is the screw dislocation density, D_{edge} is the edge dislocation density. D_{screw} density is achieved using (002) plane in symmetric scan. D_{edge} density could be extracted using a skew symmetric scan in the (121) plane. D_{screw} and D_{edge} density are calculated as following:

$$D_{screw} = \frac{\beta^2_{(002)}}{9\, b_{screw}^{\,2}} \qquad \textit{Equation 2.41}$$

$$D_{edge} = \frac{\beta^2_{(121)}}{9\, b_{edge}^{\,2}} \qquad \textit{Equation 2.42}$$

Where, (β) is the FWHM (in radian) measured by XRD rocking curves, and (b) is the Burgers vector length (b_{screw} = 0.5185 nm, b_{edge} =0.3189 nm) [25].

The measurement of XRD has been done using two systems; the first is D8 Discover - Bruker instrument in the laboratory of imaging-characterization in KAUST with the assistance of PhD student Bilal Janjua. The GaN/InGaN measurement has been recorded using Cu Kα radiation in Omega and Omega-2Theta scanning modes. The second system used in this project is the DRX (D8 PASSEUR) in the Unite for Catalysis and Solid State Chemistry in Lille1, the measurement has been performed by the research director Pascal Roussel.

II.3.1.2.   *Scanning Electron Microscopy (SEM)*

SEM is a microstructural technique used to analyze surface topography and to enable view of cross section of a sample. It allows extracting data such as surface texture, profile, thickness etc... It consists of generation of focused beam of high-energy electrons interacting with atoms; the derived signals provide information about surface morphology and chemical composition. This tool has been developed over optical microscopy because of the limitation of light wavelength while electrons have shorter wavelength enabling improved resolution.

In our study, the Supra 55 with field effect gun in the IEMN has been used to characterize our samples. It ensures resolutions of 1.7 nm at 1 kV and magnification varying from 20X to 900 000X.

II.3.1.3.   *Transmission Electron Microscopy (TEM)*

TEM is an enhanced microscopy system reaching a very high resolution comparing to the conventional optical or scanning electron microscopy. It enables observing a crystal at the atomic scale and provides analysis of defects and interfaces in epitaxial layers. However, this technique requires a careful preparation of the sample using Focus Ion Beam (FIB) technique. An electron source delivers a beam which is focused on the sample by means of lenses. When electrons beam arrive on the atoms, scattered and diffracted electrons are collected to generate bright field (BF) and dark field (DF) imaging using a ring-shaped detector. BF and DF are used in order to obtain defects and thickness analysis besides atomic number.

Energy Dispersive X-Ray Analysis (EDX) is an attachment technique to TEM instrument permitting the identification of the elemental composition of materials at a nanometer scale. Elemental mapping of the micro-analyzed zone of the sample is generated using EDX detectors.

In our study, EDX has been used to quantify the indium/gallium composition in the InGaN/GaN layers.

Gilles Patriarche from Laboratoire de Photonique et de Nanostructures (LPN) has kindly investigated all TEM analysis for numerous samples. He has used Jeol 2200FS TEM system, equipped with an ultra-high resolution objective lens.

II.3.1.4.   *Atomic Force Microscopy (AFM)*

AFM is a powerful technique used to scan the surface of a sample using a mechanical probe of about ten nanometers in diameter. Scanning surface is could be performed by tapping or touching the surface. At high resolution, the response of the probe toward the surface force of sample enables the extraction of three-dimensional image. The principle is based on the interactions of Van der Walls between the probe and the atoms of the sample surface allowing the measurement of the sample topography.

In our study, AFM measurement has been performed in order to obtain the surface morphology and to evaluate the density of dislocations of samples. Analysis of ($1 \times 1\mu$m2), ($5 \times 5\mu$m2) and ($10 \times 10\mu$m2) areas in non-contact mode, have been investigated for each sample in order to extract the root mean square (RMS) roughness. Several systems have been used in our study, Dimension 3100 instrument in IEMN, Agilent 5500 SPM in KAUST and VEECO Nano-Scope IV in CRHEA.

II.3.2. Optical characterization techniques

II.3.2.1.   *Photoluminescence spectroscopy*

Photoluminescence (PL) is a generation of light emission (typically laser source) when exposed to optical photoexcitation due to photon absorption. In the case of the semiconductor, the principle operation is to excite electrons from the valence band with a photon having energy greater than the material band gap so they reach the conduction band. Electron-hole pairs are created in the material as a result of photon absorption. Electrons get higher energy state before they come back to a lower energy level with emission of a photon. PL measurement is involved in the emitted photon as well as its energy is related to the material band gap. The shape and

intensity of PL peaks enable the evaluation of the material quality regarding defects, impurities and dopants.

The first measurement has been performed in KAUST (Photonics Lab) using the Mounted Free Space Photoluminescence (Figure 2.5). It has been used with the assistance of Bilal Janjua. The technique consists of laser source of excitation (266 nm), focus lenses, collimation lenses, and silicon detector mounted in the Adnor Monochromator.

The second measurement has been accomplished in KAUST by means of micro-photoluminescence (μPL) spectroscopy system (Jobin Yvon's LabRAM ARAMIS). The optical excitation has been delivered using Helium-Cadmium (HeCd) laser which emits at 325 nm with spot size < 10 μm.
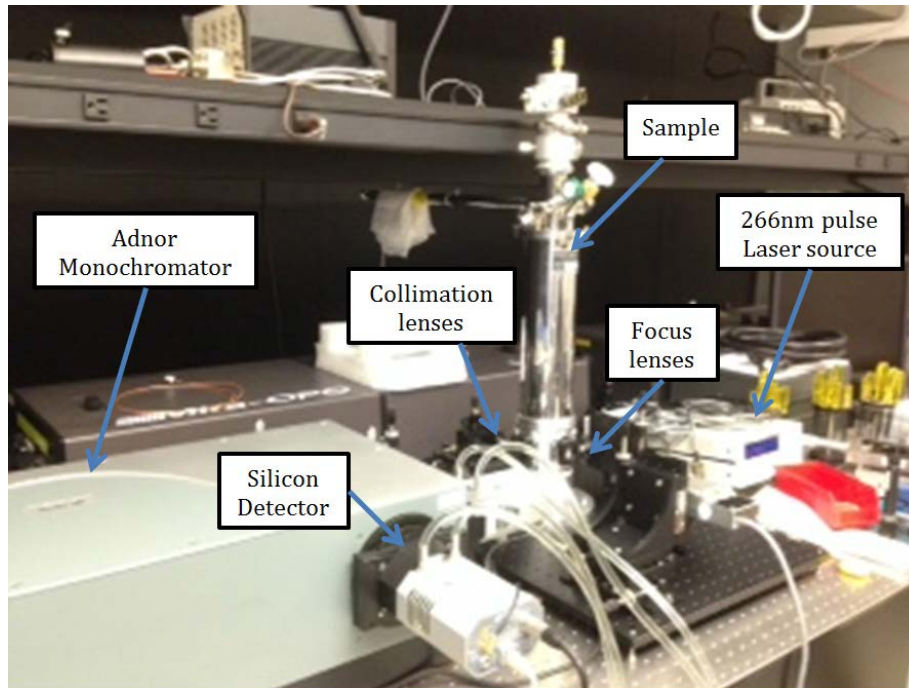
Figure 2.24: Mounted Free Space Photoluminescence.

II.3.2.2. *Spectrophotometer*

The spectrophotometer measurement is a significant technique related to the transmission, reflection and absorption. It provides optical information such as transmittance, absorbance and energy gap of the material without any contact on the sample. When optical beam of light is

guided toward a material, some of the beam is reflected, the other part of beam passes through the material where some of it will be absorbed (Figure 2.6).
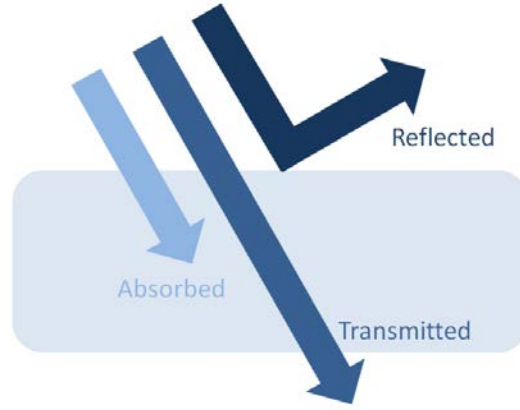
Figure 2.25: Optical path of a light beam through a material.

In spectrophotometer, the absorbance (A) is usually the measured parameter in output. It presents the ability of a medium to absorb the light which passes through it. According to Beer-Lambert's law, the absorbance is the decimal logarithm of the ratio between the intensity of energy at a given wavelength, before passing through the medium (I_0), and the intensity of transmitted energy (I) [26]. The formula is expressed as the following:

$$A = log_{10} \frac{I_0}{I} \qquad\qquad \text{Equation 2.43}$$

The relationship between the absorption coefficient (α) and the intensity of energy before and after passing the medium having width (L) is given by:

$$I = I_0 \, e^{-\alpha L} \qquad\qquad \text{Equation 2.44}$$

The absorption coefficient related to the absorbance could be calculated as:

$$\alpha = \frac{A \, ln \, 10}{L} \approx 2.3 \, \frac{A}{L} \qquad\qquad \text{Equation 2.45}$$

In our study, the Cary 5000 UV-Vis-NIR spectrophotometer has been employed for the absorption measurement. It is working at high performance in the range of 175-3300 nm using a

PbSmart detector. Integrated spheres have been installed during our measurement in order to detect the spectral and diffused reflectance caused by the non-polished backside of the sapphire substrate. The measurement has been performed with assistance of Professor Bruno CAPOEN from Centre of Laser Research and Applications (CERLA) in Lille. The transmission measurements have been performed in KAUST using SHIMADZU-UV-3600 Plus UV-VIS-NIR Spectrophotometer with the help of Bilal Janjua in Photonics Lab.

II.3.2.3.   *Prism coupling*

It will be necessary to evaluate the porous GaN samples in our study in terms of optical properties comparing to bulk GaN. For this, the prism coupling could be the primary tool which is available in our Laboratory. The measurement of refractive index is an important factor of any optical devices. It is describing the path of light through a material which provides its physical property and purity. The value of refractive index is changing regarding the wavelength and called 'dispersion'. III-nitride structures have been optically characterized by prism coupling. This technique permits to measure refractive index, thickness and optical losses [27][28]. In our study, we use the Metricon system in IEMN for measuring the refractive index. This system has the advantage of being a flexible and adaptable for any type of material. As shown in Figure 2.7 (right), Metricon system consists of laser sources of different wavelengths (from 450 to 1539 nm), focusing optics, rutile prism (TiO2), piston (holding sample toward the prism) and detector. They are mounted on a rotatable platen controlled by an external interface connected to a computer.
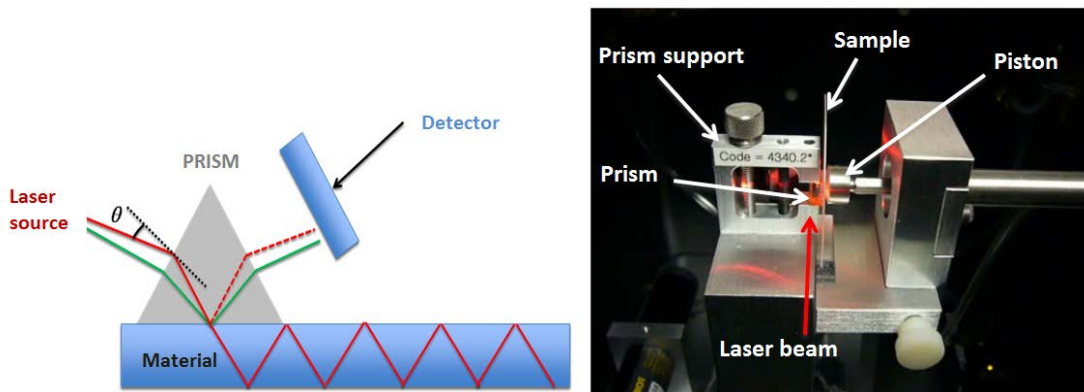
Figure 2.26: Prism coupling technique (left) and Metricon system configuration (right).

To measure the effective refractive index, we plot the guided modes spectrum at different wavelengths and for TE or TM light polarizations (ordinary and extraordinary modes). At a specific angle θ, coupling is occurred and optical wave is propagating in the material waveguide. It involves an attenuation of optical wave aside detector corresponding effective-mode indices Nm (Figure 2.7, left). The following formula allows the calculation of Nm:

$$N_m = n_p . \sin\left(A_p + arcsin\left(\sin\left(\frac{\theta}{n_p} \right) \right) \right)$$ *Equation 2.46*

According to the values of the angle θ, Nm is calculated using apex of the prism (A_p) and refractive index of the prism (n_p).

II.3.2.4.   *Ellipsometry*

As a second tool for the calculation of optical properties, the ellipsometry is an additional instrument which will confirm the refractive index values extracted by prism coupling for the porous GaN samples. As illustrated in Figure 2.8 (left), ellipsometry technique is based on the change of light polarization by reflection of light on the sample, and then detected through an analyzer. This change of polarization is quantified by the amplitude ratio (Ψ) and the phase difference (Δ).

As the measured material is typically containing roughness and oxide layer, the calculation of material parameter has to be adapted to the pseudo optical constants from the ellipsometry measurement. Using Fresnel's equations, the experimental data extracted from ellipsometry measurement (Ψ_{exp}, Δ_{exp}) are compared to a numerical model describing the theoretical values of (Ψ_{th}, Δ_{th}) [29]. Eventually, this comparison permits to obtain the closest value using regression algorithm. The flowchart of data analysis is described in the Figure 2.8 (right).
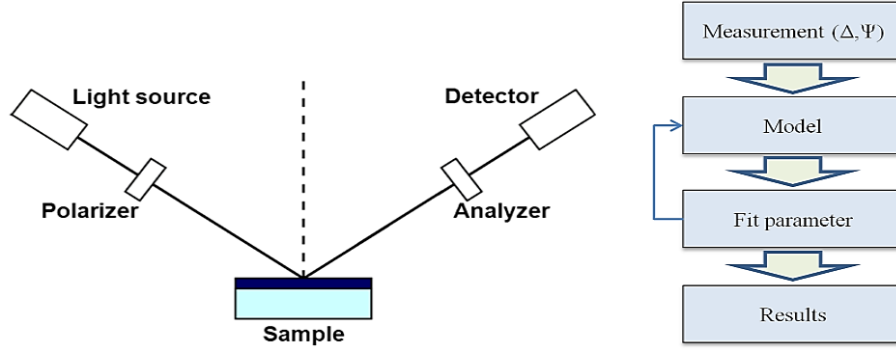
Figure 2.27: Diagram of the ellipsometry technique (left) and the flowchart of data analysis (right).

Extraction of (Δ, Ψ) values has been performed in the IEMN using HORIBA JOBIN YVON UVISEL spectroscopic ellipsometer. The measurement has been in the range of 4.55-0.75 eV (270 to ~ 1650 nm) at 60° of incident angle. The used model during the extraction of optical parameters has been developed by Eric Dumont from University of Mons in Belgium.

II.4. PIN structure with 10 % of SL and MQW InGaN

In this section, we will analyze the structural and optical characterizations of the PIN InGaN/GaN samples with 10% of indium content. The objective of the study is to investigate the microstructure in terms of crystalline quality, density of dislocation and surface morphology. Optical properties are evaluated for these samples using PL and absorption in order to obtain the cut-of wavelength of each sample. We will also report a comparative investigation of SL InGaN and MQW InGaN configurations in structural and optical analysis.

As we request the growth of PIN structure by MBE, the samples SL10-3 and MQ10-3 will be analyzed and compared to MOCVD samples (SL10-1 and MQ10-1).

II.4.1. Structural characterization

II.4.1.1. Samples grown by MOCVD

For the sample SL10-1, the high intensity peak observed clearly at 34.6° corresponds to the thick GaN buffer layer beneath the PIN structure, which indicate that the GaN is highly

oriented along the c-axis and has a single crystalline character (Figure 2.9). The observed XRD data is well matched with the ASTM data (formerly American Soc. for Testing and Materials) for hexagonal GaN. The sharp and narrow with high intensity peak indicates the fine crystallization of the material. For the InGaN peak, it is observed lower than GaN at 34.2°. It has less sharp peak and slightly lower intensity than GaN due to the indium insertion. The quality of materiel of the whole compound with the small amount of indium (10%) is considered satisfactory. The Full Width at Half Maximum (FWHM) for GaN is measured 270 arcseconds, for InGaN is about 600 arcseconds. The approximation of Indium content is obtained by comparison of measured curve with a simulated structure using LEPTOS software. The type of XRD measurement for this comparison is a rocking curve omega measurement and the average indium percentage is about 11 %. The estimation of indium composition is also possible using Vegard's law (Equation 2.3). First of all, we have to calculate the c lattice parameter for InGaN using Bragg's law (Equation 2.1), with c equivalent to 2d. It is calculated in consideration to the angle θ for InGaN rocking curve measurement and λ known to be 0.15406 nm. The value of c parameter for InGaN layer is 0.5253 nm. We will consider that the values of c parameter for GaN and InN are 0.5185 nm and 0.5705 nm respectively. We conclude that the c parameter of InGaN correspond the composition of 13 % of indium which is an acceptable value due to the inhomogeneity of indium distribution in the InGaN layer.

The calculation of dislocation density could be extracted using the Equation 2.4. The screw dislocation density and the edge dislocation density are related to the FWHM (in radian) measured by XRD rocking curves with b_{screw} = 0.5185 nm and b_{edge} =0.3189 nm [25]. In our study, we will estimate only the screw density for SL10-1 sample because the measurement of XRD and the FWHM values were performed at (002) plane in symmetric scan. For the edge dislocation density, the FWHM data should be extracted using a skew symmetric scan in the (121) plane, which was not carried out. The estimation of the screw dislocation density for the sample SL10-1 is about $D_{screw} = 7.6 \times 10^7$ cm^{-2}.
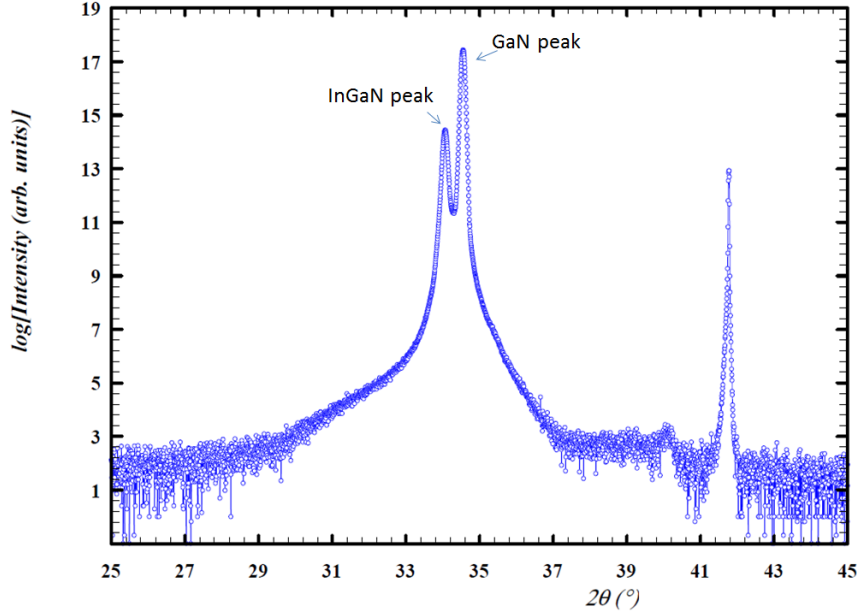
Figure 2.28: XRD 2Theta scan measurement for SL10-1 sample grown by MOCVD.

For the sample MQ10-1, the high intensity peak observed clearly at 72.7° corresponds to the thick GaN buffer layer beneath the PIN structure, which indicates that the GaN is highly oriented along the c-axis with sharp and narrow peak (Figure 2.10). For the InGaN/GaN MQW, it exhibits satellite peaks, the position and the intensity of peak is changing due the unexpected interfaces change of wells in the InGaN/GaN period. The series of peaks (satellite peaks) numbered from -4 to +4 could provide information about indium composition, period numbers and well thickness. The position of main MQW peak (position '0') enables the calculation of the average indium content in the InGaN/GaN period and not the indium content in the InGaN layer. We will consider that MQW layers are assumed to be relaxed in order to determine the indium composition. The approximation of Indium content is obtained by comparison of measured curve with a simulated structure using LEPTOS software. The type of XRD measurement for this comparison is a rocking curve omega measurement and the average indium percentage is about 12 %. The Full width at half maximum (FWHM) for InGaN is about 405 arcseconds due to the period interface roughness and may also be related to the alloy fluctuation. It presents a lower FWHM than SL10-1 sample which leads us to consider the high quality of MQW comparing to SL configuration.
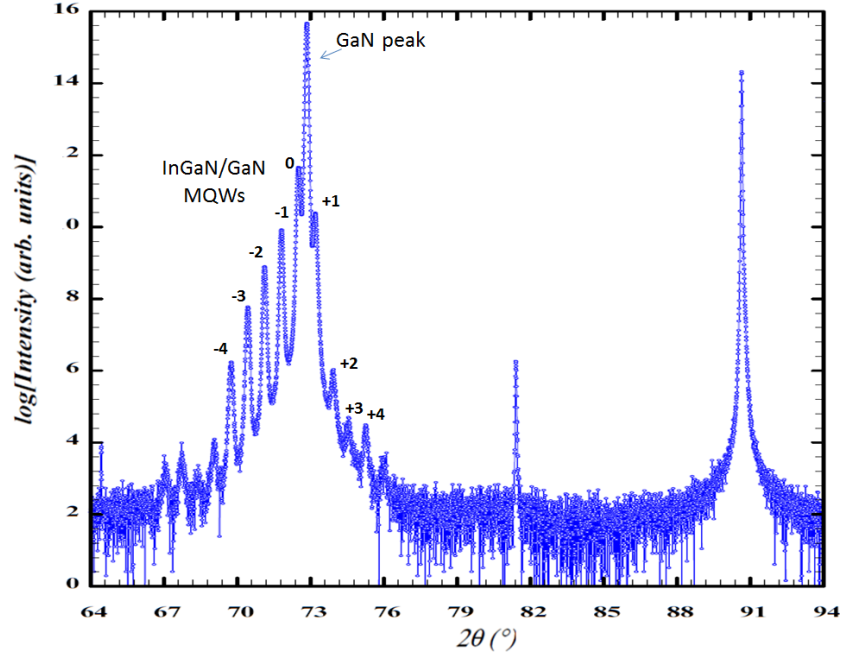
Figure 2.29: XRD 2Theta scan measurement for MQ10-1 sample grown by MOCVD.

The estimation of the screw dislocation density for the sample MQ10-1 is about $D_{screw} = 7 \times 10^7$ cm^{-2} which is slightly lower than SL10-1 sample due to the improved quality of MQW configuration.

The TEM characterization of the sample SL10-1 permits to evaluate the material quality in terms of threading dislocation using cross-section images in different axis. It also allows to verify the thickness of the structure. In order to identify the threading dislocation as edge or screw type, it is important to have TEM preparation samples using FIB technique with two different axis.

The preparation of two FIB foils (the one at 90° of the other) allows to have the [1120] and the [1100] zone axis. Layers epitaxially grown on sapphire are often subject to a rotation of 30° between the substrate and the InGaN/GaN epitaxial layer. That is why, it is advisable to work with [1120] zone axis for GaN in order to see the stacking faults. The [1100] zone axis permits to see the dislocations, and we can also perform the chemical analysis by EDX, but not to distinguish stacking faults.

In our study, samples have been prepared by tilting along the [1100] and [1120] axis on thin foils by FIB in IEMN with the help of David Troadec. Gilles Patriarche from LPN has

characterized sample foils using Jeol 2200FS TEM system. In the right image of Figure 11, the edge dislocations illustrated by bleu arrows refers to the absence, replacement or extra of atoms in a side of crystal unit leading to errors in localized area and not in any direction away from this error [30].
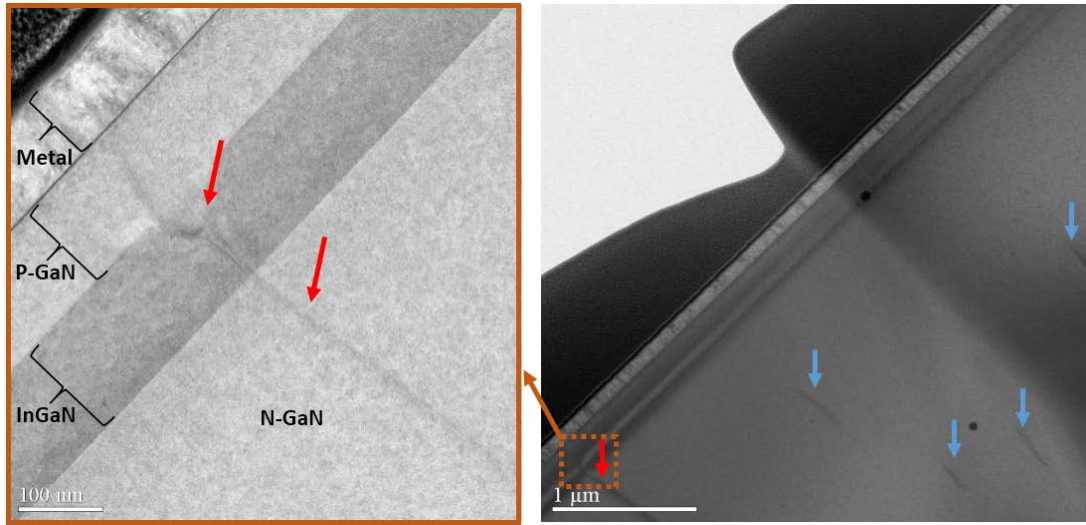
Figure 2.30: TEM cross section image along [1120] in dark field (left) zoomed from image in right side for sample SL10-1 grown by MOCVD.

The left image in Figure 2.11 is a zoomed zone from the right image, and presents the screw dislocation in red arrows. It presents distortion on one direction of an error migrating up through the structure in a spiral form beyond the unit structure [31]. Besides, Errors could be generated at the interface of GaN/InGaN or GaN/sapphire due to the large lattice mismatch and propagate until forming V-pit form in the surface [32]. TEM images of sample SL10-1demonstrate a measured thickness of 130 nm of InGaN, higher than the expected thickness which was 100 nm in accordance with sample provider. A metal layer (Titanium) has been used in the FIB preparation and deposited on P-GaN. The thickness of P layer is calculated about 105 nm comparing to the estimated thickness of 100 nm. Using EDX technique attached to the TEM instrument, the percentage of indium composition in the InGaN layer is estimated to be 9-10 % as shown in the Figure 2.12. The overall investigation of the TEM images for sample SL10-1 demonstrates that material quality of the sample allows to be exploitable due to the insertion of low percentage of indium content (10% in this case). The general view of P-GaN layer demonstrates very smooth surface with low deformation density. The surface morphology of P-GaN layer will be studied thereafter using AFM.
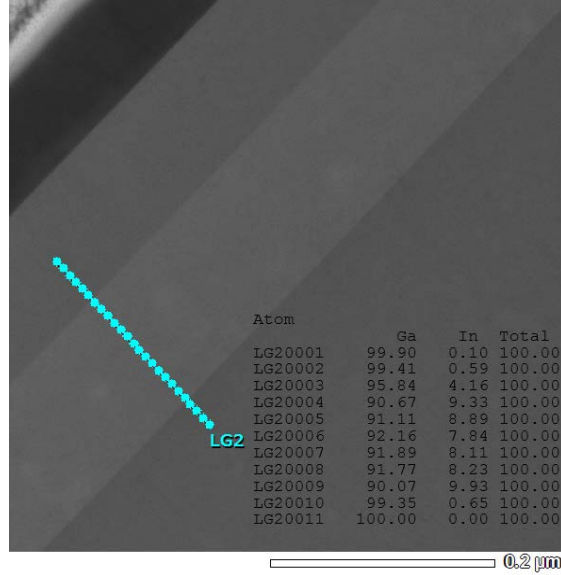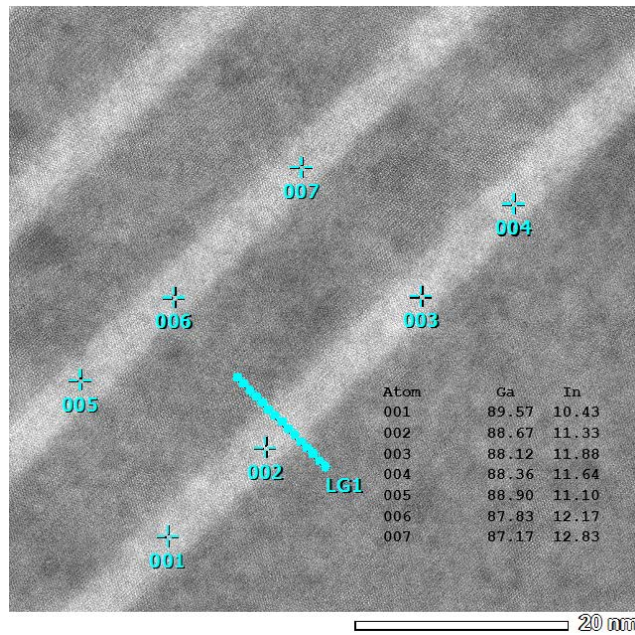
Figure 2.31: EDX for Ga and In composition via TEM cross section image along [1112] zone axis for sample SL10-1 grown by MOCVD.

In the same way, TEM characterization of the sample MQ10-1 has been performed in the same conditions as sample SL10-1.   The evaluation of the material quality of MQW configuration enables to carry out a comparative study with SL configuration in terms of structure. The Figure 2.13 (left) reveals dislocation crossing the QW toward the top surface originated from defect during GaN growth, it will form a v-pit to the top layer (P-type layer), illustrated in red arrow.

We can see that the number of QW confirms the estimated design to be 10 periods as shown in the Figure 2.13 (right). During TEM analysis, it has been observed that the thickness of InGaN well increase from the bottom toward the top of the structure: going from 3.3 nm to 3.8 nm (+/- 0.1nm) while the expected thickness has been 2.5 nm. The thickness of GaN barrier in the InGaN/GaN period has measures about 12 to 13 nm which it is very close to the designed structure with thickness of 12 nm. Yellow arrow in the Figure 2.13 (right), presents a localized deformation of InGaN well and could be related to indium-rich zone during growth which disturb the regularity of QW formation [33]. The surface morphology demonstrates an improved quality comparing to the sample SL10-1 due the significant reduction of threading dislocation.
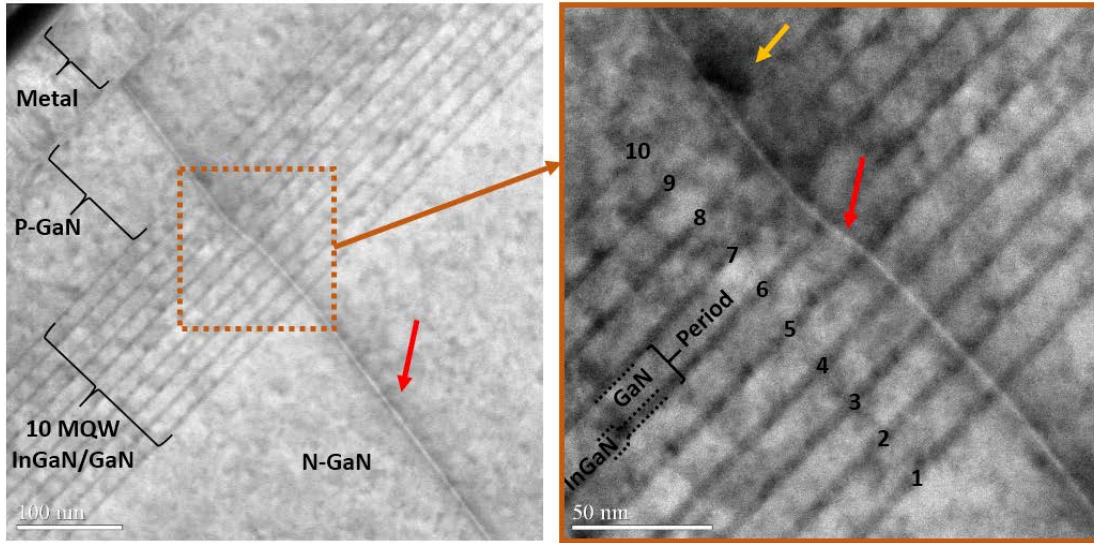
Figure 2.32: TEM cross section image along [1100] in bright field (left) and zoomed zone in right side for sample MQ10-1 grown by MOCVD.

Using EDX analysis, the percentage of indium composition in the InGaN well is varying from 10-12 % as illustrated in Figure 2.14, which is suitable regarding to our recommendation.

Atom	Ga	In
001	89.57	10.43
002	88.67	11.33
003	88.12	11.88
004	88.36	11.64
005	88.90	11.10
006	87.83	12.17
007	87.17	12.83

Figure 2.33: EDX for Ga and In composition via TEM cross section image along [1100] zone axis for sample MQ10-1 grown by MOCVD.

II.4.1.2.   *Samples grown by MBE*

MBE samples with the same indium percentage (10%) have been characterized using TEM technique in order to compare the material quality to the MOCVD samples. In the Figure 2.15, general view of the MBE sample (SL10-3) in cross section demonstrates the high density of dislocation. The threading dislocation seems to be originated from the interface of GaN buffer layer and the template substrate due to a large lattice mismatch. The template substrate is composed of thin GaN on AlN layer grown on sapphire. The threading dislocations extend vertically toward the top layer but low number of dislocations propagate into the surface due to the growth new layer (SL InGaN). This layer will suppress some defects as illustrated by the white arrow in Figure 2.15 (b). However, the growth of SL InGaN may create new defects which propagate to the top surface (P-GaN layer) and creating v-shaped pit as presented by red arrows (Figure 2.15, c). As the indium content is low to be 10% of the epitaxial InGaN, the density of created defect remains tolerable. The MQW sample grown by MBE hasn't been characterized by TEM due to technical issue during FIB preparation. A complementary analysis between the MOCVD and MBE samples will be discussed in the AFM analysis.
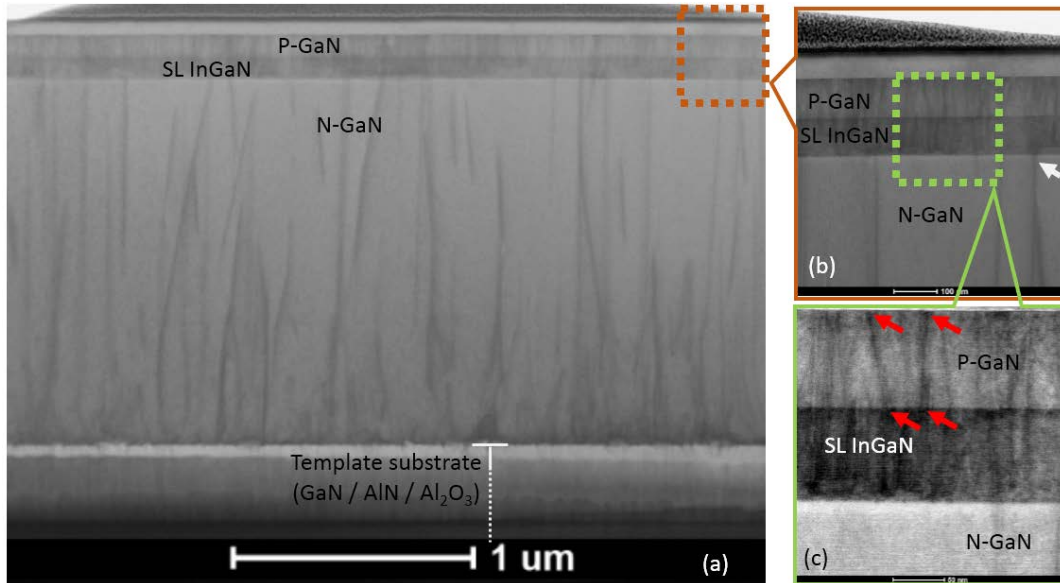
Figure 2.34: (a) TEM cross section image of general view along [1120] for sample SL10-3 grown by MBE, (b) and (c) figures are zoomed zones.

AFM analysis for MOCVD samples (SL10-1 and MQ10-1) have been performed in order to investigate the surface morphology and confirm results issued by XRD and TEM previously.

Figure 2.16 (a) shows 5×5 µm^2 surface analysis for the sample SL10-1 grown by MOCVD. A homogenous surface with roughness root mean square (RMS) of 0.58 nm has been found. However, a lots of small pits on the structure are founds as black dots. It presents the threading dislocation demonstrated previously in the TEM cross section and propagating up to the surface. It is the result of chemical inhomogeneity during growth as well as the strain between substrate and GaN buffer layer due to the lattice mismatch. Figure 2.16 (b) presents the profile of the surface morphology for the same sample. It demonstrates that some wave-shaped are presents in the surface but still acceptable for a low percentage of indium (10%) in the InGaN. The density of threading dislocation for the sample SL10-1 is estimated to be 5×10^8 cm^{-2}.
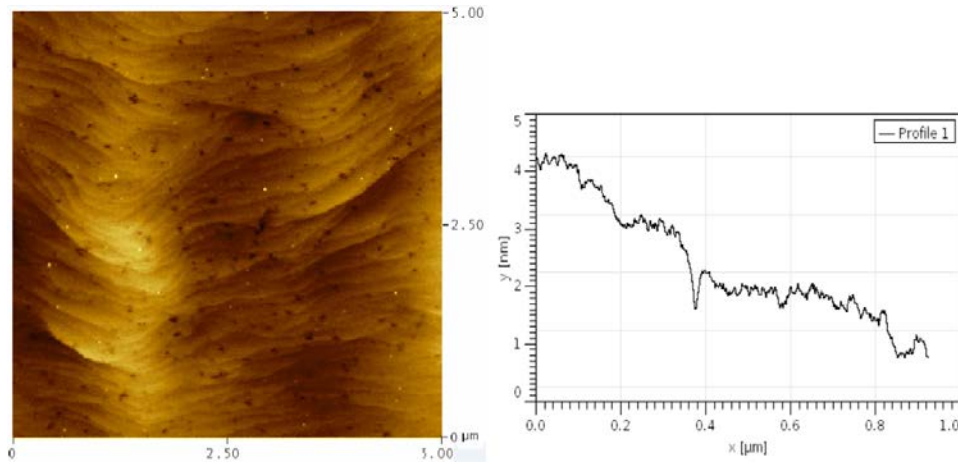
Figure 2.35: AFM analysis of 5×5 µm^2 (a), and profile (b) for sample SL10-1 grown by MOCVD.

Figure 2.17 (a) demonstrates lower threading dislocation for 2×2 µm^2 of sample MQ10-1 comparing to the sample SL10-1. Superior smoothness has been identified and significantly reduced defects (pits) due to the optimization of MQW configuration. The calculated roughness in RMS is about 0.42 nm slightly lower than RMS reported for sample SL10-1. The surface profile in Figure 2.17 (b) demonstrates a homogenous morphology with reduced wave-shaped. The density of threading dislocation for the sample MQ10-1 is estimated to be 1×10^8 cm^{-2} which is lower than the dislocation density for the SL configuration. This analysis confirm the previous investigation issued by XRD and TEM and conclude that MQW configuration in low indium percentage (10%) is an optimal structure due to the reduction of density of defects.
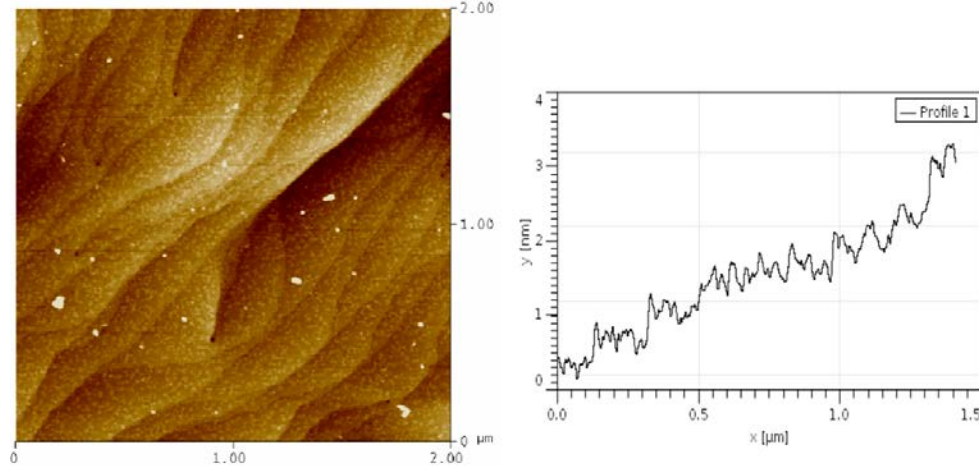
Figure 2.36: AFM analysis of 2×2 µm^2 (a), and profile (b) for sample MQ10-1 grown by MOCVD.

The analysis of MBE samples (SL10-3 and MQ10-3) have been performed by AFM technique in order to carry on the comparative study achieved by TEM. As we supposed, this comparison will help us to consider a configuration with optimized growth technique for the rest of the study allowing to add more indium content in the InGaN layer. Figure 2.18 (a) shows the 5×5 µm^2 for the sample SL10-3. The process used for MBE growth has reformed the surface texture when comparing to the sample SL10-1. Defects related to inferior layers are presented on forms of grains conducting inhomogeneity on the surface as shown in Figure 2.18 (b). These defects have been anticipated as we analyzed it earlier in the Figure 2.15 (a) by TEM technique. When taking in consideration the low percentage of indium in the InGaN layer, the calculated roughness in RMS of about 6.6 nm is considered higher than supposed to be.

For the sample MQ10-4 grown also by MBE, it exhibits another type of surface texture comparing to the sample SL10-3. Several stages are observed in different levels and no more grains-shaped presents here as presented in the Figure 2.18 (c). V-defects are concealed and covered by the superposing levels. However the roughness in RMS is about 2.3 nm which is considered not very accurate due to surface texture as shown in the Figure 2.18 (d). The densities of threading dislocation for the sample SL10-3 and MQ10-4 are estimated to be 1×10^9 and 8×10^8 cm^{-2} which indicate lower material quality comparing to the MOCVD samples.
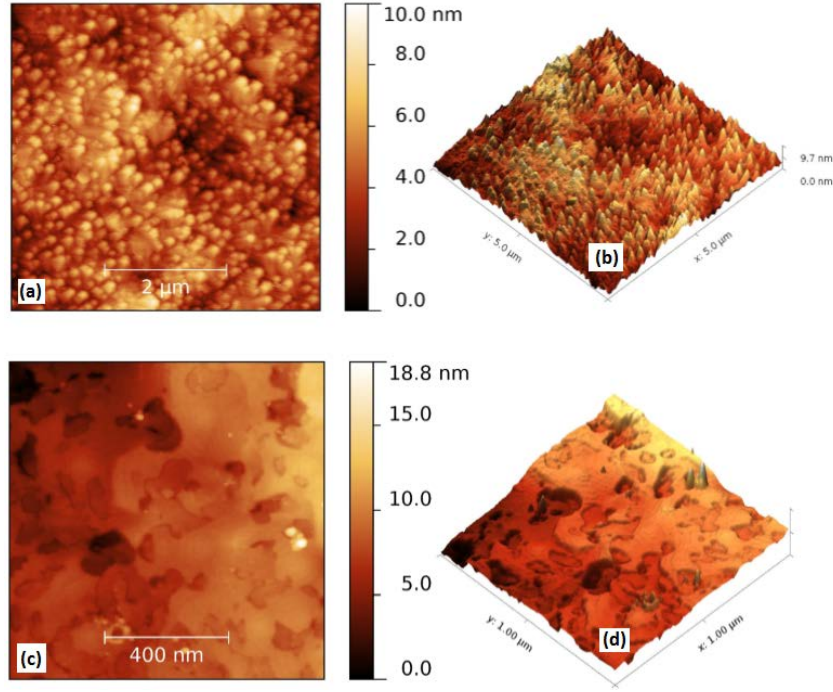
Figure 2.37: AFM analysis of 5×5 µm^2 for sample SL10-3 (a), related profile (b), AFM analysis of 1×1 µm^2 for sample MQ10-3 (c) and related profile (d).

This AFM analysis conducts to make link to the growth process used to obtain this sample. It can be clearly noticed that samples grown by MBE technique (SL10-3 and MQ10-4) reveal an obvious difference in terms of surface morphology comparing the MOCVD samples (SL10-1 and MQ10-1). This clarifies that poor crystalline quality of the MBE epilayer is the principal reason of defects in surface roughness. Overall evaluation of the structural results performed here clearly indicates that MOCVD samples have better crystal quality as compared to MBE samples. Remarkable crystal quality and improved surface morphology in MOCVD samples have been identified. Reducing defects (pits) during material growth is a major concern. These defects have electronic states near the valance band and are the main raison of the leakage paths in GaN-based diodes which reduce the device performance.

II.4.2.   Optical characterization for samples grown by MOCVD and MBE

In this section we will evaluate the optical properties for the GaN/InGaN structure with 10% of indium content grown by MOCVD and MBE. PL and absorption measurement will be discussed for samples SL10-1, MQ10-1, SL10-3 and MQ10-3. A comparative study for the

different configuration will be performed in order to evaluate the optical properties and to validate the reported results in structural characterization.

II.4.2.1.   *Photoluminescence*

Using the Mounted Free Space Photoluminescence illustrated previously in Figure 5, samples will be excited at room temperature, guided by focus and collimation lenses and then detected by silicon detector. Figure 2.19 illustrates the PL measurement for samples SL10-1 and MQ10-1. The sharp single PL peak corresponding to near-band edge transition in the epitaxially MQW InGaN phase appears at 425 nm (2.91 eV) with a narrow FWHM of 12 nm for sample MQ10-1. The sample SL10-1 reveals less sharpness with single PL peak corresponding to near-band edge transition in the SL InGaN and appears at 404 nm (3.06 eV) with larger FWHM of 27 nm. This large peak of SL configuration is related to the higher defect density comparing to the MQ configuration. Even the intensity of the PL peak for sample SL10-1 is lower than the sample MQ10-1 which provide information about the quality of the absorbent layer. PL peak of SL InGaN configuration fits with reported values in the literature while PL peak of MQW InGaN is slightly delayed [34][35]. This shift reveals the existence of indium inhomogeneity in the active region and mainly related to the composition fluctuations in as-grown InGaN alloys [36].
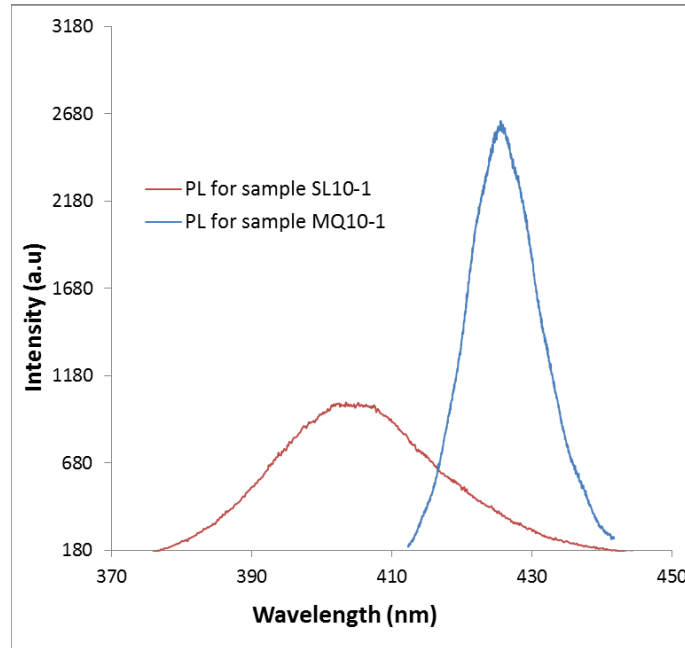
Figure 2.38: PL analysis for sample SL10-1 and MQ10-1 using Mounted Free Space PL spectroscopy.

In order to obtain a comparative analysis between MOCVD and MBE techniques, samples have been investigated using µPL spectroscopy system (Jobin Yvon's LabRAM ARAMIS). Samples have been excited using Helium-Cadmium (HeCd) laser emitting at 325 nm. For MOCVD samples (SL10-1 and MQ10-1) shown in left side of Figure 2.20, a sharp single PL peak corresponding to near-band edge transition in the epitaxially MQW InGaN phase appears at 434 nm (2.85 eV) and less sharpness peak at 401 nm (3.09eV) for the SL InGaN. InGaN peak is large and delayed for the MBE sample (MQ10-3) in the right side of Figure 2.20 at the near-band edge of 457 nm (2.71 eV) comparing to the MOCVD sample (MQ10-1). The single InGaN in the sample SL10-3 is also delayed comparing to the MOCVD sample (SL10-1) with single PL peak corresponding to near-band edge transition at 436 nm (2.84 eV). GaN peaks are almost similar in the whole samples and the high intensity peaks are detected at 360-363 nm. Comparing two samples in MQW configuration grown in different technique, FWHM for the MQ10-1 peak is lower than the MQ10-3 peak corresponding to 14 nm versus to 26 nm respectively. µPL spectroscopy confirms also that the quality of materials in terms of optical characterization is significant for the MOCVD samples. As explained previously, Shift of peaks are observed and related to the indium inhomogeneity in the active region of InGaN alloys [36].
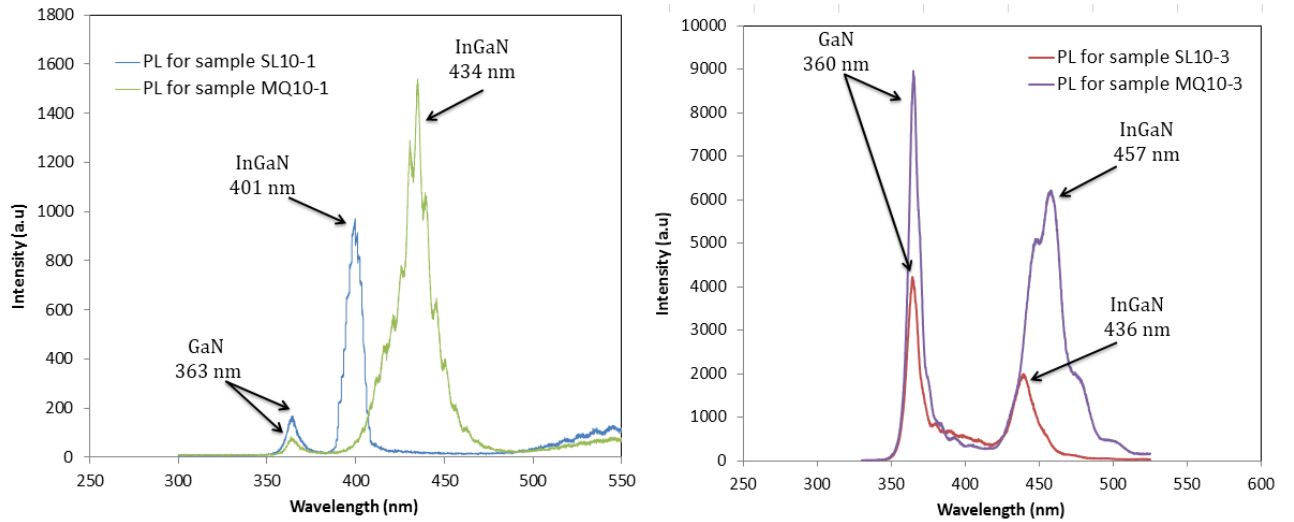
Figure 2.39: Room-temperature PL spectra of MOCVD samples SL10-1 and MQ10-1 (left) and MBE samples SL10-3 and MQ10-3 (right).

II.4.2.2. *Spectrophotometer measurement*

Absorption and transmission measurements have been carried out at room temperature in order to evaluate the optical properties of different samples. For the sample SL10-1, absorption spectrum is illustrated in Figure 2.21 (left) using Cary 5000 UV-Vis-NIR spectrophotometer. Transmission spectrum in right side of Figure 2.21 has been also performed using SHIMADZU-UV-3600 Plus UV-VIS-NIR Spectrophotometer. A first measurement of baseline has been carried out for sapphire substrate in order to have a reference. For GaN in both measurements absorption and transmission, a sharp absorption cut-off is observed at 363 nm (3.41 eV) which corresponds the GaN bandgap GaN [37][38]. It fits also to the PL measurement and confirm the GaN crystal quality. For the InGaN layer, the absorption is located in the zone 399-406 nm represented by the variation of the absorption slope in both transmission and absorption spectra. It is due to introduction of indium in the InGaN absorbent layer. It is almost the InGaN cut-off value observed in the PL spectrum. The observed modulation in the transmission spectrum (higher than 410 nm) is due to the interference within GaN and sapphire substrate. The intermediate zone between GaN and InGaN regions represented by a different form of slope is considered as the transition phase between two different materials.
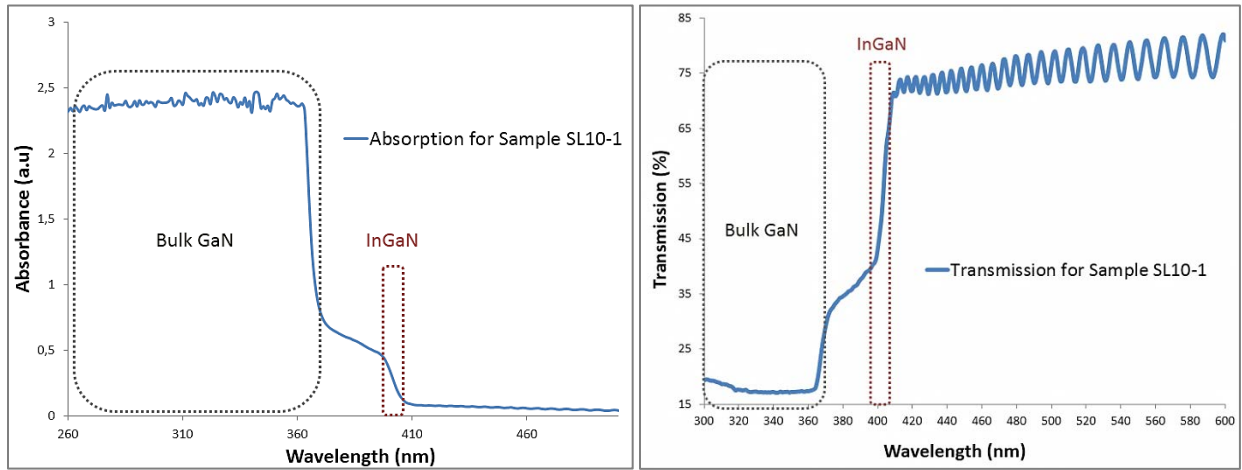
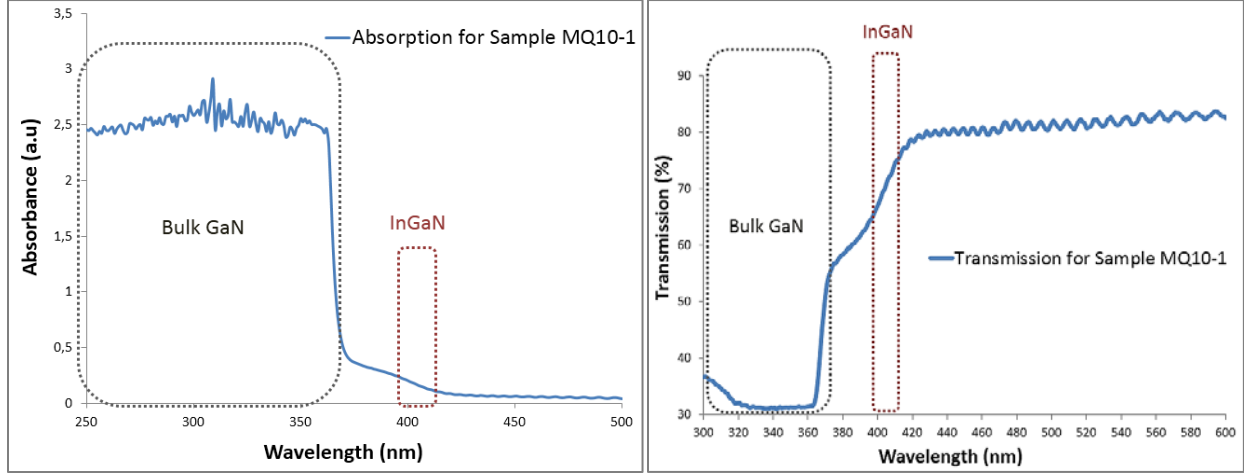*Figure 2.40: Absorption spectrum (left) and Transmission spectrum (right) for the sample SL10-1 at room temperature.*

The absorption coefficient of the absorbent layer InGaN could be calculated using the Absorbance spectrum for InGaN at room temperature. The absorption coefficient given by the Equation 2.9 is situated in the range of $1.6 \times 10^5 - 8.7 \times 10^4$ cm^{-1} for the InGaN absorption zone

399-406 nm. The Figure 2.22 illustrates the calculated absorption coefficient using the absorbance spectrum. This value of absorption coefficient is almost similar to the reported values [35][39].
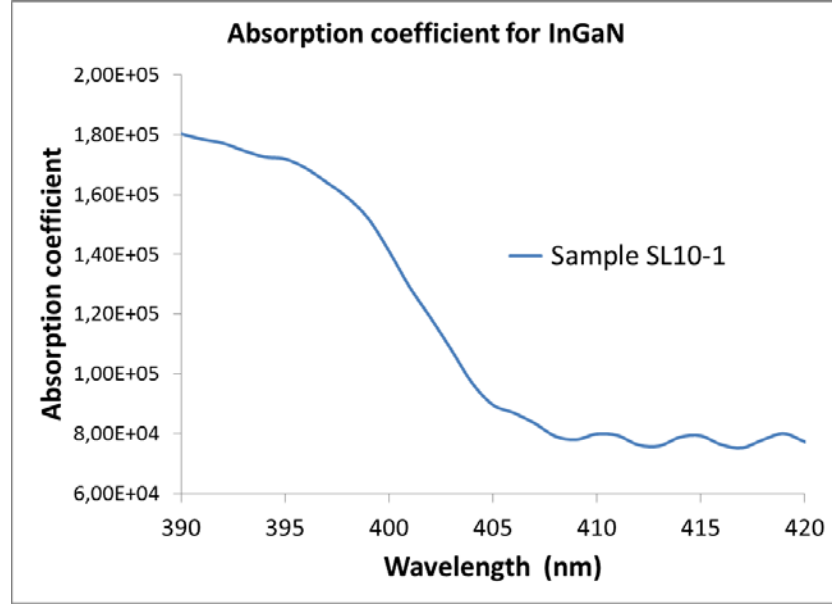
Figure 2.41: Calculated absorption coefficient for InGaN layer using absorbance spectrum for the sample SL10-1.

For the sample MQ10-1, the MQW InGaN/GaN configuration has hidden the cut-off wavelength of absorption due to the mixed absorption layer of InGaN/GaN periods. As shown in the Figure 2.23, the InGaN region is mixed to the intermediate and GaN zones. Consequently, the calculation of absorption coefficient is not possible. Concerning the GaN cut-off wavelength, it is similar than the sample SL10-1, observed at 363 nm.

Figure 2.42: Absorption spectrum (left) and Transmission spectrum (right) for the sample MQ10-1 at room temperature.

II.5.   PIN structure with 20 % of SL and MQW InGaN

In this section, samples of PIN structure containing indium composition of 20% will be analyzed. Structural and optical investigations will be detailed in order to obtain an evaluation of the crystalline quality. Increasing the indium content will certainly intensify the density of dislocation and roughen the surface of top layer. Optical properties permits to verify the bandgap of the absorbent layer through the wavelength cut-off. The both configurations SL InGaN and MQW InGaN will be compared in order to understand the MQW effect to the crystalline quality. According to the results issued by characterization of MBE samples, PIN structure with 20, 30 and 50 % of SL and MQW InGaN are only grown by MOCVD due to the significant quality of material comparing to the MBE samples.

II.5.1.Structural characterization

As shown in Figure 2.24, the high intensity of GaN peak is observed at the 17.2° correspond to the bulk layer below the PIN structure for the sample SL20 [40]. It indicates that GaN is highly oriented along the c-axis and has a single crystalline character with sharp and narrow peak. It reveals the good crystallization of GaN material with FWHM of 81 arcseconds. For InGaN, the peak is observed at 16.85° with FWHM of 234 arcseconds. The InGaN peak is

less sharped than the GaN peak due to the indium introduction into the InGaN layer. The approximation of indium content in the InGaN layer is approximately calculated 19.9 % which fit well to our recommendation.
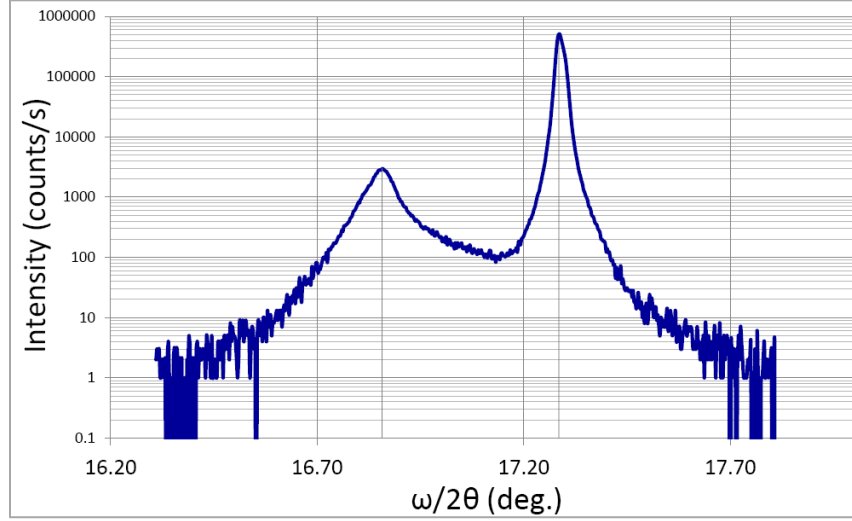
Figure 2.43: XRD scan measurement for SL20 sample grown by MOCVD.

For the sample MQ20, the thick GaN is observed also at 17.2° with high and narrow peak as illustrated in Figure 2.25 [40]. The FWHM of GaN is slightly lower than the sample SL20 and calculated to be 45 arcseconds. The InGaN/GaN MQW exhibits the same phenomena as shown before in the 10% of indium samples with several peaks which are related to the 10 periods in the InGaN/GaN absorbent layer (satellite peaks). The indium content for the InGaN layer in the MQW is calculated 18.3% (estimated 20%). The thickness of the period has been also calculated, the quantum well of InGaN is 2.6 nm (theoretic 3 nm) and the GaN barrier thickness to 8.9 nm (theoretic 10 nm).
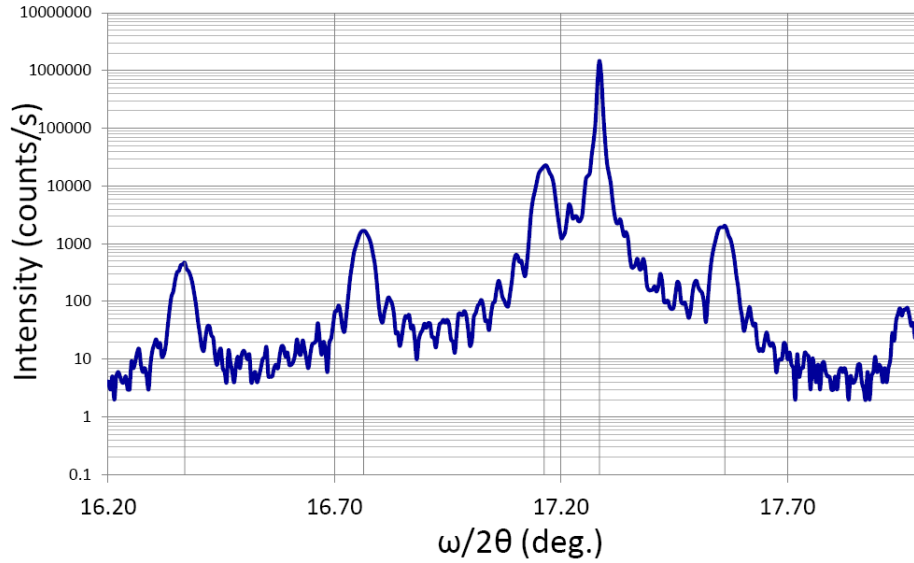
Figure 2.44: XRD scan measurement for MQ20 sample grown by MOCVD.

Samples of 20% of InGaN absorbent layer (SL20 and MQ20) have been characterized using TEM system with kind help of Gilles Patriarche. Samples have been prepared by tilting along the [1100] and [1120] axis on thin foils by FIB in IEMN with the help of David Troadec in order to see the dislocations, chemical analysis and stacking faults.

The sample SL20 has been characterized using TEM instrument to obtain information about the material quality and evaluate the threading dislocation. It permits also to compare the structure of PIN 20% of InGaN to the PIN 10% in order to investigate the insertion of indium in higher percentage. The impact of the indium augmentation in the InGaN layer will certainly degrade the InGaN growth and consequently the P-type layer. In the Figure 2.26, the general view of the PIN cross-section demonstrates the high roughness of the P-GaN surface due to the defective InGaN layer. Several zones are observed with high density of defect and inhomogeneity of indium growth during InGaN deposition. As a result, v-shaped defects on the top layer forms sharp grains (sawtooth shape) with dislocation located in the each boundary. Grains of the order 30 nm wide and v-defects up to 40 nm depth are illustrated in Figure 2.26 (up right). These defects prove that thick SL InGaN configuration with higher indium percentage in the InGaN layer leads to poor crystalline quality as well as high dislocation density. It is related principally to the excess in the critical thickness of InGaN layer [14]. The indium content has been measured using EDX system in attachment to the TEM instrument as shown in Figure 2.26 (down right). It reveals the variation of the indium content in several zones of InGaN layer, 20-27% (green

color), 28-32% (yellow color) and concentrated zone of In-rich 33-39% (red color). The In-rich zones exhibits the inhomogeneity of indium deposition due to the alloy fluctuation. These defects in the InGaN layer have led to rough layer with v-shaped pits passing through the entire absorbent layer. This allows us to anticipate high leakage current during device characterization which may be short circuit the photodiode. Concerning the thickness of P-GaN layer, the surface is defective in several areas with thickness varying from 50 to 100 nm. The surface morphology of P-GaN layer will be investigated thereafter using AFM.
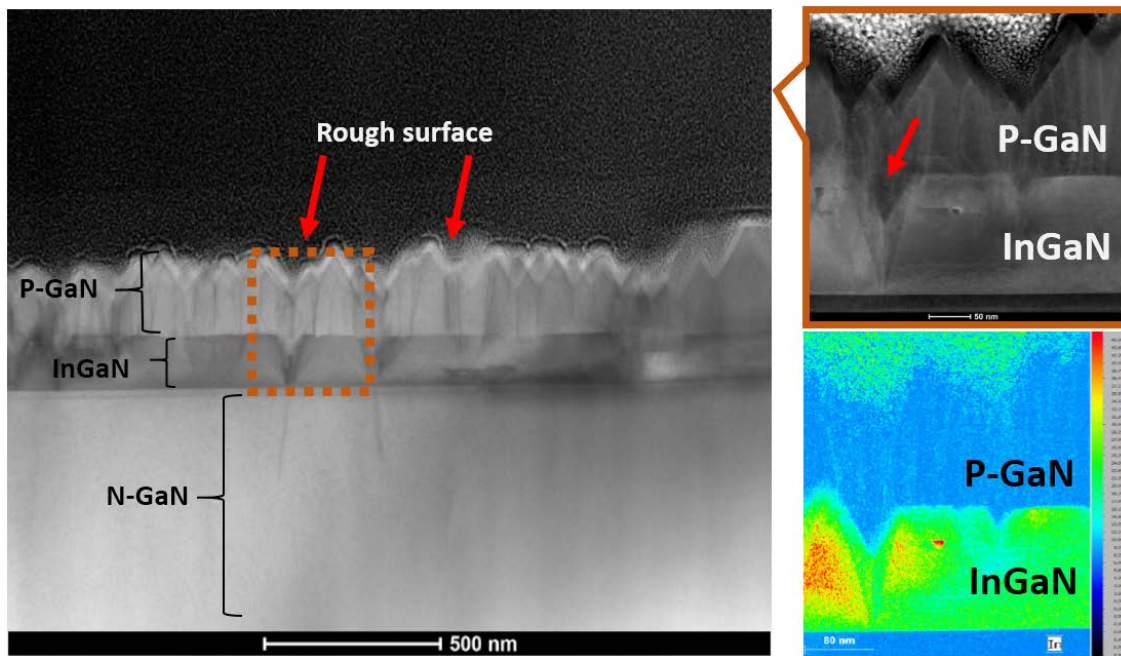
Figure 2.45: TEM cross section image of general view along [1120] for sample SL20 grown by MOCVD (left), zoomed area (up right) and EDX analysis for indium content (down right).

For the sample MQ20, Figure 2.27 (left) shows the cross-section image issued from the same conditions than the sample SL20. First impression of the surface morphology of MQW InGaN configuration demonstrates the good quality of materiel comparing the SL InGaN configuration. As explained previously, the MQW structure shows the improved quality of crystallization and provides smooth upper surface. Reduced density of defects are observed using MQW configuration due to the incorporation of very thin InGaN layer with thickness below the critical value in order to suppress defects [14]. Figure 2.27 (up right) confirms the number of QW (10 periods). The thickness of one period has been calculated to 11 nm related to InGaN and GaN

thin layer (3 and 8 nm) as shown in Figure 2.27 (down right). InGaN well thickness fits well with theoretical value while the GaN barrier is slightly lower than the estimated value (10 nm). Indium content hasn't been performed for this sample due to technical issue. TEM analysis for material with indium content around 30% is reported in the literature and defects in this type of materiel are almost similar [41].
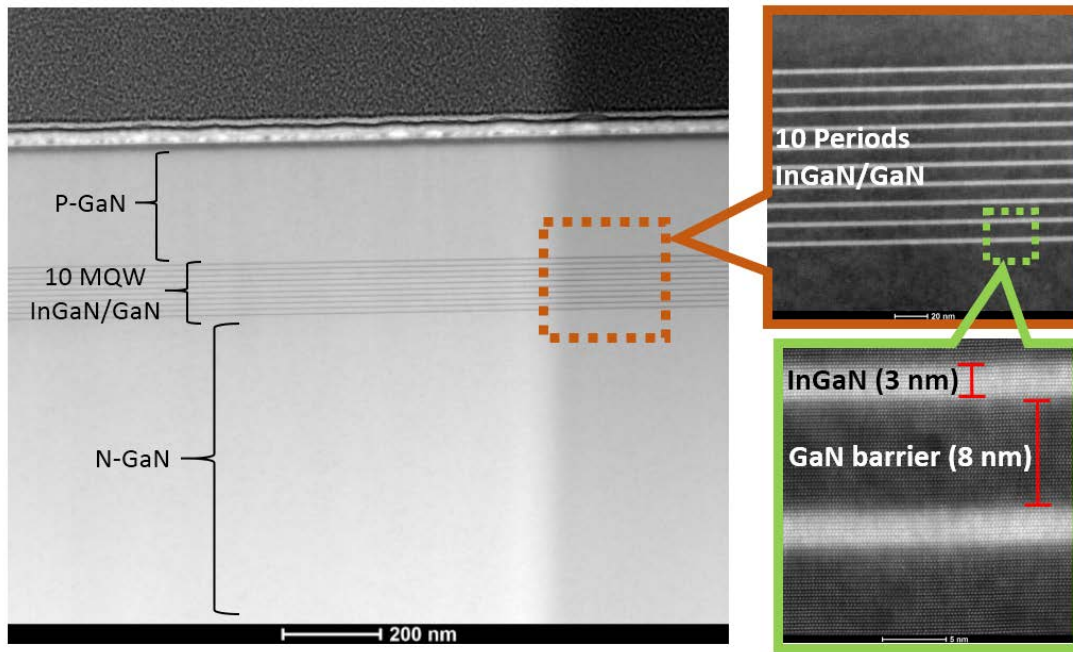
Figure 2.46: TEM cross section image of general view along [1120] for sample MQ20 grown by MOCVD (left), MQW zoomed area (up right) and calculated thickness for one period (down right).

In order to complete the structural characterization, AFM investigation has been performed in order to evaluate the surface morphology. Analysis of sample MQ20 proves the high quality of material with low dislocation density. A homogenous morphology with reduced wave-shaped is observed due to the MQW configuration which reduced defects as illustrated in Figure 2.28 (a). The roughness is calculated in RMS to be low as 1.2 nm for sample MQ20. For the sample SL20, results demonstrates the rough surface with high density of dislocation in Figure 2.28 (b). The surface morphology is almost defective and confirm the TEM analysis mentioned previously. A 3D image has been performed in in Figure 2.28 (c) in order to illustrate the surface defects and the depth of the roughness which exceed the 50 nm. The RMS roughness of the sample SL20 is calculated to be high as 33 nm. The density of dislocation is estimated to

3×10^9 and 5×10^8 cm^{-2} for samples SL20 and MQ20 respectively. We conclude that AFM analysis confirmed the previous investigation performed by XRD and TEM. The MQW configuration is significant technique providing improved materials.
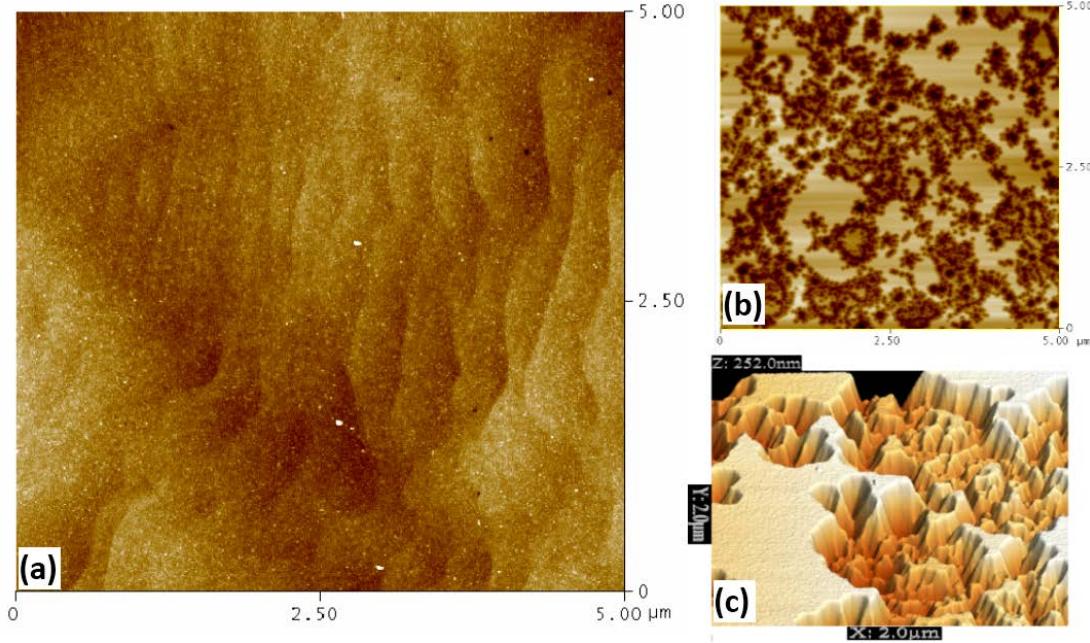
Figure 2.47: AFM analysis of 5×5 µm^2 for sample MQ20 (a) for sample SL20 (b) and 3D surface morphology for sample SL20.

II.5.2. Optical characterization

Optical properties have been investigated for samples SL20, sample MQ20 using Cary 5000 UV-Vis-NIR spectrophotometer. Respecting the same setting for both samples, Figure 2.29 (left) show the absorption spectrum at room temperature for the sample SL20. The down slope of absorption is clearly observed at 360 nm (3.44 eV) corresponding the GaN bandgap. The InGaN cut-off for the sample SL InGaN with 20% of indium is hardly observed at the interval of 436-454 nm (2.73-2.84 eV) in the spectrum slope change. This is related to the indium composition in the InGaN absorbent layer associated with indium fluctuation during the layer growth. The absorption coefficient of the absorbent layer InGaN is calculated using the absorbance spectrum for InGaN and given by the Equation 2.9, it is estimated at 5.2×10^4 cm^{-1}. It is slightly lower than 10% of InGaN absorbent layer (sample SL10) due the improved quality of lower indium content in the InGaN layer. For the sample MQ20 in Figure 2.29 (right), the cut-off wavelength of InGaN

absorption is hidden because of lack of slope change absorption spectrum. As explained previously, it may be as a result of MQW configuration with the introduction of GaN barrier above the InGaN well. Concerning the GaN cut-off wavelength, it is similar than the sample SL20, observed at 360 nm.
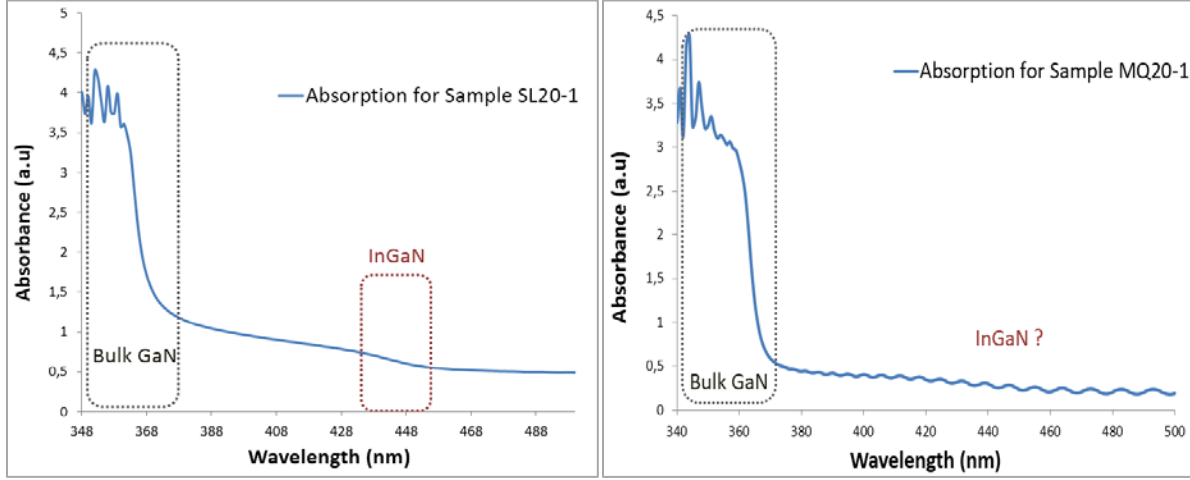
Figure 2.48: Absorption spectrum for sample SL20 (left) and sample MQ20 (right) at room temperature.

II.6. PIN structure with 30 % of SL and MQW InGaN

As planned in our program, the PIN structure with indium composition of 30% will be the next objective respecting the defined criteria with grower. Similar to the PIN structure of 20% of indium composition samples, Novagan has carried out the growth of two samples with SL and MQW InGaN the absorbent layer with 30% of indium content using MOCVD technique. It has been discussed with grower the difficulty to grow such PIN structure with high indium content. The high density of dislocation and the inhomogeneity of indium growth within the InGaN layer are the major challenge. The study of high indium content in InGaN absorbent layer will clarify obstacles related to the high cut-off wavelength of photodiode. This study permits to optimize the compromise between the high quality PIN structure with lower wavelength laser on the one hand, and the low quality of material with availability of higher wavelength laser on the other. Here, structural characterization and optical properties for samples SL30 and MQ30 will be analyzed in order to obtain a comparative study to the previous samples.

II.6.1.Structural characterization

The high intensity of GaN peak is observed at 17.38° for the sample SL30 and MQ30 in Figure 2.30 [40]. It is located in the similar position regarding the previous analysis but showing less sharpness with FWHM above 216 arcseconds comparing to 81 arcseconds calculated before. The large peak give information about the low quality of material and demonstrates the high density of dislocation. For the SL InGaN of sample SL30, the peak is observed at 16.57° with FWHM of 504 arcseconds, wider than the InGaN SL20 sample (234 arcseconds) due to the introduction of high indium content in the InGaN layer. The indium content calculated by the XRD measurement in the SL InGaN is approximately 33.7 % which is an average estimation due to the indium fluctuation during the InGaN growth. For the InGaN/GaN MQW in the sample MQ30, the peaks are less narrow than the MQW peaks for MQ20 with disappearance of some satellite peaks. The indium content for the InGaN layer in the MQW is calculated 31.4%. The thickness of the period has been also calculated, the quantum well of InGaN is 2.7 nm (theoretic 2 nm) and the GaN barrier thickness to 10.6 nm (theoretic 10 nm).
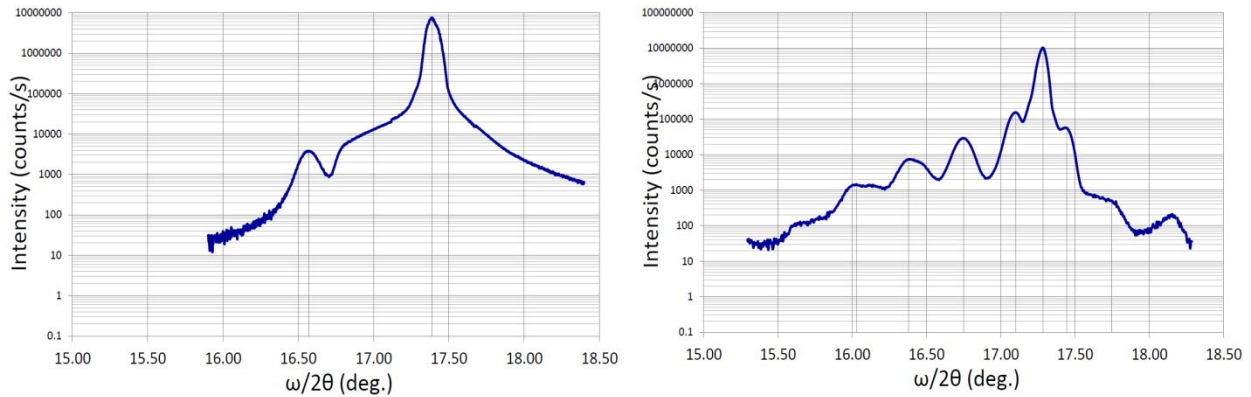
Figure 2.49: XRD scan measurement for sample SL30 (left) and sample MQ30 (right).

TEM analysis has been performed in order to investigate the cross-section layers and to observe the influence of the insertion of high indium content. Samples have been prepared by tilting along the [1100] and [1120] axis on thin foils by FIB in IEMN with the help of David Troadec in order to see the dislocations, chemical analysis and stacking faults. Gilles Patriarche have kindly characterize the samples by TEM instrument. Figure 2.31 (a) shows the general view along [1120] for sample SL30. It is clearly observed the high density of dislocation in the InGaN and P-GaN layer leading to very rough surface. The formation of v-shaped defects (red arrows

Figure 2.31 (a)) is related to the distortion of the InGaN layer due to plastic relaxation. It forms grains on top surface with dislocation located in the each boundary. V-defects are wider than 40 nm in some area with depth up to 60 nm leading to high risk of leakage current for the perspective device. These high density of defects leads to the inhomogeneity of the P-GaN layer thickness. Dislocation have also been observed during the GaN bulk layer due to the mismatch between the sapphire substrate and the nucleation layer (black arrows Figure 2.31 (a)). Many cavities have been generated during the InGaN growth, it is due to InGaN desorption during the growth of the upper layer (P-GaN) which requires a high growth temperature in raison to incorporate the dopant (yellow arrows Figure 2.31 (b)). Indium fluctuation are also observed as shown in red arrow demonstrating the inhomogeneity of indium distribution along the InGaN layer. This variation of indium content is confirmed by the EDX analysis as shown in Figure 2.31 (c) with indium composition fluctuating from 2 to 21% in this located area.
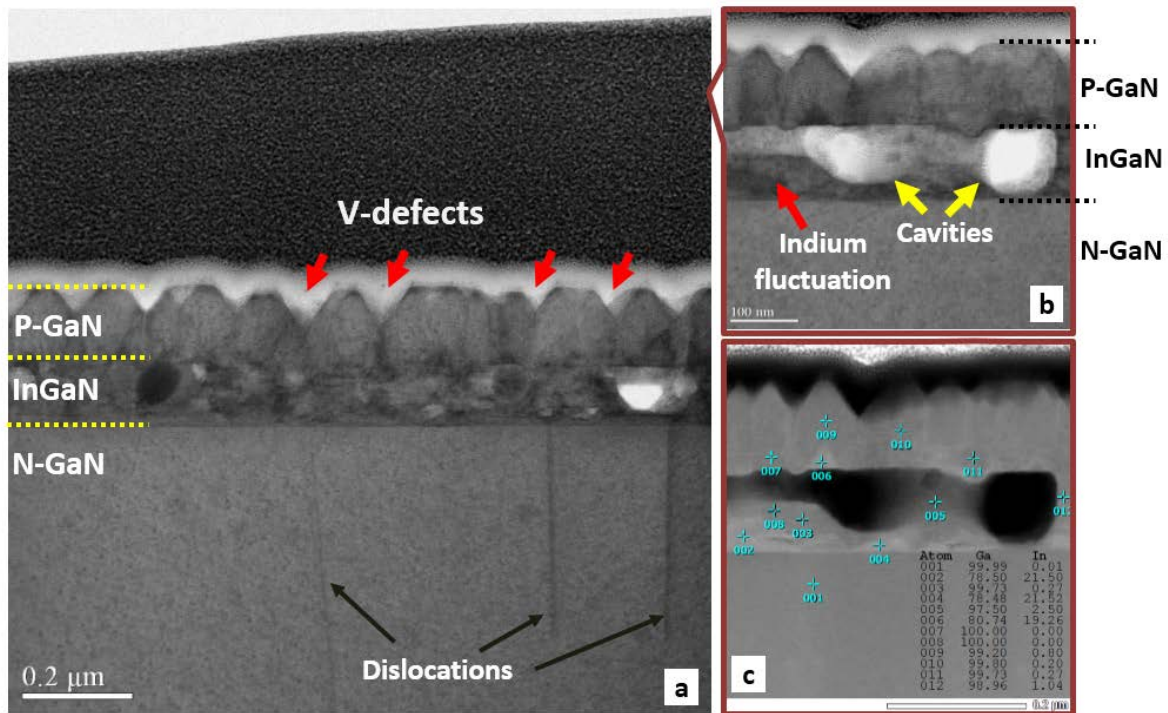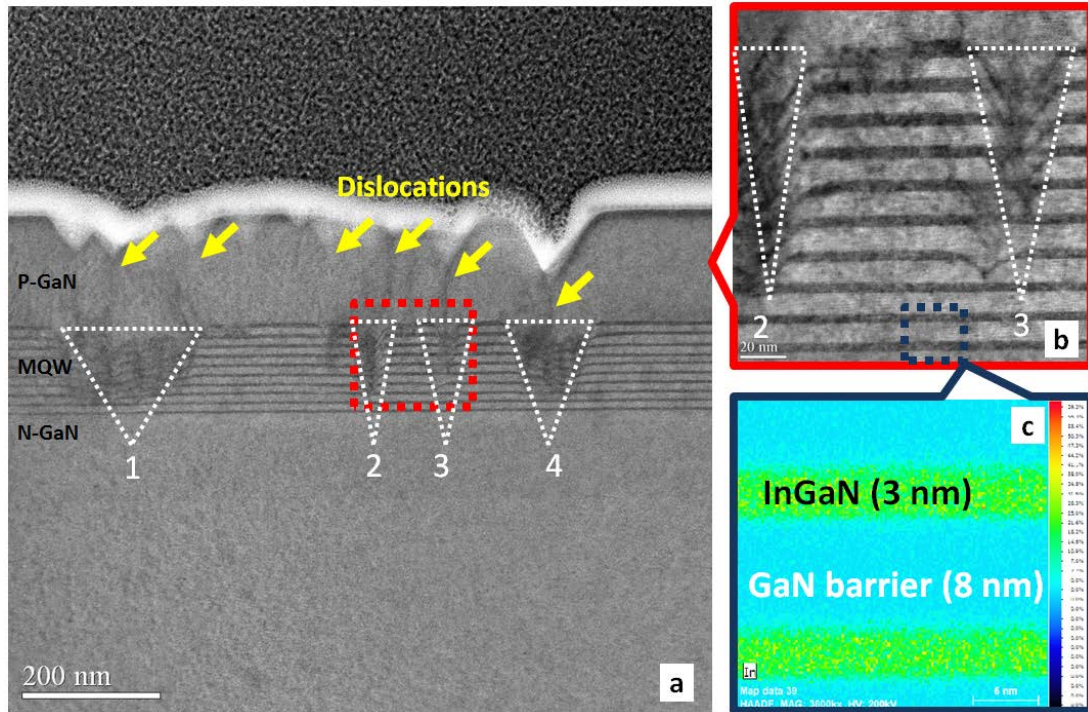

Figure 2.50: TEM cross section image of general view along [1120] for sample SL30 grown by MOCVD (a), zoomed area (b) and EDX analysis for indium content (c).

The MQW InGaN samples (MQ30) has been investigated in the same conditions than the sample SL30-1. Figure 2.32 (a) illustrates the cross section of the PIN structure with 4 pinching zones in the InGaN/GaN MQW layer (white triangles). These pinching zones generate threading

dislocations (yellow arrows) associated to plastic relaxation mechanism. It also leads to the variation of top layer thickness (P-GaN layer) above these zones. Figure 2.32 (b) confirms the number of QW (10 periods) with defective zones (2 and 3). The thickness of one period has been calculated to 11 nm related to InGaN and GaN thin layer (3 and 8 nm) as shown in Figure 2.32 (c). The indium content in the InGaN well has been calculated using EDX instrument and provides variation from 25% to 34%.

Figure 2.51: TEM cross section image of general view along [1120] for sample MQ30 grown by MOCVD (a), MQW zoomed area (b) and EDX analysis for indium content (c).

The AFM analysis will complete the structural analysis and give information on the surface morphology. The formation of defects in the samples SL30 and MQ30 is evidently observed in the TEM analysis but the roughness type of each sample deserves to be explored.

In the Figure 2.33 (left), 5×5 µm^2 for sample SL30 has been evaluated, it shows the grains shaped related to the high density of defects observed already in the TEM image. Dislocations are located in the boundary of each grain with high change in surface profile. Roughness measurement in RMS is estimated to be 14 nm which reflect the high rough surface. The 3D

analysis in the Figure 2.33 (right) ascertains the grain formation and the high density of defects. The density of dislocation cannot be precisely calculated due to hidden defects among grains.
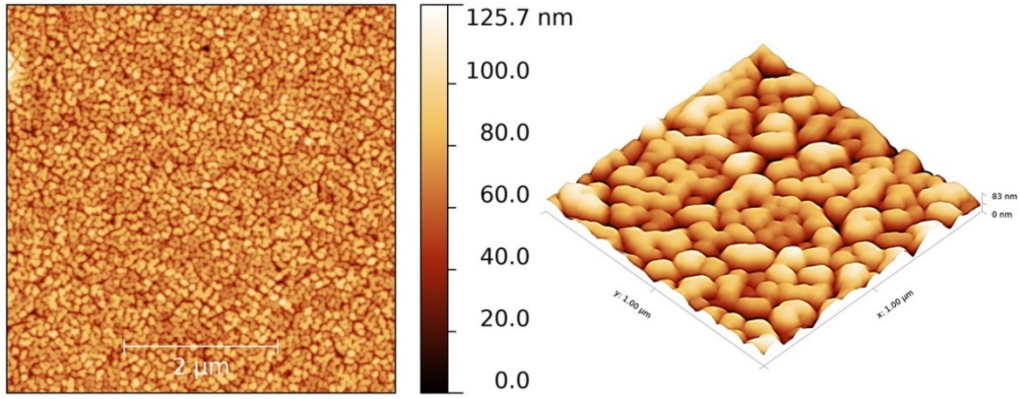
Figure 2.52: AFM analysis of 5×5 µm² for sample SL30 (left) and 3D surface morphology (right).

For the MQW configuration, sample MQ30 has been analyzed in Figure 2.34 (left). The formation of defects is different than sample SL30, the surface is less fractional with homogeneity in some areas as shown in Figure 2.34 (right). However, the roughness value of surface is considered high and attaints 12 nm in RMS. The high change in surface profile is common for both samples due to change of P-GaN layer thickness above the defective zones of InGaN layer. AFM study confirms the TEM analysis in terms of surface morphology and surface profile.
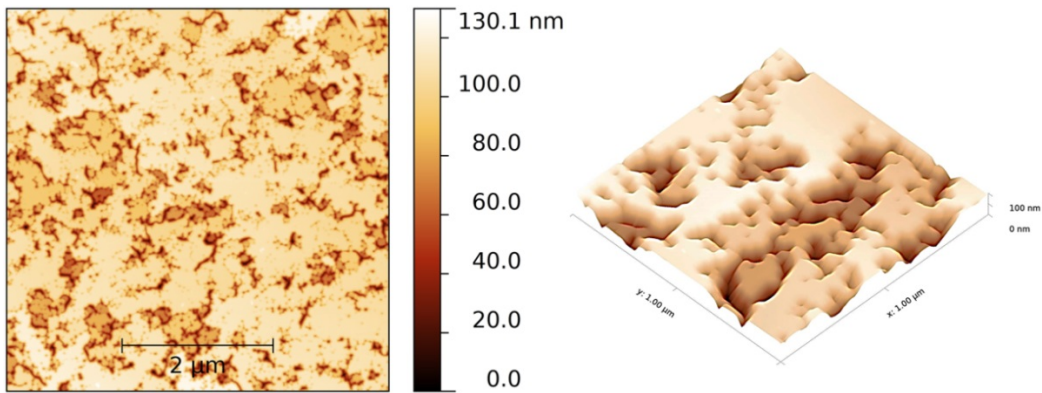
Figure 2.53: AFM analysis of 5×5 µm² for sample MQ30 (left) and 3D surface morphology (right).

II.6.2. Optical characterization

Optical properties have been performed using transmission technique for both samples SL30 and MQ30 [42]. Figure 2.35 demonstrates clearly the GaN slope absorption at 360 nm in both samples SL30 and MQ30. The InGaN absorption slope edge is hardly observed around 500 nm (2.48 eV) for the sample SL30 as shown in Figure 2.35 (left). It corresponds the cut-off wavelength of InGaN with 30% of indium content. For the sample MQ30, the cut-off wavelength of InGaN absorption is hidden because of lack of slope change in the absorption spectrum as illustrated in Figure 2.35 (right). It could be due to the MQW configuration with the insertion of GaN barrier on the InGaN well.
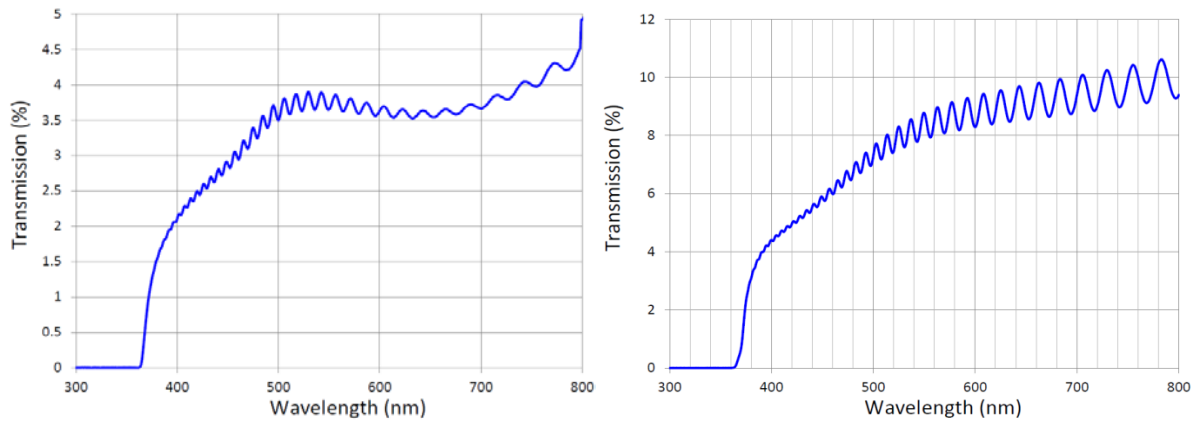
Figure 2.54: Transmission spectrum for the sample SL30 (left) and sample MQ30 (right) at room temperature.

II.7.   PIN structure with 50 % of SL InGaN

In order to achieve the limit of indium growth, it has been suggested to evaluate such structure with indium content higher than 30%. The Institute of Materials Research and Engineering (IMRE) in Singapore has provided a 50% of indium content in the InGaN/GaN sample grown by MOCVD. Due to technical problem in the MOCVD, the configuration of InGaN absorbent layer is only single layer without P-GaN layer, the MQW configuration hasn't been also performed.

Here, the high indium content will clarify the possibility to obtain such material with high cut off wavelength around 600 nm. The difficulty to grow InGaN absorbent layer with high

indium content may influence the quality of the PIN structure and generate high density of dislocation. The inhomogeneity of the InGaN layer is a result of high density of defects and may affect the top layer thickness. This analysis achieve an overview on the behavior of the indium insertion in the absorbent layer and demonstrates the relation between the indium content and the material quality. More the indium content is higher, more the material quality is defective but more the cut-off wavelength is higher. In this section, structural characterization and optical properties for samples SL50 will be analyzed in order to obtain a comparative study to the previous samples.

II.7.1. Structural characterization

XRD measurement demonstrates the GaN peak located at 17.35° which is similar to the reported GaN peaks regarding previous analysis as shown in Figure 2.36. Less sharpness and larger peak are observed comparing to samples with lower indium content. It gives information about the low crystalline quality which exhibits a high density of dislocation. The InGaN peak related to the absorbent layer is located at 16.5°. It reveals a lightly lower than sample with 30% of indium content (SL30) which indicates the higher indium content. We observe the wide peak of InGaN around 550 arcseconds which is higher than sample SL30 (504 arcseconds) revealing high density of dislocation. The estimation of the InGaN absorbent layer has been performed in order to have the indium composition, it is approximately 46%.
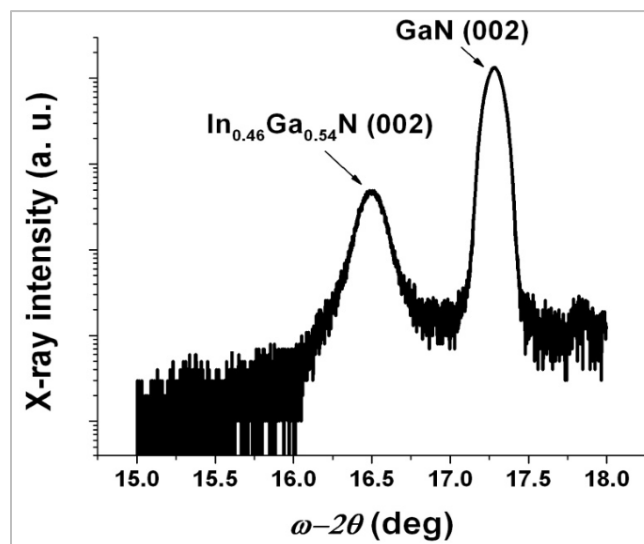

Figure 2.55: XRD scan measurement for sample SL50.

TEM analysis has been carried out in the same conditions than the previous samples. Figure 2.37 (a) shows the cross section image of general view along [1120] for sample SL50. As we have explored in the sample SL30, the presence of cavities in sample SL50 is clearly observed along the InGaN layer using bright field scan as zoomed in Figure 2.37 (b) and (c). Cavities or nano-cavities are displayed in black zones in bright field scan (white zones if dark field scan is applied). It reveals the inhomogeneity of indium distribution during InGaN growth and associated substantially to lower concentration of indium. This fluctuation in growth rate leads to grow 3D InGaN layer with sawtooth-shaped surface with roughness almost 50 nm. Each boundary of sawtooth presents a dislocation in the InGaN layer toward the top surface. Threading dislocations generated to the surface are also related to the disrupt in the interface of GaN bulk layer/sapphire substrate.
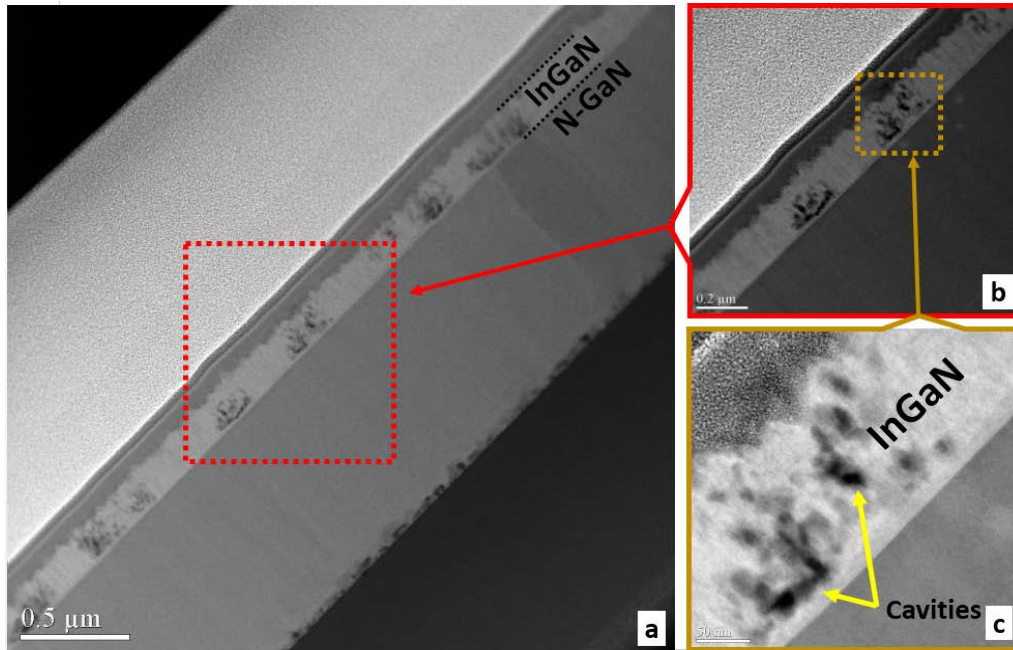
Figure 2.56: TEM cross section image of general view along [1120] for sample SL50 grown by MOCVD (a), zoomed area (b) and (c).

EDX analysis to the cross-section image has been performed in order to investigate the indium fluctuation throughout the InGaN layer. Figure 2.38 demonstrates several studied zones to evaluate the indium variation. LG2 scan in the cross section image has been located in proper zone where practically non cavities exist. The EDX analysis demonstrates the good distribution of indium throughout the InGaN layer with average of indium content around 42%. LG1 scan has been located in zone partially containing cavities, the EDX analysis shows fluctuation in the

indium distribution varying from 20 to 45 %. Regarding LG3 scan, the zone concerned presents a large number of cavities which results further variation in indium distribution fluctuating from 13 to 46 %.
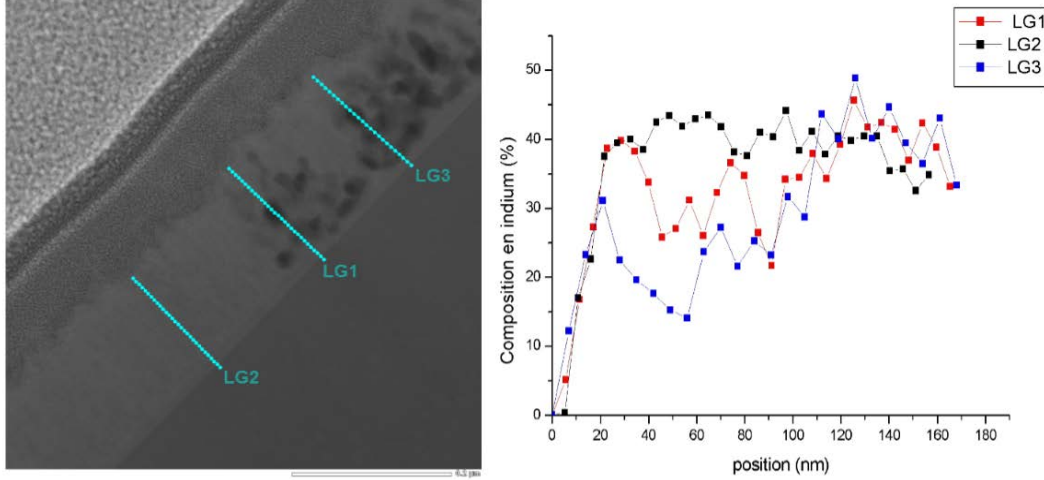

Figure 2.57: EDX analysis for indium content for sample SL50.

AFM analysis in Figure 2.39 (a) of 1×1 μm^2 proves the TEM analysis and shows the grans-shaped defects on the surface. It is evidently related to the high density of dislocation located in each grain boundary. Figure 2.39 (b) illustrates 3D surface morphology image clarifying the grain-shaped defects. AFM analysis of sample SL50 is almost similar to sample SL30 where the indium content in both structure is considered high in SL configuration. Roughness measurement in RMS is estimated to be 11 nm which reflect the high rough surface. However this value isn't very accurate due to high change in surface profile as shown in Figure 2.39 (c).
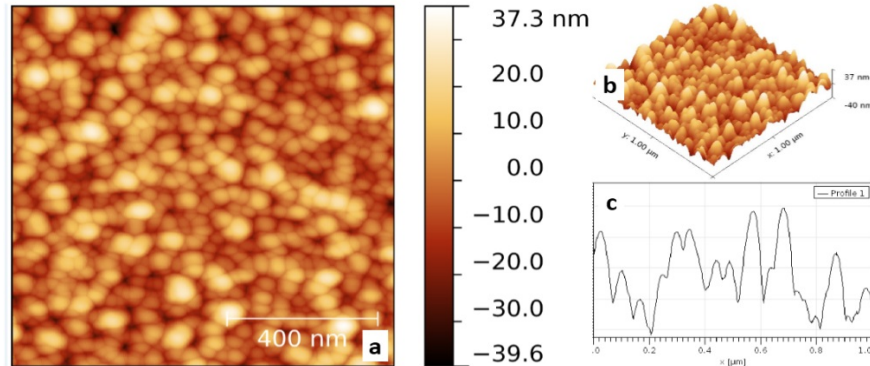
Figure 2.58: AFM analysis of 1×1 μm^2 (a), 3D surface morphology (b) and surface profile (c) for sample SL50.

II.7.2. Optical characterization

Sample SL50 has been optically characterized using absorption technique in IMRE Singapore laboratory. Figure 2.40 shows the measurement of InGaN absorption spectrum, it presents a starting absorption at 690 nm (1.78 eV). It is principally related to the InGaN layer absorption with indium content around 50%. A simulated fit curve has been presented in order to adjust the absorption cut-off wavelength, it shows an absorption at 629 nm (1.97 eV). The GaN absorbance is clearly observed at 364 nm (3.4 eV). Comparing to the sample SL30, we observe the high cut-off wavelength in the red zone of visible spectrum for the sample SL50 while the sample SL30 absorbs around 500 nm in the cyan-green zone.
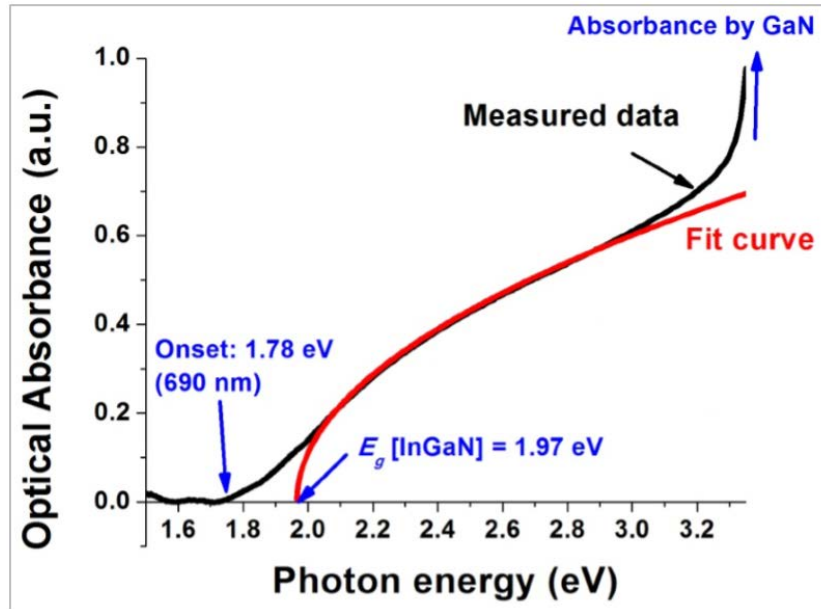
Figure 2.59: Absorption spectrum for sample SL50 at room temperature.

II.8.   Characterization of nanostructured GaN

In this section, the optical waveguiding properties into porous GaN structure have been studied. In collaboration with KAIST in Korea, samples have been grown on sapphire substrate by MOCVD. The microstructure has been characterized in IEMN in order to extract the change in refractive index related to the bulk material. The control of the refractive index into GaN is therefore fundamental for the design of active and passive optical devices. The control of light

emission in the photodiode is a major interest in order to enhance the light collection efficiency. The objective of this study is to demonstrate that optical properties of GaN can be adjusted by controlling the pores size and spacing. Toward the demonstration of GaN-based optoelectronic devices, it is essential to control the light emission by an increased coupling of the active material with optical modes. As explained in chapter 1, an improved photodetector could be consequently a significant emitter in LED mode for LIFI applications. On the way to enhance such optical devices for these applications, the development of technical process is key element enabling the realization of original structures. Efforts have already been achieved with other material systems using cavities such as photonic crystal, micro-pillars, etc. [43][44]. For GaN, Different techniques have been used to nanostructure the material. Nano-structuration has led to the enhancement of the collection efficiency using photonic crystals and surface gratings [45][46][47].

Samples BK (bulk GaN), POR20 (20% porosity) and POR40 (40% porosity) have been performed by growing a first layer of 400 nm of undoped GaN film on sapphire substrate. It is followed by the growth of 800 nm of n-type GaN (n~1×10^{18} cm^{-3}). Sample BK such as a bulk GaN is considered to be a reference for the following of the study. Concerning the sample POR20 and POR40, they have been subjected to electrochemical (EC) etching using potassium hydroxide (KOH) electrolyte. GaN sample and Platinum electrode are connected to the positive and negative terminals of a voltage source. Both were immersed in KOH at room temperature with application of a constant DC voltage. Figure 2.41 shows the sample structure of GaN bulk layer subjected to be etched by KOH base.
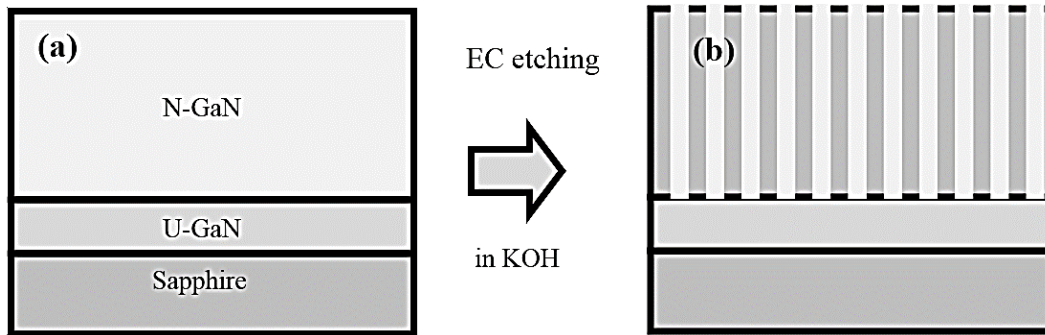

Figure 2.60: Sample structure for bulk GaN (a) and porous GaN (b)

In order to improve the etching process, there is no UV light illumination onto the sample surface. The etching process is very sensitive to the doping concentration and only N-type doped

GaN is etched. A set of etching parameters including bias voltage and current, molar concentration of KOH acid, etching temperature and time have been employed to develop the pore shapes and sizes on the GaN. A 20% and 40% of porosity are achieved on two different samples using 20V and 100V of electrochemical voltage respectively. Both samples are immersed for 1 minute in KOH with molar concentration of 0.2 M at 20 °C. Once the electrochemical process is completed, samples are rinsed in deionized water then in methanol before drying.

AFM analysis has been performed for the sample POR1 in order to evaluate the surface morphology. The calculated roughness RMS is estimated to be 0.34 nm for the sample BK and 1.34 nm for the sample POR20 as shown in Figure 2.42 (left). TEM cross section investigation has been performed for the sample POR20, it demonstrates the nanoporous n-GaN layer after KOH electrochemical process. The average spacing between pores is ~ 100 nm and the average pore radius is ~ 40 nm.
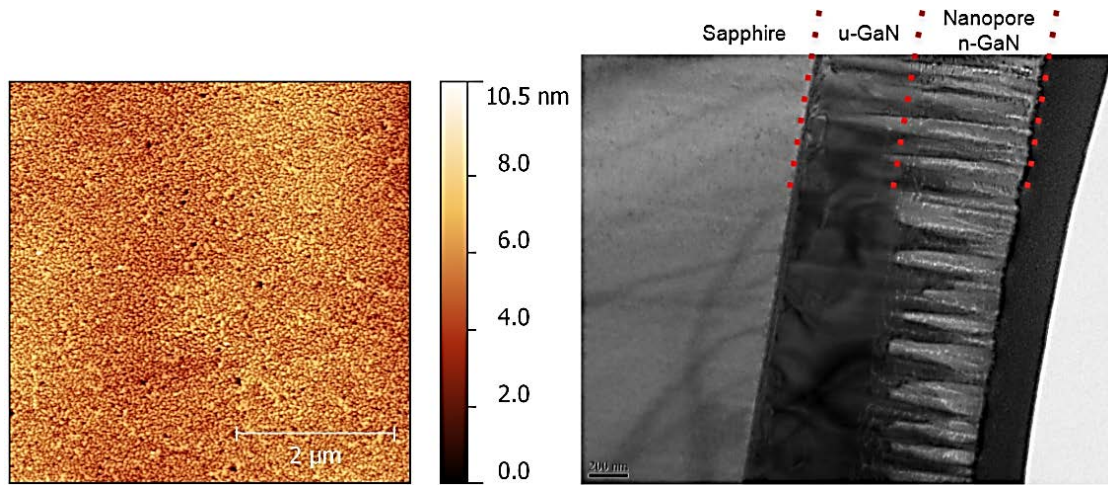

Figure 2.61: 5×5 µm² AFM analysis (left) and TEM cross section image for sample POR20.

Surface characterization has been performed by SEM at the operating voltage of 10 kV to examine the etching profile and formation of nanoporous structure for the sample POR40. Figure 2.43 shows nanostructured surface containing pores for 40% of porosity comparing to the bulk surface before KOH etching process. It is noted that the porous density (pore size, etching depth and interdistance) is controlled by varying the etching conditions by means of applied bias, etching time and KOH concentration.
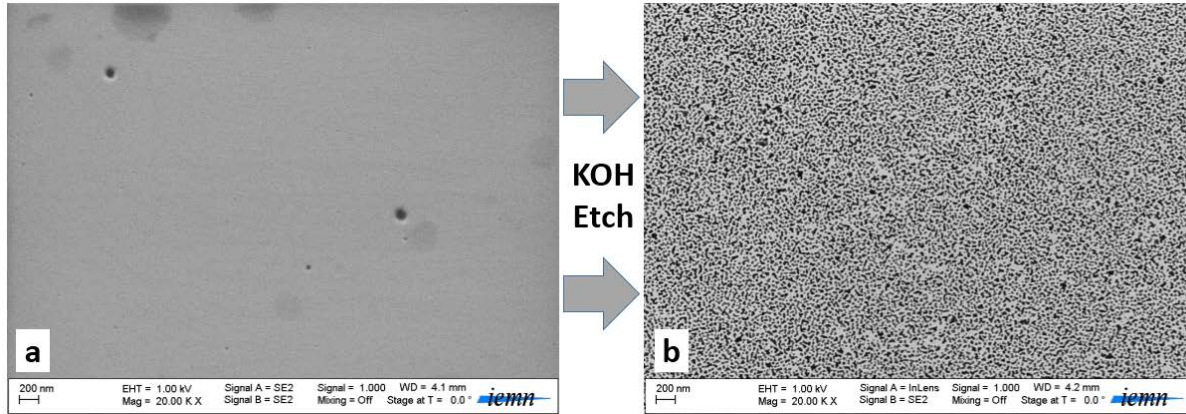
Figure 2.62: SEM surface image of (a) bulk GaN sample (BK) and (b) nanoporous GaN sample (POR40).

The evaluation of refractive index dispersion will be discussed using two different techniques, ellipsometry and guided-wave prism coupling. As explained in the prism coupling characterization, Metricon instrument will be used to determine the refractive index. It is a direct method allowing the observation of the evanescent coupling of light through a prism. The incident beam of laser source will excite the different guided modes. The optical evaluation demonstrates the possibility to couple optical signal into the nanoporous GaN structure. Different laser sources varying from 450 to 1539 nm have been used into the film waveguide through a rutile prism (TiO_2). The refractive index has been measured for both bulk GaN and porous GaN samples (BK and POR20). In order to measure the refractive index, spectra of TE (ordinary mode) and TM (extraordinary mode) guided modes are extracted using different wavelengths and different polarizations. TE and TM modes are excited respectively using TE and TM polarized light with the optical axis normal to the surface. As light wavelength is higher than the pore size, layer could be considered uniform and exhibits a refractive index by effective medium approximations. The fact is that the GaN porous structure layer consists of a bulk GaN and air inside the pores leading to have a lower refractive index comparing to the bulk reference sample.
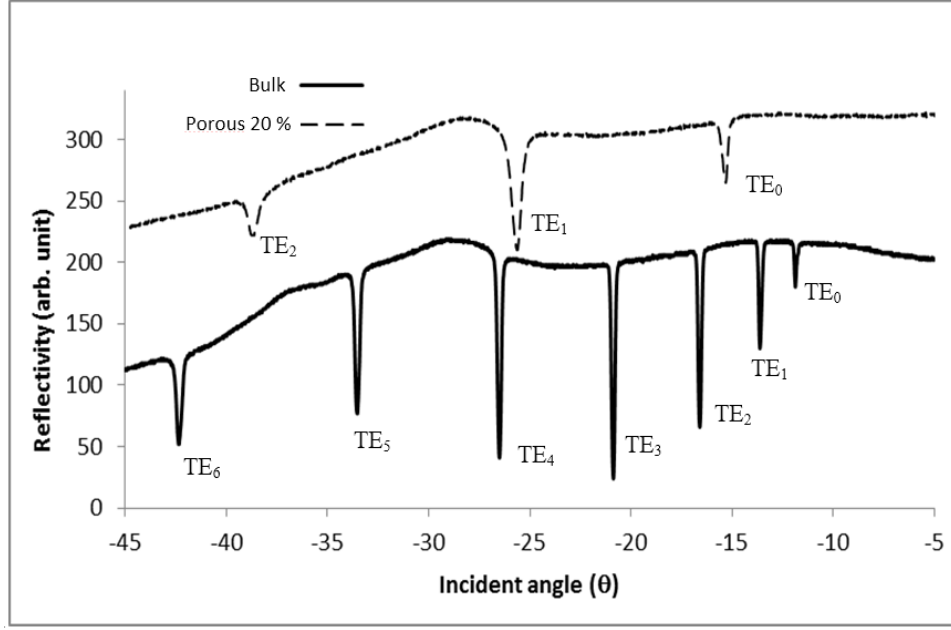
Figure 2.63: Ordinary guided-mode reflectivity spectra obtained at 975nm for bulk GaN and porous GaN (porosity of 20 %) using prism coupler.

In Figure 2.44, we report the TE guided-mode reflectivity spectrum excited at 975 nm for BK and POR20 samples. Seven sharp dips are observed for both bulk and porous samples at different angles θ related to the guided modes of excitation. Dips are identified from TE_0 to TE_6 for sample BK and TE_0 to TE_2 for the sample POR20. Once these modes are determined with related angular positions of excitation, the refractive index is calculated using the Equation 2.10. For the sample POR20, with 20% of porosity, the ordinary refractive index is $n_0=2.285$ and the extra-ordinary index is $n_e=2.315$ at 975 nm. Comparing to the sample BK, the ordinary refractive index is $n_0=2.29$ and the extraordinary index is $n_e=2.33$ which is slightly higher than porous GaN for the same wavelength. The sharpness of dips reveals the good confinement of the light into the propagated layer. It indicates the good quality and homogeneity of structure. These results are in agreement with reported values using ellipsometry technique [29].

We have performed the measurement of refractive index in several laser sources for both samples BK and POR20. In the Table 3, refractive indices are measured in TE and TM modes using different laser sources. The comparative study has been carried out for the sample with 20% of porosity. Measurement of the refractive index for the sample POR40 hasn't led to extract the TE and TM modes due to the rough surface of the top layer blocking the light propagation.

111

Wavelength (nm)	Sample BK		Sample POR20	
	TE	TM	TE	TM
450	2.4470	2.4956	2.4102	2.4493
633	2.3476	2.3876	2.3399	2.3777
975	2.2911	2.3308	2.2857	2.3157
1539	2.2612	2.2951	2.2490	2.2631

Table 11: Refractive indices in ordinary and extraordinary modes for samples BK and POR20 excited at different wavelengths extracted from prism coupling.

The refractive index obtained for bulk GaN and the porous samples in TE and TM polarization are decreasing when increasing the wavelength of excitation. The difference in refractive index values between samples BK and POR20 remains similar whatever the laser source used. This indicates the stability of refractive index against the laser source. In the Figure 2.45, variation of ordinary and extraordinary indices dispersion are presented versus wavelength varying from 450 to 1539 nm for bulk and porous GaN structure. We can estimate that GaN structures with larger pore sizes exhibit lower refractive indices due to the large volume fraction of air. As the value of refractive index for the sample POR40 hasn't been extracted, ellipsometry technique is employed to evaluate the optical properties for this sample as well as other samples.
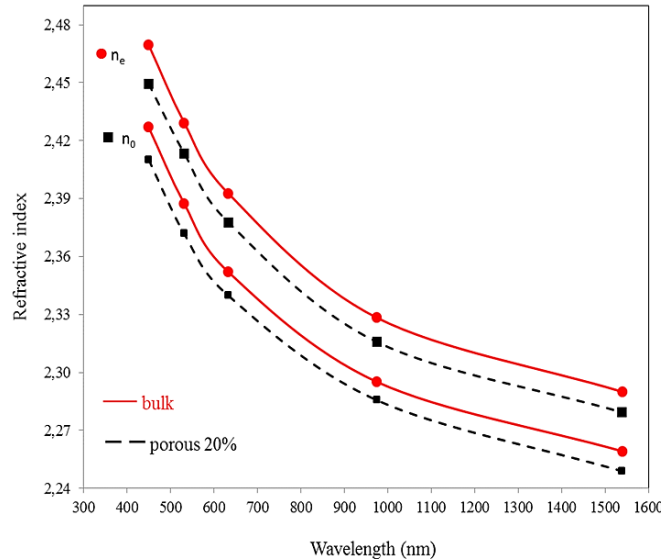

Figure 2.64: Ordinary and extraordinary refractive indices dispersion for bulk and porous (20%) GaN samples extracted from prism coupling.

Ellipsometry technique has the possibility to confirm the refractive index values extracted by prism coupling for the porous GaN samples. Extraction of (Δ, Ψ) values has been performed in the IEMN using HORIBA JOBIN YVON UVISEL spectroscopic ellipsometer (Figure 2.46). The measurement has been in the range of 4.55-0.75 eV (270 to ~ 1650 nm) at 60° of incident angle.
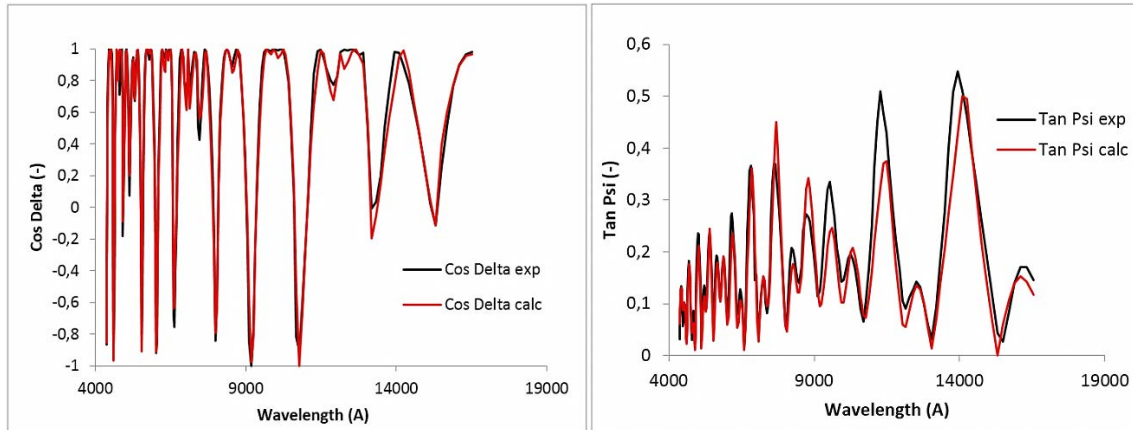

Figure 2.65: Extraction of Tan (Psi) and Cos (Delta) for sample POR40 using ellipsometer.

Eric Dumont from University of Mons in Belgium has developed a model for our study in order to calculate the refractive index. The developed model based on the (Δ, Ψ) values reveals the refractive index for bulk GaN and two different porosity. Figure 2.47 exhibits the variation of refractive indices as function of wavelengths for different porosity compared to bulk GaN sample. Comparing to the prism coupling measurements, the bulk values are almost similar. For the sample POR20, values are inferiors in ellipsometry than the prism coupling technique. It is due to the more sensitive effects of voids (air) in the film, this influences the global value of the index leading to lower refractive index values. Sample POR40 has lower values than POR20 varying from 1.73 to 1.85 due to the high density of porosities in the film which decrease the global index. This phenomena has already demonstrated in other materials as anodized aluminum oxide (AAO) [48].
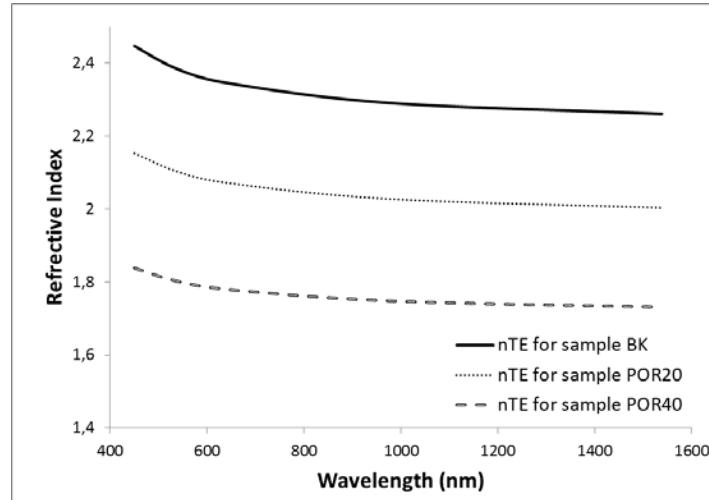
Figure 2.66: Ordinary refractive indices dispersion for bulk GaN, porous GaN (20%) and porous GaN (40%) samples extracted from ellipsometry.

The evaluation of the refractive index across the GaN layer from top surface until the sapphire substrate has been studied. In Figure 2.48, the profile of the refractive index is demonstrated at 633nm for the sample POR40. Top surface probably reveals to an oxide layer increasing the index value. This oxide layer is followed by the nanostructured GaN and its index indicates 1.8 at 633 nm for 40% of porosity.
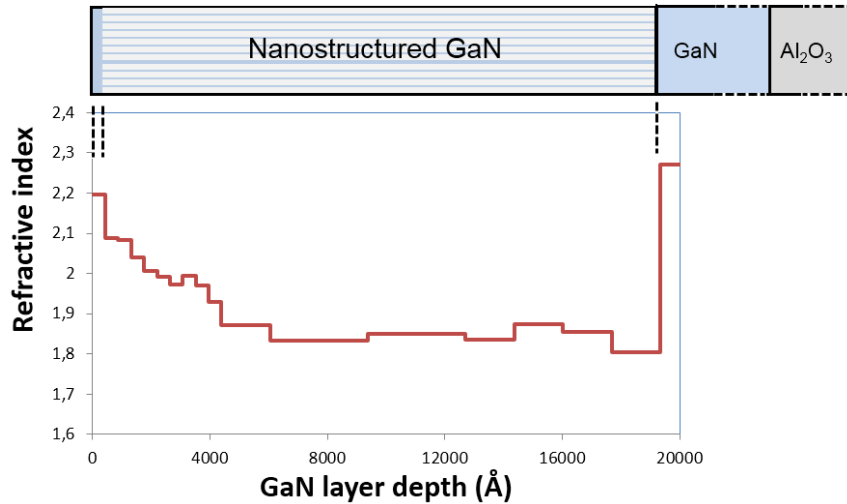
Figure 2.67: Profile of refractive index across the GaN layer for sample POR40.

In this chapter, the investigation of martial quality has been performed. Structural, microstructural and optical properties have been studied. PIN structures with InGaN as absorbent layer varying from 10 to 50 % of indium content have been analyzed. The material quality has been compared in each other for different configuration as SL InGaN and MQW absorbent layers. Several types of defects have been investigated by TEM instrument with the help of the cross section FIB foils. Surface morphology have been studied and correlated to the TEM results.

It has been noted that the material quality decreases when increasing the indium content. The incorporation of indium above 10% in the SL InGaN configuration creates areas of high concentration of indium and cavities leading to increased surface roughness to 3D defects. Consequently, the material is plastically relaxed creating numerous structural defects.

MQW configuration has revealed an optimized structure even in higher indium insertion in the InGaN layer. MQW configuration exhibits a higher material quality than SL configuration due lower density of defects. Results from EDX analysis have reflected an estimation of optical properties in terms of indium content and wavelength cut-off of the absorbent layers. TEM investigation has been a significant tool to evaluate the quality of material. However, the micro-zone analysis gives only an estimation of the growth quality in small area, structural defects may vary from zone to other.

Critical indium content in InGaN layer is observed at 50% resulting high density of defects and very rough surface. Higher indium content in the InGaN layer will affect the photodiode performance and high leakage current is expected during the next step of fabrication.

Optical waveguiding properties have been studied for bulk and porous GaN structures. Samples have been grown and structured by KAIST and characterized in IEMN. Prism coupling and ellipsometry techniques have been used in order to investigate the refractive index. The dispersion of refractive index for several porous GaN has been studied and compared to the GaN bulk material. Profile of the refractive index is demonstrated throughout the nanostructured and GaN layers.

The control of the refractive index into GaN is therefore fundamental for the design of active and passive optical devices. The objective has been to control the light emission besides the enhancement of the light collection efficiency as a perspective in our study.

In the next chapter, design, fabrication and device characterization of the expected photodiodes are studied. Several designs have been developed in order to optimize the device performance. Numerous photodiode dimensions have been conceived in order to improve the technical process. Once the photodiodes are fabricated, device characterizations have been performed in order to investigate the static and dynamic response.

References

[1]   D. V. P. McLaughlin and J. M. Pearce, "Analytical model for the optical functions of indium gallium nitride with application to thin film solar photovoltaic cells," *Mater. Sci. Eng. B*, vol. 177, no. 2, pp. 239–244, Feb. 2012.

[2]   R. F. Webster, D. Cherns, L. E. Goff, S. V Novikov, C. T. Foxon, A. M. Fischer, and F. A. Ponce, "Indium Nitride and Indium Gallium Nitride layers grown on nanorods," *J. Phys. Conf. Ser.*, vol. 471, no. 1, p. 12025, 2013.

[3]   M. Yamada, T. Mitani, Y. Narukawa, S. Shioji, I. Niki, S. Sonobe, K. Deguchi, M. Sano, and T. Mukai, "InGaN-Based Near-Ultraviolet and Blue-Light-Emitting Diodes with High External Quantum Efficiency Using a Patterned Sapphire Substrate and a Mesh Electrode," *Jpn. J. Appl. Phys.*, vol. 41, no. Part 2, No. 12B, pp. L1431–L1433, Dec. 2002.

[4]   T. Mehrtens, M. Schowalter, D. Tytko, P. Choi, D. Raabe, L. Hoffmann, H. Jönen, U. Rossow, a Hangleiter, and a Rosenauer, "Measuring composition in InGaN from HAADF-STEM images and studying the temperature dependence of Z-contrast," *J. Phys. Conf. Ser.*, vol. 471, p. 012009, Nov. 2013.

[5]   F. A. Ponce, S. Srinivasan, A. Bell, L. Geng, R. Liu, M. Stevens, J. Cai, H. Omiya, H. Marui, and S. Tanaka, "Microstructure and electronic properties of InGaN alloys," *Phys. Status Solidi*, vol. 240, no. 2, pp. 273–284, Nov. 2003.

[6]   B. R. Jampana, C. R. Weiland, R. L. Opila, I. T. Ferguson, and C. B. Honsberg, "Optical absorption dependence on composition and thickness of InxGa1−xN (0.05<×<0.22) grown on GaN/sapphire," *Thin Solid Films*, vol. 520, no. 22, pp. 6807–6812, Sep. 2012.

[7]   A. Gokarna, A. Gauthier-Brun, W. Liu, Y. Androussi, E. Dumont, E. Dogheche, J. H. Teng, S. J. Chua, and D. Decoster, "Optical and microstructural properties versus indium content in InxGa1−xN films grown by metal organic chemical vapor deposition," *Appl. Phys. Lett.*, vol. 96, no. 19, p. 191909, 2010.

[8]   M. Gartner, C. Kruse, M. Modreanu, a. Tausendfreund, C. Roder, and D. Hommel, "Optical characterization of InxGa1−xN alloys," *Appl. Surf. Sci.*, vol. 253, no. 1, pp. 254–

257, Oct. 2006.

[9]   W. Yang, S. Zhang, J. J. D. McKendry, J. Herrnsdorf, P. Tian, Z. Gong, Q. Ji, I. M. Watson, E. Gu, M. D. Dawson, L. Feng, C. Wang, and X. Hu, "Size-dependent capacitance study on InGaN-based micro-light-emitting diodes," *J. Appl. Phys.*, vol. 116, no. 4, p. 044512, Jul. 2014.

[10]   Z. Z. Chen, Z. X. Qin, X. D. Hu, T. J. Yu, Z. J. Yang, Y. Z. Tong, X. M. Ding, and G. Y. Zhang, "Study of photoluminescence and absorption in phase-separation InGaN films," *Phys. B Condens. Matter*, vol. 344, no. 1–4, pp. 292–296, Feb. 2004.

[11]   K. . O'Donnell, I. Fernandez-Torrente, P. . Edwards, and R. . Martin, "The composition dependence of the InxGa1−xN bandgap," *J. Cryst. Growth*, vol. 269, no. 1, pp. 100–105, Aug. 2004.

[12]   L. Liu and J. H. Edgar, "Substrates for gallium nitride epitaxy," *Mater. Sci. Eng. R Reports*, vol. 37, no. 3, pp. 61–127, 2002.

[13]   L. Li, D.-G. Zhao, D.-S. Jiang, Z.-S. Liu, P. Chen, L.-L. Wu, L.-C. Le, H. Wang, and H. Yang, "The effects of InGaN layer thickness on the performance of InGaN/GaN p—i—n solar cells," *Chinese Phys. B*, vol. 22, no. 6, p. 068802, 2013.

[14]   D. Holec, P. M. F. J. Costa, M. J. Kappers, and C. J. Humphreys, "Critical thickness calculations for InGaN/GaN," *J. Cryst. Growth*, vol. 303, no. 1 SPEC. ISS., pp. 314–317, 2007.

[15]   C.-C. Kao, H. . Huang, J. . Tsai, C. . Yu, C. . Lin, H. . Kuo, and S. . Wang, "Study of dry etching for GaN and InGaN-based laser structure using inductively coupled plasma reactive ion etching," *Mater. Sci. Eng. B*, vol. 107, no. 3, pp. 283–288, Mar. 2004.

[16]   Z. Zhu, "OPTICAL AND STRUCTURAL CHARACTERIZATION OF InGaN/GaN MULTIPLE QUANTUM WELL STRUCTURES IRRADIATED BY HIGH ENERGY HEAVY IONS," *Master's Thesis*, 2008.

[17]   Y. C. Lin, S. J. Chang, Y. K. Su, T. Y. Tsai, C. S. Chang, S. C. Shei, C. W. Kuo, and S. C. Chen, "InGaN/GaN light emitting diodes with Ni/Au, Ni/ITO and ITO p-type contacts,"

Solid. State. Electron., vol. 47, no. 5, pp. 849–853, May 2003.

[18] C. J. Youn, T. S. Jeong, M. S. Han, J. W. Yang, and K. Y. Lim, "Optical Degradation of InGaN / GaN Multi Quantum Well LED Structures Induced by the Mg-Doped p-GaN Activation Temperature," vol. 41, no. 5, pp. 778–782, 2002.

[19] S. J. Leem, Y. C. Shin, E. H. Kim, C. M. Kim, B. G. Lee, W. H. Lee, and T. G. Kim, "High-breakdown-voltage InGaN / GaN MQW LED Achieved by Using a Varied-barrier-growth-temperature Method," vol. 55, no. 3, pp. 1219–1222, 2009.

[20] O. Soltanovich and E. Yakimov, "Capacitance-voltage and admittance investigations of InGaN/GaN MQW LEDs: frequency dependence," *Phys. Status Solidi*, vol. 10, no. 3, pp. 338–341, Mar. 2013.

[21] Y. Chiou, Y. Su, S. Chang, J. Gong, Y. Lin, S. Liu, and C. Chang, "High Detectivity InGaN – GaN Multiquantum Well," vol. 39, no. 5, pp. 681–685, 2003.

[22] M. a Moram and M. E. Vickers, "X-ray diffraction of III-nitrides," *Reports Prog. Phys.*, vol. 72, no. 3, p. 036502, Mar. 2009.

[23] B. D. Cullity and S. R. Stock, "Elements of X-ray diffraction, 3rd edition," *Prentice Hall*, p. Chapter 1, 2001.

[24] O. Ambacher and J. Majewski, "Pyroelectric properties of Al (In) GaN/GaN hetero-and quantum well structures," *J. Physics-Condensed Matter*, vol. 14, pp. 3399–3434, 2002.

[25] X. H. Zheng, H. Chen, Z. B. Yan, Y. J. Han, H. B. Yu, D. S. Li, Q. Huang, and J. M. Zhou, "Determination of twist angle of in-plane mosaic spread of GaN films by high-resolution X-ray diffraction," *J. Cryst. Growth*, vol. 255, no. 1–2, pp. 63–67, Jul. 2003.

[26] V. Gold, *Compendium of Chemical Terminology*. 1997.

[27] A. Stolz, E. Cho, E. Dogheche, Y. Androussi, D. Troadec, D. Pavlidis, and D. Decoster, "Optical waveguide loss minimized into gallium nitride based structures grown by metal organic vapor phase epitaxy," *Appl. Phys. Lett.*, vol. 98, no. 16, p. 161903, 2011.

[28] B. Alshehri, S.-M. Lee, J.-H. Kang, S.-H. Gong, S.-W. Ryu, Y.-H. Cho, and E. Dogheche,

"Optical waveguiding properties into porous gallium nitride structures investigated by prism coupling technique," *Appl. Phys. Lett.*, vol. 105, no. 5, p. 051906, Aug. 2014.

[29] J.-H. Lee, B. Lee, J.-H. Kang, J. K. Lee, and S.-W. Ryu, "Optical characterization of nanoporous GaN by spectroscopic ellipsometry," *Thin Solid Films*, vol. 525, pp. 84–87, Dec. 2012.

[30] J. Elsner, R. Jones, P. K. Sitch, V. D. Porezag, M. Elstner, T. Frauenheim, M. I. Heggie, S. Oberg, and P. R. Briddon, "Theory of Threading Edge and Screw Dislocations in GaN," *Phys. Rev. Lett.*, vol. 79, no. 19, pp. 3672–3675, 1997.

[31] S. Keller, B. P. Keller, D. Kapolnek, A. C. Abare, H. Masui, L. A. Coldren, U. K. Mishra, and S. P. Den Baars, "Growth and characterization of bulk InGaN films and quantum wells," *Appl. Phys. Lett.*, vol. 68, no. 22, pp. 3147–3149, 1996.

[32] T. L. Song, "Strain relaxation due to V-pit formation in InxGa1-xN/GaN epilayers grown on sapphire," *J. Appl. Phys.*, vol. 98, no. Copyright 2005, IEE, pp. 84901–84906, 2005.

[33] J. Bai, T. Wang, Y. Izumi, and S. Sakai, "Study of dislocations in InGaN/GaN multiple-quantum-well structure grown on (1 1 2?? 0) sapphire substrate," *J. Cryst. Growth*, vol. 223, no. 1–2, pp. 61–68, 2001.

[34] J. Wu, W. Walukiewicz, K. M. Yu, J. W. Ager, E. E. Haller, H. Lu, and W. J. Schaff, "Small band gap bowing in In 1−x Ga x N alloys," *Appl. Phys. Lett.*, vol. 80, no. 25, p. 4741, 2002.

[35] F. K. Yam and Z. Hassan, "InGaN: An overview of the growth kinetics, physical properties and emission mechanisms," *Superlattices and Microstructures*, vol. 43, no. 1. pp. 1–23, 2008.

[36] W. Shan, W. Walukiewicz, E. E. Haller, B. D. Little, J. J. Song, M. D. McCluskey, N. M. Johnson, Z. C. Feng, M. Schurman, and R. A. Stall, "Optical properties of InxGa1-xN alloys grown by metalorganic chemical vapor deposition," *J. Appl. Phys.*, vol. 84, pp. 4452–4458, 1998.

[37] J. F. Muth, J. H. Lee, I. K. Shmagin, R. M. Kolbas, H. C. Casey, B. P. Keller, U. K.

Mishra, and S. P. DenBaars, "Absorption coefficient, energy gap, exciton binding energy, and recombination lifetime of GaN obtained from transmission measurements," *Appl. Phys. Lett.*, vol. 71, no. 18, p. 2572, 1997.

[38] H. Morkoç, *Handbook of Nitride Semiconductors and Devices Vol. 1: Materials Properties, Physics and Growth*, vol. 1. 2009.

[39] J. J. Song, W. Shan, T. Schmidt, X. H. Yang, A. Fischer, S. J. Hwang, B. Taheri, B. Goldenberg, R. Horning, A. Salvador, W. Kim, O. Aktas, A. Botchkarev, and H. Morkoc, "Optical studies of epitaxial GaN based materials," *Phys. Simul. Optoelectron. Devices Iv*, vol. 2693, pp. 86–96, 1996.

[40] Novagan, "XRD measurement issued from data sheet," 2015.

[41] H. K. Cho, J. Y. Lee, C. S. Kim, G. M. Yang, N. Sharma, and C. Humphreys, "Microstructural characterization of InGaN/GaN multiple quantum wells with high indium composition," *J. Cryst. Growth*, vol. 231, no. 4, pp. 466–473, 2001.

[42] Novagan, "Transmission measurement issued from data sheet," 2015.

[43] S. Reitzenstein, C. Hofmann, A. Gorbunov, M. Strauß, S. H. Kwon, C. Schneider, A. Löffler, S. Höfling, M. Kamp, and A. Forchel, "AIAs/GaAs micropillar cavities with quality factors exceeding 150.000," *Appl. Phys. Lett.*, vol. 90, no. 25, 2007.

[44] R. Shankar, R. Leijssen, I. Bulu, and M. Lončar, "Mid-infrared photonic crystal cavities in silicon.," *Opt. Express*, vol. 19, no. 6, pp. 5579–86, 2011.

[45] L. Zhang, J. Teng, S. J. Chua, and E. a. Fitzgerald, "Design and fabrication of subwavelength nanogratings based light-emitting diodes," *Appl. Phys. A*, vol. 103, no. 3, pp. 827–830, Feb. 2011.

[46] O. V. Bilousov, H. Geaney, J. J. Carvajal, V. Z. Zubialevich, P. J. Parbrook, a. Giguère, D. Drouin, F. Díaz, M. Aguiló, and C. O'Dwyer, "Fabrication of p-type porous GaN on silicon and epitaxial GaN," *Appl. Phys. Lett.*, vol. 103, no. 11, p. 112103, 2013.

[47] C. B. Soh, C. B. Tay, R. J. N. Tan, a P. Vajpeyi, I. P. Seetoh, K. K. Ansah-Antwi, and S.

J. Chua, "Nanopore morphology in porous GaN template and its effect on the LEDs emission," *J. Phys. D. Appl. Phys.*, vol. 46, no. 36, p. 365102, Sep. 2013.

[48] S.-H. Gong, A. Stolz, G.-H. Myeong, E. Dogheche, A. Gokarna, S.-W. Ryu, D. Decoster, and Y.-H. Cho, "Effect of varying pore size of AAO films on refractive index and birefringence measured by prism coupling technique.," *Opt. Lett.*, vol. 36, no. 21, pp. 4272–4, 2011.

Chapter III.   Fabrication and characterization of PIN photodiodes

III.1.   Introduction

Having performed structural and optical characterization of the provided samples, we proceed to the photodiode fabrication with the objective to realize a micro-photodetector. The investigation of material quality has provided a significant information regarding the performance of the expected device. It has showed the influence of the indium content in the InGaN absorbent layer in terms of wavelength cut-off and density of defects. Here, the device fabrication process has been subjected to several stages. Device fabrications have been performed in the clean room of IEMN. Safety training and employment of different equipment have been carried out with the help of permanent technicians and engineers. Fabrication process including chemical treatment, photolithography, etching and metal deposition have been performed in the III-V platform of the clean room. Samples concerned in the fabrication phase are SL10-1, MQ10-1, SL10-3, MQ10-3, SL20, MQ20, SL30, and MQ30. These samples represent PIN structures with different indium content (10%, 20% and 30%) using different configuration of InGaN absorbent layer (SL and MQW) and different growth type (MBE and MOCVD). The sample SL50 representing the 50% of indium content will not be processed due to the absence of P-GaN layer related to technical issue of MOCVD during sample growth.

The GaN material is known to be challenging in the fabrication process. It requests more precaution and preventive measures comparing to other materials. Achieving lower resistance of p-ohmic contact is the mutual difficulty in the GaN community. It is due to the complication in growing heavily doped P-GaN and the absence of contact metals having a work function larger than P-GaN [1]. These two factors lead to high specific contact resistance of P-GaN inhibiting the achievement of high performance of devices. To date, a considerable effort has been performed to achieve lower ohmic contact to P-GaN by using various contact metals [2] [3]. Annealing effect on the ohmic contact in different gas atmospheres has been studied [4][5][6]. The annealing investigation has demonstrated the improvement of electrical properties due to the formation of high hole concentrations caused by removal of hydrogen atoms which bonded with Mg atoms [7].

The GaN surface contaminations have a great amount of attention. It is known very sensitive to the chemisorption of oxygen and other atomic impurities [8]. Native oxide layer is

frequently formed on the top surface resulting the contamination of the P-GaN layer. Interfacial insulating oxide with a thickness of 1–2 nm has a strong impact on the electrical response of the device due to high resistive contact [9]. Consequently, to achieve sufficiently low-resistance ohmic contacts it is imperative to perform a surface treatment before such fabrication process. In the literature, various surface treatments have been employed to remove the oxide layers [10][11][12]. In our fabrication process, the development of surface treatment will be detailed hereafter.

During our technological process, optical microscopy, SEM and profilometer instrument have been used in each stage of photodiode fabrication in order to monitor the fabrication stages. These instruments permit to validate the photolithography quality and confirm the profile of etched layers.

During the conception phase of the expected photodiode, many designs have been discussed in order to achieve a high quality micro-photodiode regarding the fabricated ones in the literature. The fabrication of micro-photodiode is still a challenge for the GaN/InGaN material. The majority of reported studied of GaN/InGaN photodiodes have concerned the broad-area photodiodes developed for solid-state lighting (SSL) [13] or photovoltaic applications [14]. Photodiode typical emission areas are typically in the range of $300{\times}300$ µm^2 up to 1 mm^2. While the fabrication of micro-photodiodes with emission areas below $50{\times}50$ µm^2 has insufficiently studied on InGaN/GaN materials. Recently, investigation on size-dependent capacitance in InGaN-based µ-LED has been reported [15]. Capacitance characteristics of µ-LEDs have been evaluated in relation of the change of device size which affect its performance in many aspects. A µ-LED array has been reported for Visible-Light Communications (VLC) [16]. It reveals higher modulation bandwidths comparing to the broad-area LED due their capability to be driven at higher current densities using µ-LED of 50 µm diameter [17].

Our study should be aimed to fabricate µ-photodiodes ranging from $5{\times}5$ µm^2 to $100{\times}100$ µm^2 as well as broad-area photodiodes ranging from $100{\times}100$ µm^2 to $1000{\times}1000$ µm^2. The fabrication of large scale photodiodes allows to validate the material quality as well as the exploration of the photodiode response in large scale. It permits also to optimize the fabrication process such as photolithography, etching, metal deposition and passivation. Thereafter, the

fabrication of micro-photodiodes will be investigated in order to evaluate the photodiode size effect on the photodiode capacitance which affect the photodiode speed, in other word the increase of frequency. To achieve this objective, it is important to inspect every step in the design and fabrication process. Four major factors considered here to fabricate a micro-photodiode. The first is the isolation of the photodiode through mesa etching. The second is the extension of p and n-type contacts outside photodiode. The third is the planarization of different contacts levels. The last is the passivation of the whole photodiode.

The isolation of the photodiode as first factor is achieved via mesa etching. It is a very essential step permitting the deposition of contact pads outside the mesa on an undoped material or on a sapphire substrate. This process will avoid capacitance effect due to metal insulator semiconductors structure. Mesa etching will be processed in several steps using numerous types of etching masks. Photoresist, metal and SiO^2 are the types of masks to be studied. The etching depth will be also investigated in a number of phases: low, medium and high etching depth. For that, the etching process using inductively coupled plasma (ICP) will be studied above all. The extension of p and n-type contacts outside photodiode as second studied factor will permit to enlarge metal pads in order to provide sufficient area for the use of probes during electrical characterization. The third factor which is the planarization, permits to have the same level of contacts with the aim of connecting a spiral antenna to p and n –type pads. The last factor is the passivation, it ensures long-term stability of the photodiode junction and improve the device reliability. It will also limit surface phenomena inducing parasitic currents.

The choice of metal types for p and n contacts will be studied using transmission line measurement permitting to determine the contact resistance between the metal and the N-GaN/P-GaN layers. The annealing of the proposed metal types will be also investigated using different temperatures in different atmospheres. Electrical characterization will be performed using KEITHLEY instrument in clean room facility at IEMN.

In this chapter, techniques of electrical characterizations will be detailed. The study of inductively coupled plasma (ICP) for mesa etching using different masks will be investigated. Several designs for the fabrication of photodiodes will be detailed. Each design has the objective to evaluate the PIN structure for a specific dimension. Large scale photodiodes will be fabricated

using design 1. Fabrication of micro-photodiode with dimensions ranging from 5×5 µm² to 100×100 µm² will be discussed. Design 2 will be related to the fabrication of planar micro-photodiodes. Vertical micro-photodiodes will be performed using design 2. As soon as the fabricated photodiodes are optimized, we will proceed to the characterization phase. Photocurrent, responsivity and external quantum efficiency will be measured using photonic set-up. Besides, Capacitance-voltage measurement C-V will be extracted. To obtain the cut-off frequency of the fabricated photodiodes, a set-up of noise measurement has been installed and will be detailed.

III.2.   Electrical characterizations techniques

III.2.1. External Quantum Efficiency measurements

In order to investigate the photodiode response, the external quantum efficiency (EQE) represents a significant element to describe the relation among the number of incident photons and the number of collected electrons by the photodiode at specific energy. It allows the comparison of different photodiodes with different indium content and different dimension of p-active layers. EQE is based on the responsivity of the photodetector at given energy of absorbed photon as shown in the Equation 1.1 mentioned in chapter 1. The responsivity (A/W) illustrates the ratio between the photocurrent of the photodiode and the incident power of the light source (Equation 1.2). In photonics Lab at KAUST, the setup of EQE measurement has been used for our experiment. The setup consists of Newport Arc lamp source of 1000 W Hg (Xe), Monochromator, Newport power supply, Newport power-meter, optical setup and Keithley signal generator connected to Labview software in order to exploit results as shown in Figure 3.1. The intensity of the monochromatic incident light has been adjusted in each wavelength using Thorlabs Absorption ND Filter Kit in order to obtain a fixed output power. Wavelength are subjected to sweep from 360 nm to 500 nm to permit the evaluation of the photodiode response at different photon energy.
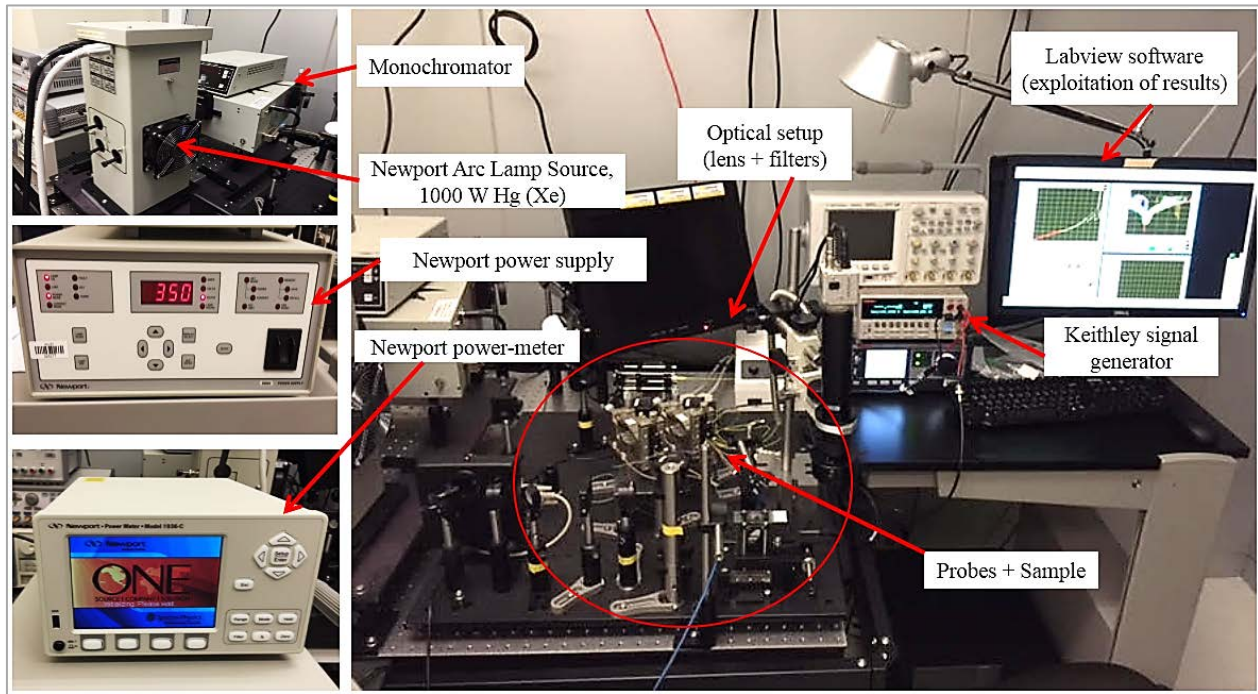
Figure 3.68: Setup of EQE measurement using monochromatic incident light.

III.2.2. Photocurrent measurement using laser source

The measurement of photocurrent is essential to evaluate the photodiode performance. In the IEMN, an optical setup has been optimized to perform this type of measurement with laser source of 405 nm. Figure 3.2 (a) reveals the optical setup consisting of superzoom HD camera, fiber-coupled laser source, stripped and cleaved optical fiber, screen display and probes connected to Keithley signal generator with Labview software in order to exploit results. Figure 3.2 (b) demonstrates the stripped and cleaved optical fiber installed with precaution on the metal support toward the experimented photodiode.   Figure 3.2 (c) exhibits the output power measurement at the end of optical fiber of the fiber-coupled laser source using photodiode power sensor. The sensor has to cover the laser diode wavelength and maximal power of laser. The photodiode sensor is ranging from 400 - 1100 nm with power measurement from 500 nW to 500 mW.
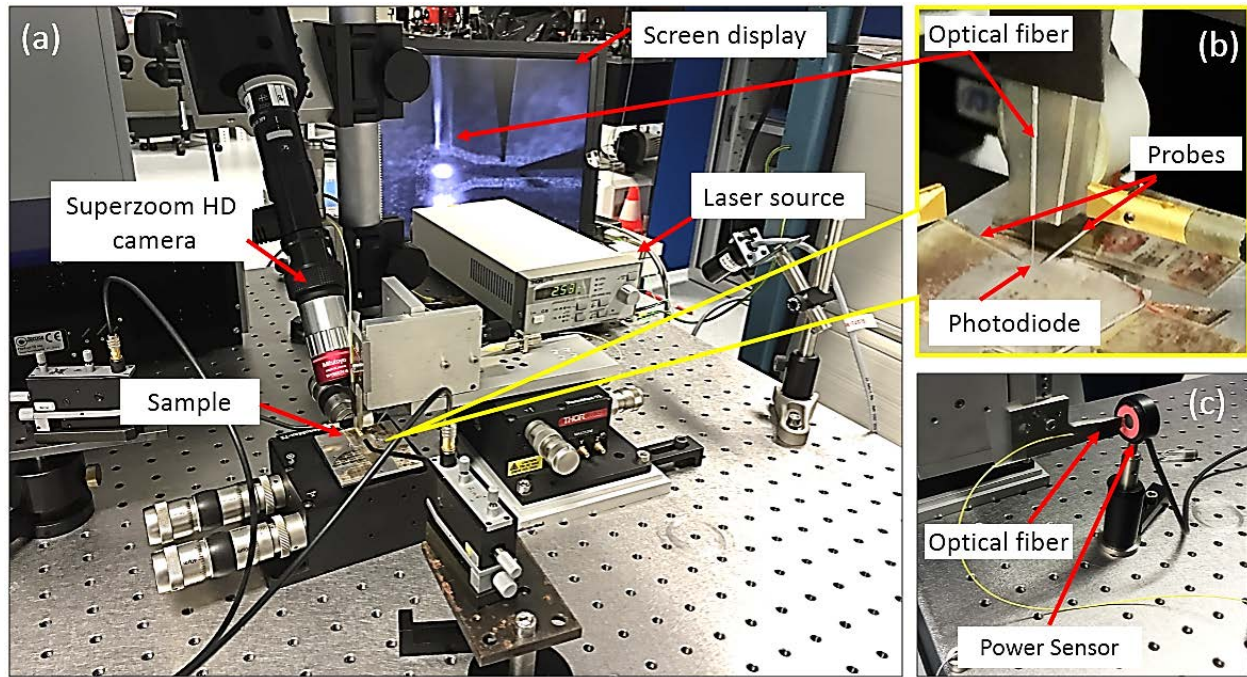
Figure 3.69: Setup of photocurrent measurement using laser source as incident light.

III.3.   Set-up of noise measurement

The setup of noise measurement is performed using the setup of photocurrent measurement with laser source as incident light. It consists of Noise-Figure-Meter connected to the RF adapter which is connected to RF probes and Keithley signal generator. RF coplanar probes and laser spot are adjusted on the photodiode with the help of Superzoom HD camera, lamp and related screen display. The measurement will be performed under reverse bias in two conditions: in the dark and under illumination by laser source. The setup of noise measurement is illustrated in Figure 3.3.
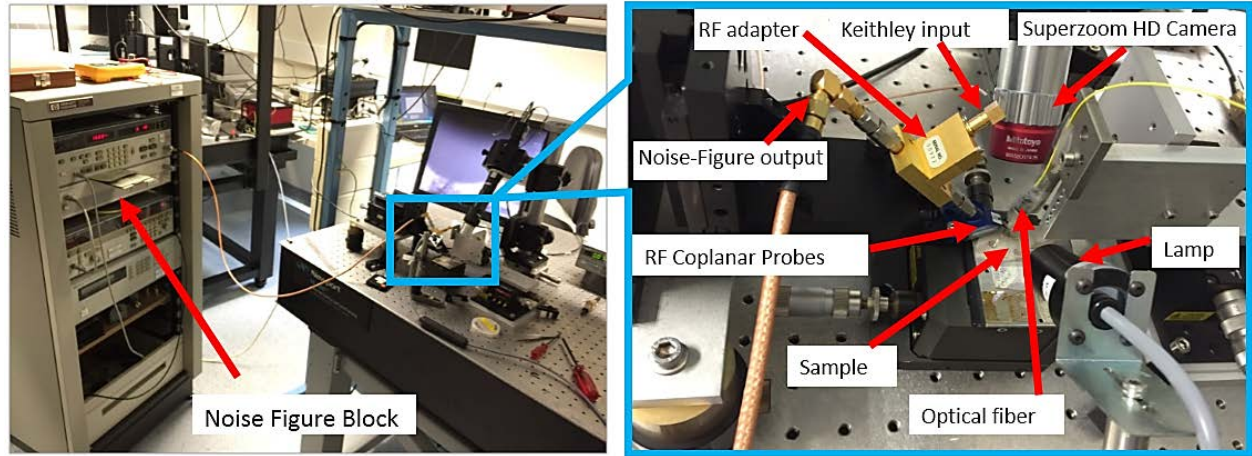
Figure 3.70: Setup of noise measurement using Noise-Figure-Meter.

III.4.   Study of GaN deep etching

The fabrication quality of GaN-based photodiode depends on several factors. One of the important factors is the dry etching process. Generally, the etching process is optimized with the respect of essential criteria as improved etch rate, minimal surface roughening, enhanced reproducibility and a high degree of anisotropy. These properties are achieved using inductively coupled plasma (ICP). This technique exhibits to have a fast etching rate using many parameters affecting the etching quality as flow rate of etching gas, RF power, chamber pressure, and used mask. Cl_2/Ar based plasmas are frequently used for ICP reactor. Sidewall quality and surface morphology of such etched structure are critical for the fabrication of vertical devices with high ratio aspect. Few studies concerning the deep GaN etching have been reported [18][19]. Actually, for photovoltaic and LED applications, photodiodes are fabricated with low etching depth (> 1µm) [20][21].

In our study, GaN based structures are deposited on sapphire substrate. Deep etching process will be performed in order to define independent mesa. Different configurations of etching masks has been defined. Photoresist (AZ9260), metal (Ni) and silicon dioxide (SiO_2) will be used as etching masks. The objective is to assess surface morphology, mesa edges and the etching sidewall quality. Several dimensions of etched mesas ranging from 5×5 to 150×150 µm²

will be evaluated as function of etching profile. The effect of different mask on the etched mesa will be discussed for depth varying from hundreds of nanometers up to 6 µm.

Photolithography for photoresist etching mask has been performed using AZ9260 of 4 µm thick on GaN/sapphire (sample A) by means of optical mask with different mesa dimensions. Besides, photolithography has been prepared for deposition of SiO_2 and Ni etching masks for samples B&C respectively. 300 nm of Ni and SiO_2 have been deposited by RF sputtering technique on GaN/sapphire and then patterned by lift-off. Oxford plasmalab 100plus system in the clean room of IEMN has been used to achieve ICP dry etch. Etching conditions were adjusted to 10 SCCM (standard cubic centimeters per minute) of Cl_2 flow rate, 30 SCCM of Ar, 10 mTorr (millitorr) of total pressure. RF power was held constant at 40 W as well as ICP power fixed to 100 W. The low ICP power has the objective to avoid degradation of the etching masks and improve etching selectivity. Measured etching depth has been obtained using profilometer instrument and surface morphology was examined using SEM.

For sample A, the photoresist used as etching mask has exhibited poor persistence to the ICP etching process. The maximum optimized depth has been obtained at 500 nm. Figure 3.4 (a) demonstrates that the quality of the etched mesa was acceptable for larger dimensions (from 50×50 to 200×200 µm^2). Concerning smaller mesas smaller than 40×40 µm^2, the etching process has been limited in terms of quality and shape showing defective areas in the mesa edges as illustrated in Figure 3.4 (b). Less than 10×10 µm^2 of mesa dimension hasn't been realized.
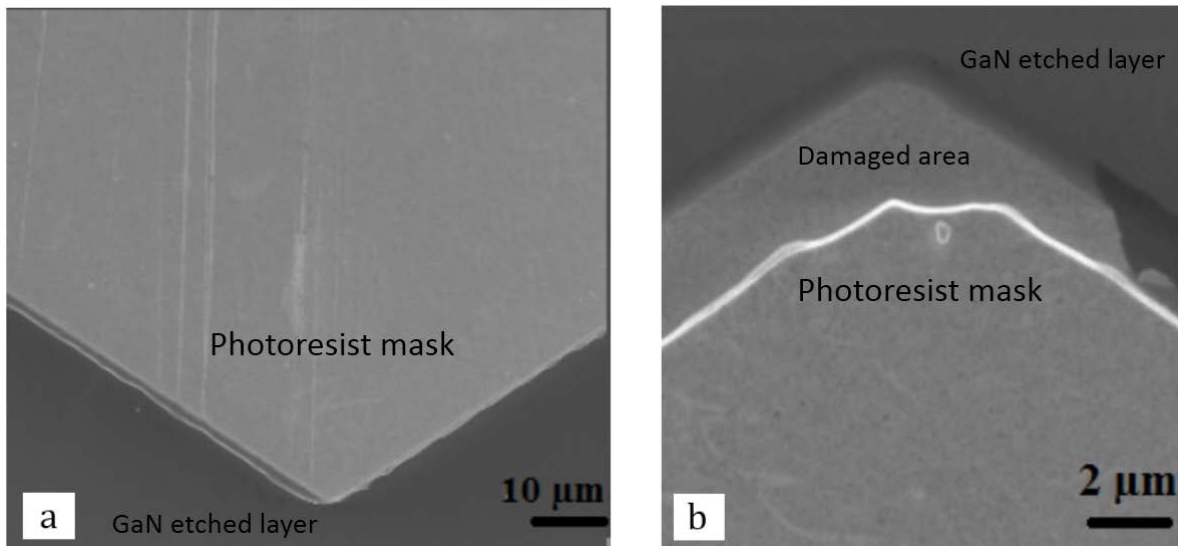
Figure 3.71: Image issued from SEM using photoresist etching mask for 500 nm of etching depth, (a) mesa with dimension of $100 \times 100 \mu m^2$ and (b) mesa with dimension of $20 \times 20 \mu m^2$.

Concerning the SiO_2 mask etch, sample B has been divided in two small samples in order to be etched in two phases. The first sample B1 will be in the range of 1 µm in order to inspect the endurance and the toughness of the SiO_2 mask. For the second sample B2, we try to increase the etching depth up to 4 µm. We arranged the ICP etching recipe in order to obtain 1µm approximately for sample B1. After a quick check by optical microscope, we noted that the SiO_2 etching mask was slightly damaged but still in acceptable condition. After removing the SiO_2 etching mask by wet etching process, we visualized the effect of ICP etching on the mesa using SEM. As shown in Figure 3.5, the quality of etching mesa was satisfactory for larger mesa as well as for smaller mesa dimensions. The etching profile was measured by profilometer indicating 1.34 µm.
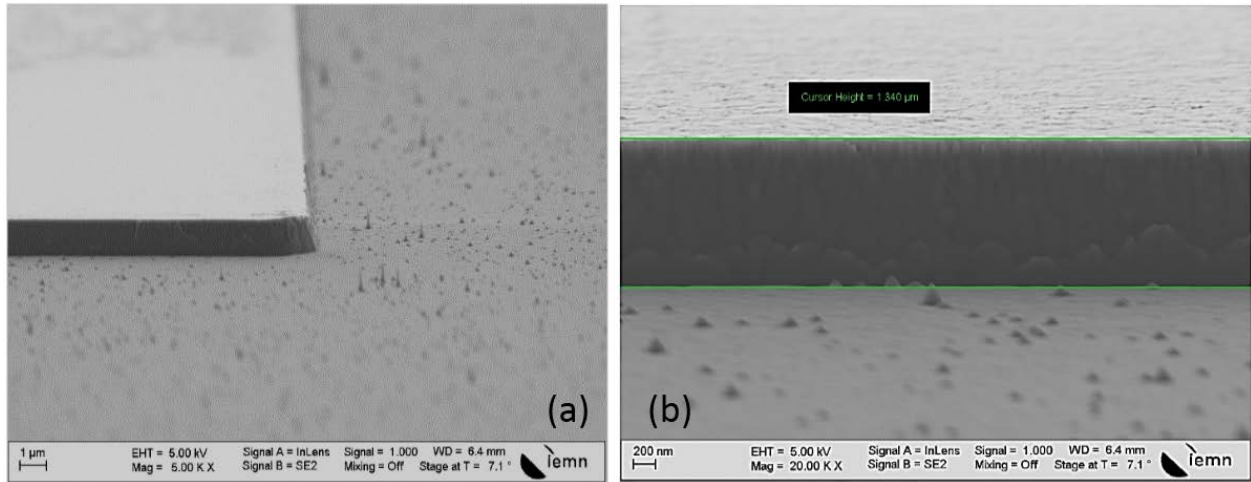
Figure 3.72: Image issued from SEM for mesa etching using silicon dioxide mask for sample B1 (a) general view of etching corner area, (b) cross-section of etching profile by SEM with etching depth of 1.34 µm.

Secondly, we applied a deep etching profile in order to analyze the maximal endurance and the toughness of the SiO_2 mask. We arranged the ICP etching recipe in order to obtain 4 µm approximately for sample B2. After a quick check by optical microscope, we noted that the SiO_2 etching mask was almost damaged. After removing the SiO_2 etching mask by wet etching procedure, we visualized the effect of ICP etching process on the mesas using SEM. As shown in

Figure 3.6 (a), the quality of etching mesa was satisfactory for mesa larger than $20{\times}20$ µm^2 but limited quality for mesa below this dimension. We observed minor surface damage on the GaN top layer for certain mesa due to extended and aggressive ICP attack which reduces the mask surface. The etching profile was measured to 4.2 µm as illustrated in Figure 3.6 (c). Damaged areas are observed in the border to mesa indicating the limitation of SiO$_2$ etching mask. Mesas smaller than $20{\times}20$ µm^2 are often damaged and inexploitable as shown in Figure 3.6 (b). The formation of columnar defects also have been appeared using SiO$_2$ cover-plate in this range of etching profile. Colomnar defects are generaly due to micro-masking effect [22][23]. They are originated from sputtering of hard mask materials which deposit particules on the etched surface and creat a local micro-mask.
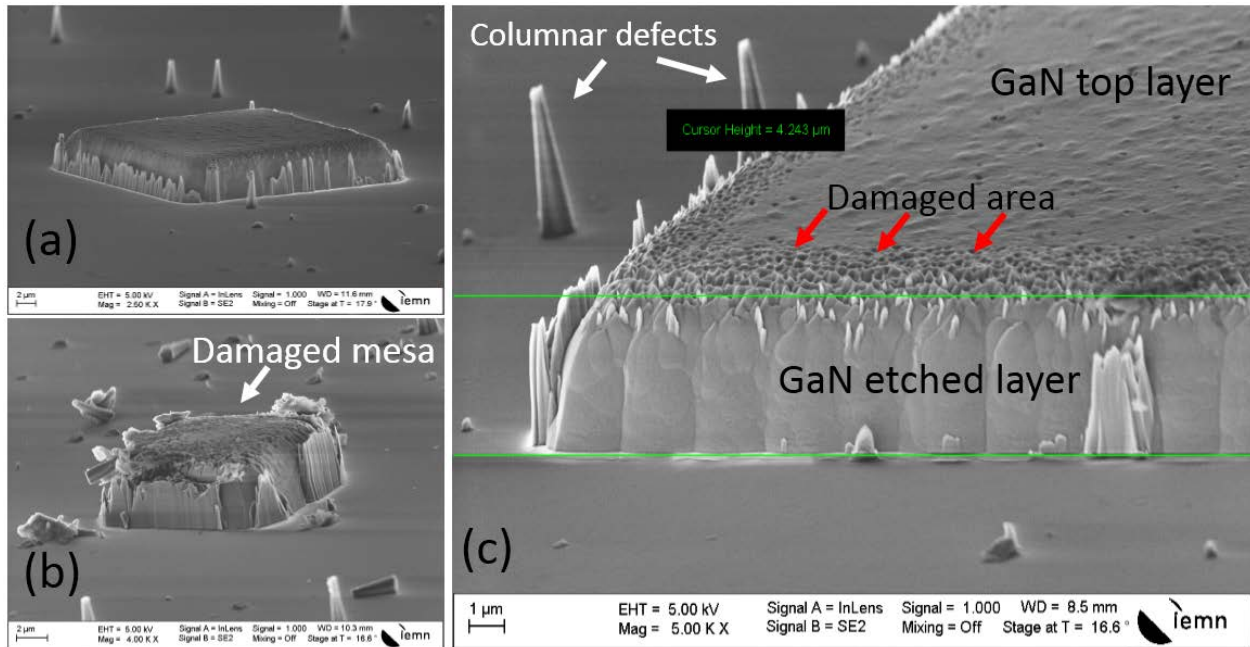
Figure 3.73: Image issued from SEM for (a) $20{\times}20$ µm^2 mesa etched using silicon dioxide mask, (b) damaged $5{\times}5$ µm^2 mesa showing a poorness quality of etching process and (c) cross-section of etching profile with etching depth of 4.3 µm.

SiO$_2$ etching mask reveals improved mesa etching for mesas larger than $20{\times}20$ µm^2 with etching profile not exceeding 4 µm. It represents a limitation for mesa lower than these dimensions leading to damaged structure and defective surface due to removal of cover-plate mask by hard ICP attack. Higher thickness of SiO$_2$ etching mask could be proposed (larger than

500 nm), however optical photolithography of such micro-mesa (lower 10×10 μm^2) will be subjected to lift-off difficulty.

The third configuration consists of metal etching mask (Ni) performd on the sample C. Respecting the same conditions than the previous experiments, the etching qualite seems to be better than other cover-plate materials. For a first check of sample C, the quality of the etching process is significant for the large mesas and moreover for the smaller ones. The etching profile obtained using Ni mask is smooth in comparison with the SiO_2 and photoresist masks. The first measurement of etching profile gives 3 µm. Deep etch of sample C has been carried out as a second phase in order to see the limitation of Ni mask. ICP power has been increased from 100 to 500 W and mesa with 6 µm thickness were etched (until sapphire substrate). Etching rate has been recorded with higher ICP power and reaches 200 nm/min. Figure 3.7 (a) shows the GaN etched layer down to sapphire substrate with respect to etching angular shape. Metal mask seems to be tough against high ICP attack and reduced erosion of mask edges are observed as illustrated in Figure 3.7 (b). Less columnar defects and high-selectivity are observed in the metal case demonstrating improved and enhanced cover-plate mask. This is due to a reduced amount of micro-masking particles generated from cover-plate mask.
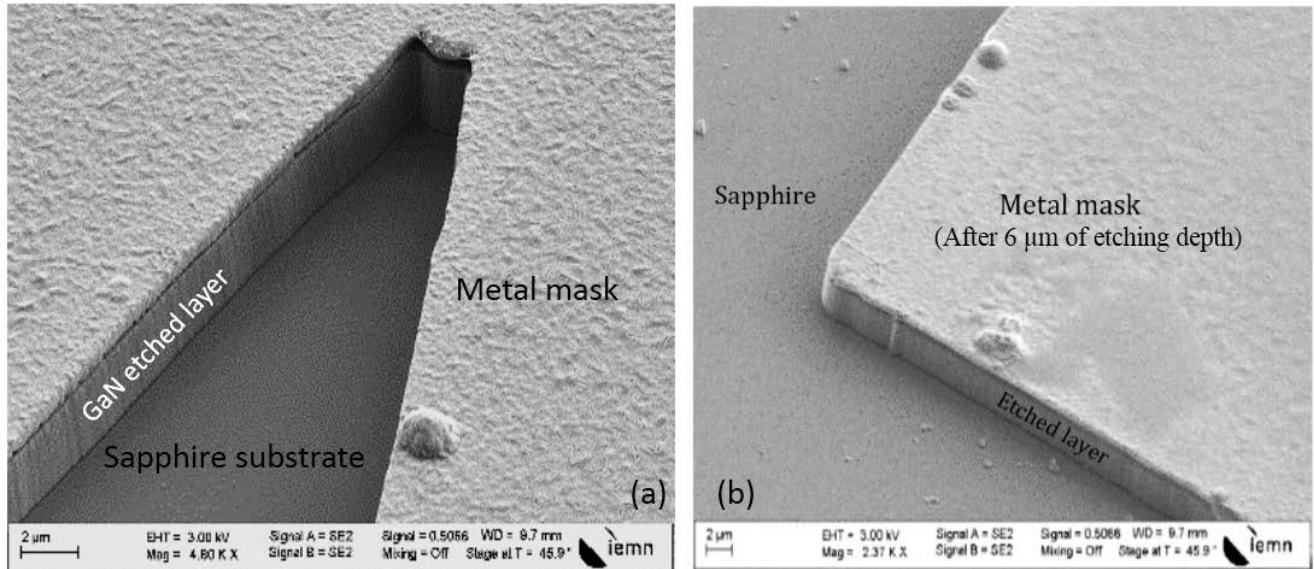

Figure 3.74: SEM images for etching angular shape using metal mask (a) general view of improved cover-plate mask with mesa etched to sapphire substrate (b)

The Ni masks has permitted to study the ICP power parameter demonstrating a key element in the etching rate. The different values used in this experiment have led to extract different etching conditions. Increasing the ICP power leads to increase chemical component of the etch flow within identical conditions. Figure 3.8 shows the significant influence on the etch rate and the DC bias when increasing the ICP power.
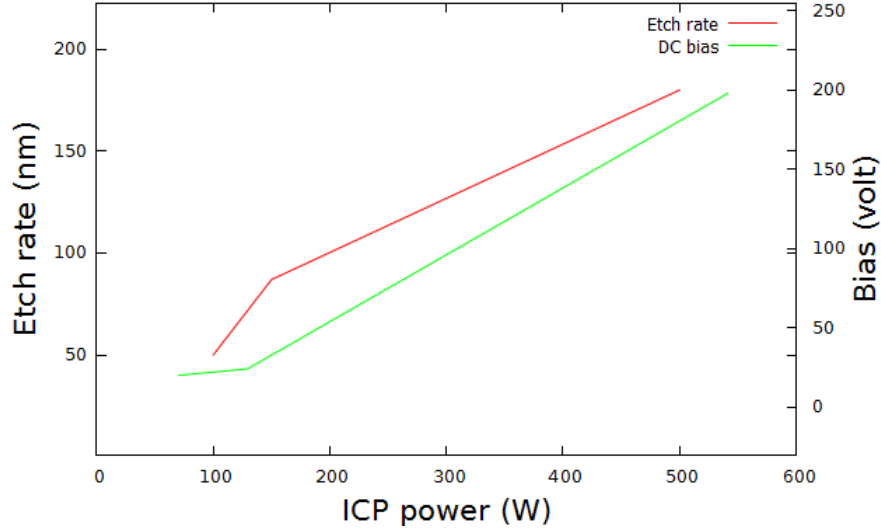

Figure 3.75: Etch rate of GaN and the corresponding DC bias as a function of ICP power.

The conclusion of the etching process indicates that the Ni mask reveals an improved mask for the deep etch process comparing to SiO_2 and photoresist masks in the case of micro-mesa etching. The type of etching mask will certainly play an important role in the device performance due to PIN junction and possible contamination of sidewall during etching process. That is why we will proceed to PIN etching process using SiO_2 for planar photodiode fabrication (low etching depth) and Ni mask for vertical photodiode fabrication (high etching depth). Subsequently, the evaluation of electrical response in each case will divulge the effect of each type of cover-plate mask. Regarding the photoresist mask, it doesn't agree with our requirements due to poor persistence to the ICP etching process.
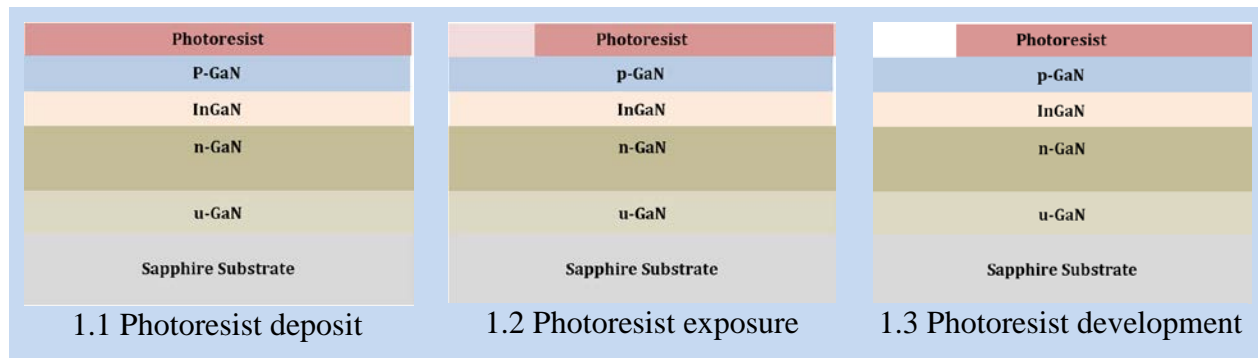
III.5. Fabrication of large-scale photodiode: Design 1

In this section, the fabrication of large-scale photodiode will be discussed. This phase permit to validate the material quality as well as the evaluation of the InGaN/GaN photodiode response in static and dynamic at large scale. It is considered as preliminary work before proceeding to micro-device fabrication. It allows also to optimize the fabrication process in different stages as photolithography, etching process and metal depositions. Four phases are planned to perform the large-scale photodiode fabrication: 1) p-contact deposition, 2) etching process to reach N-GaN layer, 3) n-contact deposition and 4) annealing. This sequence permit to deposit the p-contact as first step in order to avoid surface contaminations during sample maneuvering. It will improve the p-contact quality and consequently the device response. However, the annealing of p-contact at low temperature is not possible due to high temperature annealing of n-contact metals in last step. The resolution of annealing issue is to consider an intermediate temperature annealing for both contacts. Photodiodes haven't been passivated due to lack of optical mask. Etching process will be performed in order to obtain planar mesa. Photoresist will be employed as cover-plate mask in the etching phase due to large-scale mesas. In the fabrication process, we will proceed different samples with different indium compositions (10%, 20% and 30% of indium content) in different configuration (SL and MQW) of InGaN absorbent layer. This allows to evaluate the device performances in same conditions. Samples SL10-1, SL20, SL30, MQ10-1, MQ20 and MQ30 will be proceeded in the fabrication phase. Metals have been optimized to be palladium/gold (Pd/Au) of thicknesses (35/120 nm) for p-contact type and titanium/aluminum/nickel/gold (Ti/Al/Au) of thickness (10/30/300 nm) for n-contact with metal sequence from bottom to top layer. The p-contact metal combination has been chosen according to reported studies demonstrating the high work function of Pd metal associated with his high reactivity with low contact resistance [3]. Concerning the choice of n-contact metals, several combinations have been reported in the literature [24][25]. A first combination is tested to be Ti/Al/Au for the large-scale photodiode. Other combinations will be deeply studied in the next micro-device fabrication. Several forms of photodiodes are proposed here, photovoltaic design with comb structure, and circle design. Photovoltaic structure permit to improve the photodetection using comb design on the surface of p-active layer. Electrical characterization of this design enables efficiently the extraction of photocurrent so accordingly the responsivity as well as the external quantum efficiency (EQE). The circle structure with different diameters

permit to evaluate the photodiode in dynamic characterization using capacitance-voltage measurement. This will provide information about the change of capacity as function of metal surfaces. In this work, the fabrication of first photodiodes has been carried out in Laboratoire de Photonique et de Nanostructures (LPN) with the help of Dr. Sofiane Belahsene who provided immensely valuable assistance.

III.5.1. Comb and circle structures: fabrication process

GaN and relative alloys are known to be challenging in the fabrication process due to the difficulty to achieve low resistance of ohmic contact. Surface treatment of samples will be performed in order to eliminate chemisorption of oxygen and other atomic impurities which form a native oxide layer. Samples are subjected to smooth cleaning using O_2 Plasma for 20 min at 170°C of substrate temperature. A cleaning sequence using trichloroethylene, acetone, isopropanol and deionized water are achieved for four minutes in ultra-sonic bath at 40°C for each solution before drying. An intensive cleaning has been considered using Aqua Regia (HNO_3: HCl = 1:3) solution at 160°C for 10 min. This type of surface treatment has been demonstrated to remove GaO_x formed on p-type GaN [12]. Eliminating these impurities will decrease the barrier height for the transport of holes ensuring the good ohmic contacts. Boiling the Aqua Regia solution will improve the p-type contact and decrease the resistivity [26]. After performing surface treatment, optical microscopy has been used to check the surface state. The flowchart of the fabrication process has been discussed to optimize different phases as shown in Figure 3.9.
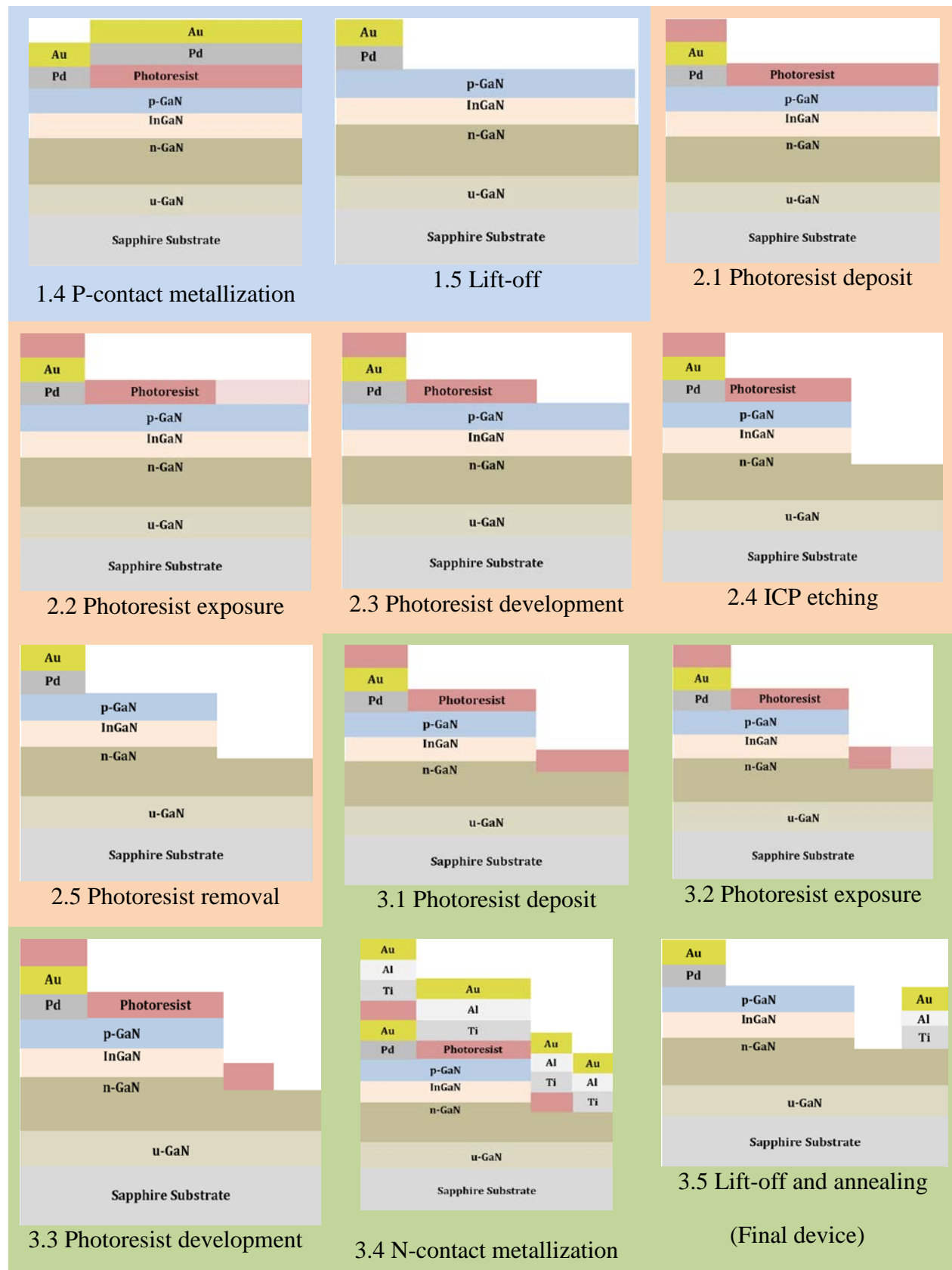

1.1 Photoresist deposit   1.2 Photoresist exposure   1.3 Photoresist development

1.4 P-contact metallization

1.5 Lift-off

2.1 Photoresist deposit

2.2 Photoresist exposure

2.3 Photoresist development

2.4 ICP etching

2.5 Photoresist removal

3.1 Photoresist deposit

3.2 Photoresist exposure

3.3 Photoresist development

3.4 N-contact metallization

3.5 Lift-off and annealing

(Final device)

Figure 3.76: Flowchart of fabrication process for large-scale photodiode using design 1.

The flowchart represents the p-contact metallization (Pd/Au) as first step through the deposition, exposure and development of photoresist then metallization in E-beam Evaporation reactor before metal left-off (bleu zones). Figure 3.10 (a) and (b) represent the pattern aperture before and after the deposition of p-contact. In second step, mesa etching has been performed using ICP reactor through optical photolithography as explained in the flowchart (orange zone). The etching depth was measured about 350 nm permitting to reach the N-GaN layer.). Figure 3.10 (c) shows the photoresist deposition protecting the p-active layer for etching process in order to reach the N-GaN layer. Afterward, the deposition of n-contact metallization (Ti/Al/Au) has been performed respecting the flowchart in green zone. In order to remove GaN cap layer and native oxide on the ohmic contact area due to sample maneuvering, it has been taken into account a surface preparation after photolithography and just before metal deposition of n and p-contacts. Surface cleaning in HCI: Di water (1: 1) for 30 seconds has been implemented. Besides, smooth Argon plasma etching at 250 eV for 30 seconds is achieved inside the E-beam Evaporation reactor just before metal deposition.). Figure 3.10 (d) illustrates the patterns for the expected n-contacts before metallization. Annealing is carried out using rapid thermal annealing (RTA). A study of several annealing parameters are cited hereafter.
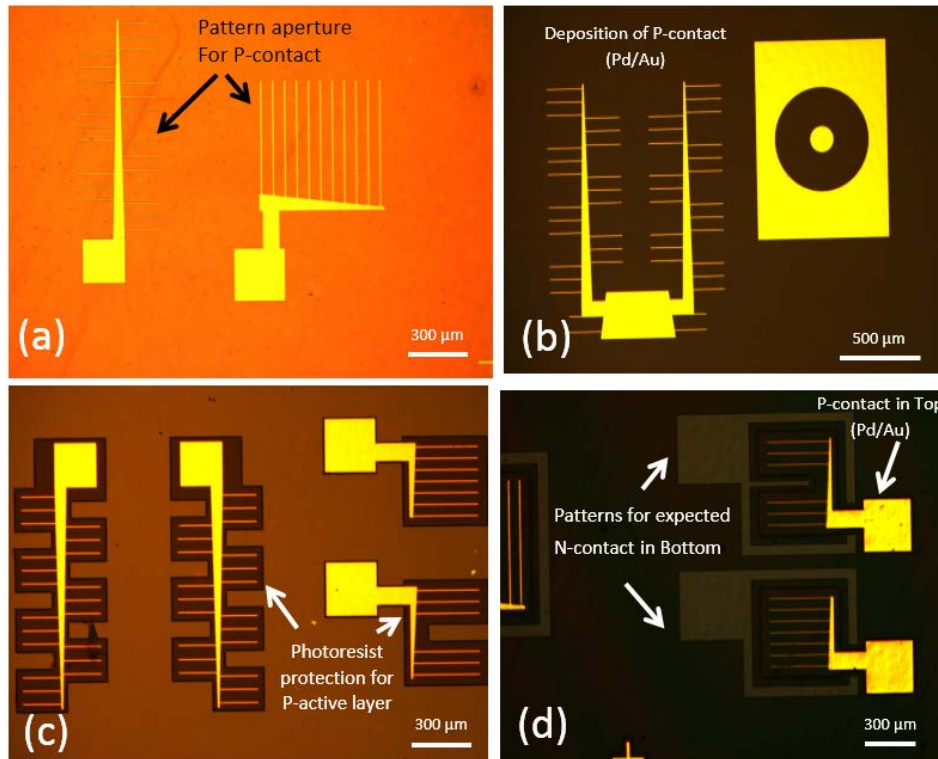
Figure 3.77: Images issued from optical microscopy during fabrication process showing pattern aperture before (a) and after (b) p-contact deposition, photoresist deposition protecting the p-active layer (c) and patterns for the expected n-contacts before metallization (d).

III.5.2. Study of annealing effect

The final devices are in different design as explained previously. Photovoltaic design is illustrated in the Figure 3.11. In the left side of this figure, photodiodes are captured before annealing where the photodiodes in the right side are issued after contact annealing. It is shown in the annealed photodiodes that the thermal annealing strongly affect the surface morphology of n-contact combination (Ti/Al/Au) and consequential the decrease in the density of agglomerates [6].
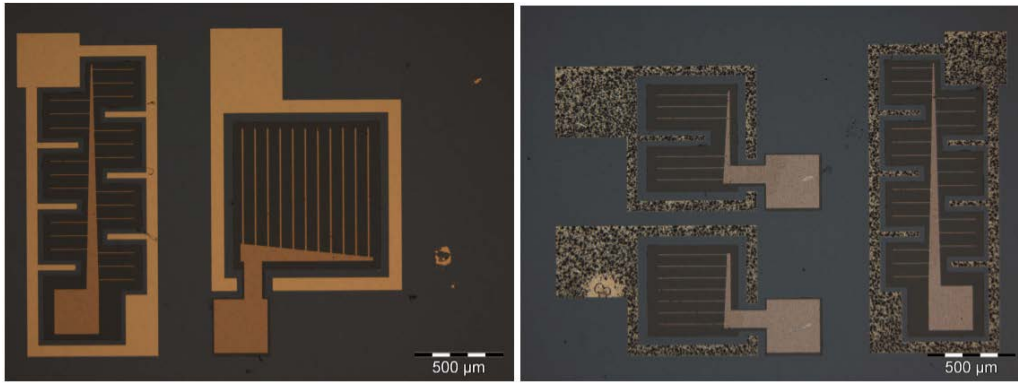
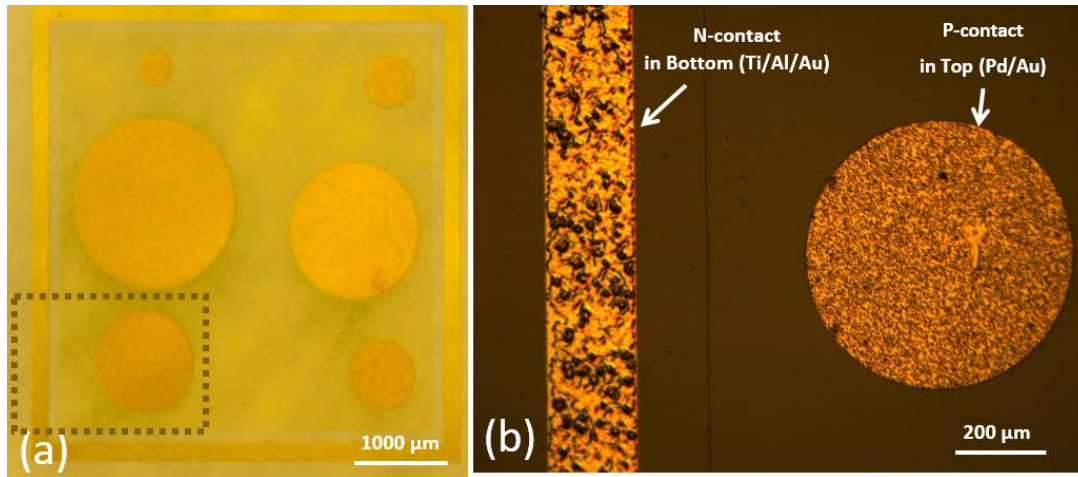*Figure 3.78: Images issued from optical microscopy for fabricated photodiodes in photovoltaic design before (left) and after annealing (right).*

The circle design has been also performed through different size as illustrated in Figure 3.12. Different diameters of p-contact in top layer will permit to evaluate the photodiode in dynamic characterization using capacitance-voltage measurement. Images in Figure 3.12 are issued using optical microscopy before annealing in the left side and after annealing in right side with affected surface morphology of bottom n-contact.

Figure 3.79: Images issued from optical microscopy for fabricated photodiodes in circle design before annealing (left) and zoomed area after annealing (right).

One sample in PIN structure has been dedicated to the study of annealing temperatures using RTA. It has been divided in four small samples. Three intermediate annealing temperatures have been proposed and compared to room temperature (sample 1): 500°C for 3 minutes under air atmosphere (sample 2), 700°C for 2 minutes under N_2 atmosphere (sample 3) and 500°C for 2

minutes under N_2 atmosphere (sample 4). Figure 3.13 demonstrates the electrical response of three different photodiodes annealed to different atmosphere, time and temperatures performed for the same photodiode cell. We conclude that the optimal configuration for the photodiode annealing in intermediate temperature for both n and p-contacts is 500°C for 2 minutes under N_2 atmosphere. It represents a lower turn-on voltage which is attributed to the reduction of the gallium oxide layer related to the N_2 atmosphere effect [3]. This leads to the reduction of the specific contact resistance in the metal/semiconductor interface improving the I-V performance [27]. It has been considered the lower serial resistance for the sample 4 comparing to others samples. It represents 36 Ω versus 42, 54 and 45 Ω for samples 3, 2 and 1 respectively. Deep study of annealing parameters is crucial to enhance the device response. Different parameters are subjected to be altered in order to obtain the optimal configuration. This will be one of the perspective studies succeeding this work.
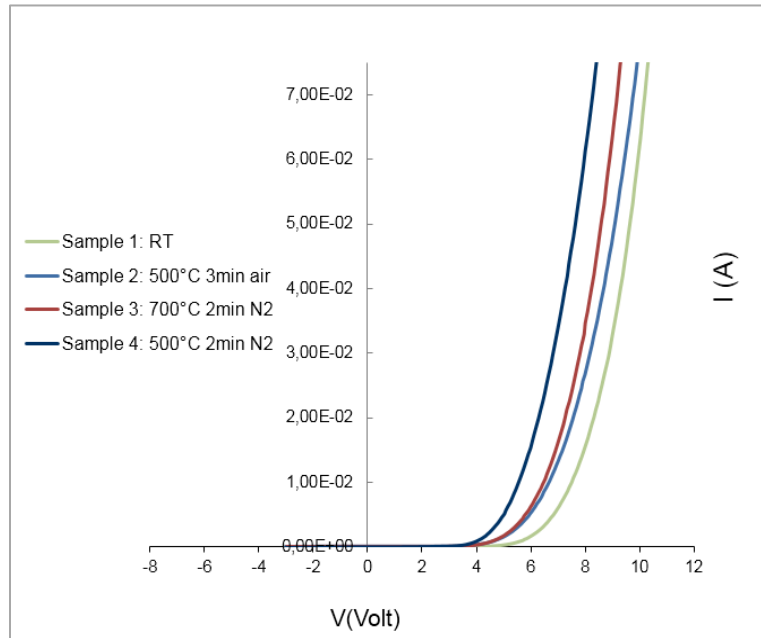
Figure 3.80: Study of annealing temperatures for different atmospheres, time and temperatures compared to room temperature sample (RT).

III.5.3. Current-voltage characterizations

Once the fabrication process are performed for different samples in three different indium compositions, current-voltage measurement have been performed using KEITHLEY instrument. Figure 3.14 (right) illustrates the electrical response of samples MQ10-1, MQ20 and MQ30 for MQW configuration fabricated in the same conditions. Sample MQ10-1 demonstrates a good response comparing to MQ20 and MQ30 due to its turn-on voltage located at 3.3V. This value is close to the bandgap value of absorbent layer at 10% of InGaN material revealing the reduction of the spreading resistance and the increase in the conductivity [28]. The serial resistance is low as 11 Ω for the sample MQ10-1. Where the sample MQ20 and MQ30 represents a shift in the turn-on voltage (4 and 5 V respectively) which theoretically should be lower than sample MQ10 in the ideal case. These values are similar to those reported in the literature [29][30]. The increase of turn-on voltage could be partially associated to the increase of serial resistance [31]. They are calculated 22 Ω for sample MQ20 and 30 Ω for sample MQ30. This voltage shift in the material may possibly be as a result of barrier degradation related to low quality of material for 20% and 30% of InGaN material. It has been confirmed by structural characterizations in the chapter 2 that the increase of indium composition leads to lower structural quality which is associated to higher density of dislocation. Consequently, leakage currents are frequently observed and directly proportional to the increase of indium content. Figure 3.14 (left) demonstrates the increase of leakage current of the MQ30 (about -1 µA at -2 V) leading to shift of turn-on voltage where the sample MQ10 has a very low leakage current. Sample MQ20 represents an intermediate case between the high quality of sample MQ10-1 and the low quality of sample MQ30. It represents -50 nA in leakage current at -2V comparing to -3 nA for MQ10-1.
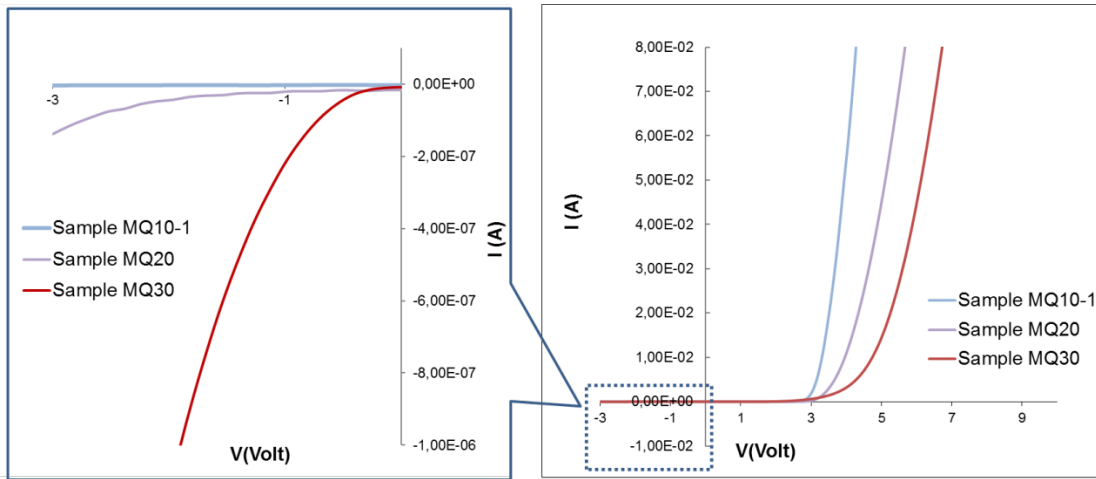
Figure 3.81: Comparison of Current-Voltage measurements for different indium composition 10%, 20% and 30% (right) and leakage current in reverse voltage zone (left).

A comparison of light emission has been achieved when forward bias is applied (LED mode) for all fabricated samples. For each indium content, the color of light emission is in agreement with the optical cut-off wavelengths investigated in the optical characterization in chapter 2. Figure 3.15 illustrates the light emission for different samples during electrical characterization when forward bias is applied. Colors have been associated to their related wavelengths on the visible electromagnetic spectrum. It has been previously proven that the increase of indium content intensifies defects and accordingly increases the dislocations density. This hypothesis has been similarly confirmed by the comparison of light intensity for different samples grown with different indium content during photodiode characterizations. Sample MQ10-1 has achieved higher light intensity where the sample MQ30 has acquired the lower intensity of light emission. MQ20 has an intermediate intensity due to the intermediate quality of material between samples MQ10 and MQ30.
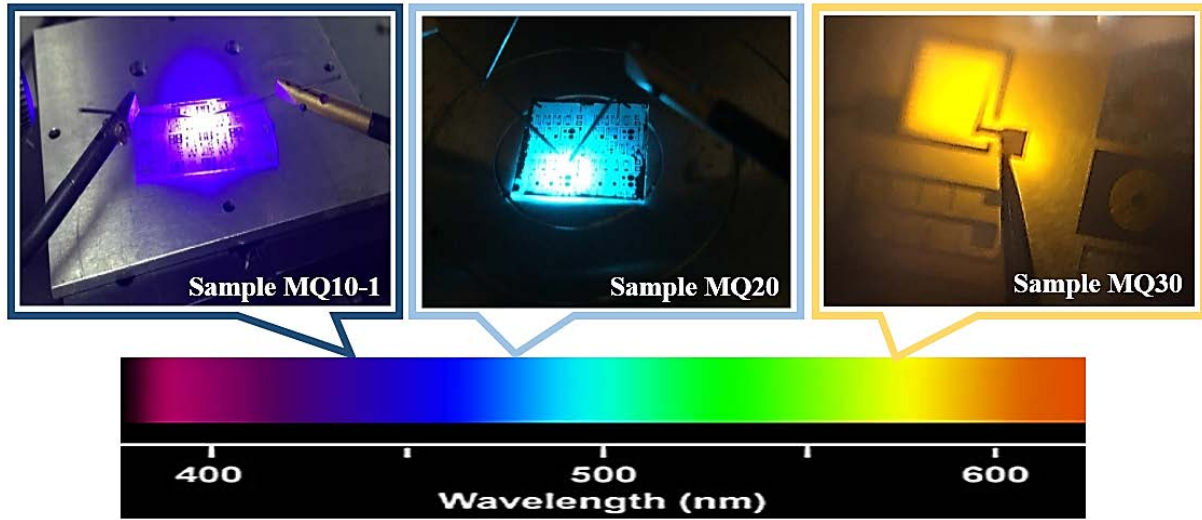
Figure 3.82: Light emission when forward bias is applied for samples MQ10-1, MQ20 and MQ30 and their related wavelength cut-off on visible electromagnetic spectrum.

III.5.4. Influence of the MQW configuration on the device performance

The MQW effect on the device performance has been observed comparing the SL configuration. Figure 3.16 illustrates the electrical response for the same cell in both InGaN configurations for samples SL10-1 and MQ10-1. Lower serial resistance is observed for the sample MQ10-1 related to I-V slope proving the enhanced quality of material crystallography. It is related to the lower density of defects already reported in the structural characterization in chapter 2. Besides, samples grown using MQW configuration have demonstrated high intensity of light emission comparing to samples grown by SL configurations as a result of improved material quality as shown in the inset of Figure 3.16.
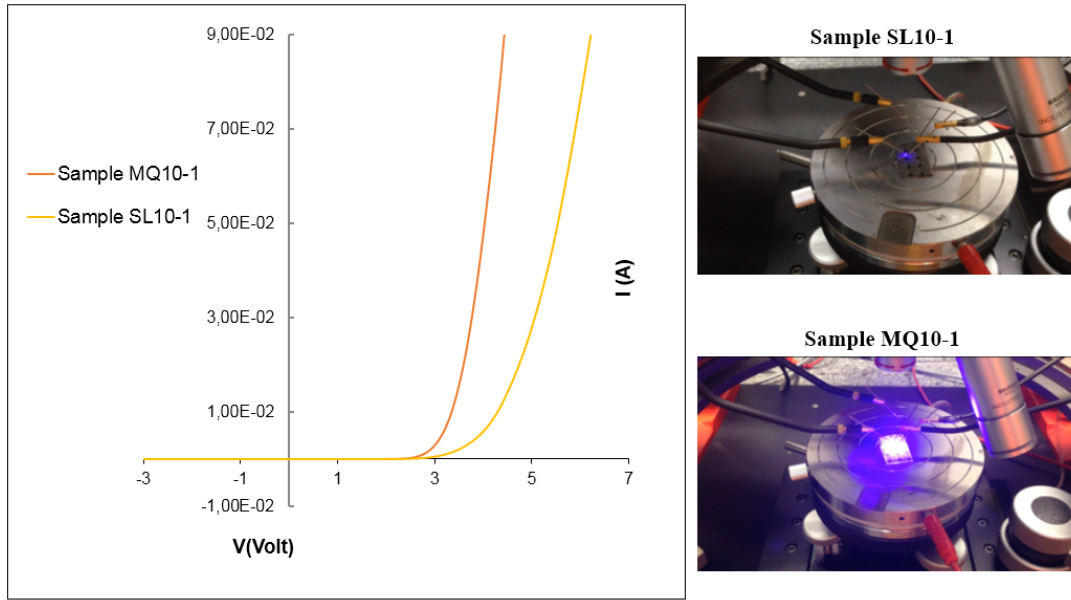
Figure 3.83: InGaN MQW versus InGaN SL configuration for samples SL10-1 and MQ10-1.

III.5.5. Influence of the growth technique on the device performance

The influence of the growth technique on the device performance has been electrically studied. Static response for fabricated photodiodes of samples MQ10-1 and MQ10-3 grown respectively by MOCVD and MBE techniques are illustrated in Figure 3.17. It is noted that both samples are fabricated in the same conditions. MOCVD sample demonstrates good electrical response with an average serial resistance of 20 Ω and a leakage current of –45 nA for applied reverse voltage of -5V. MBE sample represents higher serial resistance of 35 Ω and five times more leakage current of –250 nA observed in the same voltage value. This is perhaps due to the high density of threading dislocations related to the MBE growth comparing to MOCVD technique for the fabricated samples. Defects are probably indicated by the high leakage current values.
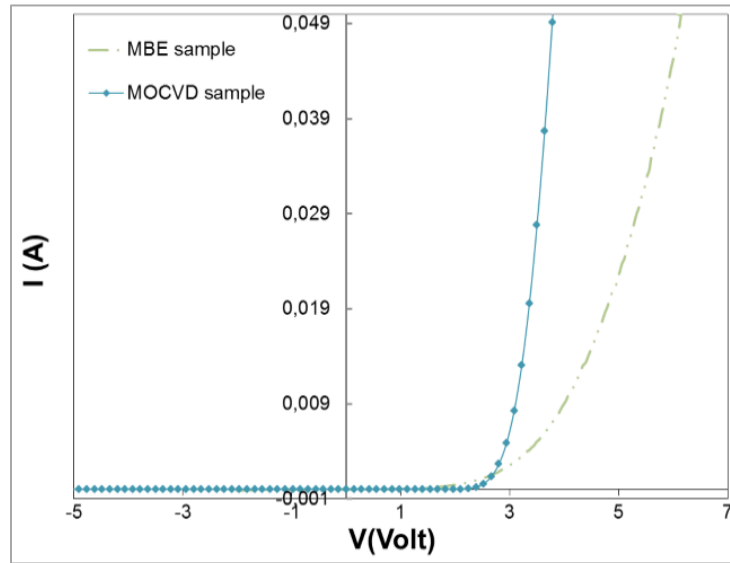
Figure 3.84: Growth technique effect on the photodiode response for samples MQ10-1 and MQ10-3 grown by MOCVD and MBE techniques respectively.

III.5.6. External Quantum Efficiency measurements

In order to calculate the EQE, the measurement of photocurrents related to the photodiode response have been carried out for samples SL10-1, MQ10-1, SL30 and MQ30. The optical setup of Figure 3.1 has been used to perform this measurement by means of monochromatic incident light. The first objective of the EQE measurement is to detect the absorbed wavelength providing the higher photocurrent. This will facilitate the identification of the excitation laser wavelength which will be used thereafter. The second objective is certainly the photodiode responsivity so the EQE value. Figure 3.18 demonstrates photocurrents under excitation of incident light at different wavelengths for samples SL10-1 and MQ10-1. The experimented photodiode is a large-scale of $300{\times}300$ µm^2 for both samples. The I-V characteristics have been performed in log scale to reveal photocurrents in absolute value comparing to dark current. The wavelength of 370 nm has exhibited the higher photocurrent value of 4 µA subtracted from the dark current at 0 V for sample MQ10-1 (right side in Figure 3.18). This leads to expect a higher EQE at this wavelength. Slightly lower photocurrents are shown for wavelengths in the range of 380 to 420 nm which represents the near-band edge transition for the InGaN absorbent layer. Higher wavelengths than 420 nm of light excitation is providing very low photocurrent response. Concerning the sample

147

SL10-1 (left side in Figure 3.18), the photocurrent values are slightly lower than values related to samples MQ10-1, and it represents a maximal photocurrent of 1 µA at the wavelength 370 nm for 0 V. The lower value of photocurrent for sample SL10-1 has been expected comparing to sample MQ10-1. This could be due to the improved quality of material associated to the MQW configuration.
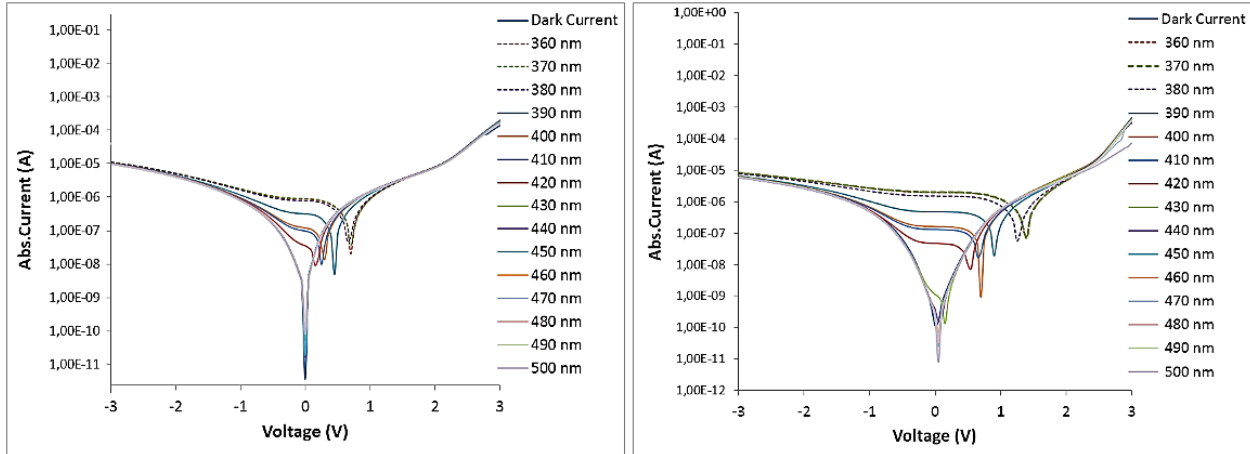

Figure 3.85: Measured photocurrents at wavelengths varying from 360 nm to 500 nm in log scale for samples SL10-1(left) and MQ10-1 (right).

Samples SL30 and MQ30 have been also characterized at the same condition than the previous samples. Very low photocurrent values are observed for both configurations as shown in Figure 3.19. It seems that the 30% of indium content of InGaN absorbent layer affects the device performance due to the high density of defects and consequently higher leakage currents already shown in Figure 3.14 (left).
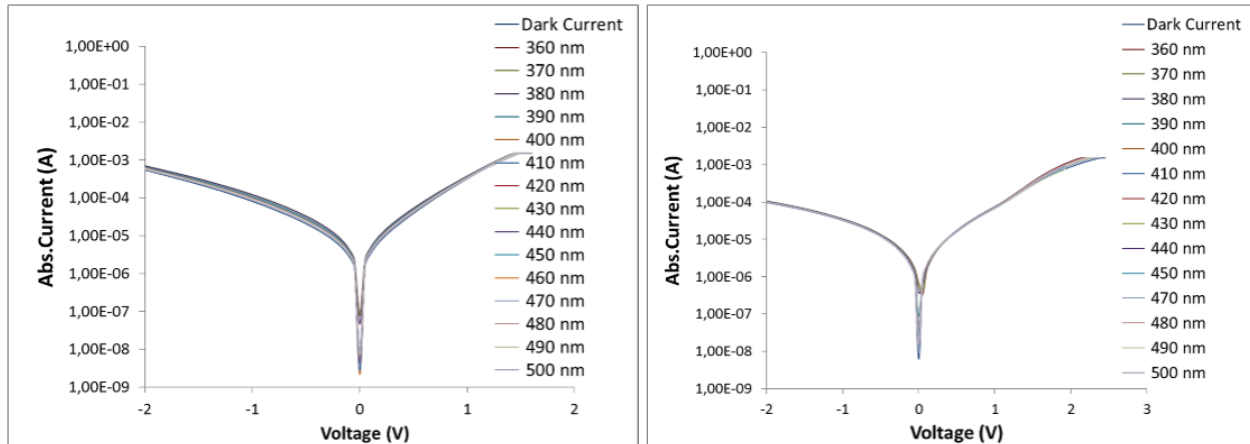
Figure 3.86: Measured photocurrents at wavelengths varying from 360 nm to 500 nm in I-V log scale for samples SL30 (left) and MQ30 (right).

Once the photocurrent values are measured, responsivity and subsequently the EQE are calculated as function of the bandgap of each wavelength according to Equation 1.1 and Equation 1.2. As shown in Figure 3.20 (left), the high efficiency is observed at 370 nm for samples SL10-1 and MQ10-1 with EQE of 22% and 32% respectively. These values are comparable to those reported in the literature demonstrating EQE to a range of 10 to 40% [21][32]. Samples SL30 and MQ30 show very low EQE as expected due to the low photocurrent values and related high leakage currents. The maximum value is obtained at 500 nm for 6 and 10% of EQE for SL30 and MQ30 respectively.
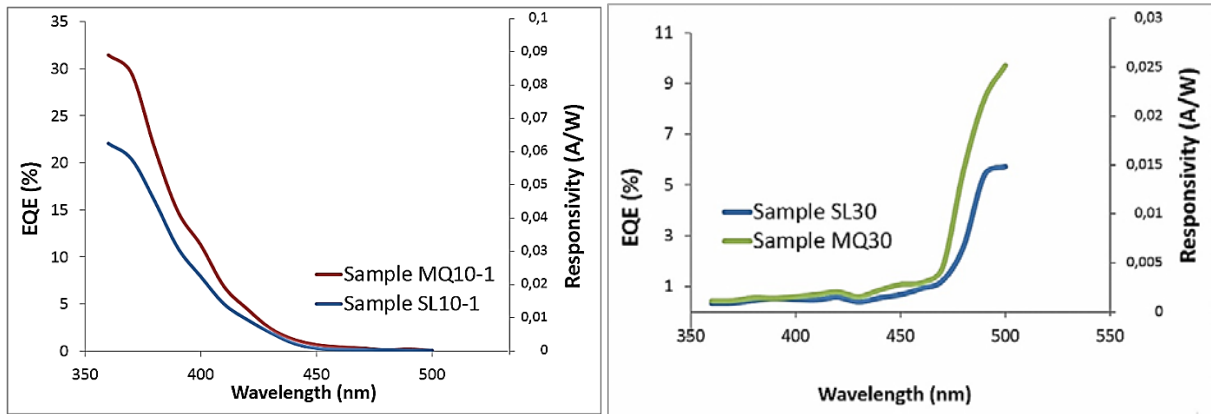

Figure 3.87: Responsivity and EQE of samples SL10-1 and MQ10-1 (left), samples SL30 and MQ30 (right).

III.5.7. Photocurrent measurement using laser source

The measurement of photocurrent is based on two important factors, the wavelength of incident light and its output power. For this, the consideration of powerful incident light has conducted the use of a laser source. Besides, fiber-coupled laser source is the optimal choice due to the facility to focalize a laser beam using stripped and cleaved optical fiber. The wavelength and the maximum provided power of laser source has been adequately discussed. As we explained in the EQE measurement, the first objective was to detect the absorbed wavelength providing the higher photocurrent. Consequently, the higher photocurrent values are related to

wavelengths varying from 360 to 420 nm as illustrated in Figure 3.18. Unfortunately, fiber-coupled laser sources with wavelengths lower than 400 nm are hardly found. The lower wavelength of fiber-coupled laser source has found in the market to be 405 nm by Thorlabs. Its output power attains 100 mW which is considered acceptable in our case.

According to the optical setup of Figure 3.2, the photocurrent measurements have been carried out for several large-scale photodiodes. The first measurement has been performed in order to investigate the laser power effect on the photocurrent values. Figure 3.21 demonstrates the variation of photocurrent values as function of output power of laser source for voltage values varying from 0 to -3 V for sample MQ10-1. The higher photocurrent value of 1.3 mA is observed at -3 V for a maximal power of laser source at 80 mW. It is obvious that the higher laser power is applied, the higher photocurrent is obtained. A non-saturation phenomena of photocurrents has been observed during this measurement. A higher reverse voltage is expected to be applied in order to investigate the photocurrent saturation for different size of photodiodes.
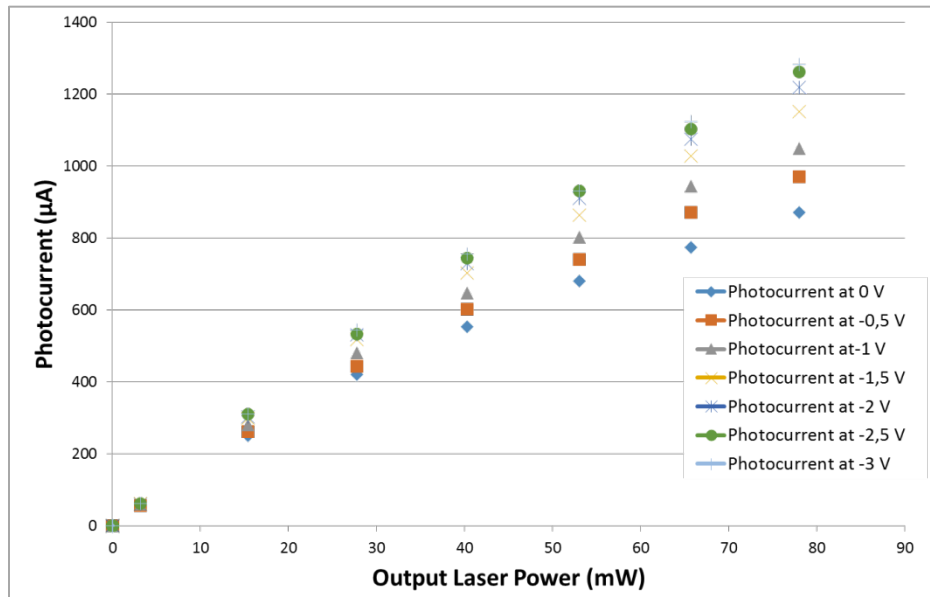

Figure 3.88: Photocurrent measurements as function of output laser power with fixed reverse voltage for sample MQ10-1.

Hereafter, samples with different indium contents will be subjected to photocurrent measurement and will be evaluated to each other in terms of photodiode response. Each measurement of photocurrent has considered dark current measurement followed by three

photocurrent measurements at different powers of incident laser with 35 mW, 50 mW and 75 mW. Figure 3.22 (left) demonstrates the dark measurement for sample MQ10-1 comparing to photocurrent measurement at different laser powers for photodiode 300×300 µm². The increase of photocurrents is observed once the laser power is increased and attains 1.2 mA at -4 V for laser power of 75 mW. The leakage current of dark measurement is considered to be 531 nA at -4 V. Sample SL10-1 exhibits abnormally higher photocurrent values than values reported for MQ10-1 as shown in Figure 3.22 (right) for photodiode 300×300 µm². The high value of photocurrent for sample SL10-1 can be explained by the fact that the high leakage currents for dark measurement (around 100 µA at first I-V curve) increases for each I-V measurement under laser excitation and consequently it is added to the photocurrent value.
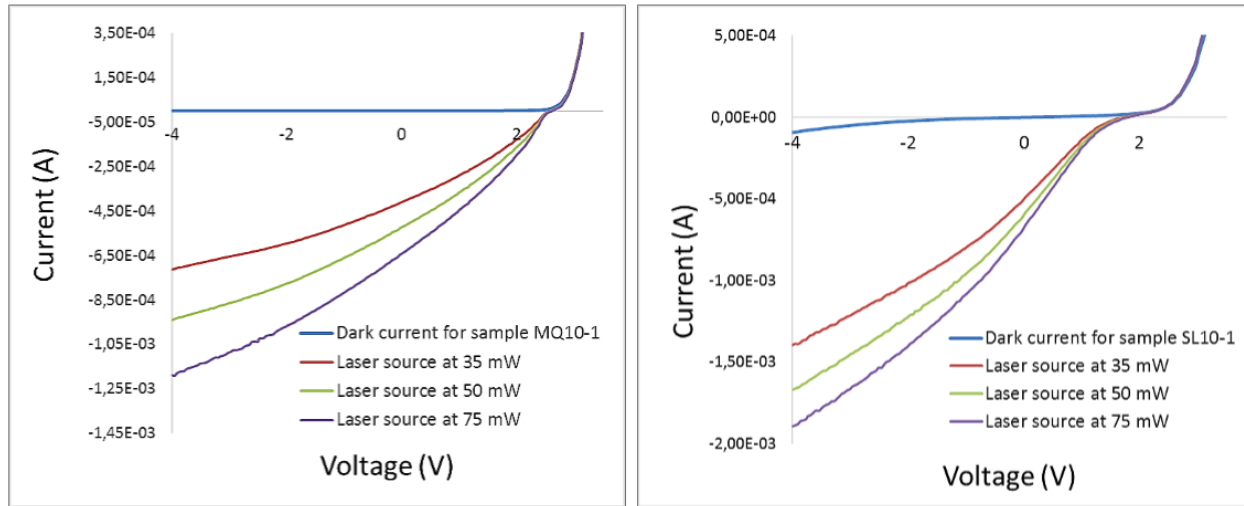

Figure 3.89: I-V characteristics for dark and photocurrent measurements at different laser power for samples MQ10-1 (left) and SL10-1 (right).

For both figures, the saturation zone of photocurrents has not been observed. For this, one photodiode 300×300 µm² of sample MQ10-1 will be exposed to high reverse voltage until breakdown voltage I order to investigate the saturation zone. Figure 3.23 (left) reveals photocurrent measurements until breakdown voltage which is observed at -20 V for the sample MQ10-1. Before the photodiode breakdown, photocurrent value has reached a maximum of 3.2 mA at laser power of 75 mW and a leakage current of dark measurement attaining 370 µA. The related EQE measurement is shown in Figure 3.23 (right) and achieves a maximum of 13 %.
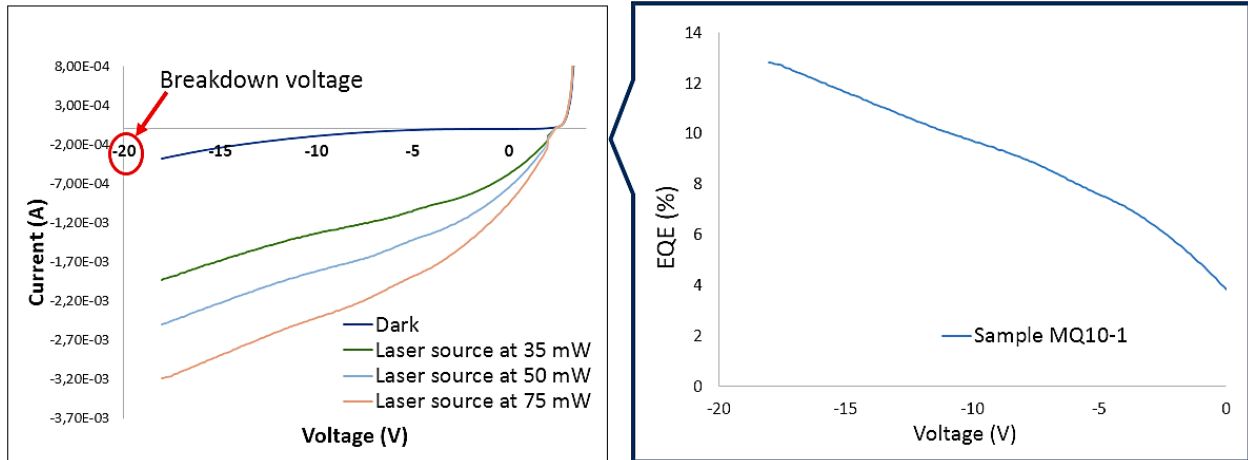
Figure 3.90: I-V characteristics for dark and photocurrent measurements at different laser power until breakdown voltage for samples MQ10-1(left) and related EQE as a function of reverse voltage.

However, the saturation of photocurrent is still not observed even when applying high reverse voltage until breakdown photodiode. In this case, the dimension of p-active layer related to photodiode area and the indium content will be subjected to change in order to study the saturation phenomena.

A photodiode of 200×200 µm^2 of sample MQ20 will be exposed to higher reverse voltage until photodiode breakdown. This photodiode reveals lower p-active area than the precedent one and expected to have lower photocurrent due to its lower improved quality comparing to MQ10-1. Figure 3.24 (left) exhibits I-V characteristic as performed previously for three different powers of laser source. A saturation zone is observed starting from -12 V until photodiode breakdown at -20 V. The related EQE measurement is shown in the right side of Figure 3.24. It reveals also the saturation zone providing 12 % of EQE. The reduced p-active area and the lower photocurrent values (comparing to sample MQ10-1) have led to earlier saturation of photocurrent. However, the investigation of such saturation zone could be associated to the carrier velocity in the GaN material and related alloys. Holes or/and electrons velocity are subjected to saturation phenomena at identical or different electrical field. In the first chapter (Figure 1.22), it has been reported the peak electron velocity of 1.9×10^7 cm/s, attained at 225 kV/cm [33][34]. We can associate this reported value to the 100 nm of our absorbent layer and conclude electron saturation velocity attained at -2.2 V. It means that the electron velocity doesn't cause the late photocurrent

saturation and consequently the saturation of holes velocity could be a probable reason. The calculation of the hole transport properies of wurtzite GaN using Monte Carlo simulator has been reported by Oguzman et al. and indicated 5×10^6 cm/s at 1000 kV/cm [35]. In our case, the saturation of photocurrent has been observed at -12 V corresponding 1200 kV/cm of electrical filed calculated with an absorbent layer of 100 nm. This value seems to be very close the simulated saturation velocity of holes reported by Oguzamn et al.

We belive that the measurement of photocurrent saturation versus reversed bias voltage could be a way to extract the holes saturation velocity versus electrical feld. A profond study of this phenomena could be significant to be developped in the future.
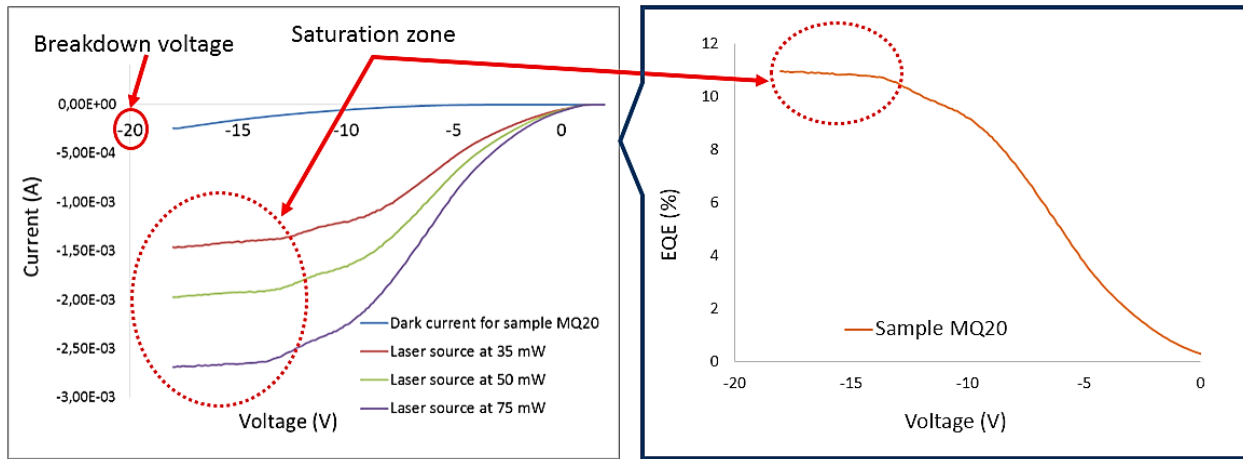

Figure 3.91: I-V characteristics for dark and photocurrent measurements at different laser power until breakdown voltage for samples MQ20 (left) and related EQE as a function of reverse voltage.

Samples with 30 % of InGaN absorbent layer have been also characterized. Figure 3.25 represents higher photocurrent values comparing to those reported previously for photodiode dimension of 300×300 µm^2. The high leakage currents are clearly observed for both samples SL30 and MQ30 reaching 3.6 mA and 350 µA respectively. It is related to the possible barrier degradation demonstrating the low quality of material. The increase of leakage currents affect the photocurrent values when excited by laser source. The high value of photocurrent for both samples can be explained by the fact that the high leakage currents for dark measurement increases for each I-V measurement and consequently it is added to the photocurrent values.
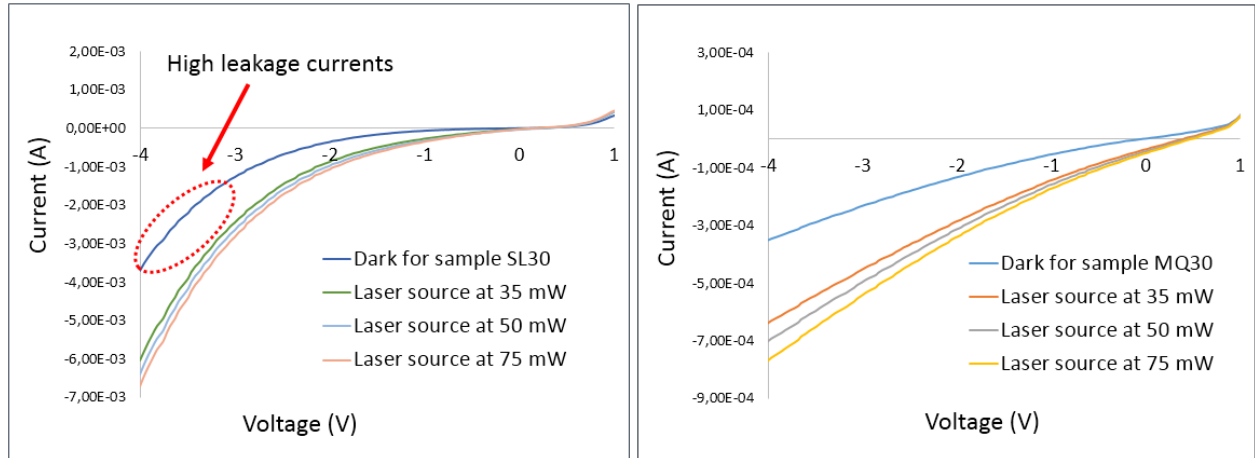
Figure 3.92: I-V characteristics for dark and photocurrent measurements at different laser power for samples SL30 (left) and MQ30 (right).

In conclusion, MQW configuration demonstrates higher overall photocurrent leading to higher quantum efficiency comparing to SL configuration. Leakage currents are frequently observed and directly proportional to the increase of indium content which is associated to higher density of dislocation. An additional work should be focused on the reduction of leakage current in order to improve the photodiode response. Several approaches have been reported in the literature in order to achieve lower leakage current. Photodiode treatment using N_2 plasma followed by rapid thermal annealing have been enhanced the I–V characteristics of experimented photodiodes and decreased the leakage currents [36]. It is due to the reduction of etch-induced damages caused by Cl_2-base plasma. Besides, N_2O plasma treatment has been also used to reduce reverse leakage current by two orders of magnitude compared to no-treated photodiodes [37], as well as treatment using sulfur solutions [10]. All of these treatments have to be experimentally evaluated and accordingly achieving a synthesis of enhanced results. Unfortunately, the lake of time during our study doesn't allow to reach this objective.

III.5.8. Capacitance-Voltage characterizations

Capacitive measurements have been carried out in IEMN. For the large-scale photodiodes, three different dimensions of both SL and MQW configurations have been evaluated at 10 MHz. All samples of different indium contents have been dynamically characterized and exhibited similar response. Therefore, only samples SL10-1 and MQ10-1 are

154

studied here. Capacitances as function of applied voltages have been extracted as shown in the Figure 3.26. Experimented photodiodes of sample MQ10-1 exhibit lower capacitance than photodiodes of sample SL10-1. It has been noted the lower capacitance values has been reported for lower mesa dimensions as 19 pF for $200{\times}200$ μm^2 photodiode of MQW configuration. The higher capacitance value has been recorded to 380 pF for $1000{\times}1000$ μm^2 photodiode of SL configuration. According to the relation between the capacitance and the photodiode surface detailed in the first chapter (Section 1.4.1, Equation 1.6), the effect of the photodiode size is proportional to the photodiode capacitance response which influences the photodiode speed, in other word the frequency regarding Equation 1.5. It has been observed similar trends for all photodiodes no matter their sizes. A positive capacitance is shown under reverse bias then increases to a peak under forward bias then drops down. The drop phenomena under forward bias may due to the extension of the depletion region width [38]. Comparable C-V trends have been commonly observed in the literature dominated by the similar physical mechanism regardless of their sizes [39][40].
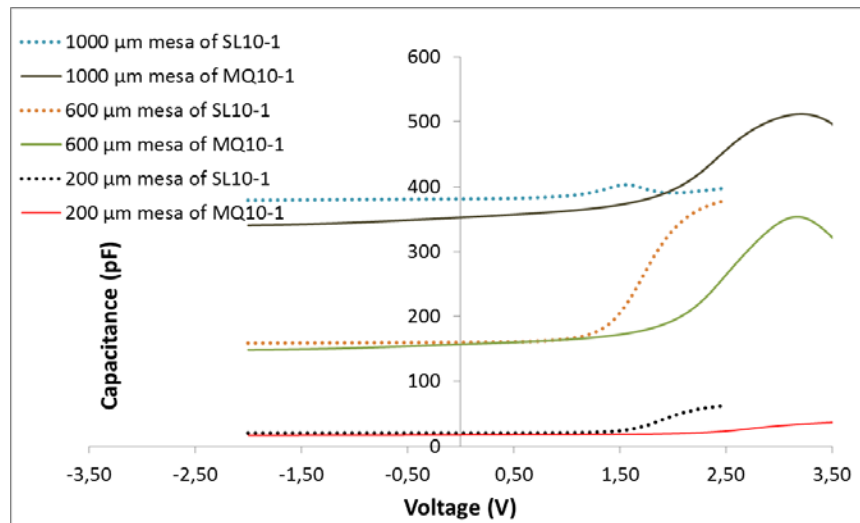

Figure 3.93: C-V characteristics for different mesa dimensions of both SL and MQW configurations.

The investigation on size-dependent capacitance for large-scale photodiodes has been carried out for photodiodes ranging from $100{\times}100$ μm^2 to $1000{\times}1000$ μm^2. According to the relation between the capacitance and the photodiode surface detailed in the first chapter (Section 1.4.1, Equation 1.6), the effect of the photodiode size is proportional to the photodiode

capacitance. Figure 3.27 (left) illustrates the effect of photodiodes size on the related capacitance. The zoomed area in the right side of Figure 3.27 reveals lower capacitance value as 3.4 pF for photodiode mesa of 100×100 μm^2.
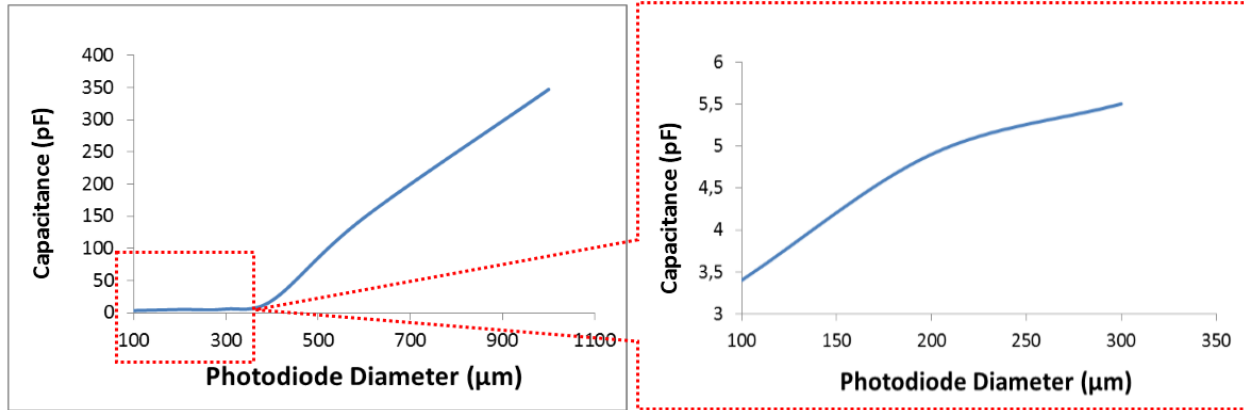

Figure 3.94: Size-dependent capacitance for different large-scale photodiodes (left) with zoomed area (right).

The cut-off frequency related to RC constant and detailed in the first chapter (Section 1.4.1, Equation 1.5) could be extracted using reported capacitance as a function of photodiode mesa dimensions. Figure 3.28 shows higher cut-off frequency of 940 MHz for photodiode mesa dimension of 100×100 μm^2. Conversely, the lower cut-off frequency of 9 MHz is observed for 1000×1000 μm^2 demonstrating the influence of the capacitance on the dynamic response of device.
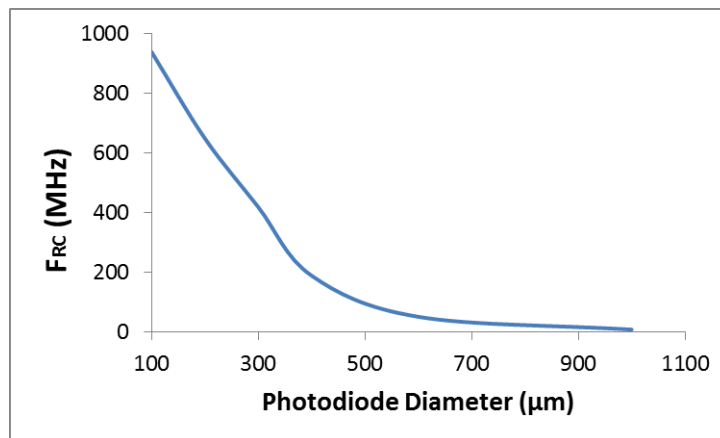

Figure 3.95: Cut-off frequency related to RC constant for different large-scale photodiodes.

III.6.   Fabrication of planar micro-photodiode: Design 2

Beforehand, the fabrication of large scale photodiodes has allowed the validation of the material quality as well as the exploration of the photodiode response in large scale. It has permitted also the optimization of the fabrication process such as photolithography, etching, metal deposition and annealing. Hereafter, the second design has been performed on order to achieve a high quality micro-photodiode. The fabrication of μ-photodiodes will be aimed to achieve mesas ranging from 5×5 µm^2 to 100×100 µm^2 as well as 200×200 µm^2 in order to optimize fabrication process for the new conceived design. The objective of the micro-device fabrication is the evaluation of the photodiode size effect on the photodiode capacitance which affect the device speed and consequently the cut-off frequency.

In this configuration, the photodiode mesa is etched as first phase in order to achieve small dimension mesas. Large contact pads will be extended away of mesa in order to connect probes. The disadvantage of etching mesa as first phase is the possibility of p-layer degradation due to mesa etching process and surface contamination. Contact resistivity for p and n-type will be investigates using Transmission Line Measurement method (TLM) due to new process comparing to design 1.

III.6.1. Flowchart and fabrication process

As explained in the introduction of this chapter, we have to optimize several factors in the fabrication process to achieve an improved μ-photodiode. Five main steps are conceivable: 1) the isolation of the photodiode through the first mesa etching, 2) a second etching process to reach N-GaN layer, 3) the planarization of contacts and mesa passivation of whole device, 4) the deposition of n-contact followed by RTA, 5) the deposition of P-contact followed by RTA. As we considered the fabrication of planar μ-photodiodes, the deep etching process is not considered here. Only 1 µm depth profile will be performed during the isolation of the photodiode for the first mesa etching.

Figure 3.29 illustrates the flowchart of first phase in the fabrication process using optical mask 1. It consists of deposition of etching mask after performing optical photolithography. The etching mask is considered a SiO_2 cover-plate layer deposited by RF sputtering technique. The ICP dry etching is adjusted to 10 SCCM of Cl_2 flow rate, 30 SCCM of Ar, 10 mTorr of total pressure. RF power was held constant at 40 W as well as ICP power fixed to 100 W. Approximately 1 µm of depth profile is achieved at the end of etching process measured by profilometer instrument after removing the etching mask.
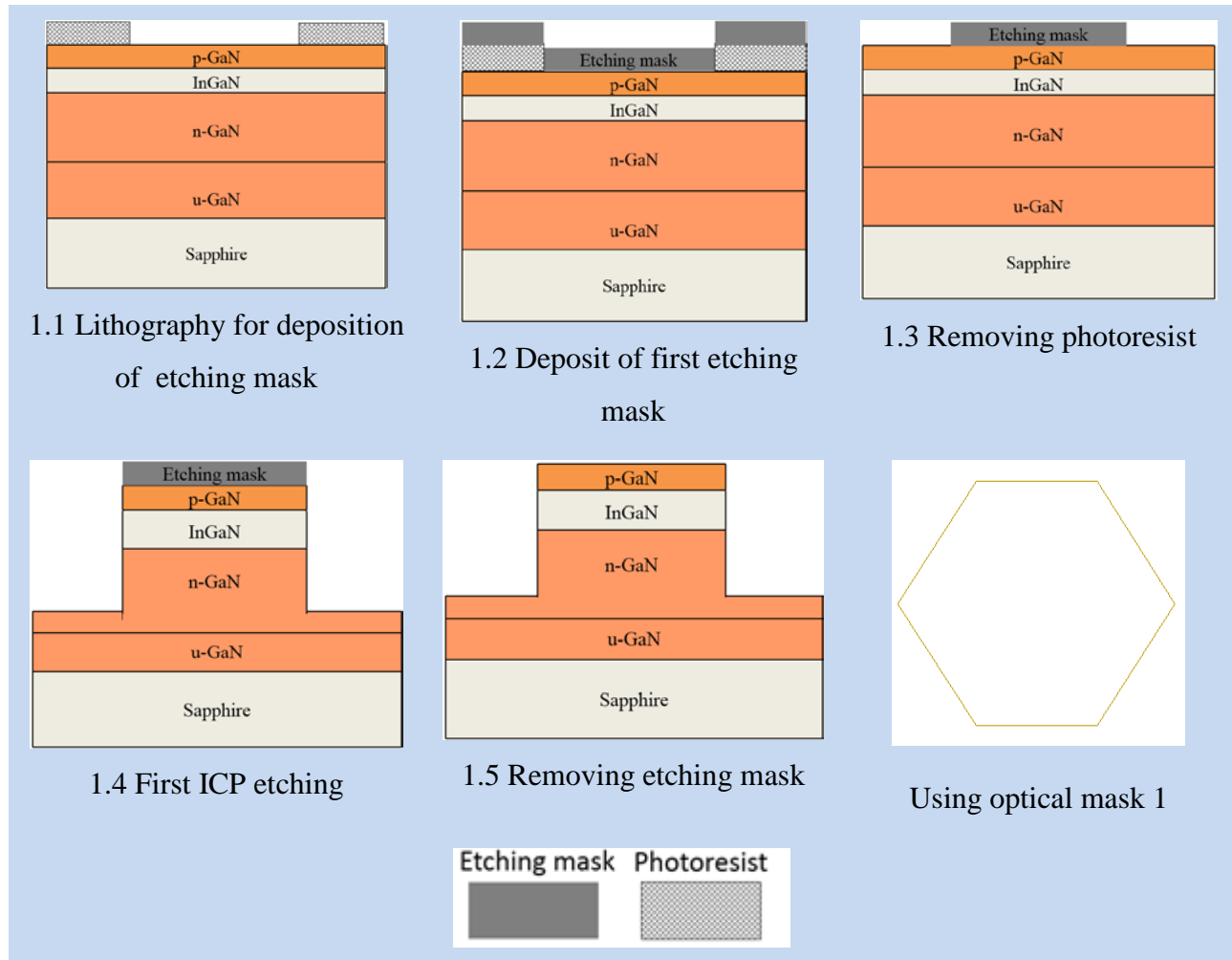

Figure 3.96: Flowchart of phase-1 for mesa etching process.

The second phase of fabrication process consists of second etching in order to reach the N-GaN layer for the deposition of expected n-contact thereafter. Photolithography has been carried out using optical mask 2. SiO_2 cover-plate has been used for the deposition of second

etching mask deposited by RF sputtering technique. The ICP etching process has been achieved with respect to the same parameters as the first etch. Figure 3.30 shows the flowchart of phase-2 for the fabrication process. The achieved depth profile is measured about 410 nm by profilometer.
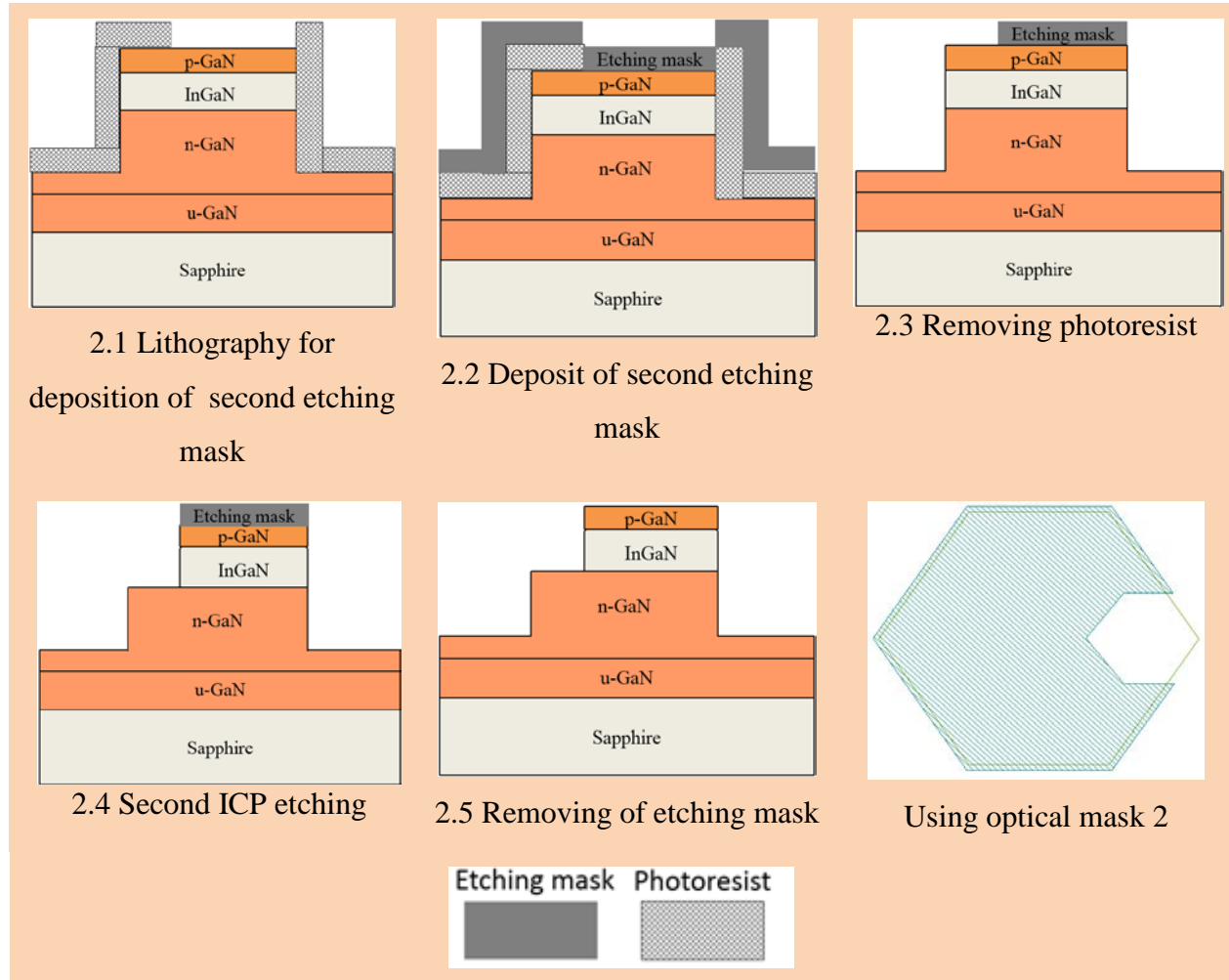

2.1 Lithography for deposition of second etching mask

2.2 Deposit of second etching mask

2.3 Removing photoresist

2.4 Second ICP etching

2.5 Removing of etching mask

Using optical mask 2

Figure 3.97: Flowchart of phase-2 for reaching N-GaN layer.

Figure 3.31 (left) represents the SiO$_2$ etching mask after photolithography for photodiode diameter of 30 µm. In the right side, the SiO$_2$ etching mask is illustrated after ICP dry etch. It demonstrates the strength of cover-plate against ICP attack and reduced erosion of mask edges are observed.
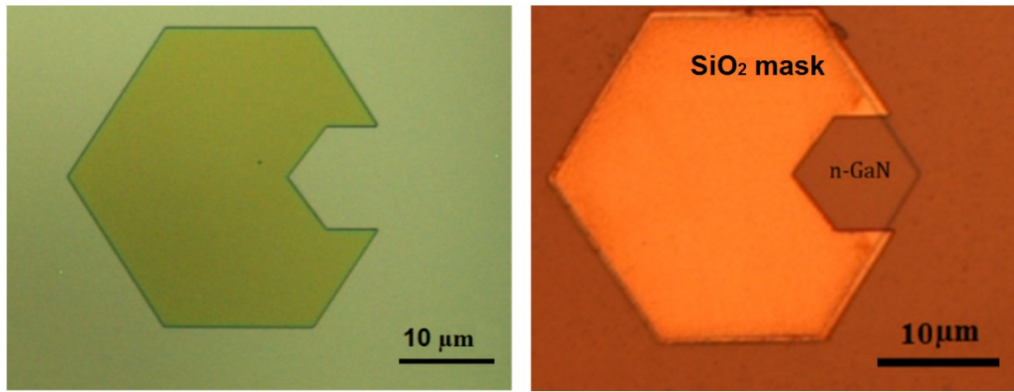
Figure 3.98: Image issued from optical microscopy demonstrating SiO$_2$ cover-plate before second etch (left) and after (right).

Phase-3 of the fabrication process consists of passivation of the etched mesa in order to ensures long-term stability of the photodiode junction and improve the device reliability. The passivation will also limit surface phenomena inducing parasitic currents. Additional objective of SiO$_2$ deposition is the planarization permitting to have the same level of future n and p-contacts on insulated surface. SiO$_2$ deposition is performed using two different method in order to investigate the electrical response of photodiode. The first is deposited using Plasma-enhanced chemical vapor deposition (PECVD) at 300 °C then patterned after photolithography using Reactive-ion etching (RIE). The second SiO$_2$ is deposited using RF sputtering technique. Figure 3.32 shows the fabrication process of phase-3 with optical photolithography using optical mask 3 for the PECVD SiO$_2$ case.
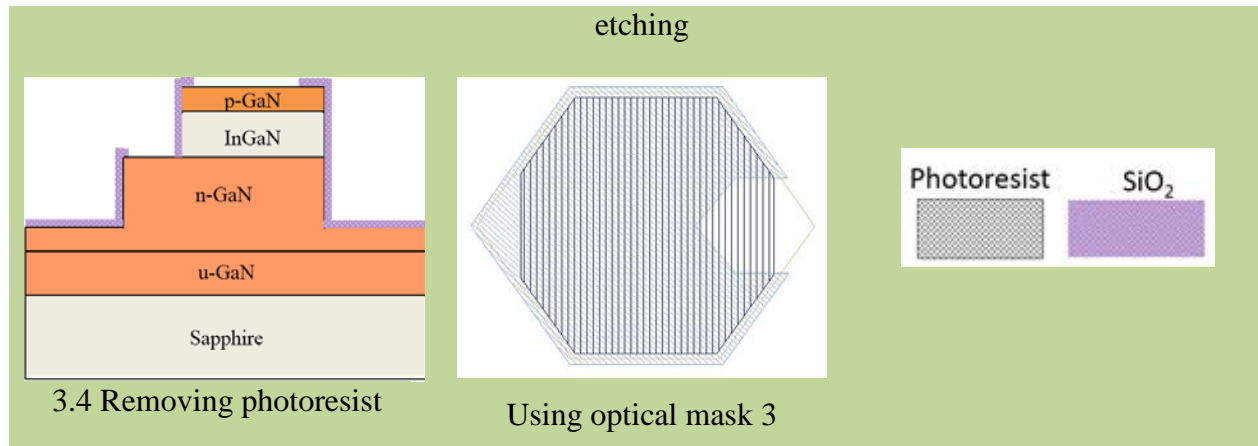

3.1 Deposition of SiO$_2$ 3.2 Lithography for RIE   3.3 RIE etching of SiO$_2$
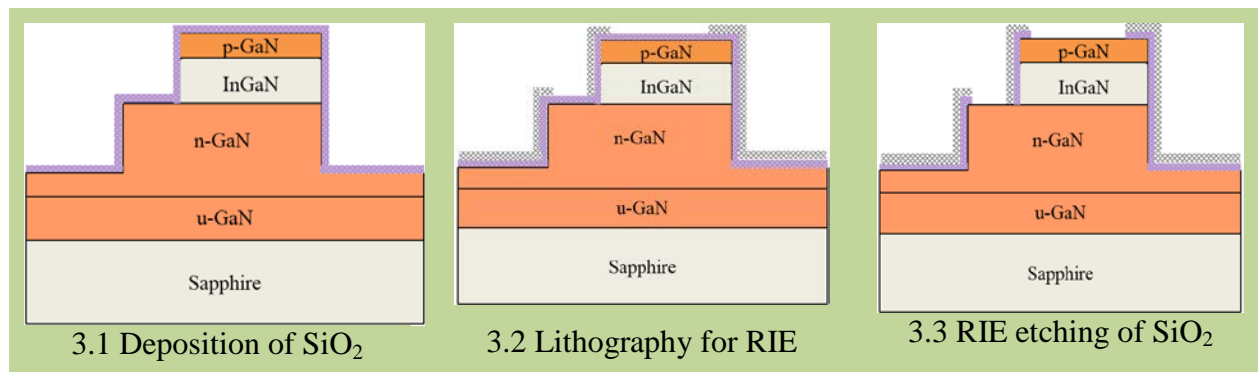
Figure 3.99: Flowchart of phase-3 for planarization of contacts and mesa passivation.

Figure 3.33 shows the passivation using SiO_2 deposited by PECVD in order to isolate the etched mesa. Besides, the first and second dry etch is illustrated in the figure with total etching depth of 1µm.
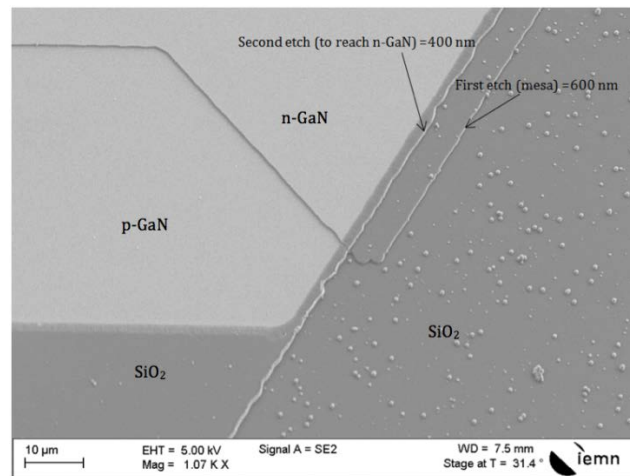

Figure 3.100: Image issued from SEM showing SiO_2 passivation as well as first and second etching process.

As noted beforehand, the extension of p and n-type contacts outside photodiode will permit to enlarge metal pads in order to provide sufficient area for the use of probes during electrical characterization. For this reason, the deposition of n-contact will be carried out on the SiO_2 bottom level. The p-contact has been planned to be deposited in the last step due to its lower annealing temperature comparing to n-contact annealing. Figure 3.34 illustrates the fabrication process of n-contact deposition (phase-3) using optical mask 4.
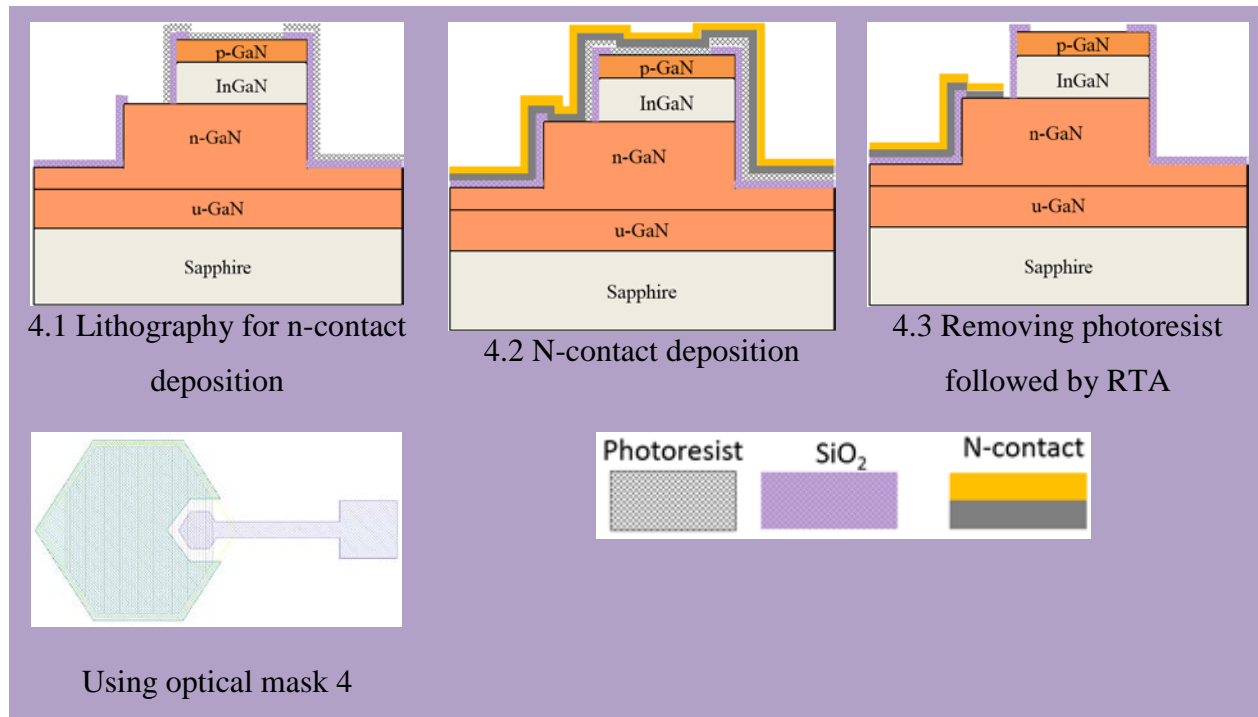
161

4.1 Lithography for n-contact deposition	4.2 N-contact deposition	4.3 Removing photoresist followed by RTA

Using optical mask 4

Figure 3.101: Flowchart of phase-4 for n-contact deposition.

The metal combination of n-contact has been studied using TLM in order to obtain a lower contact resistivity. The optimized metal combination has been achieved using Ti/Al/Ni/Au with thickness of (10/100/40/100 nm) respectively. Ti/Al combination have been widely used in the literature with decreased resistivity after annealing. It is attributed to the formation of TiN in the metal/semiconductor interface by chemical reaction between nitrogen of GaN and Ti which cause the appearance of nitrogen deficiencies in GaN and act as donors [41]. The introduction of nickel metal is supposed to make a diffusion barrier between Ti/Al and Au metal in the top. It has been reported that the use of Ni has significantly reduced the specific contact resistance [42]. Concerning the annealing parameters, several configurations have been experimented using TLM method with different temperatures, atmospheres, and annealed time which plays a role in the formation of metallic phases. The best contact resistivity reported in our work for n-contact has been 7×10^{-6} Ω.cm^2 which is considered satisfactory [43]. It has been achieved under 850°C of RTA for 30 seconds of annealing procedure. It has consisted of a slope of 40 °C/s then permanent temperature of 400 °C for 30s then a second slope 15 °C/s up to 850°C and finally cooling down. The n-contact deposition before and after annealing is illustrated in Figure 3.35.
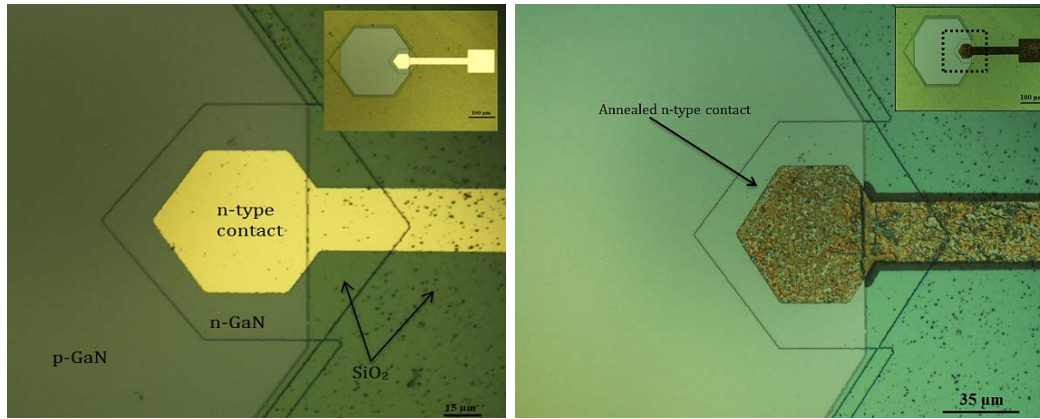
Figure 3.102: Image issued from optical microscopy demonstrating n-contact before (left) and after (right) annealing.

It is known that achieving lower resistance of p-ohmic contact is the common difficulty in the GaN community. It is due to the complication in growing heavily doped P-GaN and the absence of contact metals having a work function larger than P-GaN [1]. To date, a considerable effort has been performed to achieve lower ohmic contact to P-GaN by using various contact metals [2] [3]. Pd metal with its high work function (5.12 eV) makes it attracted candidate for ohmic surface layer [3]. It is due to the contact formation on the p-GaN acting as an acceptor in GaN. In our case, the deposition of p-contact will be performed using Pd/Au metal combination as used for the large-scale photodiode. The thickness of metals are 35 nm for Pd and 120 nm for Au. Figure 3.36 illustrates the fabrication process of phase-5 for p-contact deposition using optical mask 5 followed by RTA.
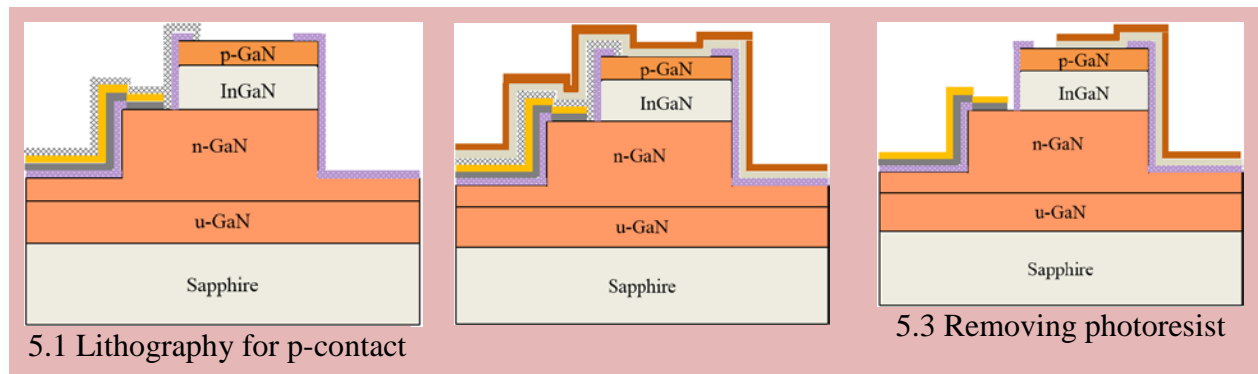
Figure 3.103: Flowchart of phase-5 for p-contact deposition.

The annealing investigation has demonstrated the improvement of electrical properties due to the formation of high hole concentrations. The best annealing parameters have been demonstrated for RTA at 450°C for 1 minute under N_2 atmosphere with contact resistivity of 2×10^{-1} $\Omega.cm^2$ in the case of SiO_2 passivation using PECVD and 5×10^{-4} $\Omega.cm^2$ in the case of SiO_2 deposited by RF sputtering technique [44]. Electrical characteristics for both methods will be studied hereafter.
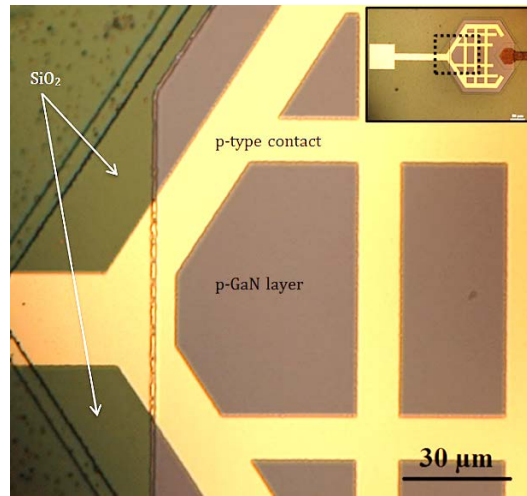

Figure 3.104: Image issued from optical microscopy demonstrating p-contact deposition.

We have fabricated several forms during the fabrication process in order to evaluate the photodiode characteristics and conclude the best photodiode response. Photodiodes with coplanar transmission line have been moreover fabricated. It will be used for the dynamic characterization in order to extract the cut-off frequency.

In Figure 3.38, we have conceived several forms of photodiode (left) in addition to photodiodes connected to coplanar pads (right).
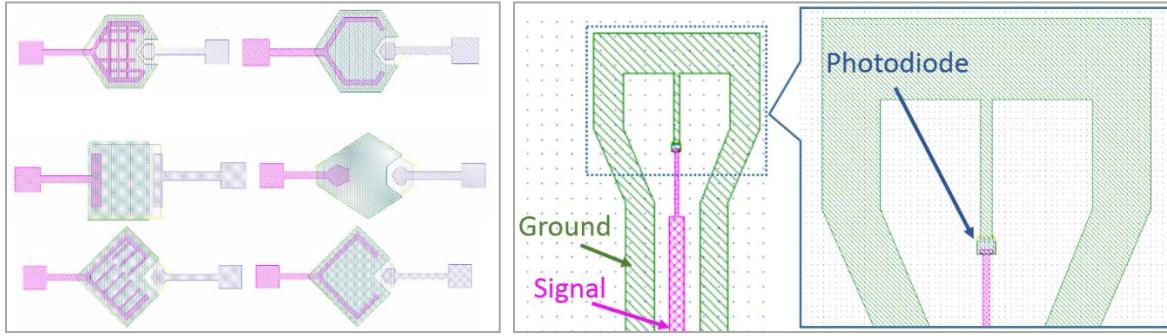
Figure 3.105: Image issued from optical masks demonstrating several designs of photodiodes (left) as well as photodiodes connected to coplanar transmission line (right).

All of photodiodes have been subjected to verification using SEM in order to have an overall outlook of the fabricated photodiodes. It has been verified the quality of passivation besides contact depositions. Photodiodes with dimensions varying from 10×10 µm^2 to 200×200 µm^2 are shown in Figure 3.39 in addition to coplanar photodiodes.

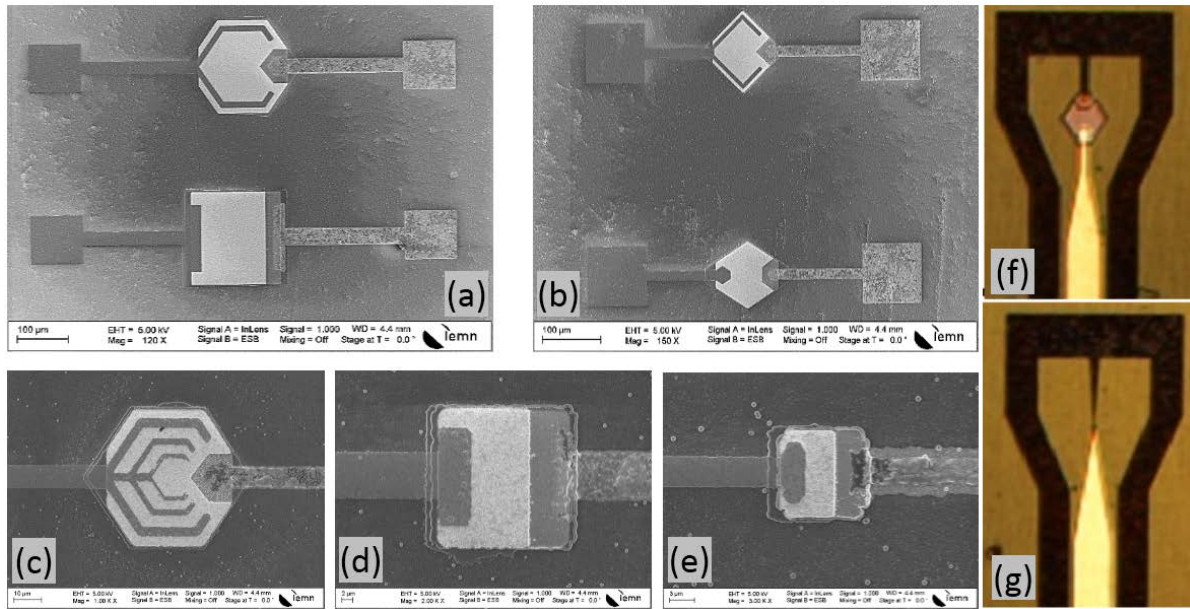*Figure 3.106: Image issued from SEM showing photodiodes (a) 200×200 µm^2, (b) 100×100 µm^2, (c) 50×50 µm^2, (d) 20×20 µm^2 and (e) 10×10 µm^2. Photodiodes connected to coplanar pads with dimensions (f) 100×100 µm^2 and (g) 10×10 µm^2.*

III.6.2. The influence of passivation on photodiode response

165

During the mesa passivation in the fabrication process in phase-3, we have investigated the influence of SiO_2 type on the photodiode characteristic. Two possible depositions of SiO_2 are proposed: the first is performed by sputter deposition at room temperature, the second is done using PECVD at 300°C. The advantage of PECVD deposition is the improved quality of SiO_2 due to the high temperature deposition, where the sputtering deposition is achieved at room temperature. The passivation process using PECVD consists to deposit the SiO_2 layer on the whole surface then patterned by RIE in order to prepare contact pads for metal deposition. The disadvantage of PECVD is the RIE phase which is required to remove properly the SiO_2 layer which could damage the N-GaN and particularly the P-GaN surface layer. The advantage of the sputtering deposition SiO_2 is the possibility to remove it easily using lift-off process as well as the deposition of thick layer.
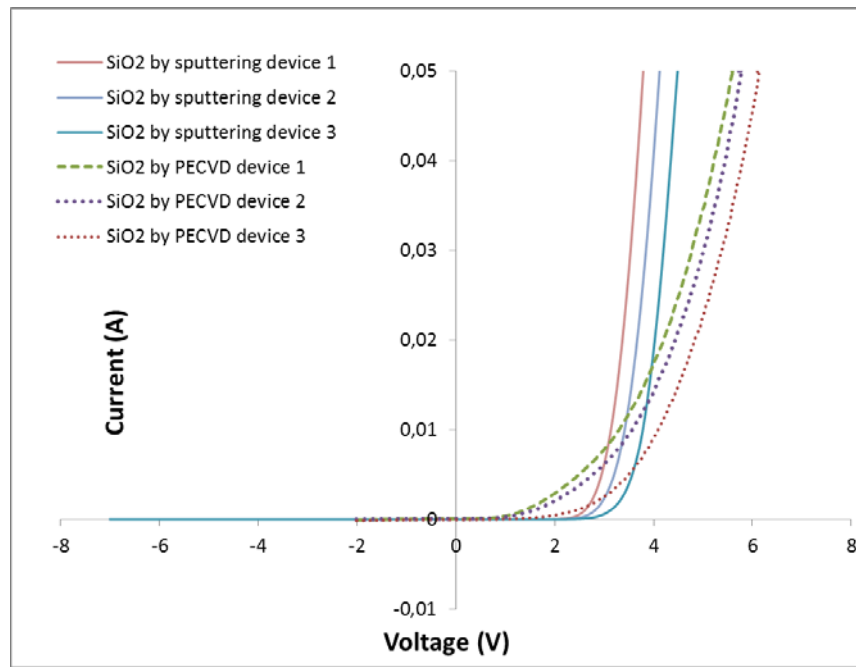
Figure 3.107: Mesa passivation effect on the device response for SiO₂ sputter deposition versus SiO₂ PECVD.

After annealing process for both experimented samples, contact resistivity of 2×10^{-1} $\Omega.cm^2$ has been achieved for p-contact in the case of SiO_2 passivation using PECVD and 5×10^{-4} $\Omega.cm^2$ in the case of SiO_2 deposited by RF sputtering technique. Figure 3.40 demonstrates the comparison of both passivation methods using SiO_2 sputter deposition and SiO_2 PECVD for three

different sizes of devices. The I-V characteristic of photodiodes using SiO_2 sputter deposition demonstrates better electrical response comparing to devices using SiO_2 PECVD. This could be explained by the RIE effect in the PECVD which should be optimized. Optimal etching by RIE is required in order to protect p-surface layer. If over etching is performed, RIE will attack the P-GaN layer and degrade its quality. If insufficient etching is carried out, SiO_2 residue will be present on the P-GaN surface and affect the contact resistivity. The passivation using sputter deposition is performed using photolithography protecting the expected contact pads before SiO_2 deposition. After the deposition, patterning is achieved by lift-off process which preserve the contact surfaces.

III.6.3. Photocurrent measurement using laser source

After the fabrication phase, we will proceed to the electrical characterization in order to obtain the μ-photodiode response in terms of photocurrent values. As explained beforehand, the photocurrent measurements are carried out to investigate the laser power effect on the photocurrent values using optical setup in Figure 3.2. Each measurement of photocurrent has considered dark current measurement followed by three photocurrent measurements at different powers of incident laser with 35 mW, 50 mW and 75 mW. Figure 3.41 illustrates images issued from super-zoom HD camera during photocurrent measurement for photodiodes connected to coplanar pads (a, b) and rectangle pads (c). Optical fiber of laser source is adjusted to cover the p-active surface and excite the photodiode.
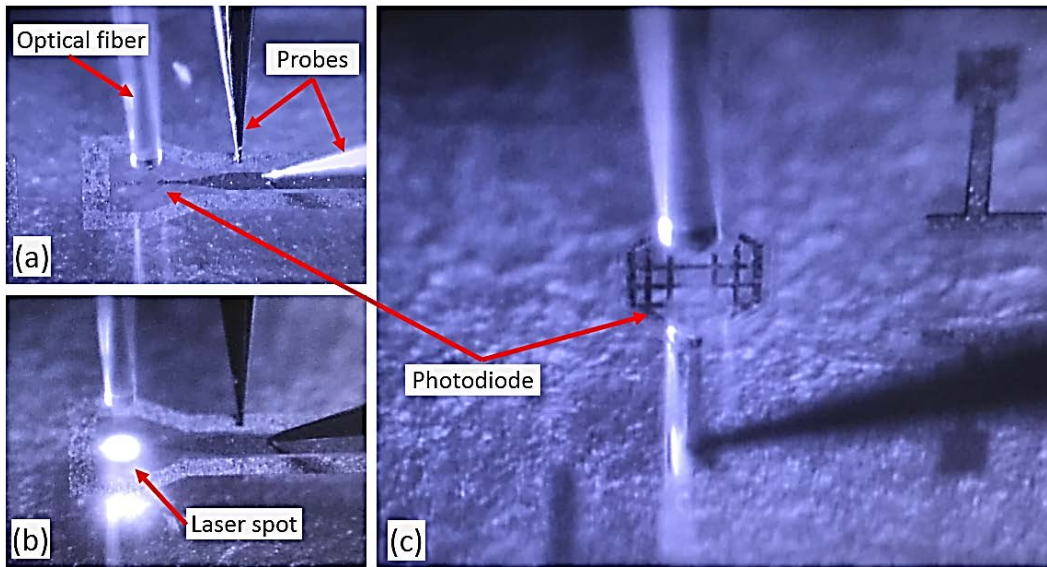
Figure 3.108: Image issued from super-zoom HD camera showing coplanar photodiode in dark measurement (a) under illumination (b) and regular photodiode (c).

Figure 3.42 (left) demonstrates the dark measurement for sample MQ10-1 comparing to photocurrent measurement at different laser powers for μ-photodiode 50×50 μm². The increase of photocurrents is observed once the laser power is increased and attains 158 μA at -3 V for laser power of 75 mW. The leakage current of dark measurement is considered to be 52 nA at -3 V which is considered very low due to small dimension of photodiode. Sample MQ-20 exhibits higher photocurrent values than reported for MQ10-1 as shown in Figure 3.42 (right) for μ-photodiode 50×50 μm². The high value of photocurrent for sample MQ-20 can be explained by the fact that the high leakage currents for dark measurement (around 3.65 μA at -3 V) increases for each I-V measurement under laser excitation and consequently it is added to the photocurrent value.
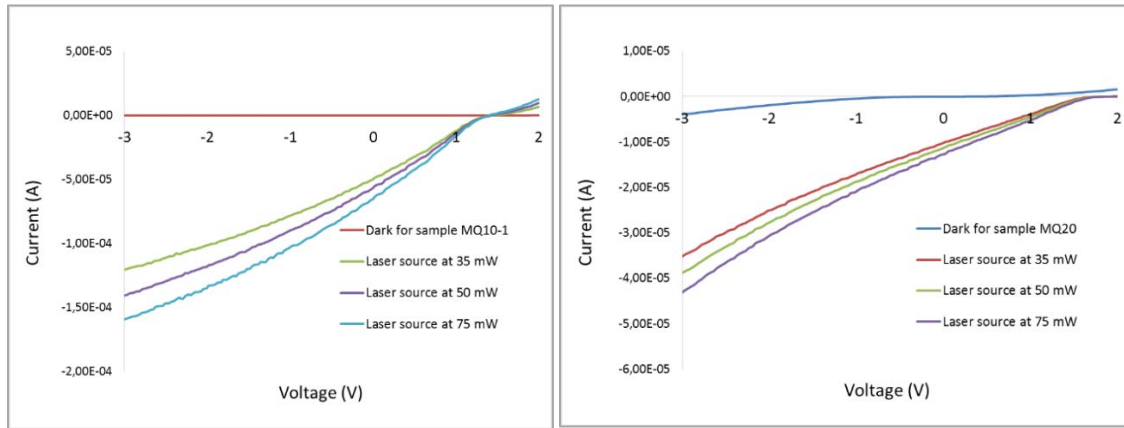
Figure 3.109: I-V characteristics for dark and photocurrent measurements at different laser power for µ-photodiodes of samples MQ10-1 (left) and MQ20 (right).

A µ-photodiode of 50×50 µm^2 of sample MQ10-1 has been exposed to higher reverse voltage until µ-photodiode breakdown. Figure 3.43 exhibits I-V characteristic as performed previously for three different powers of laser source. A saturation zone is clearly observed starting from -12 V until photodiode breakdown at -20 V revealing 395 µA of maximal photocurrent. This seems to have the same behavior than the large-scale photodiode throughout the saturation phenomena. However, lower photocurrent value is observed here comparing to large-scale photodiode due to the p-active layer dimension. As we explained previously, such saturation zone could be associated to the carrier velocity. The saturation of holes velocity have been calculated to be a probable reason. It demonstrates photocurrent saturation at -12 V corresponding 1200 kV/cm with related absorbent layer of 100 nm.
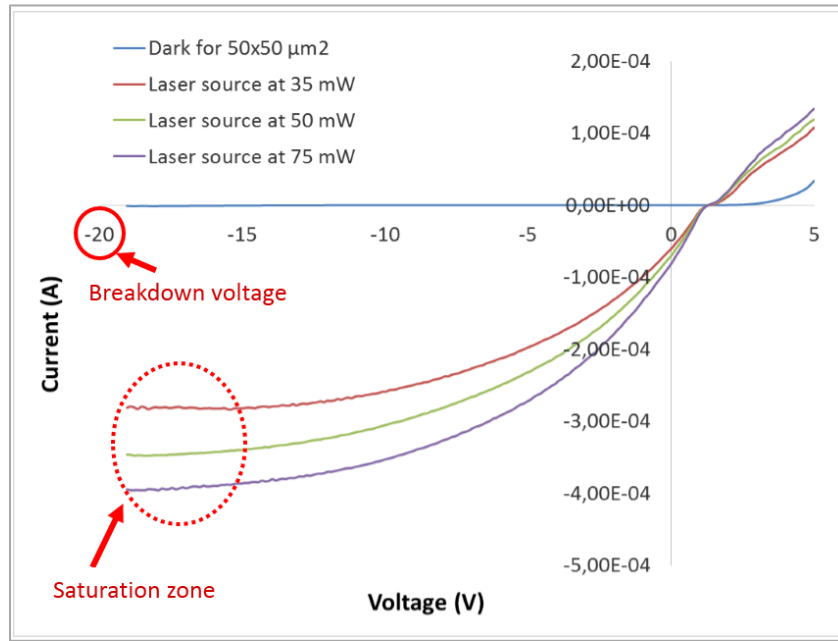
Figure 3.110: I-V characteristics for dark and photocurrent measurements at different laser powers until breakdown voltage for 50×50 μm² μ-photodiode of sample MQ10-1.

III.6.4. Capacitance-Voltage characterizations

The Capacitive measurements have been performed for planar μ-photodiodes as was already done for large-scale photodiodes. All samples of different indium content have been characterized. Hereafter only sample MQ10-2 has been figured in order to evaluate the size effect on the dynamic response of the photodiode. According to the relation between the capacitance and the photodiode surface detailed in the first chapter (Section 1.4.1, Equation 1.6), the effect of the photodiode size is proportional to the photodiode capacitance. Figure 3.44 illustrates the C-V characteristics for different μ-photodiodes with diameter ranging from 10 µm to 100 µm. It reveals the lowest capacitance value as 557 femto farad (fF) for μ-photodiodes diameter 10 µm.

Figure 3.111: C-V characteristics for different µ-photodiodes of sample MQ-10-2.
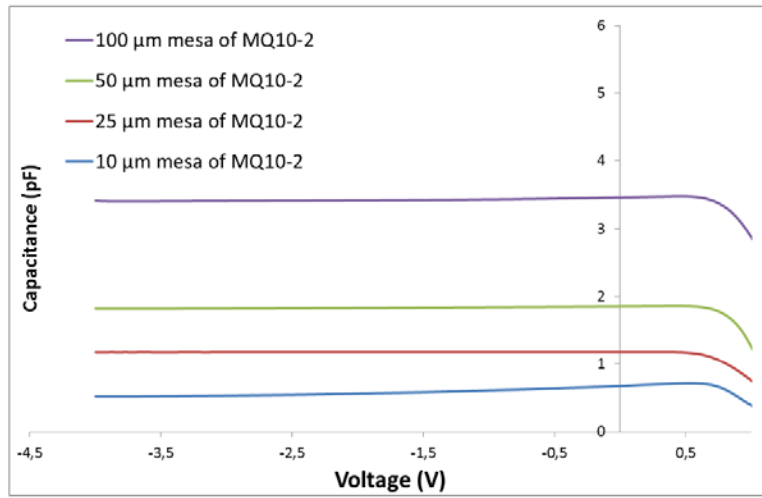
The influence of the photodiode size on the capacitance value is illustrated in Figure 3.45 (left). It shows the increase of capacitance when photodiode dimension is increased. It is related to the relation between the capacitance and the photodiode surface detailed in the first chapter (Section 1.4.1, Equation 1.6). Besides, the cut-off frequency related to RC constant could be achieved using related capacitance value as explained in the first chapter (Section 1.4.1, Equation 1.5). It shows the increase of cut-off frequency when the related capacitance represents lower value, in other word, the photodiode dimension becomes smaller. Figure 3.45 (right) shows higher cut-off frequency of 6.09 GHz for µ-photodiode diameter of 10 µm. Conversely, the lower cut-off frequency of 910 MHz is observed for photodiode diameter of 100 µm demonstrating the influence of the capacitance on the dynamic response of device.
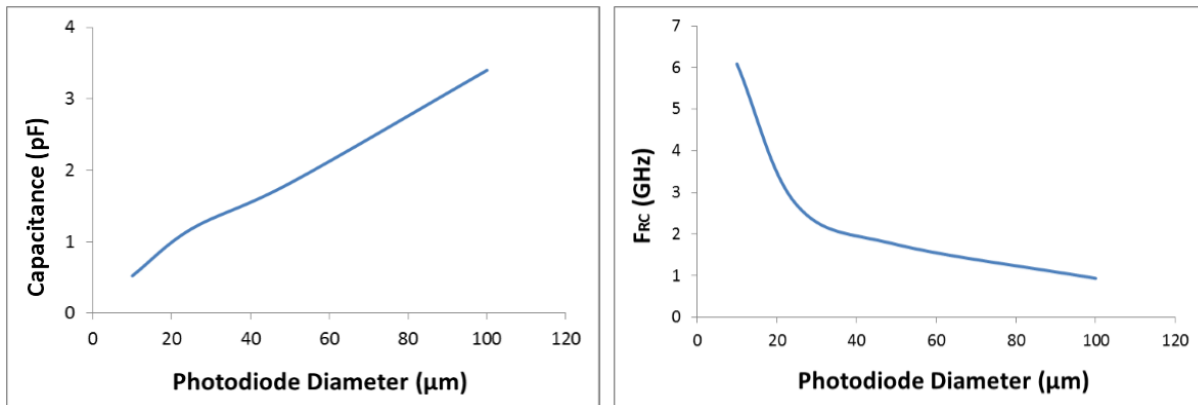

Figure 3.112: Size-dependent capacitance for different µ-photodiodes (left) and cut-off frequency related to RC constant as function of photodiode diameter (right).

The C-V measurement previously provides total capacitance which is includes the photodiode capacitance as well as the parasitic capacitance. Parasitic capacitance is non-zero capacitance due to metal conductors such as wires, metal pads or coplanar waveguides lines. Its value is significant at higher frequencies. Measuring theoretically the photodiode capacitance will provide the parasitic capacitance value by subtraction of $C_{measured}$ and $C_{theoretical}$. If we consider the photodiodes diameter of 10 µm, the photodiode capacitance is calculated to be 88.5 fF using Equation 1.6. The parasitic capacitance is calculated to be 468.5 fF which is considered high leading to reduced cut-off frequency. It is responsible of cut-off frequency drop from 36.17 GHz to 6.09 GHz. Design of coplanar waveguiding lines should be improved in order to optimize the parasitic capacitance.

III.7.   Extraction of cut-off frequency using noise measurement

It is well known that the dynamic behavior of a photodiode is governed by two main phenomena. The first is the transit time of the carriers in the deserted area, and the second is the capacitance of the photodiode associated with the external load circuit. In other words, both phenomena define the influence of the surface, the deserted area and the load resistance on the photodiode response. However, a limitation of cut-off frequency due to the capacity and the load circuit has been expressed using Equation 1.5 in chapter 1. Besides, a limitation of cut-off frequency could be subjected to the carrier transit time in the desert area as defined in Equation 1.3. In our study, the transit time is assumed sufficiently small in the order of picoseconds with 100 nm of absorbent layer. It means that the cut-off frequency related to the RC circuit is the dominated factor for the photodiode cut-off frequency.

One of the simplest method to achieve the cut-off frequency of the photodiode is the measurement of the noise. It consists of the measurement of the photodiode noise as function of variable frequency. The drop of the noise is related to the limitation of the photodiode frequency response. The absence of the noise at such frequency demonstrates the cut-off frequency of the photodiode. At -3dB of the noise characteristic, the cut-off frequency is achieved. This method has been used by Jean-Philippe GOUY in 1989 in the IEMN. It shows a significant way to achieve the dynamic response of fabricated photodiodes [45].

Among the different noise components (thermal noise, shot noise, Transit-time noise, etc...), the most important for the photodiode, is the shot noise. This noise is mainly due to the velocity distribution of the carriers. Shot noise should vary according to the photodiode current, while the thermal noise related to both photodiode and Noise-Figure-Meter should be constant. The noise intensity is performed using the setup of noise measurement as illustrated in Figure 3.3.

Figure 3.46 demonstrates the noise intensity as function of frequency for photodiode with diameter of 100 µm connected with coplanar lines. The photodiode has been under reverse bias in order to achieve the shot noise in dark and under illumination of laser source. The curve shows a drop of shot noise related to the photodiode current when frequency is increased. The difference in noise intensity between dark (N_{dark}) and under illumination ($N_{photocurrent}$) is detected very small when bias is applied for small photodiode dimensions. The $N_{photocurrent}$ - N_{dark} in average value is roughly 0.8 dB. The minor value of photocurrents (< 100 µA) is possibly the main reason to achieve low difference in noise response. Besides, the sensibility of Noise-Figure-Meter doesn't allow the detection of low noise intensity comparing to itself noise. The cut-off frequency at -3dB is estimated to be 300 MHz.

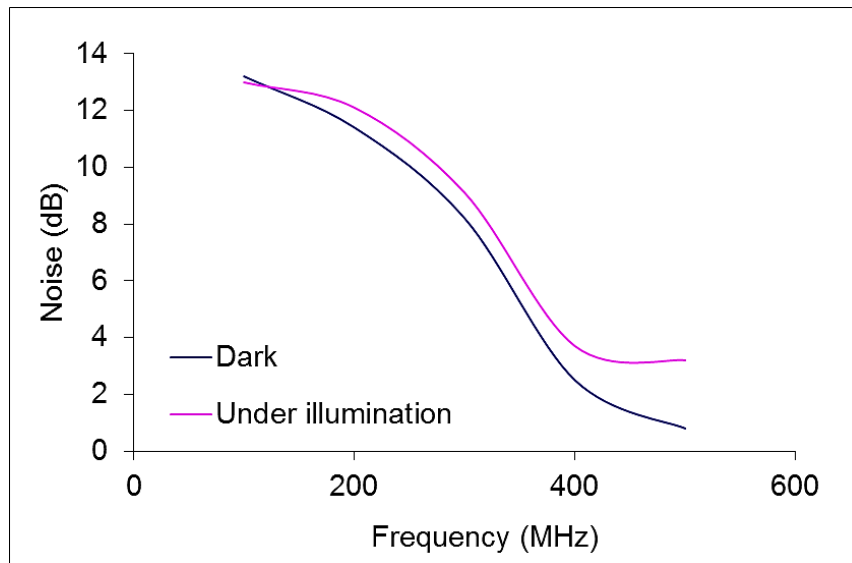*Figure 3.113: Noise measurement for 100×100 µm^2 photodiode using Noise-Figure-Meter.*

The experiment of noise measurement has been performed for smaller coplanar photodiode with 25 µm diameter. Figure 3.47 illustrates the noise intensity detected by Noise-

Figure-Meter for the dark and under illumination of laser source. It is noted that the photocurrent here is low as 10 µA demonstrating $N_{photocurrent}$ - N_{dark} in average value of 0.1 dB. Interferences on microwave reflection coefficient shown on the figure are due to the impedance mismatch between Noise-Figure-Meter (50 Ω) and photodiode impedance (> 300 Ω). A trend average curve is drawn in order to estimate the cut-off frequency which is calculated to be 1.45 GHz at -3dB.
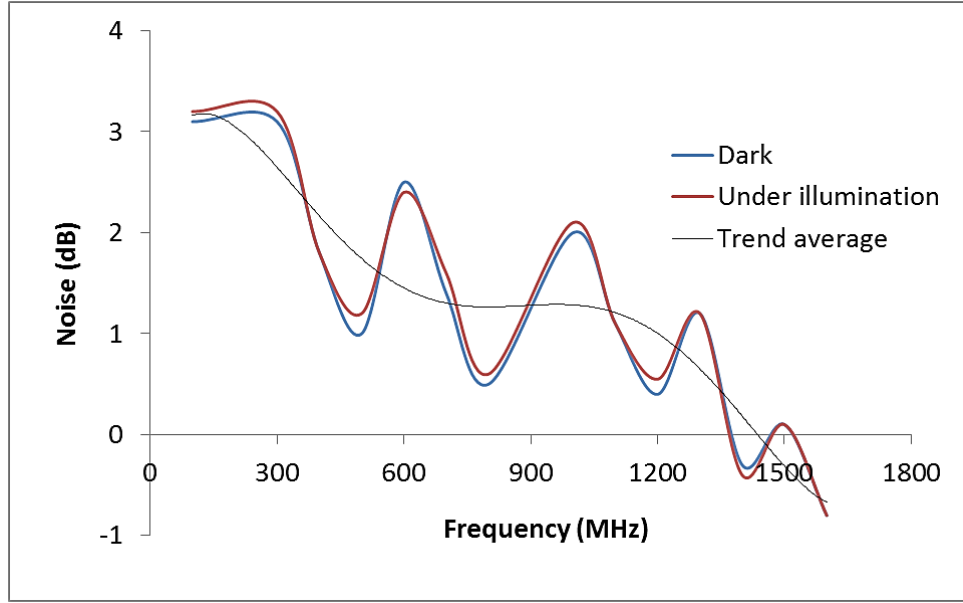
Figure 3.114: Noise measurement for 25×25 µm^2 photodiode using Noise-Figure-Meter.

The reported values of cut-off frequency issued using noise measurement are compared to those calculated theoretically by Equation 1.5 and Equation 1.6 as well as values calculated through C-V measurements. *Table 3.1* shows the reported values of cut-off frequencies for both 100 and 25 µm photodiode diameters. The theoretical calculation are higher than other reported values because calculation doesn't take into account metal coplanar lines which add circuit of inductance and related capacities. This leads to parasitical capacitance and the cut-off frequency is dramatically reduced. Value issued from C-V for 100 µm photodiode diameter is close to value issued from noise measurement even the coplanar lines reduce slightly the cut-off frequency. For the 25 µm photodiode diameter, the C-V measurement demonstrates the high influence of the coplanar waveguiding lines on the cut-off frequency. The optimization of the coplanar lines should performed in the perspective design in order to reduce the influence of the parasitic capacitance.

	Fc theoretical	**Fc** via C-V	**Fc** via noise
$100{\times}100\ \mu m^2$ photodiode	410 MHz	390 MHz	300 MHz
$25{\times}25\ \mu m^2$ photodiode	6.3 GHz	2.7 GHz	1.45 GHz

Table 3.12: Comparison of cut-off frequency issued using theoretical calculation, C-V measurements and noise measurement.

It noted in the noise measurement that a very high shot noise is requested in the perspective fabrication of photodiodes in order to achieve a large difference in noise for dark and under illumination currents. Shot noise is related to high photocurrent values, that is why improvement of photodiode response is recommended in future works.

As the coplanar μ-photodiodes have been fabricated and optimized, vertical μ-photodiodes are subjected to be developed. The fabrication of coplanar μ-photodiodes have been an intermediate phase. In the next section, the fabrication of vertical μ-photodiodes are based on the study of GaN deep etching reported beforehand.

III.8.   Fabrication of vertical micro-photodiode

The study of GaN deep etching has permitted to understand different obstacles to achieve vertical mesa. Different configurations of etching masks has been performed. Photoresist, metal and SiO_2 have been used as cover-plate etching masks. The high depth profile has been achieved using metal mask. This opens the way towards the fabrication of vertical photodiode. The isolation of the photodiode is achieved via mesa etching. It allows the deposition of contact pads outside of the mesa on undoped material or on sapphire substrate. This process will avoid capacitance effect due to metal insulator semiconductors structure. While Few studies concerning the deep GaN etching have been reported [18], it seems valuable to study vertical photodiode [46][47]. Actually, one of the most promising devices is the vertical LEDs demonstrating high efficiency and high power lighting [48]. Moreover, it shows better current spreading and enhanced heat dissipation comparing to lateral structure [49]. In our study, the fabrication of planar μ-photodiodes has been   a preparatory stage before the fabrication of vertical

photodiodes. Concerning the flowchart of the fabrication, we will follow the same than the design 2 with an increase etching profile of 6 µm until sapphire substrate using metal cover-plate mask. Vertical photodiodes have been achieved as illustrated in Figure 3.48. Images are issued from 3D optical microscopy showing 6.2 µm of photodiode vertical profile (left) comparing to lateral photodiode (right).
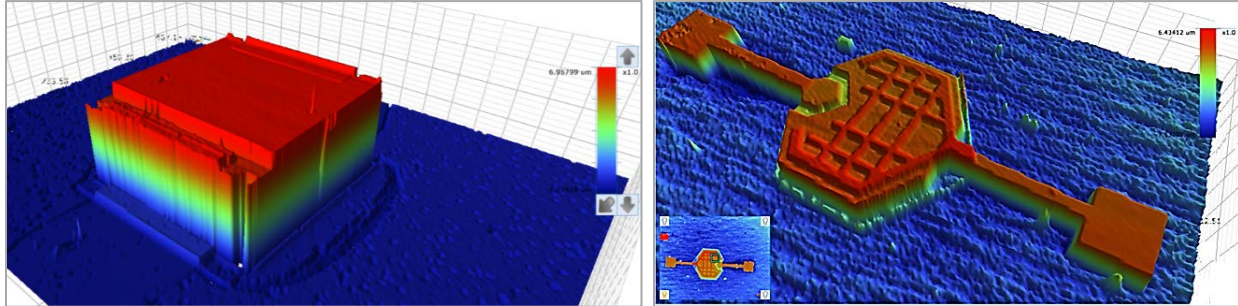
Figure 3.115: Images issues from 3D optical microscopy showing vertical device (left) and planar device (right).

I-V characteristics for vertical photodiode have extracted and compared to planar photodiode. Figure 3.49 shows the electrical characterization of vertical 50×50 µm photodiode in comparison with planar photodiode of same dimensions. The vertical photodiode exhibits more leakage current than the planar one in the reverse bias. It may be related to the sidewall contaminations which probably contain residues of metal etching mask. The shift of turn-on voltage in the vertical photodiode could be associated to the decrease of metal thickness along the vertical profile which affect the direct bias behavior and increase the serial resistance. More optimizations in the fabrication of µ-photodiodes have to be reached in order to achieve high quality of vertical devices. An additional work in the perspective of this work will be detailed.

Figure 3.116: I-V characteristics for vertical and planar µ-photodiodes of sample MQ-10.

In this chapter, we have described the fabrication and device characterization of PIN photodiodes. Different designs have been performed for planar large-scale and micro-scale photodiode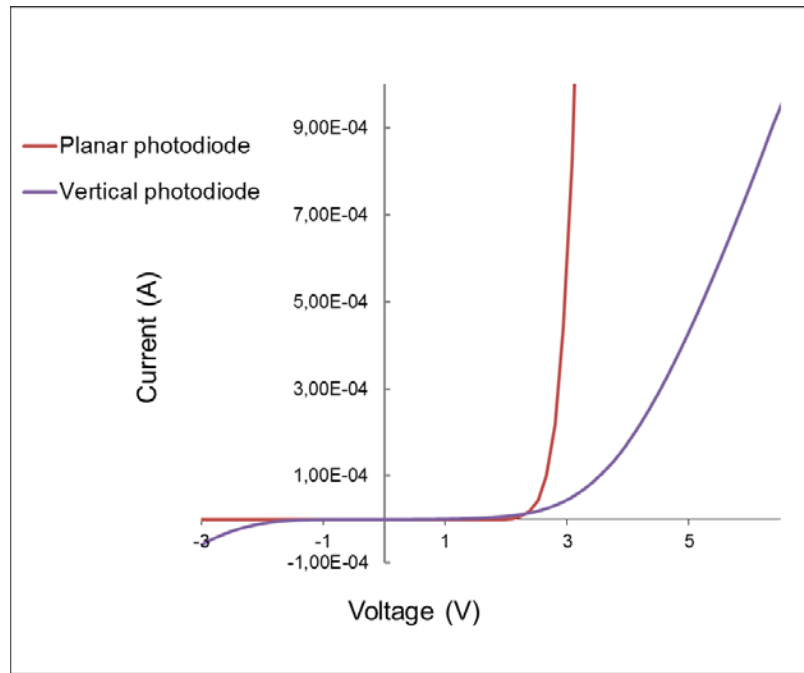 ranging from 10×10 µm^2 to 1000×1000 µm^2. Electrical characterizations techniques have been detailed in order to extract external quantum efficiency as well as photocurrent measurement using laser source. The setup of noise measurement has been described to obtain the cut-off frequency of fabricated photodiodes. Study of GaN deep etching and annealing effect has been also presented. The metal mask has showed an enhanced cover-plate permitting to reach 6 µm of etching depth with less columnar defects and high-selectivity. Besides, fabrication process has been optimized in terms of photolithography, etching, metal deposition and passivation. Moreover, the influence of the MQW configuration and growth technique on the device performance have been also studied. C-V characteristics have been demonstrated higher cut-off frequency of 6.09 GHz for µ-photodiode diameter of 10 µm. Noise measurement has been performed in order to achieve the cut-off frequency using Noise-Figure-Meter. The reported frequency at -3dB is almost 1.45 GHz for 25 µm photodiode diameter. The fabrication of vertical micro-photodiode has been achieved and then compared to planar photodiode.

General conclusions and perspectives

The objective of this thesis is the study the material quality issued from commercial and institutional provider. It permits to investigate the different configurations of material growth using MBE and MOCVD. The indium content is investigated as function of absorbent wavelength in the PIN structure. The study of material quality provided information about the expected device performance permitting to achieve high quality photodetector. The second objective is the design of PIN structure suitable for different size of photodiode and adapted to the requirements of device characterization. Fabricated photodiodes were statically and dynamically characterized in order to achieve the photodiode response. The challenge in the fabrication of InGaN/GaN materials is to obtain high quality of device. The III-Nitride compounds are known in the research community to be problematic in the fabrication process. Several optimizations and tests in clean room were tested before proceeding the photodiode fabrication. III-Nitride based high speed devices have been described including their applications and the principal of the photodiode as a key element in the fabrication phase. The different fundamental properties as piezoelectric polarization, mechanical properties, crystal growth techniques and substrates have been illustrated.

The investigation of martial quality has been performed. Structural, microstructural and optical properties have been studied for PIN structures with InGaN as absorbent layer varying from 10 to 50 % of indium content. The material quality has been compared in each other for different configuration as SL InGaN and MQW absorbent layers. Several types of defects have been investigated by TEM instrument with the help of the cross section FIB foils. Surface morphology have been studied and correlated to the TEM results. It has been noted that the material quality decreases when increasing the indium content. The incorporation of indium above 10% in the SL InGaN configuration creates areas of high concentration of indium and cavities leading to increased surface roughness to 3D defects. Consequently, the material is plastically relaxed creating numerous structural defects. MQW configuration has revealed an optimized structure even in higher indium insertion in the InGaN layer. MQW configuration exhibits a higher material quality than SL configuration due lower density of defects. Results from EDX analysis have reflected an estimation of optical properties in terms of indium content

and wavelength cut-off of the absorbent layers. TEM investigation has been a significant tool to evaluate the quality of material. However, the micro-zone analysis gives only an estimation of the growth quality in small area, structural defects may vary from zone to other. Critical indium content in InGaN layer is observed at 50% resulting high density of defects and very rough surface. Higher indium content in the InGaN layer will affect the photodiode performance and high leakage current has been expected during the next step of fabrication.

Among the most important optical property which possesses GaN material and related alloys is the absorption coefficient which directly influence the device operation. It has value in excess of $10^5 cm^{-1}$ comparing to GaAs (10^4 cm^{-1}) and Si (10^3 cm^{-1}). It means the incident light will be efficiently absorbed in very short thickness of material. This parameter allows designing a PIN structure with very thin intrinsic layer which will reduce the transit time and subsequently increasing the cut-off frequency. This makes GaN a primary candidate for high speed photodetectors.

Optical waveguiding properties have been studied for bulk and porous GaN structures. Samples have been grown and structured by KAIST and characterized in IEMN. Prism coupling and ellipsometry techniques have been used in order to investigate the refractive index. The dispersion of refractive index for several porous GaN has been studied and compared to the GaN bulk material. Profile of the refractive index is demonstrated throughout the nanostructured and GaN layers. The control of the refractive index into GaN is therefore fundamental for the design of active and passive optical devices.

The fabrication of photodiode has been performed using different designs. The first stage has the realization of large-scale photodiode ranging from 100×100 µm^2 to 1000×1000 µm^2. It has allowed the validation of the material quality as well as the exploration of the photodiode response in large scale. Besides, the optimization of the fabrication process has been the objective of the large-sale photodiode fabrication in terms of photolithography, etching, metal deposition and passivation. After that, the second phase has been the fabrication of µ-photodiodes in planar and vertical configurations. It has permitted to evaluate the photodiode size effect on the photodiode capacitance which affect the photodiode speed, and consequently the cut-off frequency.

The study of the GaN deep etching using ICP has clarified the difficulty of etching process. Several cover-plates have been used to optimize the profile depth. The metal mask has showed an enhanced cover-plate permitting to reach 6 µm of etching depth with less columnar defects and high-selectivity. The SiO_2 etching mask has demonstrated a limitation resulting damaged areas and the formation of columnar defects.

The optimization of fabrication process has been an important factor to achieve photodiodes ranging from 5×5 µm^2 to 100×100 µm^2. The investigation of material quality in the second chapter has provided a significant information regarding the performance of the fabricated devices. It has showed the influence of the indium content on the electrical response of the photodiode.

The study of annealing effect has provided an optimal configuration for the large-scale photodiode. For both n and p-contacts, 500°C for 2 minutes under N_2 atmosphere have been considered resulting lower serial resistance. It has represented a lower turn-on voltage attributed to the reduction of the gallium oxide layer due to the N_2 atmosphere effect.

The MQW effect on the device performance has been studied. The comparison with SL configuration has showed lower serial resistance for MQW sample related to I-V slope. It has proved the enhanced quality of material crystallography for the MQW configuration.

The influence of the growth technique on the device performance has been electrically investigated. Static response for fabricated photodiodes grown by MOCVD and MBE techniques have been examined. MOCVD samples have demonstrated good electrical response with low serial resistance and lower leakage current in reverse bias.

To investigate the photodiode response, EQE has been represented a significant element to evaluate different photodiodes with different indium content and different dimension of p-active layers. The measurement of photocurrent using laser source has been prepared in order to investigate the photodiode performance. EQE has been investigated by means of monochromatic incident light in order to detect the absorbed wavelength providing the higher photocurrent. The wavelength of 370 nm has exhibited the higher photocurrent value leading to 32% of EQE for sample MQ10-1. Slightly lower photocurrents have been noted for wavelengths in the range of 380 to 420 nm which represents the near-band edge transition leading to EQE lower than 22%. In

the case of samples with 30% of indium, the maximum EQE value has been obtained at 500 nm for 10% of EQE. It has be related to the high density of defects and consequently higher leakage currents.

Using laser source, samples have been subjected to laser excitation in order to study the related photocurrent in reverse bias as a function of the laser power. Photocurrents have been observed with a saturation zone starting from -12 V until photodiode breakdown at -20 V. The investigation of such saturation zone have been possibly associated to the carrier velocity in the GaN material and related alloys. Electrical field calculation has demonstrated that holes velocity could be a probable reason of the late photocurrent saturation. The cut-off frequency related to RC constant has been extracted using reported capacitance as a function of photodiode mesa dimensions. Cut-off frequency ranging from 9 MHz to 940 MHz have been calculated for large-scale photodiodes demonstrating the influence of the capacitance on the dynamic response of device.

For the planar µ-photodiodes, the fabrication process has been optimized in order to achieve micro mesa with 1 µm depth etching. Large contact pads have been designed to be extended away of mesa in order to connect probes. Using TLM, contact resistivity for p and n-type has been improved in terms of metal combination and annealing parameters. Enhanced I-V characteristic of photodiodes passivated by SiO_2 sputter deposition has demonstrated better electrical response comparing to devices using SiO_2 PECVD. Concerning the electrical characterization, lower photocurrent values with saturation zone have been observed comparing to large-scale photodiode due to the p-active layer dimension. C-V characteristics have demonstrated higher cut-off frequency of 6.09 GHz for µ-photodiode diameter of 10 µm. Noise measurement has been performed in order to achieve the cut-off frequency using Noise-Figure-Meter. The reported frequency at -3dB is almost 1.45 GHz for 25 µm photodiode diameter.

Vertical µ-photodiodes have been fabricated with high etch profile of 6 µm exhibiting more leakage current than the planar photodiode. Sidewall contaminations containing residues of metal etching mask have been a possible reason of higher leakage current. The shift of turn-on voltage is probably related to the reduction of metal thickness along the vertical profile.

According to fabrication process used in this thesis, optimization of photodiode fabrication are required. An improvement of design 2 has been discussed in order to achieve high quality of p-contact. The disposition of p-contact as first step will permit to avoid any surface contamination due to different technological process. The only disadvantage of this process is the annealing temperature. As the p-contact requiring lower annealing temperature is deposited before n-contact which required higher temperature, we are in the obligation to make one annealing process for both contacts. This temperature of this annealing have been already experimented in design 1 with optimal configuration in intermediate temperature. Both n and p-contacts are expected to be annealed in 500°C for 2 minutes under N_2 atmosphere. However, deep study of annealing parameters is crucial to enhance the device response. Different parameters as temperature, atmosphere and annealing time are subjected to be altered in order to obtain the optimal configuration.

An improved micro-photodiode fabrication has been designed in order to deposit p-contact as first step (design 3). It will be similar than the design 2 but the first optical mask will be dedicated to p-contact deposition. More optimizations in the fabrication of μ-photodiodes using design 3 have to be reached in order to achieve high quality of planar and vertical devices.

Concerning the photodiode characterization, it has been noted that the reduced p-active area and the lower photocurrent values have led to earlier saturation of photocurrent. However, the investigation of such saturation zone could be associated to the carrier velocity in the GaN material and related alloys. Consequently the saturation of holes velocity could be a probable reason. In our case, the saturation of photocurrent has been observed at -12 V corresponding 1200 kV/cm of electrical filed. The measurement of photocurrent saturation versus reversed bias voltage could be a way to extract the holes saturation velocity versus electrical feld. A profond study of this phenomena could be significant to be developped in the future.

In the C-V measurement, it has been noted the parasitic capacitance is highly considered. It is known that this capacitance is responsible of cut-off frequency reduction. Design of coplanar waveguiding lines should be improved in order to reduce the influence of the parasitic capacitance. Coplanar waveguiding lines with reduced metal width and length could be a resolution of this issue leading to lower total capacitance.

The challenge in the achievement of high quality P-GaN/I-InGaN/N-GaN layers is the growth of high quality p-doped GaN layer, besides the deposition of good quality of p-type ohmic contact. A possible solution in the replacement of p-GaN layer by p-InGaN layer could be investigated. The higher concentration of holes in the p-InGaN layer comparing to p-GaN layer may improve the p-layer. The activation energy of acceptors is lower in the p-InGaN layer due to lower energy bandgap.

The Uni-Travelling-Carrier (UTC) photodiode proposed by Ishibashi et al. (NTT Lab) has demonstrated the possibility to provide high speed and high saturation output [72]. The structure is based on the separation of the absorption zone and the depletion region (Figure 3.50). Consequently, among the photogenerated carriers in the absorption layer, only electrons move across toward the depletion zone, while the holes which are the majority charges generated in p-type region do not have hand in the time transit of the structure. In addition, due to the high mobility and the high saturation velocity of the electrons comparing to holes, the saturation phenomena occurs at a higher saturation current density. The growth of such UTC structure should be discussed with grower in order to inspect the possibility to grow p-InGaN layer as absorption layer as well as the p^+ layer.
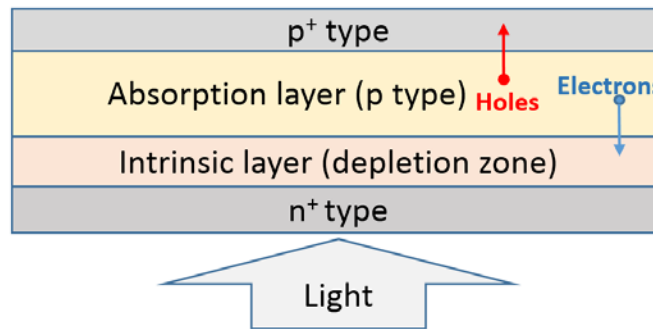

Figure 3.117: UTC-photodiode structure.

During electrical characterizations, the high intensity of light in LED mode have been observed when direct bias is applied. Figure 3.51 demonstrates the designed photodiode used primarily as photodetector but exhibited high intensity of LED light. Figure 3.51 (a and b) illustrates a photodiode of 100×100 μm^2, (e) illustrates a photodiode of 50×50 μm^2, (c and d) illustrates a photodiode of 25×25 μm^2 and (f) shows photodiode array of 25×25 μm^2. Recently, investigation on InGaN-based µ-LED has been reported [15]. A µ-LED array has been reported

for Visible-Light Communications (VLC) [16]. It reveals higher modulation bandwidths comparing to the broad-area LED due their capability to be driven at higher current densities using µ-LED [17].
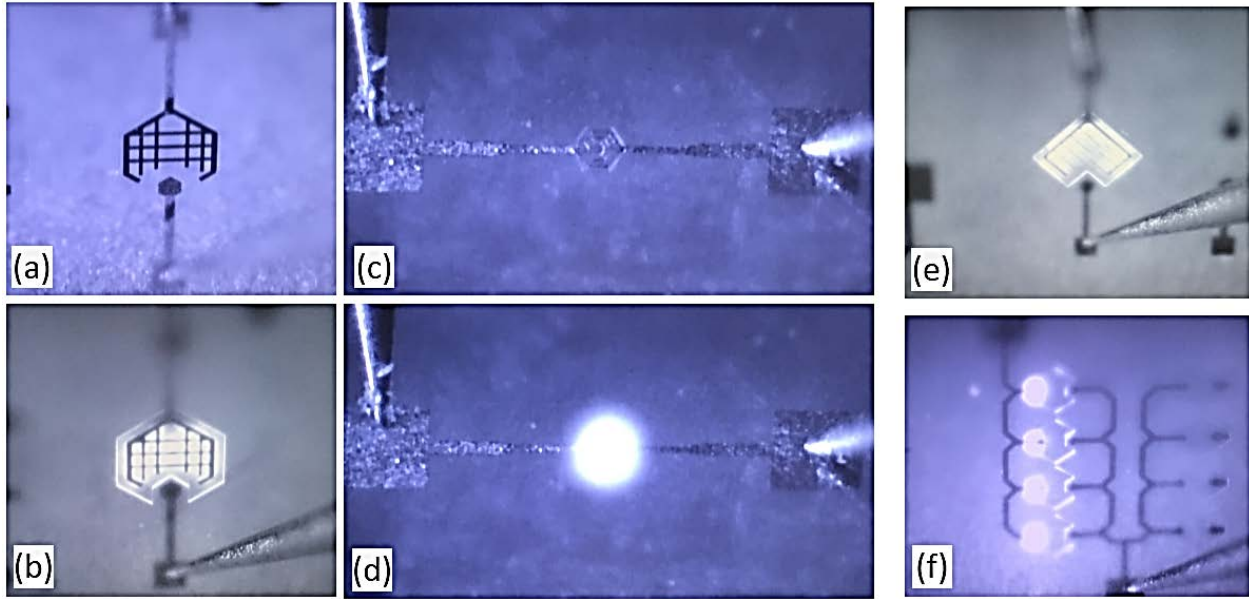

Figure 3.118: High intensity of LED when direct bias is applied.

Light Fidelity (Li-Fi) as a consequent application using µ-LED deserves to be studied. Nowadays, the wireless connectivity has become a fundamental commodity leading to massive deployment of wireless systems. The limitation of RF spectrum has been a major concern due to the spatial reuse and channel interference. Visible light communication (VLC) has been introduced as a potential technique to avoid the RF limitation [74]. Similar to Wi-Fi (Wireless Fidelity), Li-Fi is a part of optical wireless communications (OWC) technology. It is employed instead of radio frequency waves and carries much more information up to 100 times faster than existing contemporary Wi-Fi technique. It is a wireless technology using visible light, infra-red and near ultraviolet communication. Li-Fi is supposed to be a high speed and bidirectional network technology and could be a complement to Wi-Fi technology, cellular data communication or even being as a potential alternative. The term Li-Fi has been invented in 2011 by Harald Haas "professor of mobile communications at the University of Edinburgh in United Kingdom" at his TED Global Talk where he introduced the idea of "Wireless data from every light" [75]. His idea is to transmit far more data efficiently and do it in the way that is more secure and widespread using a single LED. It means one more functionality will be added to the

illumination of LED and will be the wireless data transmission by fitting small microchip in order to achieve cleaner and greener future. Li-Fi is supposed to move to higher frequency such as it is classified nm-wave communication. Moreover, Li-Fi is more secure than Wi-Fi because the reach of light is limited by walls and light cannot penetrates it while Wi-Fi is susceptible to be hacked. Figure 3.52 shows the concept of indoor Li-Fi technology (image from The Indian Awaaz).
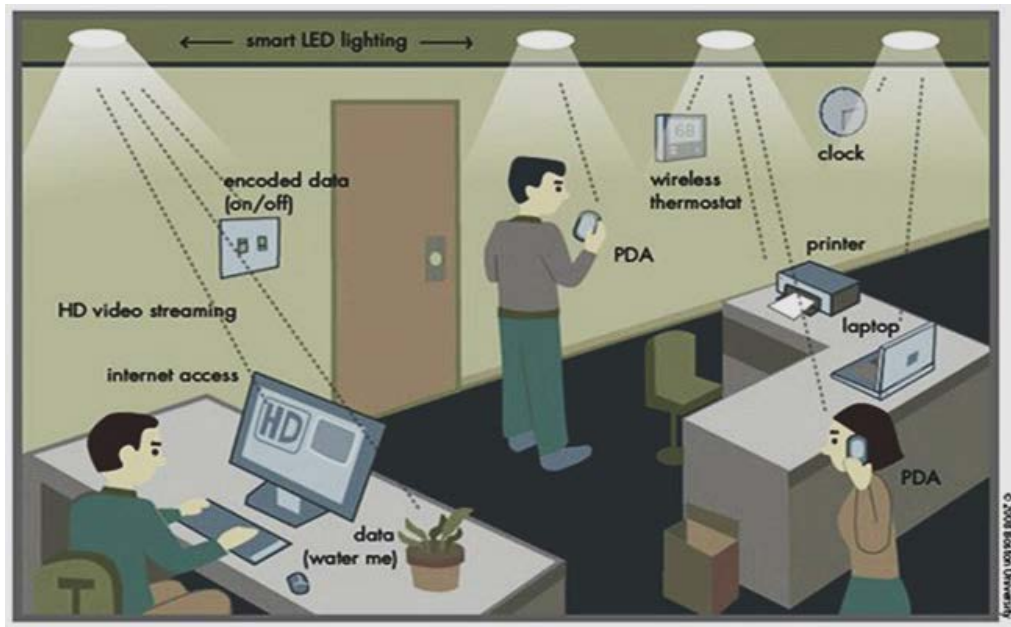
Figure 3.119: Concept of indoor Li-Fi technology.

As explained previously, our primary objective has been to optimize a high speed GaN-based μ-photodetector. During our fabrication process, the quality of fabricated photodiode has been significant including high intensity of light. This will offer the possibility to work toward the GaN-based μ-LED such as perspective work following this thesis. The different compositions of InGaN in the PIN structures may well provide a widespread study in diverse color LED.

References

[1] J. K. Ho, C. S. Jong, C. C. Chiu, C. N. Huang, C. Y. Chen, and K. K. Shih, "Low-resistance ohmic contacts to p-type GaN," *Appl. Phys. Lett.* , vol. 74, pp. 1275–1277, 1999.

[2] M. Suzuki, T. Kawakami, T. Arai, S. Kobayashi, Y. Koide, T. Uemura, N. Shibata, and M. Murakami, "Low-resistance Ta/Ti ohmic contacts for p-type GaN," *Appl. Phys. Lett.*, vol. 74, pp. 275–277, 1999.

[3] S. Belahsene, G. Patriarche, D. Troadec, S. Sundaram, A. Ougazzaden, A. Martinez, and A. Ramdane, "Microstructural and electrical investigation of Pd/Au ohmic contact on p-GaN," *J. Vac. Sci. Technol. B, Nanotechnol. Microelectron. Mater. Process. Meas. Phenom.*, vol. 33, no. 1, p. 010603, Jan. 2015.

[4] Y. Bai, J. Liu, H. J. Shen, P. Ma, X. Y. Liu, and L. W. Guo, "Effect of annealing on the characteristics of Pd/Au contacts to p-type GaN/Al0.45Ga0.55N," *J. Electron. Mater.*, vol. 41, no. 11, pp. 3021–3026, 2012.

[5] N. C. Das, M. L. Reed, A. V. Sampath, H. Shen, M. Wraback, R. M. Farrell, M. Iza, S. C. Cruz, J. R. Lang, N. G. Young, Y. Terao, C. J. Neufeld, S. Keller, S. Nakamura, S. P. Denbaars, U. K. Mishra, and J. S. Speck, "Optimization of annealing process for improved InGaN solar cell performance," *J. Electron. Mater.*, vol. 42, no. 12, pp. 3467–3470, 2013.

[6] W. Macherzyński, A. Stafiniak, A. Szyszka, J. Gryglewicz, B. Paszkiewicz, R. Paszkiewicz, and M. Tłaczała, "Effect of annealing temperature on the morphology of ohmic contact Ti / Al / Ni / Au to n -AlGaN / GaN heterostructures," *Opt. Appl.*, vol. XXXIX, no. 4, pp. 1–7, 2009.

[7] Y. Koide, T. Maeda, T. Kawakami, S. Fujita, T. Uemura, N. Shibata, and M. Murakami, "Effects of annealing in an oxygen ambient on electrical properties of ohmic contacts to p-type GaN," *J. Electron. Mater.*, vol. 28, no. 3, pp. 341–346, 1999.

[8] V. M. Bermudez, "Study of oxygen chemisorption on the GaN(0001)-(1x1) surface," *J. Appl. Phys.*, vol. 80, no. 0001, pp. 1190–1200, 1996.

[9]   X. A. Cao, S. J. Pearton, G. Dang, A. P. Zhang, F. Ren, and J. M. Van Hove, "Effects of interfacial oxides on Schottky barrier contacts to n- and p-type GaN," *Appl. Phys. Lett.*, vol. 75, pp. 4130–4132, 1999.

[10]   C. Huh, S.-W. Kim, H.-S. Kim, H.-M. Kim, H. Hwang, and S.-J. Park, "Effects of sulfur treatment on electrical and optical performance of InGaN/GaN multiple-quantum-well blue light-emitting diodes," *Appl. Phys. Lett.*, vol. 78, no. 12, p. 1766, 2001.

[11]   J.-L. Lee, "Transparent Pt Ohmic Contact on p-Type GaN with Low Resistivity Using (NH[sub 4])[sub 2]S[sub x] Treatment," *Electrochemical and Solid-State Letters*, vol. 3. p. 53, 1999.

[12]   J. K. Kim, K.-J. Kim, B. Kim, J. N. Kim, J. S. Kwak, Y. J. Park, and J.-L. Lee, "Effects of surface treatment using aqua regia solution on the change of surface band bending of p-type GaN," *J. Electron. Mater.*, vol. 30, pp. 129–133, 2001.

[13]   S. Nakamura, N. Senoh, N. Iwasa, and S. I. Nagahama, "High-Brightness InGaN Blue, Green and Yellow Light-Emitting-Diodes with Quantum-Well Structures," *Japanese J. Appl. Phys. Part 2-Letters*, vol. 34, no. 7A, pp. L797–L799, 1995.

[14]   X. Zheng, R. H. Horng, D. S. Wuu, M. T. Chu, W. Y. Liao, M. H. Wu, R. M. Lin, and Y. C. Lu, "High-quality InGaN/GaN heterojunctions and their photovoltaic effects," *Appl. Phys. Lett.*, vol. 93, no. 2008, pp. 2006–2009, 2008.

[15]   W. Yang, S. Zhang, J. J. D. McKendry, J. Herrnsdorf, P. Tian, Z. Gong, Q. Ji, I. M. Watson, E. Gu, M. D. Dawson, L. Feng, C. Wang, and X. Hu, "Size-dependent capacitance study on InGaN-based micro-light-emitting diodes," *J. Appl. Phys.*, vol. 116, no. 4, p. 044512, Jul. 2014.

[16]   D. Tsonev, H. Chun, S. Rajbhandari, J. J. D. McKendry, S. Videv, E. Gu, M. Haji, S. Watson, A. E. Kelly, G. Faulkner, M. D. Dawson, H. Haas, and D. O'Brien, "A 3-Gb/s single-LED OFDM-based wireless VLC link using a gallium nitride micro-LED," *IEEE Photonics Technol. Lett.*, vol. 26, no. 7, pp. 637–640, 2014.

[17]   J. J. D. McKendry, D. Massoubre, S. Zhang, B. R. Rae, R. P. Green, E. Gu, R. K.

Henderson, a. E. Kelly, and M. D. Dawson, "Visible-Light Communications Using a CMOS-Controlled Micro-Light- Emitting-Diode Array," *J. Light. Technol.*, vol. 30, no. 1, pp. 61–67, 2012.

[18] S. Pearton, C. Abernathy, F. Ren, J. Lothian, P. Wisk, and A. Katz, "Dry and wet etching characteristics of InN, AlN, and GaN deposited by electron cyclotron resonance metalorganic molecular beam epitaxy," *J. Vac. Sci. Technol. A*, vol. 11, no. 4, p. 1772, 1993.

[19] Y. Zhang, M. Sun, D. Piedra, M. Azize, X. Zhang, T. Fujishima, and T. Palacios, "GaN-on-Si vertical schottky and p-n diodes," *IEEE Electron Device Lett.*, vol. 35, no. 6, pp. 618–620, 2014.

[20] A. Kadiyala, K. Lee, L. Rodak, L. Hornak, D. Korakakis, and J. Dawson, "Improvement in the Light Extraction of Blue InGaN/GaN-Based LEDs Using Patterned Metal Contacts," *IEEE J. Electron Devices Soc.*, no. c, pp. 1–1, 2013.

[21] J. Yang, D. G. Zhao, D. S. Jiang, P. Chen, J. J. Zhu, Z. S. Liu, L. C. Le, X. G. He, X. J. Li, H. Yang, Y. T. Zhang, and G. T. Du, "Photovoltaic response of InGaN/GaN multi-quantum well solar cells enhanced by inserting thin GaN cap layers," *J. Alloys Compd.*, vol. 635, pp. 82–86, 2015.

[22] H. Yoshida, T. Urushido, H. Miyake, and K. Hiramatsu, "In situ monitoring of GaN reactive ion etching by optical emission spectroscopy," *Japanese J. Appl. Phys. Part 2-Letters*, vol. 40, no. 4A, pp. L313–L315, 2001.

[23] S. C. Hung, Y. K. Su, S. J. Chang, S. C. Chen, L. W. Ji, T. H. Fang, L. W. Tu, and M. Chen, "Self-formation of GaN hollow nanocolumns by inductively coupled plasma etching," *Appl. Phys. A Mater. Sci. Process.*, vol. 80, no. 8, pp. 1607–1610, 2005.

[24] S. W. Zeng, B. P. Zhang, J. W. Sun, J. F. Cai, C. Chen, and J. Z. Yu, "Substantial photo-response of InGaN p–i–n homojunction solar cells," *Semicond. Sci. Technol.*, vol. 24, no. 5, p. 055009, May 2009.

[25] J.-P. Shim, M. Choe, S.-R. Jeon, D. Seo, T. Lee, and D.-S. Lee, "InGaN-Based p–i–n Solar

Cells with Graphene Electrodes," *Appl. Phys. Express*, vol. 4, no. 5, p. 052302, May 2011.

[26] D.-W. Kim, J. C. Bae, W. J. Kim, H. K. Baik, J.-M. Myoung, and S.-M. Lee, "The improvement of electrical properties of Pd-based contact to p-GaN by surface treatment," *J. Electron. Mater.*, vol. 30, pp. 183–187, 2001.

[27] X. Li, Z. Shi, G. Zhu, M. Zhang, H. Zhu, and Y. Wang, "High efficiency membrane light emitting diode fabricated by back wafer thinning technique," *Appl. Phys. Lett.*, vol. 105, no. 3, pp. 1–5, 2014.

[28] Z. Shi, X. Li, G. Zhu, Z. Wang, P. Gr??nberg, H. Zhu, and Y. Wang, "Characteristics of GaN-based LED fabricated on a GaN-on-silicon platform," *Appl. Phys. Express*, vol. 7, no. 8, pp. 0–4, 2014.

[29] S. Oh, K.-S. Shin, S.-W. Kim, S. Lee, H. Yu, S. Cho, and K.-K. Kim, "Enhancement of Light Extraction Efficiency of GaN-Based Light-Emitting Diodes by ZnO Nanorods with Different Sizes," *J. Nanosci. Nanotechnol.*, vol. 13, no. 5, pp. 3696–3699, 2013.

[30] T. Sreenidhi, J. Chatterjee, A. DasGupta, and N. DasGupta, "Optimization of ohmic contact for the fabrication of InGaN/GaN multiple quantum well blue LED," vol. 8549, p. 85492M, 2012.

[31] S. J. Chang, W. C. Lai, Y. K. Su, S. Member, J. F. Chen, C. H. Liu, and U. H. Liaw, "InGaN – GaN Multiquantum-Well Blue and Green Light-Emitting Diodes," vol. 8, no. 2, pp. 278–283, 2002.

[32] Y.-L. Tsai, C.-C. Lin, H.-V. Han, C.-K. Chang, H.-C. Chen, K.-J. Chen, W.-C. Lai, J.-K. Sheu, F.-I. Lai, P. Yu, and H.-C. Kuo, "Improving efficiency of InGaN/GaN multiple quantum well solar cells using CdS quantum dots and distributed Bragg reflectors," *Sol. Energy Mater. Sol. Cells*, vol. 117, pp. 531–536, 2013.

[33] M. Wraback, H. Shen, J. C. Carrano, C. J. Collins, J. C. Campbell, R. D. Dupuis, M. J. Schurman, and I. T. Ferguson, "Time-resolved electroabsorption measurement of the transient electron velocity overshoot in GaN," *Appl. Phys. Lett.*, vol. 79, no. 9, pp. 1303–1305, 2001.

[34] J. Kolnik, I. H. Oguzman, K. F. Brennan, R. Wang, P. P. Ruden, and Y. Wang, "Electronic transport studies of bulk zincblende and wurtzite phases of GaN based on an ensemble Monte Carlo calculation including a full zone band structure," *J. Appl. Phys.*, vol. 78, no. 2, pp. 1033–1038, 1995.

[35] I. H. Oguzman, J. Kolnik, K. F. Brennan, R. Wang, T.-N. Fang, and P. P. Ruden, "Hole transport properties of bulk zinc-blende and wurtzite phases of GaN based on an ensemble Monte Carlo calculation including a full zone band structure," *J. Appl. Phys.*, vol. 80, no. 8, pp. 4429–4436, 1996.

[36] J.-M. Lee, C. Huh, D.-J. Kim, and S.-J. Park, "Dry-etch damage and its recovery in InGaN/GaN multi-quantum-well light-emitting diodes," *Semicond. Sci. Technol.*, vol. 18, no. 6, pp. 530–534, Jun. 2003.

[37] H.-M. Kim, C. Huh, S.-W. Kim, N.-M. Park, and S.-J. Park, "Suppression of Leakage Current in InGaN/GaN Multiple-Quantum Well LEDs by N[sub 2]O Plasma Treatment," *Electrochem. Solid-State Lett.*, vol. 7, no. 11, p. G241, 2004.

[38] Z. Zhang, S. T. Tan, Z. Kyaw, W. Liu, Y. Ji, Z. Ju, X. Zhang, X. W. Sun, and H. V. Demir, "p-doping-free InGaN/GaN light-emitting diode driven by three-dimensional hole gas," vol. 263501, pp. 0–5, 2013.

[39] L. F. Feng, Y. Li, C. Y. Zhu, H. X. Cong, and C. D. Wang, "Negative terminal capacitance of light emitting diodes at alternating current (AC) biases," *IEEE J. Quantum Electron.*, vol. 46, no. 7, pp. 1072–1075, 2010.

[40] W. Yang, S. Zhang, J. J. D. Mckendry, J. Herrnsdorf, P. Tian, Z. Gong, Q. Ji, I. M. Watson, E. Gu, M. D. Dawson, L. Feng, C. Wang, and X. Hu, "Size-dependent capacitance study on InGaN-based micro-light-emitting diodes," vol. 044512, 2014.

[41] M. E. Lin, Z. Ma, F. Y. Huang, Z. F. Fan, L. H. Allen, and H. Morkoç, "Low resistance ohmic contacts on wide band-gap GaN," *Appl. Phys. Lett.*, vol. 64, pp. 1003–1005, 1994.

[42] Z. Fan, S. N. Mohammad, W. Kim, Ö. Aktas, A. E. Botchkarev, and H. Morkoç, "Very low resistance multilayer Ohmic contact to n-GaN," *Appl. Phys. Lett.*, vol. 68, pp. 1672–

1674, 1996.

[43] A. Soltani, A. BenMoussa, S. Touati, V. Hoël, J.-C. De Jaeger, J. Laureyns, Y. Cordier, C. Marhic, M. a. Djouadi, and C. Dua, "Development and analysis of low resistance ohmic contact to n-AlGaN/GaN HEMT," *Diam. Relat. Mater.*, vol. 16, no. 2, pp. 262–266, Feb. 2007.

[44] J. K. Kim, J.-L. Lee, J. W. Lee, H. Eoi Shin, Y. Jo Park, and T. Kim, "Low resistance Pd/Au ohmic contacts to p-type GaN using surface treatment," *Appl. Phys. Lett.*, vol. 73, no. 1998, p. 2953, 1998.

[45] J.-P. GOUY, "ETUDE COMPARATIVE DE LA PHOTODIODE PIN DE LA PHOTODIODE A AVALANCHE ET DU PHOTOCONDUCTEUR SUR MATERIAUX I l 1 - V," *Ph.D Thesis*, 1989.

[46] M. Te Lin, S. P. Ying, M. Y. Lin, K. Y. Tai, and J. C. Chen, "High power LED package with vertical structure," *Microelectron. Reliab.*, vol. 52, no. 5, pp. 878–883, 2012.

[47] J. H. Lee, J. T. Oh, S. B. Choi, Y. C. Kim, H. I. Cho, and J. H. Lee, "Enhancement of InGaN-based vertical LED with concavely patterned surface using patterned sapphire substrate," *IEEE Photonics Technol. Lett.*, vol. 20, no. 5, pp. 345–347, 2008.

[48] H. Kim, K. Kim, S. Lee, and K. Baik, "Design and fabrication of vertical-injection GaN-based light-emitting diodes," vol. 19, no. July, pp. 937–942, 2011.

[49] H. Kim, K. K. Kim, K. K. Choi, H. Kim, J. O. Song, J. Cho, K. H. Baik, C. Sone, Y. Park, and T. Y. Seong, "Design of high-efficiency GaN-based light emitting diodes with vertical injection geometry," *Appl. Phys. Lett.*, vol. 91, no. 2, 2007.

Abstract:

III-Nitrides semi-conductor materials with flexible bandgap has revealed a major interest for the future development of optoelectronic devices. The aim of this work is to study, design and develop a PIN photodiode based on $In_xGa_{1-x}N$ and GaN materials deposited by MOCVD and MBE. Different configurations are considered for the InGaN absorbent layer: a single layer (SL) and multiple quantum wells (MQW). In order to observe the shift in the absorption wavelength, the composition of the InGaN layer ranges from10 to 50%. Structural, microstructural and optical analysis are performed using XRD, TEM, PL, AFM and SEM. We have verified that the material quality promptly degrades when increasing the indium content which impacts on the device performances. The design of the PIN structure is governed by the limitation of the active surface (from 25 to 10^4 μm^2) in order to limit the global capacitance. Different prototypes are fabricated in clean room before characterization. Static and dynamic characterizations have been realized to qualify the photodiode response. We have investigated the influence of the indium content on the electrical performance. For the large-scale photodiodes, photocurrent value has reached a maximum of 3.2 mA with laser power of 75 mW demonstrating cut-off frequency of 940 MHz. μ-photodiode has revealed 395 μA of maximal photocurrent with cut-off frequency of 1.45 GHz.

Keywords : nitrides semiconductor ; photodiode ; design and fabrication

Résumé :

Les matériaux semi-conducteurs à base de nitrures disposant de largeur de bande interdite allant de 0,7 à 6 eV, connaissent un intérêt sans cesse croissant pour le développement de dispositifs optoélectroniques du futur. Le but de ces travaux est d'étudier, de concevoir et de développer une photodiode de type PIN à base de matériaux $In_xGa_{1-x}N$ et GaN déposés par MOCVD et MBE. Elle est étudiée en considérant différentes configurations de la couche absorbante InGaN, à savoir une couche simple épaisse (SL) ou des puits quantiques (MQW). Toutefois en jouant sur la composition x en indium de la couche InGaN, cela permet la mise au point de différente longueur d'onde d'absorption dans la structure PIN. Des analyses structurales, microstructurales et optiques ont été réalisées par RX, TEM, PL, AFM et MEB pour des photodiodes PIN avec une couche absorbante InGaN de composition en indium variant de 10 à 50%. Nous avons pu vérifier que la qualité du matériau se dégradait lorsque l'on augmentait la teneur en indium et que cela impactait sur les performances de composants. La conception de la structure PIN a été définie pour différentes géométries de photodiode (de 25 à 10^4 μm^2). Des caractérisations statiques et dynamiques de dispositifs fabriquées ont été réalisées afin d'obtenir la réponse de la photodiode. Pour les photodiodes à grande échelle, la valeur de photocourant a atteint un maximum de 3,2 mA démontrant une fréquence de coupure de 940 MHz. La μ-photodiode a révélé 395 μA de photocourant et une fréquence de coupure 1,45 GHz.

Mots-clés : nitrures semiconducteurs ; photodiodes ; conception et fabrication